Development of High Performance Gas Separation Membranes through Intelligent Catalyst and Monomer Design

A Dissertation Presented for the
Doctor of Philosophy
Degree
The University of Tennessee, Knoxville

Kevin Richard Gmernicki
May 2017

Dedication

To my wife Jennie and my mom Patricia; your bravery, faith, wisdom, patience, and love are a constant inspiration to me and have helped me to achieve what I thought was impossible.

Acknowledgements

To my advisor Brian, thank you for being the perfect combination of mentor and friend that allowed for me to grow as both a professional and an intellectual. You are one of the most creative and thorough scientists I have encountered during my academic career and I truly believe that you will continue to break huge ground in the fields that you decide to explore. I wish you the best of luck.

To my committee, Dr. David Baker, Dr. Jimmy Mays, and Dr. Mike Kilbey, I am so glad that I chose each of you. Thank you for taking the time out of your schedules to read my papers, listen to my presentations, and provide excellent feedback that I always took to heart. I feel that I am a better scientist today because of each of your individual contributions.

To all my past and present group members, I consider you all family. You helped make the day-to-day frustrations of research so much more enjoyable and you were always willing to help without question. I can only hope to have coworkers like you in the future. In particular, Lauren, I cannot think of anyone else that I would have rather shared my graduate experience with. You have taught me so much and always helped me stay on track. I wish you nothing but happiness and success in the future. Curtis, you are one of the smartest and most driven people I have ever met. Our discussions helped me through a lot of my research roadblocks and you are an absolutely awesome friend that I only wish I met sooner. Chris, you have been an excellent partner and were absolutely integral in a lot of the success I was able to achieve. Sharing an office was always a blast and I always enjoyed working with you. I wish you the greatest success in the rest of your graduate career and beyond. Lastly, Matt and Dylan, you guys were a tremendous help in the lab and were always a joy to have around.

To my collaborators and colleagues, your willingness to constantly share your insight was instrumental in my success and I extend my deepest gratitude. Kevin and Professor Freeman, thank you for taking the time to share your instrument designs and solidifying our foundation in the theory of membrane separations. To my ORNL collaborators, your additional advisement and constructive discussions were continuously helpful in choosing our research directions. Thank you for including us.

To my wife Jennie, you are simply the best. Although it was never easy, you never stopped supporting me. I appreciate it so much and honestly believe that I could not have done this without you. I love you so much and am ecstatic to start this next chapter of our life together.

To my friends and family, to this day I still don't understand what I have done to deserve the support system you constantly provide. Mom and Luthin, you two are absolutely the best and I can only aspire to be like you one day. Katelyn, you and I have been through so much together and I feel that we have grown closer every year. You have helped me in ways that you haven't even realized and I am so proud of the strong woman you have become. Corey and Christian, you guys have been with me every step of the way and provided a perfect balance to help me relax and get my mind off of the tough situations. Janet and Larry, spending time with both of you is always a blast and I take all of your advice to heart.

Abstract

Polymer membranes are a valuable tool for separating components of liquid and gas mixtures. Heavily inspired by biological systems, the idea of using the intrinsic properties of polymers to perform otherwise energy-intensive tasks is attractive for applications such as water desalination, natural gas sweetening, and post-combustion carbon capture. Of particular interest to our research group, post-combustion carbon capture is a promising potential solution aimed at reducing the carbon footprint involved with production, transportation, and storage of electrical energy generation.

Every year, the United States produces close to seven billion metric tons of carbon dioxide, of which a significant portion is generated by coal-fired power plants. With a lack of significant research breakthroughs in renewable energy sources, the continued use of coal is necessary to maintain current energy demands. To consume this resource responsibly, researchers continue to develop methods to minimize the release of greenhouse gas emissions from the combustion of coal and other fossil fuels. Polymer membranes offer an industrially scalable solution that can be easily implemented into existing infrastructure and operate at a fraction of the cost of other possible carbon sequestration solutions. However, implementing membrane solutions for this particular gas separation is extremely demanding in terms of chemical stability, thermal stability, and raw membrane performance, which requires materials designed specifically for this application.

Described herein, is a body of work directed towards the synthesis of new materials that have not been investigated for the separation of carbon dioxide and nitrogen previously. Throughout the membrane design, we chose to emphasize polymer structures with rigid backbones, significant mechanical integrity, and polar functionality that will be attracted towards carbon dioxide more so than nitrogen. These macromolecules were made via different polymerization techniques and required specific catalyst design in order to obtain the desired functionality. The results are polymer membranes that have some of the highest performance for the separation of carbon dioxide and nitrogen while maintaining a unique combination of excellent processability, mechanical strength, thermal stability, and optical transparency that could be useful in other engineering applications.

Table of Contents

List of Tables

List of Figures

Chapter 1. Introduction

1.1 Membranes

The term membrane applies to any thin material that acts as a selective barrier towards a chemical mixture (**Figure 1**). Following the discovery of this behavior, the mid-1900's consisted of significant research efforts to tailor these materials for a wide variety of commercial applications due to their simplicity, flexible operating temperatures, industrial scalability, and low operating costs.[1] As of 2014, the United States' membrane industry is valued at 4.2 billion dollars with market growth projected through 2020. The key economic sectors driving this growth include water treatment facilities, medicinal and pharmaceutical products, food and beverage production, industrial chemical processing, and gas separation modules. More specifically, tandem membrane systems of microfiltration, ultrafiltration, nanofiltration, and reverse osmosis enable water treatment plants to filter additional contaminants and achieve higher levels of purity.[2-4] In the medicinal industry, membrane technology produced revolutionary treatments such as hemodialysis and synthetic kidney transplants to clear the body of harmful agents when organs fail.[5-6] Lastly, high-performance polymer membranes allow power generators and compressors to be powered in remote locations by purifying natural gas directly at the work site.[7] Each application has specific design characteristics in order to maximize membrane performance but, virtually all of these industries stand to benefit from the fundamental research and development into new membrane materials. As membranes continue to evolve from simple biopolymer such as cellulose-based materials to custom-designed polymer assemblies, their potential to revolutionize all chemical separation processes becomes encouraging.

1.2 Polymer Membranes for Gas Separation

Commercial synthetic membranes span a wide assortment of materials that include glass, metals, ceramics, proteins, organic polymers, and more. In essence, any material that can be made into a thin-layer to act as a barrier can be used as a membrane. As described in **Figure 2**, each material can also be broken down into application-specific

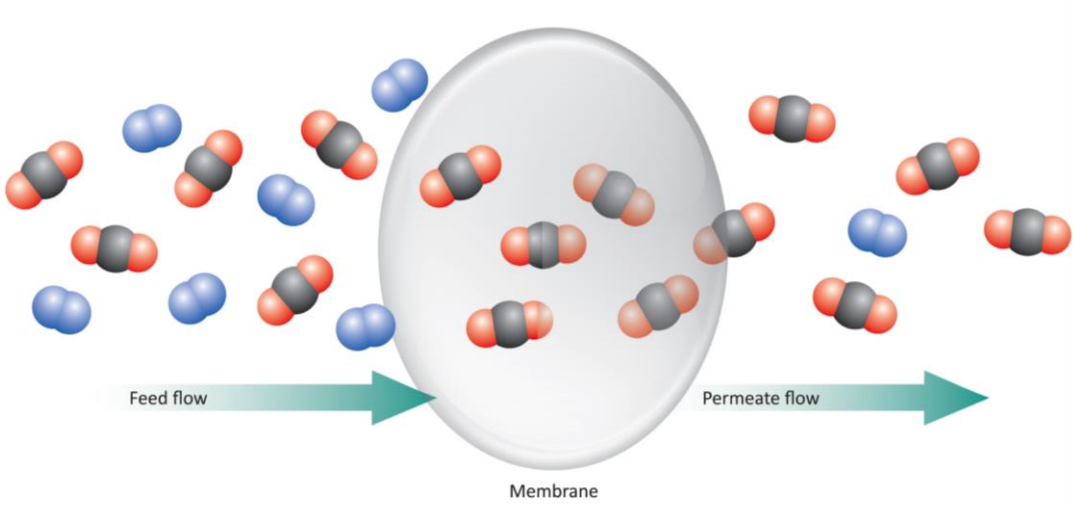

Figure 1. Basic illustration of a membrane changing the molar ratios of components in a chemical mixture.

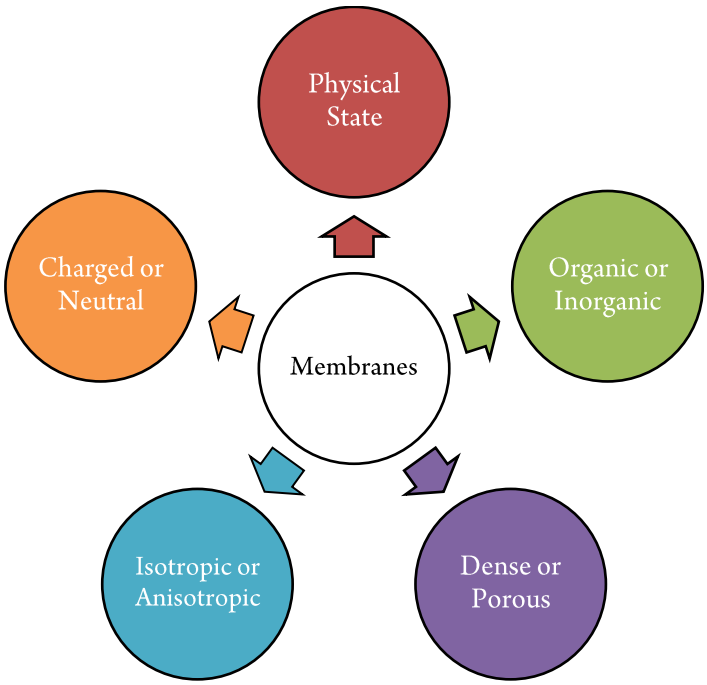

Figure 2. Diagram encompassing various considerations in choosing a membrane material.

criteria such as whether a material should be a solid or liquid, isotropic or anisotropic, symmetric or asymmetric, dense or porous, or contain a charge. Despite a near-infinite library of membrane materials, organic polymer membranes continue to be industry favorites due to their superior processability and performance tunability. In some cases, inorganic membranes show increased performance for a chemical separation under certain test conditions; however, their overwhelming complexity in manufacturing compared to rival polymer systems all but nullifies the performance gains.[7] On the other hand, organic polymers are compatible with well-established industry techniques that include melt extrusion, film blowing, injection molding, spin coating, 3D printing, and much more. Also, membrane development often demands the formation of specific pore sizes, the inclusion of particular functionalities, or the implementation of complex morphologies in order to tailor performance. With access to hundreds of organic transformations, the ability to tune these properties in polymers is well documented, and new methods to manipulate these materials are reported frequently. Lastly, thermal stability, reduced weight, and increased flexibility are other noteworthy benefits of organic polymer membranes that make them well suited for this application.

Among the largest membrane industries, gas separation is a particularly intriguing area where polymer membranes see widespread use. Around the 1980's, commercial air purification (O_2/N_2) and natural gas enrichment (CO_2/CH_4) operated predominantly by energy-intensive separation methods such as cryogenic distillation, pressure swing adsorption, or amine gas treatments (**Figure 3**).[8-10] These methods produce exceptionally

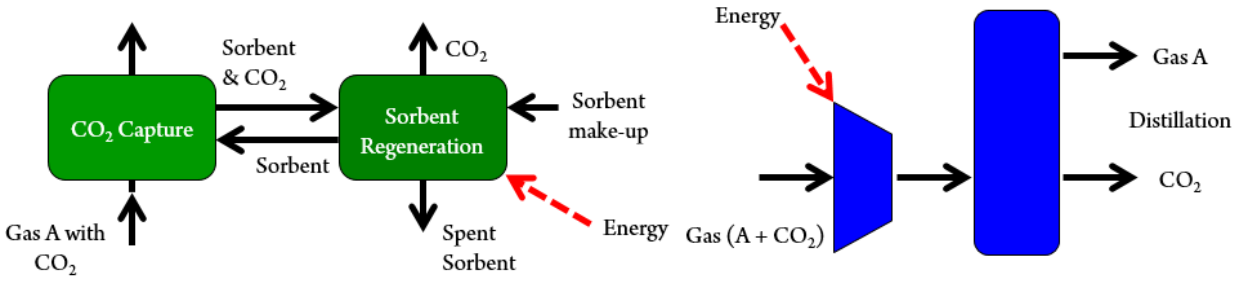

Figure 3. Illustrative depictions of amine absorption technologies (green) and cryogenic distillation (blue).

pure products but come at high operating costs due to the energy required to drive the thermal equipment responsible for regenerating sorbent or to cool the gases into to a liquid state in order for them to be separated by distillation. Polymer membranes offer an alternative that reduces operating costs through a passive separation mechanism and were capable of easily integrating into existing infrastructure. As a result, these technologies were quickly adopted to either replace existing systems or to work in tandem with them to perform multi-stage separations.

With respect to commercial gas separations, thin films of dense polymer membranes are typically employed. This is a direct result of gas molecules being several orders of magnitude smaller than other contaminants, such as microorganisms in aqueous solutions. In order to design new materials in this area, the frame of mind must change from creating pores of various sizes to a chemical mixture physically diffusing through polymer chains that are tightly packed. The following will detail the evolution of the current solution-diffusion model and define the physical parameters used to explain the observed behaviors.

1.3 The Solution-Diffusion Model and Mechanisms of Gas Diffusion

Around the mid 1900's, attempts to describe the diffusion of gas molecules within a dense polymer matrix focused on two models: the pore-flow model, and the solution-diffusion model. At the core, both models are ingrained in the laws of thermodynamics in which the driving force of membrane separations is the chemical potential gradient, which is often attributed to a concentration gradient (**Figure 4**). The driving forces of pressure, temperature, and concentration are also interrelated.[11] Following decades of controversial debate of the two models, the predominant method for explaining gas diffusion in dense polymer matrices remains the solution-diffusion model.[12-13]

In a typical experiment, feed gas is introduced to one side of the membrane at a high pressure which forces the dissolution of gas molecules at the interface. Simultaneously, the permeate side of the membrane is kept at a low pressure with this pressure gradient physically maintained through compression and vacuum equipment. After a finite period of time at a constant pressure gradient, the diffusion of gas molecules achieves steady-

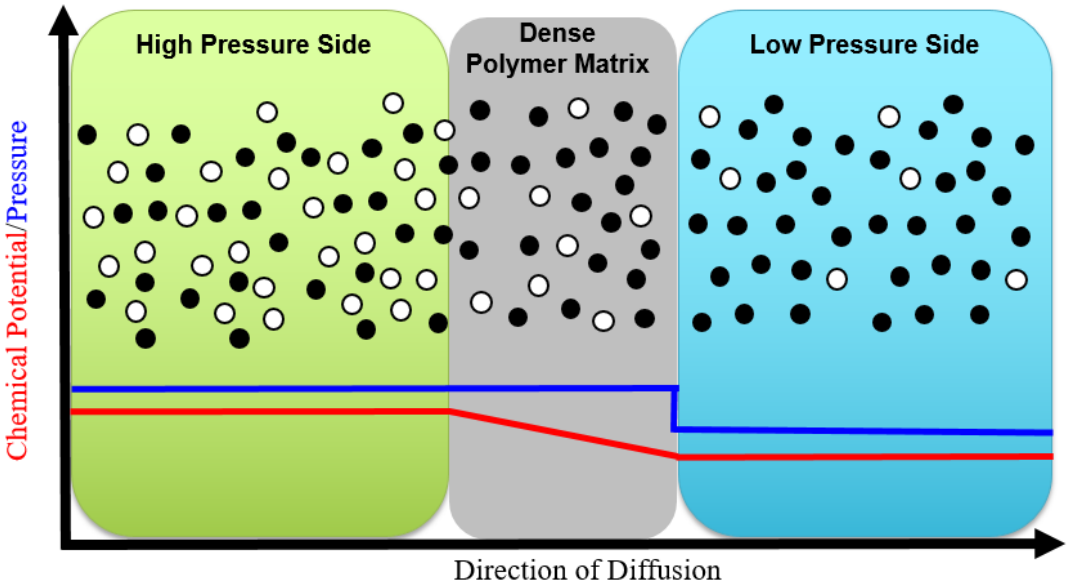

Figure 4. The solution-diffusion model of gas transport through dense polymer matrices.

state permeation. Once a membrane achieves steady-state, several methods can be used to characterize the material's gas transport properties. For our purposes, single gas measurements were conducted using the constant-volume variable pressure method as described in the Springer Handbook of Material Measurements Methods to obtain permeability and selectivity values.[14] A membrane's performance for a particular separation can be primarily categorized by the culmination of two variables: permeability and selectivity. Permeability (*P*) is a descriptor of gas throughput that is more reliable than purely considering gas flux across the membrane. Given that gas flux can be influenced by a host of variables such as the pressure gradient (ΔP), temperature (T), sample dimensions, etc., permeability serves as a robust unit that considers all experimental factors of steady-state permeation to give a value that we can compare universally across different membrane samples. The equation used to calculate permeability is described in Equation 1 where additional values include permeate volume (V_d), membrane thickness (l), membrane surface area (A), the gas constant (R = 0.278 [cm·Hg·cm^3]/[cm^3(STP)·K]), and the difference of pressure in the downstream (P_d) vs. time during permeation and the leak.

$$P = \frac{V_d l}{\Delta \mathrm{P} A R T}\left[\left(\frac{d\mathrm{P}_d}{dt}\right)_{ss} - \left(\frac{d\mathrm{P}_d}{dt}\right)_{leak}\right] \quad (1)$$

Selectivity (α) values describe a membrane's preference for a particular penetrant over another. Typically expressed in terms of a ratio between permeability values, ideal selectivity serves as a good model for predicting the behavior of polymer membranes in chemical mixtures but are used under the assumption that partial pressures of individual components play a significant role in the driving force of the separation (Equation 2).

$$\propto = \frac{P_a}{P_b} \quad (2)$$

Although permeability and selectivity values ultimately describe a membrane's performance, additional descriptors are used in order to pinpoint diffusion mechanisms and to understand the changes that are being made in membrane development. In addition to Equation 1, permeability can also be expressed as the product of diffusivity (*D*) and solubility coefficients (*S*) (Equation 3).

$$P = D \cdot S \quad (3)$$

Diffusivity coefficients describe a membranes ability to separate penetrants based on size-sieving principles. It can be estimated by analyzing the permeation curve to obtain the lag time (*θ*) or the time it takes for the membrane to reach steady-state permeation and relating that to the polymer thickness (*l*) (Equation 4).

$$D = \frac{l^2}{6\theta} \quad (4)$$

Solubility then refers to the polymer's ability to favorably interact with a particular gas, enabling it to dissolve and thus diffuse through the material (Equation 5). Gas solubility is a property that can be more accurately measured via a variety of methods such as gravimetric analysis of pressure decay to develop sorption isotherms. It can also be broken down into individual contributions of Langmuir (C_H) and Henry's Law (k_d) dependent diffusion within the polymer matrix. A polymer that has significant Langmuir gas sorption constants is able to condense a particular gas into micro voids present within the polymer structure. These micro voids act as free space that as the concentration/pressure of gas increases on the upstream side of the membrane, gas will

diffuse and occupy these spaces. Henry's Law contributions depend on the polymers' ability to continue to dissolve gas molecules by pushing aside polymer chains.

$$S = k_d p + \frac{C'_H bp}{1 + bp} \quad (5)$$

b is the virial coefficient specific to the gas and p is the fugacity.

1.4 The "Upper Bound" Relationship

As more polymer materials were evaluated for gas separation applications, researchers were able to use data mining to establish trends between chemical structure and membrane performance. Perhaps the most famous product of these efforts is the Robeson Upper Bound. Originally described in 1991, the Robeson Upper Bound has become synonymous with characterizing the gas separation properties of polymer membranes. Professor Lloyd Robeson discovered that by plotting permeability and selectivity data on a log-log plot for a particular gas pair, there exists an upper bound of performance that no membrane material could exceed.[15] For example, **Figure 5** shows the 1991 Robeson plot for polymer membranes evaluated for O_2/N_2 gas separation. When plotted in this fashion, the upper bound behavior is clearly observed and exists broadly among both glassy and rubbery polymers. As materials are designed to increase permeability, a decrease in selectivity is typically observed. Unfortunately, this behavior holds true for an assortment of gas pairs, including O_2/N_2, H_2/CH_4, CO_2/CH_4, H_2/N_2, He/CH_4, He/N_2, He/H_2, He/O_2, and H_2/O_2. Despite the negative connotations associated with the permeability-selectivity trade-off, the Robeson plot is an excellent tool for determining the current state of membrane technology. At a glance, we are able to pinpoint the frontier of the field as well as judge the performance of new materials against those reported in the literature.

In 2008, the Upper Bound was revisited to describe the improvements made in each of these areas.[16] Two of the revised Robeson plots are shown in **Figure 6** for O_2/N_2 and CO_2/CH_4 separations. In each case, there now are a myriad of new data points that surpass the Upper Bounds from 1991 and these now define the present Upper Bounds. Among these new additions, one class of polymers that pushed boundaries for both of

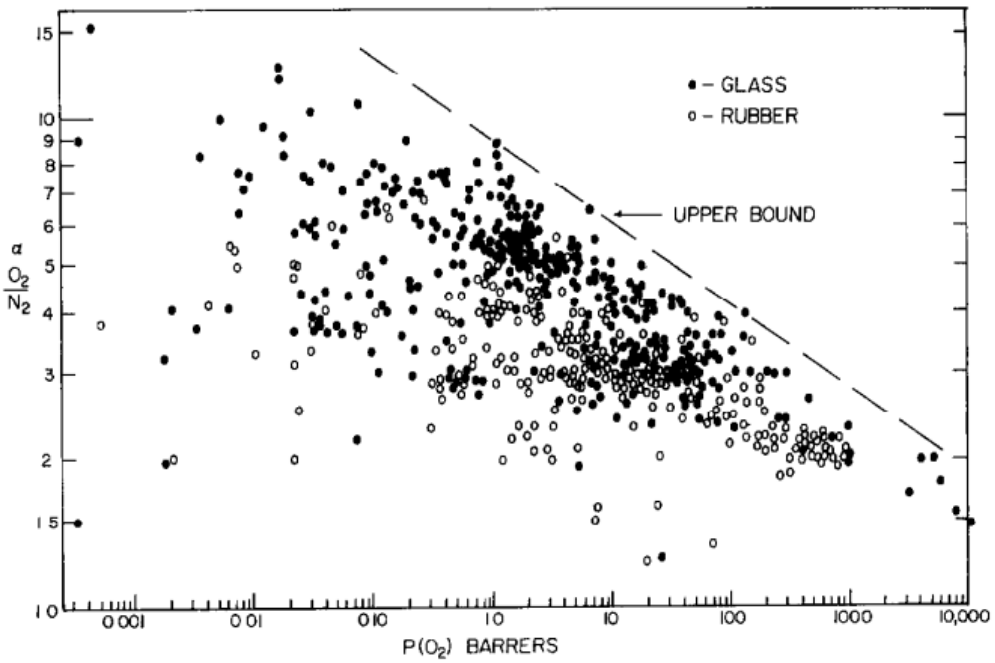

Figure 5. Upper Bound relation describing separation of O_2 and N_2 as of 1991 (reprinted with permission from ref 15. Copyright 1991 Elsevier Science Publishers B V).

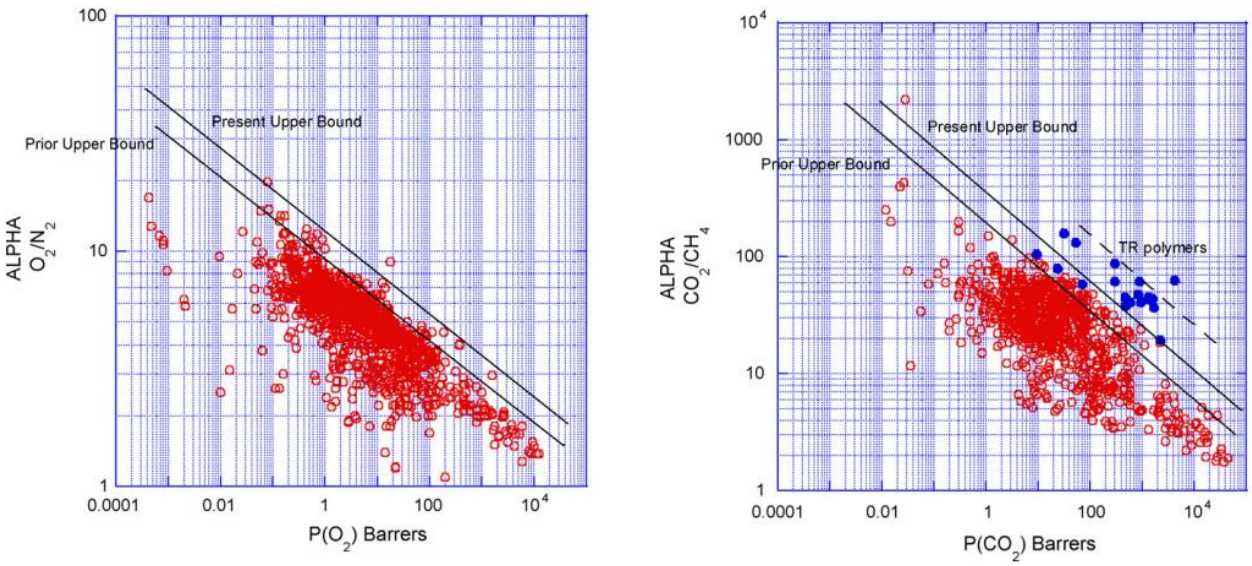

Figure 6. Revised Upper Bounds for O_2/N_2 and CO_2/CH_4 gas separations (reprinted with permission from ref 16. Copyright 2008 Elsevier B.V.).

these separations were polymers of intrinsic microporosity (PIMs). These ladder-like polymer structures exhibit extremely high fractional free volume and contorted polymer backbones that cause them to excel in gas separations known to be dominated by molecular sieving type diffusion mechanisms.[17-18] Another class of polymers that showed remarkable improvements for CO_2/CH_4 applications were thermally re-arranged polymers (TR polymers). These materials are described in more detail in section 3.5 Alternating Radical Copolymers as a means to new Thermally Re-arranged Polymers but are typically considered in a class of their own with respect to the Robeson Upper Bound. TR polymers, bilayer materials, block copolymers, or other complex morphologies can be plotted against polymers on the Robeson Upper Bound but usually provide a less direct comparison as the changes in performance are usually a result of the morphology changes and not a result of the chemical structure changes of the polymer.

1.5 Conclusions

In summary, polymer membranes represent a billion-dollar industry that remains on the rise. These membranes are seeing widespread adoption for numerous separation applications due to low operating costs, good processability, and ease of integration. Gas separation is one area where high-performance membranes have the potential to drastically reduce operating costs when compared to other methods, such as pressure swing adsorption or cryogenic distillation. As the models to explain diffusion continue to be more sophisticated, membrane performance continues to increase, despite the infamous permeability-selectivity trade-off. In the next chapter, we will look more intently on the motivations and challenges associated with one particular application at which the work described herein is directly related, the post-combustion separation of carbon dioxide from flue gas.

Chapter 2. Post-combustion Separation of Carbon Dioxide from Flue Gas

2.1 Greenhouse Gas Emissions and Climate Change

Greenhouse gases such as carbon dioxide and methane are a critical component of the Earth's atmosphere that are essential for maintaining a prosperous environment. These gas molecules are unique in their ability to absorb and emit radiation within the thermal infrared range, resulting in global temperatures that hover around a comfortable 15 °C rather than a frigid -18 °C.[19-20] This phenomenon is known as the greenhouse effect, and it is dependent upon particular concentrations of water, carbon dioxide, methane, nitrous oxide, ozone, and chlorofluorohydrocarbons in the atmosphere. In nature, these molecules participate in a number of cycles, most notably the water cycle and the carbon cycle, to maintain their effective concentration. However, the rise of modern society has led to human activity infringing on these cycles and altering the concentration of greenhouse gases in the atmosphere.

Over the course of the industrial revolution, energy-dense fossil fuels have become a staple for electrical energy generation, personal transport, and product manufacturing. In the current market, the combustion of coal and natural gas accounts for approximately two-thirds of the electrical energy produced annually in the United States (US).[21] Due to the abundant availability and low cost of coal compared to renewable energy sources, an MIT study projects the use of coal to increase until the year 2050, despite being responsible for 37% of national carbon dioxide emissions (**Figure 7**).[22] Additionally, transportation is heavily dominated by fossil fuels due to the lack of range on current electric vehicles and accounts for 31% of the carbon dioxide emissions from the US. In total, 5,560,000,000 metric tons of CO_2 are being released into the atmosphere each year in the US as a result of fossil fuel combustion.[23] The following data highlight how these enormous greenhouse gas emissions are linked to the increasing of global temperatures, rising sea levels, changes in precipitation patterns, and changes to ecosystems and habitats.

Figure 8 shows the CO_2 concentration in the atmosphere measured over several decades at the Mauna Loa volcano in Hawaii.[24] After adjusting for the local outgassing of the volcano, this isolated location has observed a 23% increase in atmospheric CO_2 levels

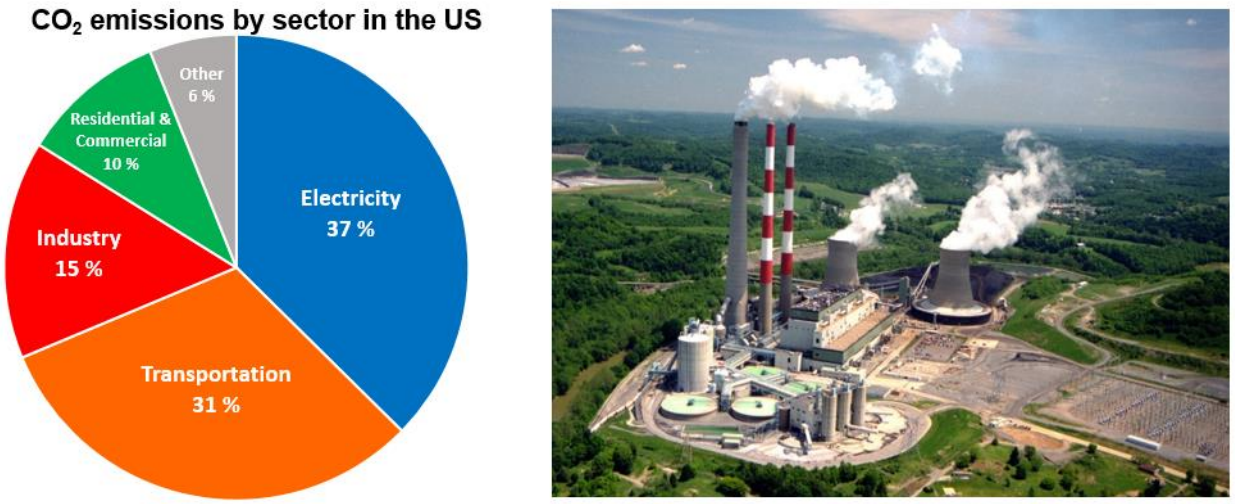

Figure 7. Distribution of CO_2 emissions in the US by sector (reproduced from ref. 23) and a coal-fired power plant.

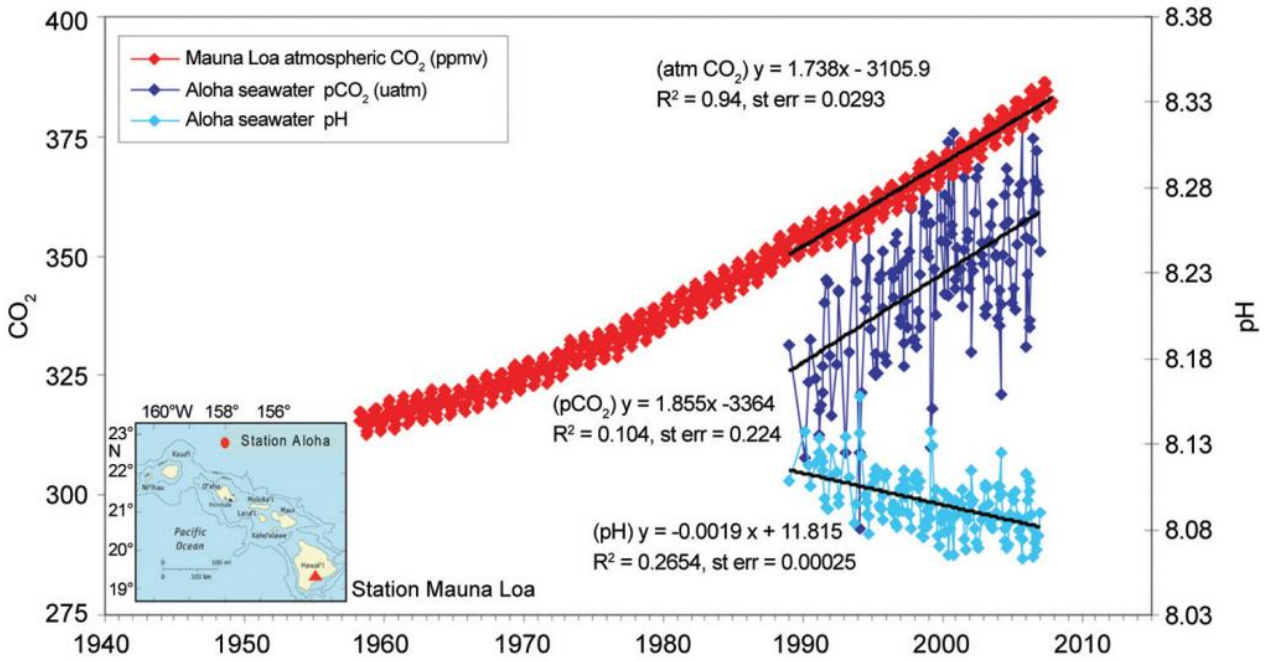

Figure 8. CO_2 concentration in the atmosphere measured at the Mauna Loa volcano plotted against CO_2 concentration and pH measured in the Pacific Ocean at Station Aloha (©American Meteorological Society. Used with permission from ref 24).

over a 50-year period (1960-2010). More broadly, a 44% increase is observed when current levels of atmospheric CO_2 content (402 ppm)[25] are compared to the pre-industrial values of the mid-1700s[26] (280 ppm). These changes in CO_2 levels can be easily attributed to the enormous volumes of anthropogenic CO_2 emissions being vented into the atmosphere across the same time period. In addition, models suggest that in tandem with these observations, average global temperatures have been steadily rising over the same period of time. According to the NASA Earth Observatory, average temperatures have increased at a rate of roughly 0.15-0.20 °C per decade since 1880.[27] Although the cause of these temperature changes cannot be precisely pinpointed, it is reasonable to assume that these changes are the product of a stronger greenhouse effect caused by the increased concentration of CO_2 in the atmosphere. Furthermore, Earth's oceans have been experiencing unusual activity that again coincides with the production of these CO_2 emissions (**Figure 8**).[24,28] As the CO_2 concentration in the atmosphere continues to increase, the concentration of CO_2 in the oceans responds with a requisite increase and an overall pH decrease. This behavior coincides with normal operation of the carbon cycle where our oceans are in constant equilibrium with CO_2 in the atmosphere. In an attempt to compensate for the vast amount of additional CO_2 emissions, it is believed that our oceans have dissolved approximately 525,000,000,000 tons of CO_2 since 1750. With an abundance of dissolved CO_2 in seawater, the origins of the decreases in pH can be explained. It is widely accepted that the excess CO_2 in the system disrupts the chemical equilibrium of the ocean by reacting with water to produce carbonic acid which subsequently breaks down into bicarbonate and hydronium ions (**Figure 9**). The production of these additional hydronium ions has caused a pH decrease of 0.1 units since from 1751 to 1996 (8.25 to 8.14).[29] Taking into consideration that pH is measured

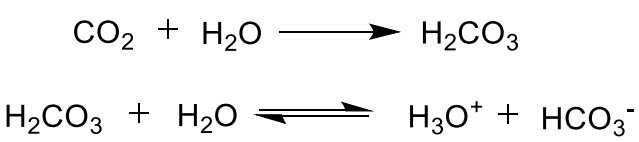

Figure 9. Scheme for the production of hydronium ions in seawater as a result of CO_2 concentrations increasing.

on a logarithmic scale, that decrease translates to a 35% increase in H^+ concentration in the world's oceans. As a result, marine life imbalances are being observed, such as organisms being incapable of producing their calcium carbonate shells.[30-33]

Lastly, there exists a vast amount of data that simulate the effects of these changes on other areas of the climate. For instance, Solomon and coworkers have developed models for predicting rising sea levels, changes in precipitation patterns, and the natural decrease of CO_2 concentration from the atmosphere upon immediately ceasing all carbon emissions.[34] In that study, they estimate that for every degree of global warming, the sea levels will rise between 0.2 and 0.6 meters as a result of glacier ice retreat and thermal expansion. Sea levels could reach a point where populated coastal cities and small islands threaten relocation. Also, they estimate that every degree of climate change is predicted to affect regional annual rainfall leading to an overall global decrease, which severe ramifications in local agriculture and ecosystems. Possibly the most alarming conclusion was that on a 1000-year time scale, CO_2 concentration plateaued somewhere around 40% higher than pre-industrial values (280 ppm). With current atmospheric concentrations of CO_2 at 402 ppm, these data show that CO_2 values will not reach their pre-industrial values over the course of the millennium if we were to cease emissions tomorrow.

In view of all of this data, the correlations that exist between excessive carbon emissions and the observed changes in the planet's climate are cause for concern. However, until viable alternatives surface, the combustion of coal and petroleum fuels is necessary to maintain the current quality of life. The combination of these concerns motivates our research in carbon capture technologies. If these models hold true, it is imperative that carbon capture technologies be designed in order to be able to capture carbon dioxide for use as a value-added product or to be disposed of by methods such as geological injection.[35,36,37]

2.2 Coal-fired Power Plants and Post-Combustion Carbon Capture

An effective method for reducing CO_2 emissions is the implementation of carbon capture technologies in coal-fired power plants. As alluded to previously, coal-fired power

plants are responsible for approximately 40% of CO_2 emissions in the US, making them primary targets for reducing the carbon footprint. Amine absorption technologies seem to be the leading candidate in this space despite the requirement that roughly 30% of the power produced by the power plant goes into operating these carbon capture processes. This drives up the costs of electricity. Recently, Merkel and collaborators of the Membrane Technology and Research (MTR) center in Menlo Park, CA demonstrated that polymer membranes show potential as an effective method of passive carbon capture for treating flue gas with minimal energy input.[38] Within the report, they describe application-specific criteria for membrane materials to meet in order to be considered for this application, as well as how to design test scenarios in the laboratory.

For instance, three approaches for targeting CO_2 are shown in **Figure 10**: oxyfueling, pre-combustion decarbonization, and post-combustion decarbonization. Out of the three, post-combustion decarbonization is unique in that this carbon capture technology could be directly integrated into the infrastructure that already exists in over 5000 power plants

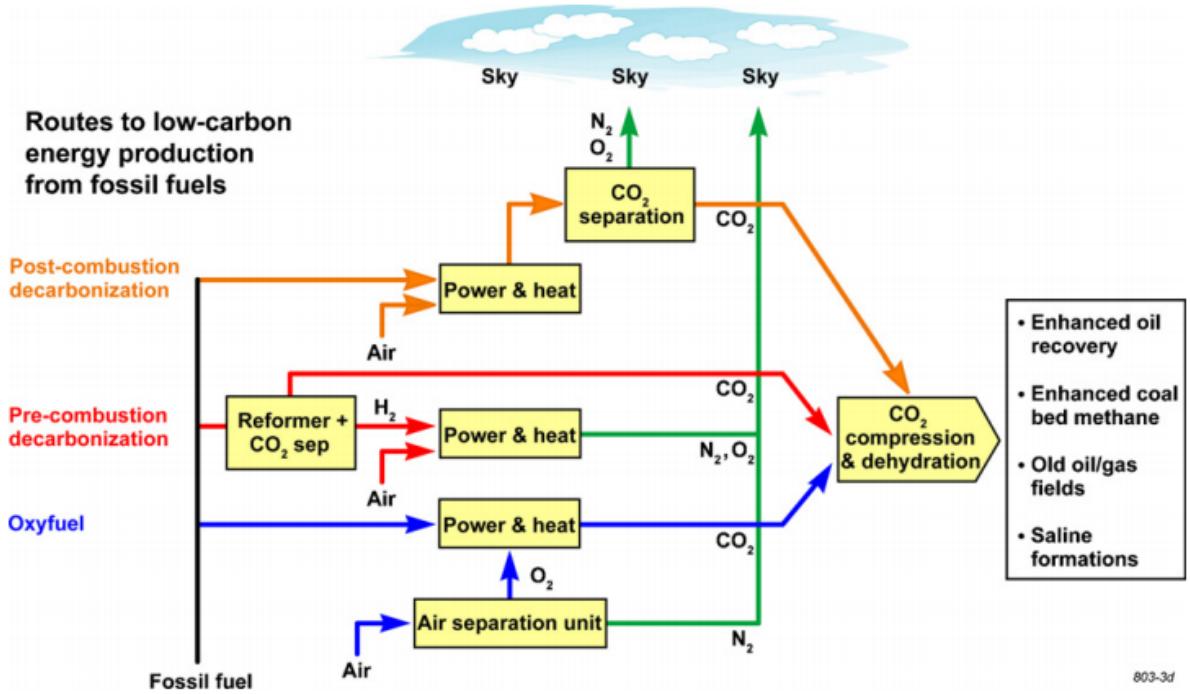

Figure 10. Coal-fired power plant and distribution of CO_2 emissions in the US (reprinted with permission from ref 32. Copyright 2009 Elsevier B.V.).

worldwide. As a result, this approach will be the focus of this discussion. A typical 600 MW coal-fired power plant produces 500 m^3 of flue gas from the combustion process every second. This gas consists of N_2 (~76-77%), CO_2 (13%), H_2O and O_2 (~10%), and ppm levels of ash, SO_x, NO_x, and heavy metal contaminants. That flowrate is 5 to 10 times larger than typical gas streams that are treated for CO_2 removal, such as in natural gas separations. In addition to the enormously large volumes of gas, the partial pressures of CO_2 in the flue gas mixture are extremely low (~0.13 bar), resulting in a low driving force for separation. The culmination of these obstacles present a significant engineering obstacle in how to maximize the driving forces of separation based upon the mechanisms described in section 1.3 The Solution-Diffusion Model and Mechanisms of Gas Diffusion). In response to this problem, a particular combination of vacuum and compression equipment that is economically viable will be required to create a pressure ratio to drive membrane separations. Based on the cost differentials between vacuum and compression equipment, a feed/permeation pressure ratio of 5 is economically viable given the polymer membranes exhibit extremely high permeance thus minimizing the membrane surface area required to accommodate the tremendous gas flow. At the same time, ideal polymer membranes would exhibit CO_2/N_2 selectivity values around 50. Beyond this degree of separation, diminishing returns in the purity of the CO_2 stream are observed and further improvements in permeability are encouraged as they would impact the cost of production more dramatically.

2.3 Inspiration for Designing High-Performance Polymer Membranes for CO_2/N_2 Separation

When developing polymer membranes for post-combustion carbon capture, materials are evaluated primarily by their performance in CO_2/N_2 separations. By analyzing the 2008 Upper Bound relationship for this gas pair (1.4 The “Upper Bound” Relationship), the upper echelon of permeability and selectivity values can be clearly observed. This allows us to gain inspiration from the structure-property relationships imbedded in the data. The 2008 Robeson Upper Bound for CO_2/N_2 is displayed in **Figure 11** and is

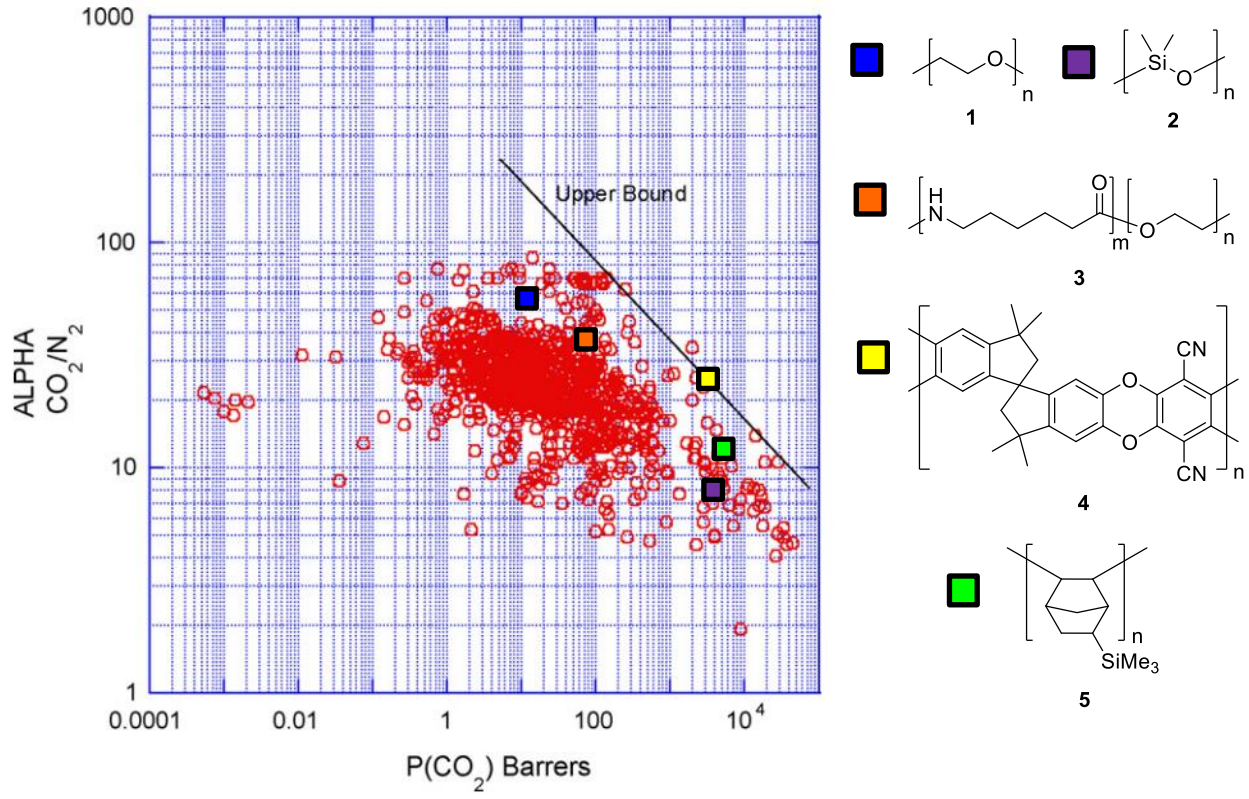

Figure 11. The 2008 Robeson Upper Bound for CO_2/N_2 (reprinted with permission from ref 16. Copyright 2008 Elsevier B.V.) and some of the highest performing polymers. Red circles indicate the data compiled by Lloyd Robeson to produce the Upper bound and notable performers for this discussion include Poly(ethylene glycol) (blue square), poly(dimethylsiloxane) (purple square), PEBAX® 1657 (orange square), PIM-1 (yellow square), and poly(5-trimethylsilyl-2-norbornene) (green square).

accompanied by structures of polymers that directly inspired us to design new membrane materials for post-combustion CO_2 capture.

Several commercially available polymers have been tested for CO_2/N_2 separations, and notable performers include poly(ethylene glycol) (PEG) (**1**), poly(dimethylsiloxane) (PDMS) (**2**), and PEBAX® 1657 (**3**). PEG is a glassy polymer that has low CO_2 permeability but one of the highest CO_2/N_2 selectivities due to the abundance of electron-rich ethylene oxide units that favorably interact with the partial positive character of the carbon in the CO_2 molecule.[39] Given the tendency of PEG to crystallize, which severely reduces gas permeability, numerous approaches aim to add a high concentration of ethylene oxide units into copolymers and polymer blends in order to improve mechanical properties and/or retain amorphous character. For example, PEBAX® 1657 combines a PEG polymer block with a polymer block of mechanically robust Nylon units to ultimately produce a rubbery copolymer with permeability and selectivity values of 100 Barrer and 50, respectively. Given the excellent balance of membrane performance in PEBAX® 1657, it has become a go-to material for mixed matrix membranes, blends, and composites over the past decade. On the opposite side of the spectrum, PDMS is a commercial rubber with high gas permeabilities, high flexibility, and an absence of physical aging.[40] The increase in chain mobility associated with flexible Si-O bonds in the polymer main-chain facilitates the transport of gas molecules across the board by a significant margin, but PDMS lacks the necessary CO_2/N_2 selectivity to be widely adopted for post-combustion decarbonization.

The other two examples that heavily inspired this work are synthetic materials designed specifically with CO_2 separations in mind; polymers of intrinsic microporosity (PIMs) and vinyl-addition polynorbornenes (VAPNBs). The first of which is PIM-1 (**4**), a cyano-functionalized PIM that exhibits permeability and selectivity values of 2300 Barrer and 25.[17-18] PIMs consist of polymer backbones that have virtually no rotational freedom in the polymer backbone outside of a spirocenter introduced through bonded cyclopentane rings. The result is a randomly contorted polymer structure with high fractional free volume (0.400), surface area (700-900 m^2/g), decomposition temperatures (>350 °C), and gas permeabilities (2350 Barrer for CO_2). Following the initial discovery of

PIMs, significant research efforts focused on increasing membrane performance by modifying the cyanide functionality, changing degrees-of-crosslinking, optimizing film casting conditions, and characterizing the specific diffusion mechanisms involved in gas separations. By breaking down the permeability values of PIM-1 into its diffusivity and solubility coefficients, a critical challenge associated with membrane separations of CO_2/N_2 is observed. The diffusivity coefficients for CO_2 and N_2 in PIM-1 are 26 and 22 (10^{-8} $cm^2 \bullet s^{-1}$), respectively, which results in a meager size-sieving selectivity of 1.18. Given the lack of noticeable differences in the kinetic diameters between the two penetrants, CO_2 = 3.30 Å and N_2 = 3.64 Å, there exists little to no opportunity to design polymers with particular pore volumes to prefer one penetrant over the other.[41] Instead, the majority of the separation occurs through solubility-controlled mechanisms such as Henry's Law and Langmuir diffusion (1.3 The Solution-Diffusion Model and Mechanisms of Gas Diffusion). With a solubility selectivity for CO_2/N_2 of 21, the microporous character and exposed electron-rich nitrile groups in PIM-1 can be attributed to the large preferential uptake of CO_2 gas. These conclusions directly inspired us toward polymer systems with rigid backbones and synthetic handles allowing electron-rich functionalities to be introduced. This ultimately led us to vinyl-added polynorbornenes (VAPNBs). VAPNBs differ from their more commonly-encountered counterparts, ring-opening metathesis polymerization (ROMP) polynorbornenes, in that the resultant vinyl-added polymers retain the rigid, bicyclic core of the norbornyl ring and no residual alkenes are present along the polymer backbone (**Figure 12**). These features produce high T_g materials that are more chemically stable and have gas permeability values that are higher by an order of magnitude in most cases.[42-46]

Yuri Yampolskii and coworkers at the Petrochemical Institute in Moscow have extensively investigated silane-functionalized VAPNBs as gas separation membranes with a great deal of success. In particular, poly(5-trimethylsilyl-2-norbornene) (**5**) achieved extremely high permeability values (4350 barrer) while preserving moderate CO_2/N_2 selectivities (α = 14.7) that was attributed to the $SiMe_3$ group having a balance between steric bulk that frustrates polymer chain packing while not having long flexible groups that allow for packing of the side-chain functionality.[46]

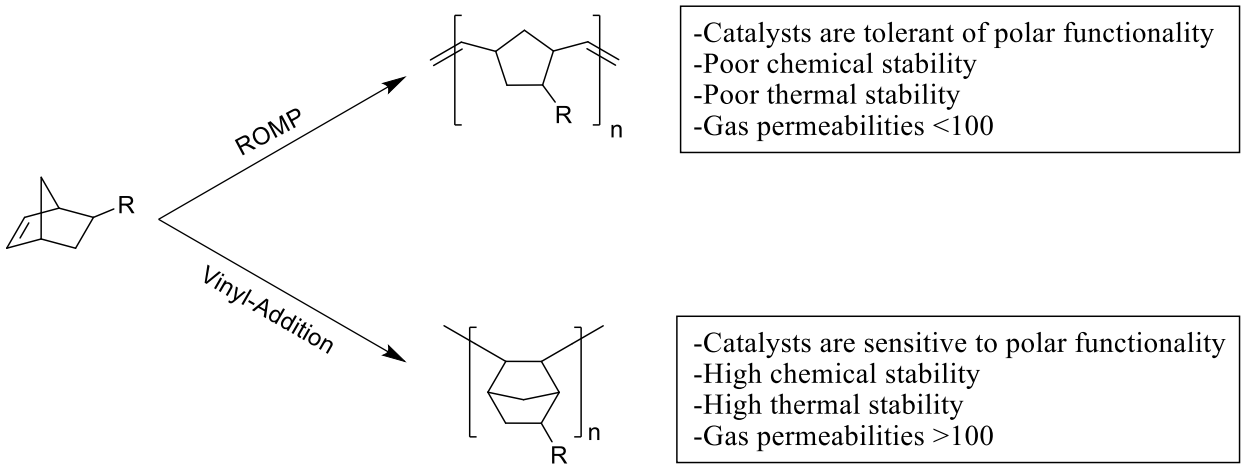

Figure 12. Comparison of ring-opening metathesis polymerization (ROMP) of norbornene versus vinyl-addition polymerization (VA) of norbornene.

Each chapter will detail how we took the following inspirations to produce notable milestones in the CO_2/N_2 separations literature. As a whole, we furthered fundamental knowledge into alternating radical copolymers with norbornene and maleimides as potential candidates for new thermally-rearranged polymers, increased the permeability and selectivity of cross-linked PDMS by modulating the cross-link density via norbornene functionalities, unlocked new functionalities in high molecular weight vinyl-added polynorbornenes through neutral nickel catalyst design, and used our new catalyst system to create siloxane-functionalized vinyl-added polynorbornenes that exhibit exceptional CO_2/N_2 gas separation properties, desirable mechanical properties, increased solubility, increased flexibility, high optical transparency than traditional vinyl-added polynorbornenes.

Chapter 3. Free-Radical Copolymerizations of *N*-phenylmaleimide and Norbornene as Scaffoldings for New Thermally-Rearranged Polymers

A version of this chapter was originally published by Kevin R. Gmernicki, Matthew Cameron, and Brian K. Long:

Reprinted with permission from Kevin R. Gmernicki, Matthew Cameron, Brian K. Long "Fundamental Investigations into the Free-Radical Copolymerization of *N*-phenylmaleimide and Norbornene" *Journal of Polymer Science Part A: Polymer Chemistry* 54(7) (2016): 985-991. DOI: 10.1002/pola.27934. Copyright 2015 Wiley Periodicals, Inc.

The author directly contributed to the entirety of this published manuscript and was aided in the synthesis of the polymers by undergraduate researcher Matthew Cameron.

Wiley Online Library permits the use of published content for student dissertations after applying for access. Permission granted on January 11th, 2017. Order #4026090705688

Experimental and supplemental information available in Appendix C: Experimental Methods and Supporting information for Chapter 3

3.1 Abstract

A fundamental investigation into the copolymerization of *N*-phenylmaleimide and norbornene via conventional free-radical polymerization techniques was conducted. Reaction conditions were optimized for molecular weight and percent yield by tuning overall concentration and initiator loading. The copolymerization kinetics were monitored using *in-situ*, variable temperature nuclear magnetic resonance and first-order behavior was observed with respect to each monomer. Although the related copolymerization of norbornene and maleic anhydride was well-known to proceed in a perfectly alternating manner, the copolymerization of norbornene and *N*-phenylmaleimide was found to deviate from strictly alternating copolymerization behavior, producing significant amounts of sequentially enchained *N*-phenylmaleimide units within the polymeric backbone. This deviation from perfectly alternating behavior was confirmed by analysis of individual monomer conversion rates and by measurement of monomer reactivity ratios using the Mayo-Lewis graphical analysis method.

3.2 Background on Alternating Radical Copolymers

In the late 1990's, perfectly alternating copolymers consisting of norbornene and maleic anhydride were extensively investigated as promising materials for 193 nm photolithography.[47-51] Though these alternating copolymers possessed several desirable properties such as good thermal stability, high glass transition temperatures, optical transparency at the wavelength of interest, and the ability to form exceptional films for

device fabrication,[51] they ultimately reached their figurative limits while attempting to balance the inherent trade-off between etching resistance and overall lithographic performance.[47]

Despite never reaching commercial use as 193 nm lithographic resists, these alternating copolymers continue to be of interest for a variety of applications today. Particularly, because of the remarkable film-forming properties and the highly rigid backbone of norbornene-*alt*-maleic anhydride copolymers, these unique polymeric materials piqued our interest as possible candidates for advanced gas separation membranes. Polymers with rigid backbones have been repeatedly shown to form membranes with remarkably high gas permeabilities.[46,52-57] Likewise, the ability to modify either monomer to incorporate functionalities that favorably interact with gases such as CO_2 are extremely desirable as efficient separation of CO_2 from non-harmful gases such as N_2 is currently a grand-challenge within the field of gas-separations.[16]

In an effort to tailor the chemical structure of these sequence-controlled copolymers for membrane-based gas separation applications, and while avoiding sometimes problematic post-polymerization modifications of the anhydride functionalities, we hypothesized that replacing the maleic anhydride units with structurally related co-monomers, such as *N*-substituted maleimides, would be an ideal pathway toward the development of those materials. A wide variety of *N*-substituted maleimides are commercially available or are easily synthesized from readily available and cheap starting materials, thereby making them ideal monomeric targets. Furthermore, it has been shown that changes in maleimide's *N*-substituent can lead to significant changes in its resultant polymer's physical properties[58-60] while the rigid cyclic nature of the maleimide, in similarity to maleic anhydride, generally increases thermal stability upon incorporation into the polymeric backbone.[59,61]

Though the radical homopolymerization of *N*-substituted maleimides, as well as its copolymerization with electron-rich olefins such as styrene, *n*-butyl vinyl ether, 3-methylenecyclopentene, and isobutene monomers have been investigated,[59-67] no such systematic and fundamental investigations into the free-radical copolymerization behavior of norbornene and *N*-substituted maleimides has ever been reported to the best of the

authors' knowledge (**Figure 13**). Additionally, given that certain controlled radical copolymerizations of *N*-substituted maleimides and electron-rich olefins have been reported to proceed in a predominantly alternating manner, but not in a strictly alternating fashion,[58-59,63,65] a fundamental study into the polymerization kinetics and relative reactivity ratios for this particular pair of monomers is needed to fully understand the structure of their resultant copolymers.

Herein, we report a fundamental investigation into the copolymerization behavior of *N*-substituted maleimide and norbornene using conventional free-radical polymerization techniques. Polymerization parameters such as concentration and initiator loading were systematically studied to ascertain their effects on polymer yield and molecular weight. Likewise, we will demonstrate that the free-radical copolymerization of norbornene and *N*-phenylmaleimide follows the aforementioned observation that changing the electron-deficient co-monomer from maleic anhydride to *N*-substituted maleimide leads to a structure that is predominantly alternating, but not perfectly alternating, and displays a significant propensity to incorporate sequential *N*-phenylmaleimide units into the copolymer chain. We will show that this deviation from perfectly alternating behavior is related to differences in the comonomers inherent reactivity ratios and individual rates of incorporation into the polymer. The reaction kinetics of these copolymerizations were followed using high temperature, *in-situ* ^{1}H NMR, which facilitated real-time monitoring of monomer consumption as the polymerizations progressed.

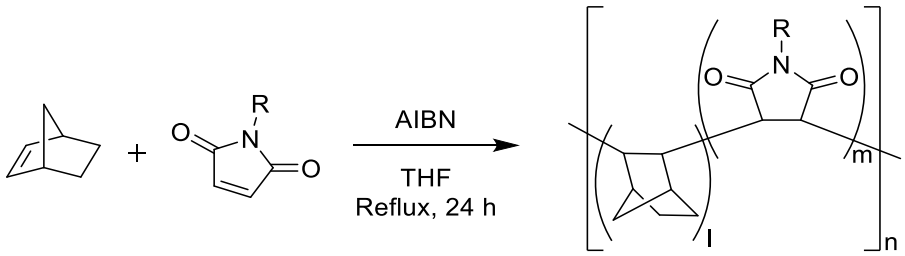

Figure 13. Free-radical copolymerization of norbornene and *N*-substituted maleimides.

3.3 Results of *in-situ* NMR Kinetics of the Copolymerization of *N*-phenylmaleimide and Norbornene

In an effort to develop a deeper understanding of the factors that influence the free-radical copolymerization of *N*-phenylmaleimide and norbornene, a systematic series of copolymerizations were conducted. There, the effects of monomer concentration and radical-initiator loading were studied with respect to the molecular weights obtained and yield of the polymer produced (**Figure 14**). To study the effects of thermal initiator loading, solution state polymerizations containing 60 wt. % solids were polymerized using varying ratios of AIBN initiator in THF (**Figure 14a** and **Figure 14b**). THF was chosen due to the limited solubility of *N*-phenylmaleimide in common organic solvents such as benzene, which have been previously used.[68] Those trials revealed that polymer yield increased rapidly as a function of AIBN loading, reaching ~60-70 % yield at an AIBN loading of 1-2 mol %, but then remained relatively constant at higher initiator concentrations. Initially, the inability to reach percent conversions greater than 70 % was concerning; however, we can now attribute this behavior to the fact that *N*-phenylmaleimide is consumed more rapidly than norbornene due to inherent differences in reactivity ratios, thereby preventing further polymerization. This result will be discussed in greater detail later. In contrast to polymer yield, molecular weights of the resultant polymers were found to decrease logarithmically as AIBN loadings were increased, yielding molecular weights as low as 2,500 g/mol at 4 mol % AIBN (**Figure 14b**) and as high as 4,300 g/mol at 0.1 mol % AIBN.

To study the effect of concentration on polymerization behavior, a series of reactions in which initiator loading was held constant (3 mol % AIBN relative to monomer) were performed (**Figure 14c** and **Figure 14d**). As the weight % solids in tetrahydrofuran (THF) was increased from 5-20 wt % a notable increase in isolated polymer yield was observed. However, as the solids content was further increased from 20-60 wt %, the yields remained relatively constant and never exceeded ~70 %. In comparison, when monitoring molecular weight as a function of weight % solids in THF, a linear relationship was observed reaching a molecular weight (M_n) of ~3,200 g/mol at 60 wt % solids, which was the limit of *N*-phenylmaleimide solubility.

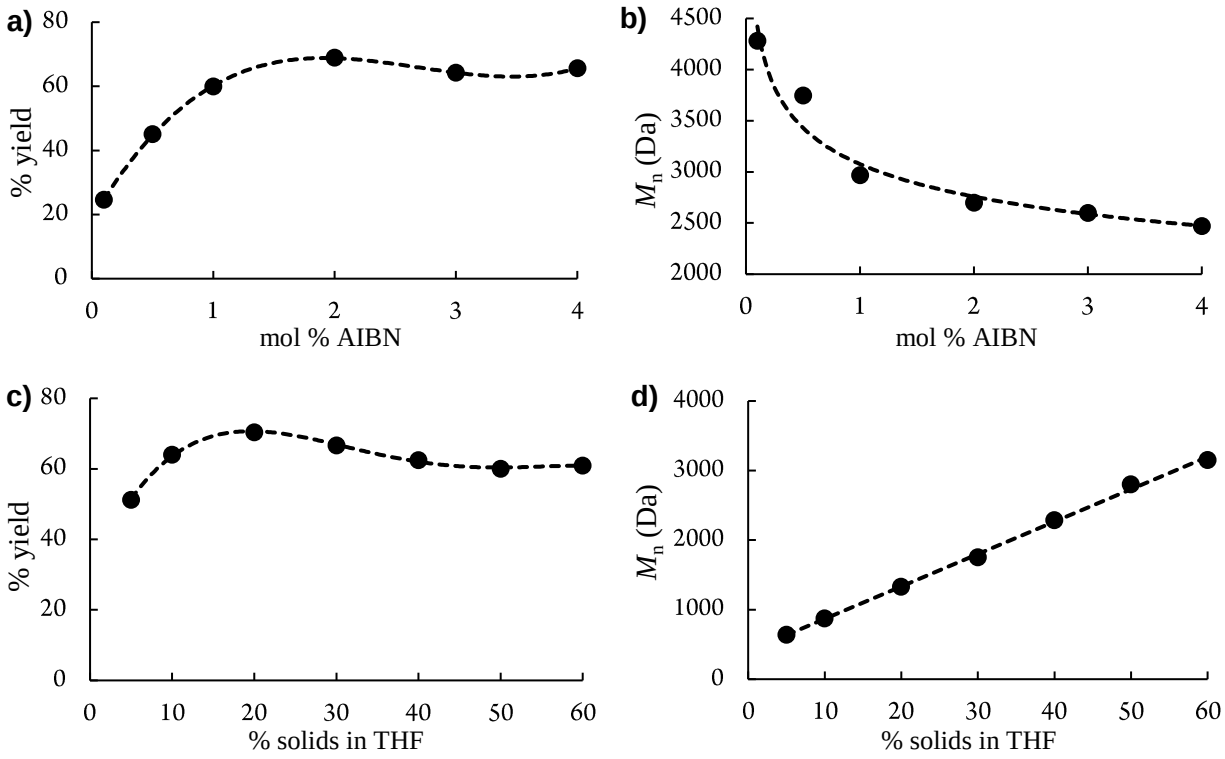

Figure 14. The effects of initiator loading as a function of **a)** % yield and **b)** molecular weight (60 wt. % solids, 50/50 *N*-phenylmaleimide/norbornene, 66 °C, 24 h), and the effects of weight % solids as a function of **c)** % yield and **d)** molecular weight (3 mol % AIBN, 50/50 *N*-phenylmaleimide/norbornene, 66 °C, 24 h).

In order to probe the mechanistic behavior of this copolymerization, *in-situ* high temperature NMR was used to monitor individual monomer concentrations during the course of the polymerization. In this work, copolymerizations were performed in sealed J. Young NMR tubes using THF-d_8 as solvent and 1,3,5-trimethoxybenzene as an inert internal standard (aryl C-H resonance at 6.05 ppm). Monomer consumption was measured by monitoring the disappearance of the baseline-resolved signals for the olefinic norbornene resonance at 5.94 ppm and the olefinic *N*-phenylmaleimide resonance at 6.73 ppm (**Figure 15**). The data collected from these spectra was used to produce the plots shown in **Figure 14.** The effects of initiator loading as a function of **a)** % yield and **b)** molecular weight (60 wt. % solids, 50/50 *N*-phenylmaleimide/norbornene, 66 °C, 24 h), and the effects of weight % solids as a function of **c)** % yield and **d)** molecular weight (3 mol % AIBN, 50/50 *N*-phenylmaleimide/norbornene, 66 °C, 24 h).. Careful analysis of **Figure 16a** clearly demonstrated that *N*-phenylmaleimide was consumed at a greater rate than norbornene, and that all *N*-phenylmaleimide was consumed after eight hours, at which time norbornene consumption ceased (~70 % consumed) and its concentration remained constant for all reaction times extending beyond this point. This observation was consistent with previous literature reports in which norbornene is well-known to be incapable of radically homopolymerizing in the absence of an electron-deficient comonomer.[69] Furthermore, this result is reinforced by **Figure 16b** in which the change in monomer concentration is plotted with respect to its comonomer, yielding a slope of 1.7544 (d[MI]/d[Nb]). For perfectly alternating copolymerizations, a slope equal to 1 should be observed. Deviation from that value of 1 strongly indicates that *N*-phenylmaleimide concentration is changing roughly 1.75 times faster than norbornene concentration during free-radical copolymerizations of *N*-phenylmaleimide and norbornene. This indicated that an inherent difference in reactivity ratios must be present between these two monomeric species, and suggested that a strictly alternating polymerization mechanism was not possible.

Further analysis revealed that first-order polymerization kinetics was observed with respect to each monomer, as evidenced by the linear relationship between ln[monomer] versus time for both *N*-phenylmaleimide and norbornene (**Figure 16c** and **Figure 16d**).

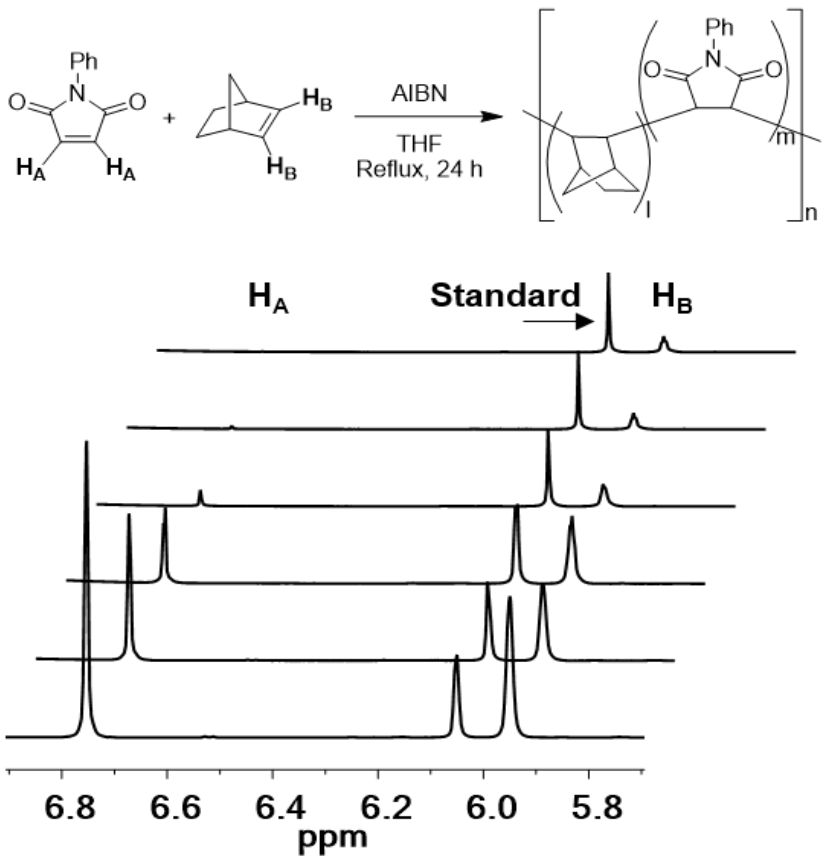

Figure 15. Stacked *in-situ* ^{1}H NMR spectra taken over the course of the polymerization at 75 °C in THF-d_8. (Note: the vinylic protons of *N*-phenylmaleimide are at 6.76 ppm, the vinylic protons of norbornene are at 5.95 ppm, and the aromatic protons of the trimethoxybenzene internal standard are at 6.06 ppm)

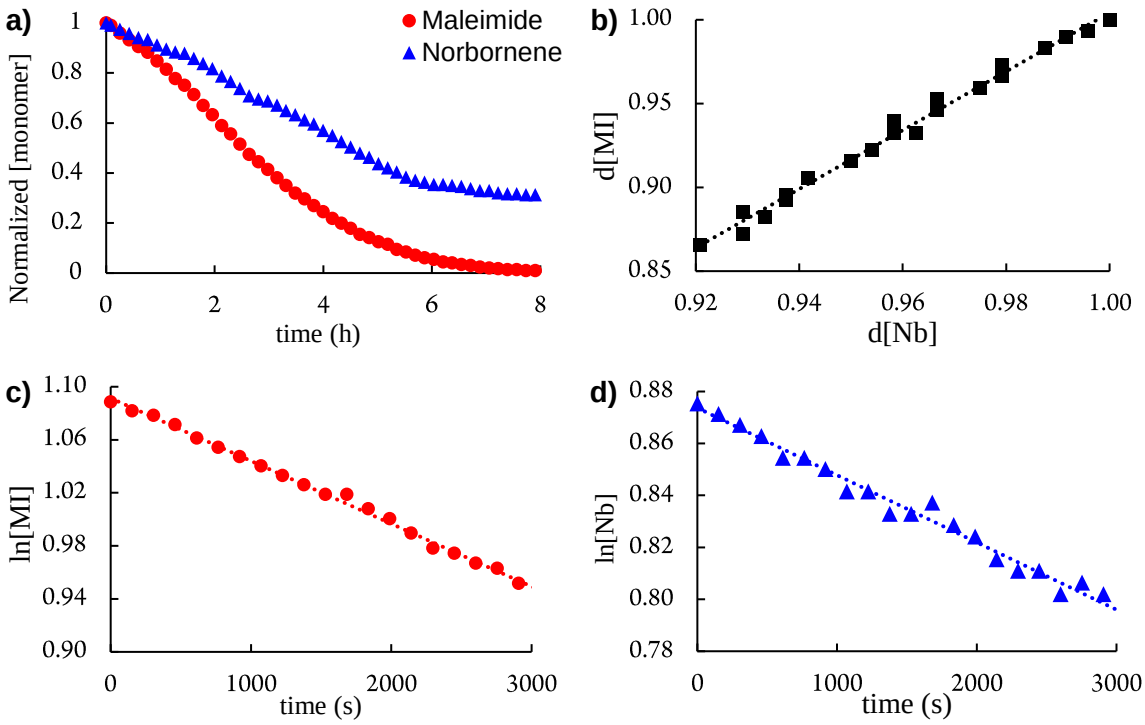

Figure 16. Plots of **a)** normalized [monomer] vs. time for a polymerization of *N*-phenylmaleimide (MI, circles) and norbornene (Nb, triangles), and **b)** d[MI] vs. d[Nb] for the copolymerization of 50/50 *N*-phenylmaleimide/norbornene, monitored via in-situ 1H NMR up to 10 % total monomer conversion. Also, first-order kinetic analysis of **c)** *N*-phenylmaleimide and **d)** norbornene as a function of time for the copolymerization of 50/50 *N*-phenylmaleimide/norbornene, monitored via *in-situ* 1H NMR analysis up to 10 % total monomer conversion.

Such analyses were performed at multiple monomer ratios (see Appendix C: Experimental Methods and Supporting information for Chapter 3) and were monitored up to 10 % total monomer consumption. **Figure 16** shows the results of a 50/50 copolymerization of *N*-phenylmaleimide/norbornene where the rate constant for *N*-phenylmaleimide incorporation was found to be $k = 4.74 \times 10^{-5}$ (**Figure 16c**), and the rate constant for norbornene incorporation was $k = 2.59 \times 10^{-5}$ (**Figure 16d**). This difference in rate constants likewise suggests that *N*-phenylmaleimide is consumed at ~1.83 times faster than norbornene, which is in strong agreement with the relationship found in **Figure 16b** (~1.75 times faster).

3.4 Graphical Analysis Using the Mayo-Lewis Equation

Based on the observations described above, which demonstrate that copolymerizations of *N*-phenylmaleimide and norbornene are not perfectly alternating, we chose to investigate the differences in monomer reactivity ratios to better understand the mechanistic details of this polymerization and its resultant polymer structures. To do this, we utilized the well-known Mayo-Lewis graphical analysis method for the free-radical copolymerization of norbornene and *N*-phenylmaleimide.[69] Though numerous methods for determining reactivity ratios may be employed, such as the Jaacks,[70-71], Fineman-Ross,[72] and Tidwell-Mortimer[73] methods, the Mayo-Lewis method was chosen due to monomer solubility limitations (Jaacks) and complications in obtaining accurate mole fractions of each monomer within the resultant polymers (Fineman-Ross, Tidwell-Mortimer), which are required for most other reactivity ratio calculations.[58,74-75] Additionally, the Mayo-Lewis method has classically been used to determine reactivity ratios for perfectly alternating norbornene/maleic anhydride copolymerizations.[75] The Mayo-Lewis graphical analysis presented herein follows the terminal copolymer model shown in **Figure 17**, and the reactivity ratios determined are defined as $r_1 = k_{11}/k_{12}$ (*N*-phenylmaleimide) and $r_2 = k_{22}/k_{21}$ (norbornene). The rearranged Mayo-Lewis equation (6), which was used for this graphical analysis is also described in **Figure 17**.

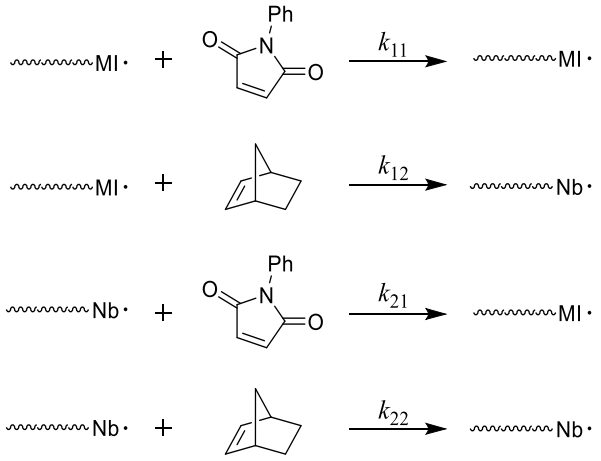

$$r_1 = \frac{k_{11}}{k_{12}} \qquad r_2 = \frac{k_{22}}{k_{21}}$$

$$r_2 = \frac{[M_1]}{[M_2]}\left[\frac{d[M_2]}{d[M_1]}\left(1 + \frac{r_1[M_1]}{[M_2]}\right) - 1\right] \quad (6)$$

Figure 17. The terminal copolymer model, definitions of reactivity ratios (r_1 = *N*-phenylmaleimide, r_2 = norbornene), as well as the rearranged Mayo-Lewis copolymer equation.

In order to perform this graphical analysis, three copolymerizations of *N*-phenylmaleimide and norbornene with different initial monomer feed ratios were monitored via *in-situ* NMR up to 10 % total monomer conversion. The results of those polymerizations are shown in **Table 1**, in which molecular weights, molecular weight distributions (M_w/M_n), and glass transition temperatures (T_g) were recorded. As expected from the optimization studies conducted in **Figure 16**, the molecular weights of the resultant polymers were low (M_n < 3,000 g/mol), however, they demonstrated high glass transition temperatures (T_g > 250 °C) in similarity to alternating norbornene/maleic anhydride copolymers. The values of d[MI]/d[Nb] were found to decrease as the *N*-phenylmaleimide/norbornene ratio was varied from 40/60 to 60/40 while the observed rate constants (k_{obs}) were found to increase. These trends intuitively make sense as small changes in *N*-phenylmaleimide concentration are minimized as its loading was increased, yet higher *N*-phenylmaleimide concentrations increased the rate of polymerization as a result of its ability to homopolymerize in addition to its propensity to propagate with norbornene. The graphical analysis was performed by assuming reactivity ratio values of -1 to +1 for *N*-phenylmaleimide (r_1) and calculating the reactivity ratio of norbornene (r_2) (see Appendix C: Experimental Methods and Supporting information for Chapter 3) using the rearranged Mayo-Lewis copolymerization equation (**Figure 17**). Those reactivity ratio

Table 1. Polymerization data of the polymers produced during the Mayo-Lewis Experiments.

entry	[MI]/[Nb][a]	M_n[b] (g/mol)	M_w/M_n	d[MI]/d[Nb][c]	k_{obs}[c]	T_g[d] (°C)
1	40/60	2300	1.55	2.16	2.65	253
2	50/50	2700	1.46	1.75	3.76	266
3	60/40	2100	1.55	1.58	4.90	255

[a]Initial monomer feed ratio. [b]Determined using gel permeation chromatography in THF at 40 °C relative to polystyrene standards. [c]Observed rate constant, determined using *in-situ* 1H NMR up to 10 % total monomer conversion. [d]Determined using differential scanning calorimetry on the second heating cycle.

values are plotted in **Figure 18**, and a clear intersection point was observed. Via the Mayo-Lewis method, the calculated intersection point is related to the reactivity ratios of each monomer. For perfectly alternating copolymerizations, a reactivity ratio of ~0 is predicted for each monomer, which originates from the definition of monomer reactivity ratios in the terminal model presented in **Figure 17**.[76] The average intersection point for the copolymerizations of *N*-phenylmaleimide and norbornene was found to be r_1 = 0.17 and r_2 = -0.33. Because these values are non-zero, we can safely conclude that the mechanism by which this polymerization proceeds is not strictly alternating, yet their small magnitude strongly supports that these copolymerizations do in fact have strong alternating tendencies. Although negative reactivity ratio values have been reported in the literature, a negative value for r_2 has no physical interpretation due to the reactivity ratio definitions highlighted in **Figure 17**, and therefore do not provide any additional mechanistic insight into this copolymerization.[77-80]

Furthermore, though the removal of unreacted monomer from the resultant polymers proved to be problematic, the resultant polymers' compositions were analyzed at various initial monomer ratios (**Figure 18b**). To do this, the mole fraction of *N*-phenylmaleimide units within the resultant polymer (χ_{MI} (polymer)) was estimated using the monomer conversion data obtained via ^{1}H NMR spectroscopy. From **Figure 18b**, a linear trend was observed in which deviation from perfectly alternating behavior (χ_{MI} (polymer) = 0.5) was witnessed as *N*-phenylmaleimide initial *N*-phenylmaleimide loading ratios (χ_{MI} (loading)) were increased. As previously noted, this behavior was attributed to *N*-phenylmaleimide's

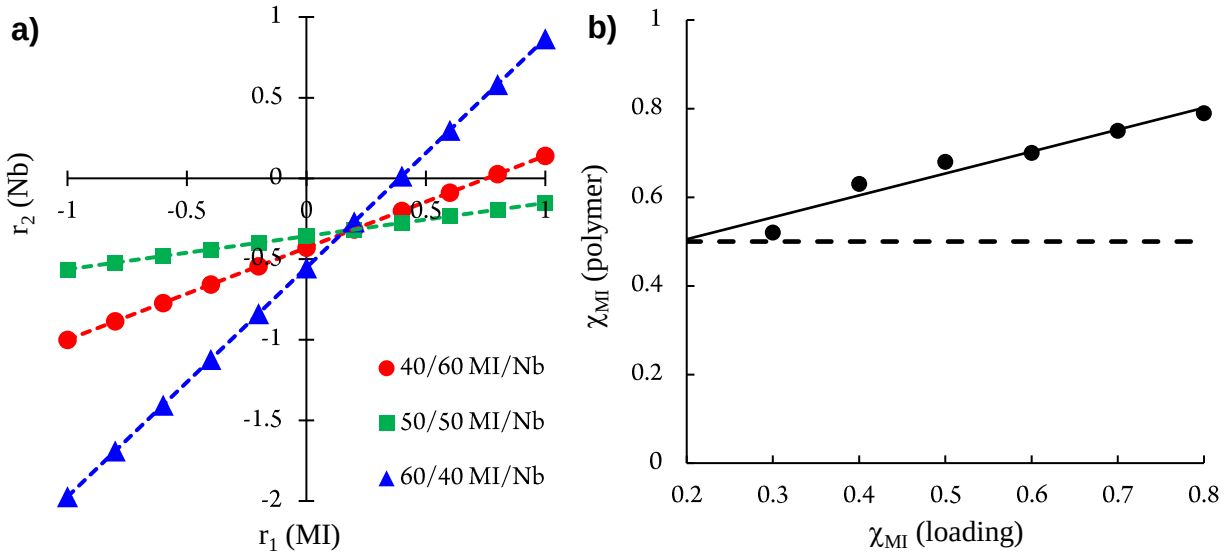

Figure 18. a) Mayo-Lewis graphical analysis for the free-radical copolymerization of *N*-phenylmaleimide (MI) and norbornene (Nb) at respective monomer loadings of 40/60 (*circles*), 50/50 (*squares*), and 60/40 *N*-phenylmaleimide/norbornene (*triangles*) **b)** Graphical depiction of the mole fraction of *N*-phenylmaleimide units present in the polymer (at 10 % total monomer conversion) versus initial *N*-phenylmaleimide loading for various monomer feed ratios (circles), χ_{MI} (polymer) was estimated using monomer conversion data obtained via ^{1}H NMR spectroscopy. Dashed line represents expected χ_{MI} for a strictly alternating copolymerization.

ability to radically homopolymerize, thereby allowing for increased frequency of subsequent *N*-phenylmaleimide units incorporated within the polymer backbone as a function of increasing *N*-phenylmaleimide concentration. For example, at initial monomer loadings of 80 mol % *N*-phenylmaleimide to 20 mol % norbornene, polymer compositions containing up to 79 mol % *N*-phenylmaleimide units were observed.

3.5 Alternating Radical Copolymers as a means to new Thermally Re-arranged Polymers

Following the fundamental investigations of these polymer systems, we began the synthesis of maleimide derivatives that add desirable functionality for CO_2/N_2 separations to the *N*-position. Directly inspired by high performing thermally re-arranged polymers (TR polymers),[35,81] *N*-(*o*-acetylphenyl)-maleimide served as a masked, radical-stable precursor aimed at investigating if the thermal re-arrangement pathway into oxazoles can be utilized in alternating copolymer systems to create additional free volume in the polymer matrix. **Figure 19** shows the monomer synthesis scheme as well as the thermal re-arrangement pathway of the resultant polymer. Starting with 2-aminophenol, maleic anhydride, and acetic acid, an acid-catalyzed amidation of maleic anhydride produced *N*-(*o*-hydroxyphenyl)-maleimide in 30 % yield.[82] Due to the ability for phenols to act as radical scavengers, i.e. hydroquinone, the hydroxyl group was protected with an acetate group rapidly through a microwave-assisted reaction vessel and an iodine catalyst to produce *N*-(*o*-acetylphenyl)-maleimide in 91 % yield.[83] Additionally, acetate protecting groups can be removed through the excessive heat that is required for the thermal re-arrangement to take place allowing for deprotection and arrangement in one step. Following monomer synthesis, copolymerization of norbornene and *N*-(*o*-acetylphenyl)-maleimide was performed using optimal initiator loadings and concentration from **Figure 14** to produce low molecular weight copolymers (M_n ~2400 g/mol) (NMRs and GPCs available in Appendix C: Experimental Methods and Supporting information for Chapter 3).

In order to investigate the viability of these polymers for the thermal re-arrangement of the *N*-(*o*-hydroxyphenyl)-maleimide to oxazole, polymers were investigated by thermal

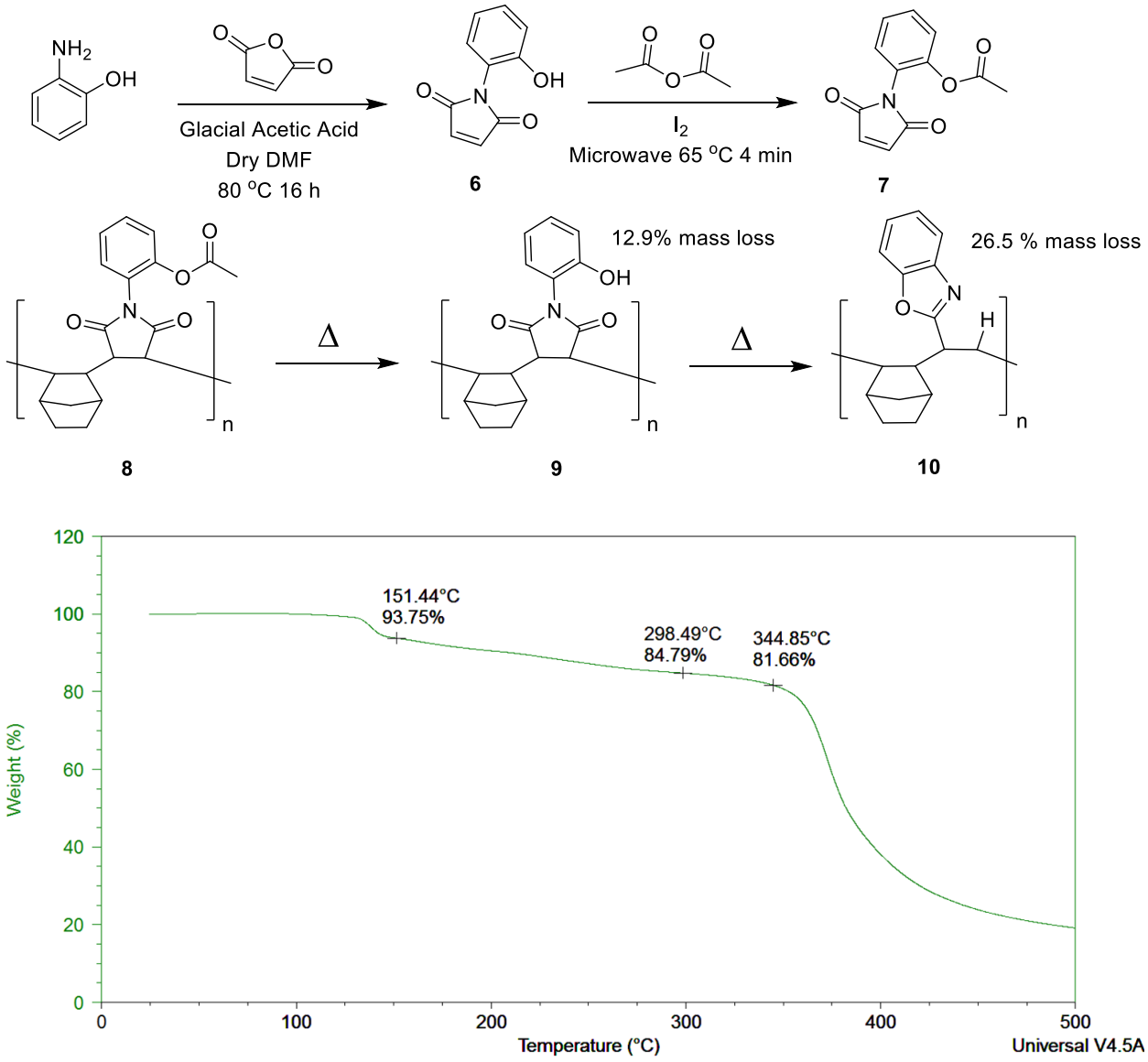

Figure 19. Synthesis and polymerization of *N*-(*o*-acetylphenyl)-maleimide and its thermal rearrangement to an oxazole.

gravimetric analysis (TGA) (**Figure 19**). Based on the mass of the polymer repeat unit, we can calculate the expected mass loss for the acetate deprotection and for oxazole formation and correlate them with the observed mass loss values in the TGA. Unfortunately, there did not seem to be any correlation with the decomposition of these polymers with the formation of the oxazole suggesting that the polymer lacked the thermal stability to decompose by the desired pathway. Also, the low molecular weights of these materials make the formation of large-defect free films for membranes difficult and were ultimately abandoned in favor of more attractive options.

3.6 Conclusions

The free-radical copolymerization of *N*-phenylmaleimide and norbornene was optimized to maximize either percent yield or molecular weight. Polymers with molecular weights up to ~4,300 g/mol were synthesized when using 0.1 mol % initiator and at a concentration of 60 wt. % total solids dissolved in THF. Though these polymers are of low molecular weight, their rigid nature, high glass transition temperatures (T_g > 250 °C), and possibilities for functionalization make them attractive candidates for a number of potential applications. Mechanistic details of these copolymerizations were investigated using high-temperature, *in-situ* ^{1}H NMR analysis. Careful examination of the kinetic polymerization data and Mayo-Lewis graphical analysis conclusively showed that the copolymerization does not follow a strict alternating sequence, but instead is a predominately alternating copolymerization that displays a strong tendency to incorporate sequential maleimide units within the polymeric backbone. These results conclusively demonstrate that when utilizing free-radical copolymerizations of electron-rich cycloolefins with electron deficient comonomers, subtle changes in electronic character of the electron-deficient comonomer can lead to significant changes in copolymer structure.

Chapter 4. Effect of Cross-Link Density on Carbon Dioxide Separation in Polydimethylsiloxane-Norbornene Membranes

A version of this chapter was originally published by Tao Hong, Zhenbin Niu, Xunxiang Hu, Kevin Gmernicki, Shiwang Cheng, Fei Fan, J. Casey Johnson, Eunice Hong, Shannon Mahurin, De-en Jiang, Brian Long, Jimmy Mays, Alexei Sokolov, and Tomonori Saito:

The author contributed by performing investigations into these materials in tandem with this work, aided in the characterization of materials, and participated in collaborative discussions surrounding this body of work.

Experimental and supplemental information available in Appendix D: Experimental Methods and Supporting information for Chapter 4

4.1 Abstract

The development of high-performance materials for carbon dioxide separation and capture will significantly contribute to a solution for climate change. Herein, (bicycloheptenyl)ethyl-terminated polydimethylsiloxane (PDMSPNB) membranes with varied cross-link densities were synthesized via ring-opening metathesis polymerization. The developed polymer membranes show higher permeability and better selectivity than those of conventional cross-linked PDMS membrane. The achieved performance (CO_2 permeability ~6800 Barrer; CO_2/N_2 selectivity ~14) is very promising for practical applications. The key to achieving this high performance is the use of an *in-situ* cross-linking method for difunctional PDMS macromonomers, which provides lightly cross-linked membranes. By combining positron annihilation lifetime spectroscopy, broadband dielectric spectroscopy, and gas solubility measurements, key parameters necessary for achieving excellent performance have been elucidated.

4.2 Background on Membranes and Coal-fired Power Plants

Due to the extensive use of fossil fuels, global carbon dioxide emissions have increased steadily over the past several decades, contributing to unpredictable climate changes.[34,84] In the USA, approximately 40% of CO_2 release can be attributed to combustion of fossil fuels for electrical energy production. For example, a typical 550 MW coal-fired power plant produces about two million cubic feet of flue gas per minute with a CO_2 concentration of 12–14%, along with water, nitrogen, oxygen, and traces of other contaminants.[85] Therefore, significant efforts have been made to reduce CO_2 emissions by applying various capture and separation technologies. Compared with most traditional techniques, such as amine-based solvent absorption, passive membrane CO_2 separation technology has drawn considerable attention because the use of high-performance passive membranes could offer a significant reduction in energy cost.[86] Moreover, membrane-based separation is an environmentally benign and sustainable methodology. In membrane separations, the two major parameters of concern are gas permeability and selectivity. Permeability (P) is defined as the product of gas flux and membrane thickness divided by the pressure difference across the membrane, which is determined by both the gas solubility (S) and gas diffusivity (D), whereas gas selectivity (α) is the ratio of permeability coefficients of any two gases. Given that the target gas pair for flue gas separation is CO_2/N_2, polymer membranes with both good CO_2 permeability and CO_2/N_2 selectivity are desirable. In general, polymer membranes are usually evaluated by using the Robeson plot and an empirically derived upper bound that reflects the inherent trade-off relationship between permeability and selectivity. In this tradeoff, membranes that yield high permeabilities are generally less selective and vice versa.[15-16,87] Unfortunately, the separation performance of commercially known membranes falls significantly below the Robeson upper bound and do not meet the separation efficiency for practical CO_2/N_2 separation. Moreover, the key issue in practical applications is the large volume of gas flow coming out of the power plant, and membranes with exceptionally high permeability are needed for practical reasons. Simply pursuing membranes with enhanced selectivity (e.g., CO_2/N_2 higher than 30) will not improve separation efficiency due to the limitation

of pressure differences in practical separations,[38] and membranes with high selectivity but poor permeability will not be useful in CO_2 separation. Therefore, a balance between membranes with high permeability and good selectivity is required for the separation of CO_2 from flue gas mixtures. In the past few decades, glassy membranes with high permeability have been developed. For example, poly(trimethylsilyl propyne) (PTMSP) is known to be one of the most permeable polymers (CO_2 permeability 29000 Barrer).[88] Another highly permeable membrane is a polymer of intrinsic microporosity (PIM-1), which has a reported CO_2 permeability of 2300 Barrer with a CO_2 /N_2 selectivity of 25.[18] However, due to severe aging issues associated with these glassy polymers, significant differences in permeability and selectivity were reported by different researchers.[18,88-91] Moreover, the separation mechanism of most glassy polymer membranes is based on size sieving, which works well for gas pairs with very different sizes, for example, CH_4/H_2 (3.80 Å/ 2.89 Å) or N_2/He (3.64 Å/2.60 Å). However, in CO_2/N_2 separation, due to similar kinetic diameters (CO_2 3.30 Å, N_2 3.64 Å), size-sieving techniques might be intrinsically limited.[87] Thus, developing a new method based on a non-size-sieving mechanism could potentially offer a solution to improved CO_2/N_2 separation efficiency. As a typical rubbery polymer at room temperature, polydimethylsiloxane (PDMS) is known to possess some of the highest permeabilities to various gases, for example, the reported permeability is 3800 Barrer for CO_2, 890 Barrer for H_2, and 400 Barrer for N_2.[40] It has also attracted much attention due to its good physical and mechanical properties (ductile), no aging issues, low cost, thermal stability, and ease of processing.[92-101] For CO_2/N_2 separation, the reported selectivity of typical PDMS membranes is around 9.5.[40] If the CO_2/N_2 selectivity of those PDMS membranes can be improved, while maintaining high permeability, the designed membrane would meet practical targets in efficiency and cost.[38] In PDMS-like rubbery polymer membranes, the liquid-like polymer matrix has a poor size-sieving ability;[102] thus the overall selectivity is often determined by different gas solubilities in the membranes.[40,103] If one compares various membranes made of PDMS polymer matrix, the gas solubilities should not be altered significantly, whereas diffusivity can be tuned by controlling the PDMS molecular architecture. One way to tune the gas diffusivity property of PDMS membranes is by introducing cross-linked networks. Many studies have been

performed on cross-linked PDMS materials due to their various applications in many fields.[104-111] The performance of cross-linked PDMS materials largely depends on the structure of the cross-linked networks and the residual end groups in the bulk material and interfaces. A previous study showed that increased cross-links in the PDMS network resulted in stronger elastic resistance and the diffusivity of a penetrant through the membrane decreased.[106] There has also been a previous study on cross-linked Matrimid membranes that reported the monotonous decrease of the permeability of different gases with increasing degrees of cross-linking.[112] In some other cases, Lin et al. reported in their study of cross-linked poly(ethylene glycol diacrylate) (XLPEGDA) that gas permeability and solubility were independent of cross-link density.[113] Some papers even claimed an increase in gas permeability with increasing cross-link density.[114] However, more comprehensive studies on the effect of the cross-link density for gas separation in rubbery polymers, such as PDMS-based membranes, are limited and a better level of understanding is necessary for further development of gas separation membranes. Herein, a facile membrane fabrication approach was applied for the preparation of PDMS-based membranes for CO_2 separation with a controlled degree of cross-linking. The room-temperature chemical cross-linking reaction of (bicycloheptenyl)ethyl-terminated polydimethylsiloxane (PDMSPNB) through ring-opening metathesis polymerization (ROMP) was developed by reacting PDMSPNB with Grubbs II catalyst in dichloromethane and drying under argon. The cross-link density was mainly controlled by the ratio of PDMSPNB to Grubbs II catalyst and was determined by rheological measurements. The use of difunctional PDMS macromonomers allowed for the preparation of free-standing films with a much lower cross-link density than conventionally reported cross-linked PDMS membranes. Owing to the low cross-link density, the synthesized membranes provide very high permeability of CO_2 up to about 6800 Barrer with a good selectivity of CO_2/N_2 (14) in single-gas permeation measurements and show similar performances for mixed-gas separation. The gas solubility, positron annihilation lifetime spectroscopy (PALS), and broadband dielectric spectroscopy (BDS) studies were carried out to provide a better understanding of the parameters controlling solubility and diffusivity.

4.3 Material Synthesis and Characterization Methods

Materials and sample preparation. PDMSPNB with a weight-average molecular weight range from 12,000 to 16,000 g/mol was purchased from Gelest Inc. A Sylgard 184 silicone elastomer kit was obtained from Dow Corning. The Grubbs II catalyst and anhydrous dichloromethane were purchased from Sigma–Aldrich. Nitrogen and carbon dioxide gas cylinders (99.99% purity) were obtained from Air Liquide. All materials were used as received.

General membrane synthesis. The scheme of the cross-linking reaction is shown in **Figure 20**. The reaction was performed by ROMP of the norbornene groups on the telechelic positions of PDMS. In a typical experiment, PDMSPNB (0.515 g, 3.68×10^{-5} mol) was dissolved in CH_2Cl_2 (6 mL), and Grubbs II catalyst (1.92 mg, 2.26×10^{-6} mol) was dissolved in CH_2Cl_2 (2 mL) separately. Then the Grubbs II stock solution (0.5 mL) was added to the solution of PDMSPNB and the mixture was shaken for 60 s before being

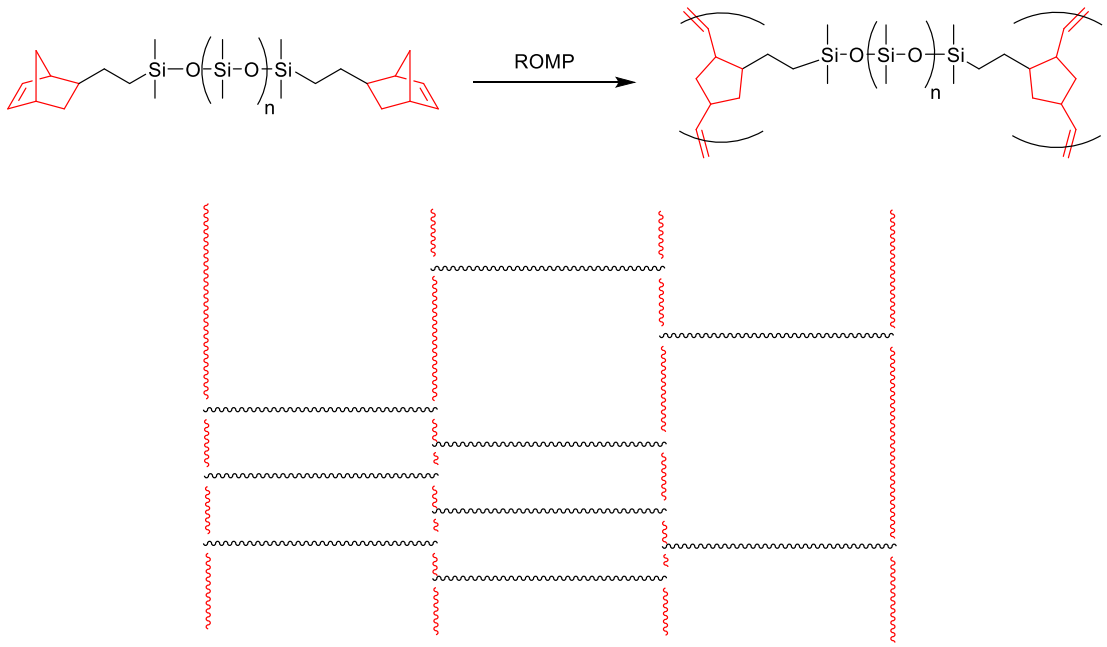

Figure 20. Scheme of cross-linking reaction of PDMSPNB and illustration of various cross-linking densities.

poured into a 100 mL polytetrafluoroethylene (PTFE) dish (with a diameter of 10 cm). The PTFE dish was then covered for 1 h and the in situ cross-linked membrane was formed. A mixture of ethyl vinyl ether (2 mL) in CH_2Cl_2 (6 mL) was added to the film to terminate the cross-linking reaction. The membrane was dried under an argon atmosphere overnight and moved into a vacuum oven for 3 days to remove residual solvent completely. Finally, the cross-linked, free-standing polymer membrane was detached from the PTFE dish and cut into approximately 2x2 cm square membranes. The thickness of each membrane was determined by using a micrometer. PDMSPNB/Grubbs II molar ratios varied from 130/0.5 to 130/10 were used during the membrane-forming process to control the cross-link density. All permeation measurements were performed within a similar time frame after curing. A conventional cross-linked PDMS membrane was synthesized and characterized as a control experiment.[115] The membrane was fabricated by mixing the Sylgard 184 silicone elastomer kit with the curing agent in a weight ratio of 10:1 with toluene as a solvent to dilute the mixture. The mixture was stirred for 15 min before being cast onto a 10x10 cm glass plate. After 1 h of curing at room temperature, the mixture was placed in an oven and heated for 3 h at 100 °C. It was then moved into the vacuum oven for 3 days at room temperature to remove residual solvent. Finally, the freestanding PDMS membrane was peeled off the glass substrate and cut for all measurements carried out in this study.

4.4 Results of Cross-linked PDMSNB with varied catalyst ratios

All membranes were formed in situ through the cross-linking reaction of PDMSPNB with Grubbs II catalyst in a PTFE dish. The as-prepared free-standing membranes showed a transparent, homogeneous, and elastic nature with thicknesses ranging from 200–250 mm With changing PDMSPNB to Grubbs II catalyst ratios, the membranes showed different ductilities due to differences in cross-link density. To elucidate the effect of the PDMSPNB to Grubbs II catalyst molar ratio, the cross-link density was quantified by melt rheology. The G’ values as a function of polymer/ catalyst ratio are shown in **Figure 21** and summarized in **Table 2**. Density values for all membranes, including conventional

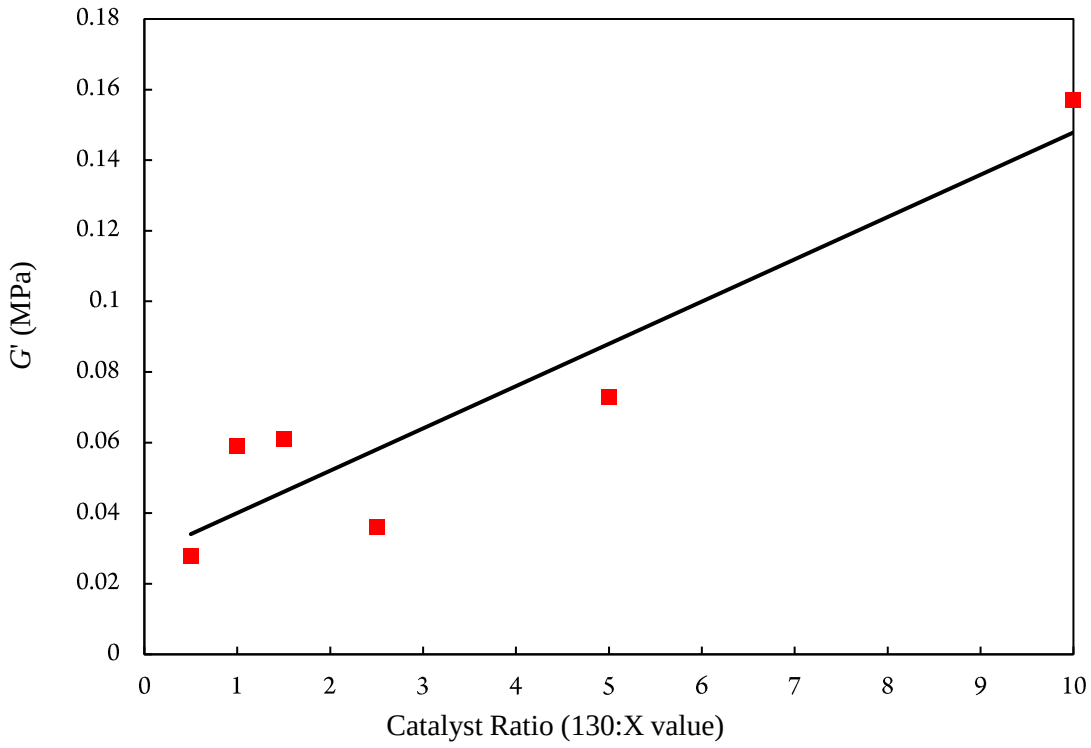

Figure 21. The value of *G*' as a function of catalyst ratio for cross-linked PDMSPNB membranes.

Table 2. Plateau value of *G*', molecular weight between cross-links, cross-link density, and glass transition temperature (T_g) as a function of different PDMSPNB/Grubbs II ratios.

entry	Ratio PDMSNB/Grubbs II	*G*' (MPa)	M_x (10^3 g/mol)	Cross-link density (mol cm^{-3} x 10^5)	T_g (K)
1	130:0.5	0.028	86.0	0.57	148
2	130:1.0	0.059	41.2	1.19	148
3	130:1.5	0.061	39.0	1.23	148
4	130:2.5	0.036	67.1	0.73	148
5	130:5.0	0.073	33.3	1.47	148
6	130:10	0.157	15.5	3.17	148
7	Conventional PDMS	0.387	6.3	7.81	150

PDMS, were obtained from density-gradient column measurements (0.9730–0.9881 g/cm^3) and an average value of 0.9800 g/cm^3 was applied in all calculations of M_x (Equation 5) and the cross-link density. The cross-link density of the conventional cross-linked PDMS membrane was also determined by rheology measurements and was calculated to be 7.81x10^{-5} mol/cm^3, which was consistent with previously reported values.[40]

4.5 Gas Permeation and separation properties of cross-linked PDMSNB

All permeability measurements of PDMSPNB membranes were performed at ambient temperature (298±1K) **Figure 22** shows a representative plot of the CO_2 and N_2 pressure increases; these were measured on the permeate side of the separation chamber in a single-gas permeation measurement.

Single-gas permeability values were calculated by using the data collected in the linear regime, according to Equation 7. in which P_a is the permeability of the gas A, V_c is

$$P_A = \frac{V_c l}{RTA_m \Delta P}\frac{dP_l}{dt} \tag{7}$$

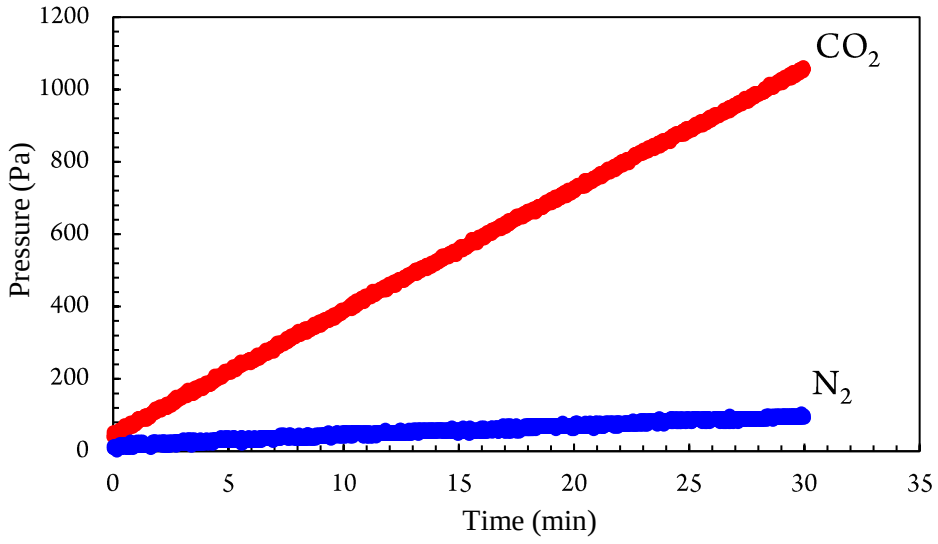

Figure 22. Pressure increase in the permeate chamber as CO_2 and N_2 diffuse through the PDMSPNB membrane; c_x = 1.19x10^{-5} mol·cm^{-3}.

the permeate volume, l is the membrane thickness, R is the ideal gas constant, A_m is the membrane area, ΔP is the difference between the upstream and downstream pressures, and (dP_1/dt) is the rate of gas pressure increase on the permeate side. In our measurements, the parameters were set as follows: V_c = 120 cm^3, ΔP = 38 kPa. The selectivity was obtained by calculating the ratio of CO_2 permeability to N_2 permeability.

The permeability of each component in the gas mixture was calculated by using Equation 8.

$$P_A = \frac{V_c l}{RTA_m \Delta P} \frac{dP_l}{dt} \frac{y_A}{x_A} \tag{8}$$

in which y_A is the mole fraction of component A on the permeate side and x_A is the mole fraction of component A on the feed side.

All single gas permeability and CO_2/N_2 selectivity data for PDMSPNB membranes with varied cross-link density as well as the conventional PDMS membrane are summarized in **Table 3** and **Figure 23**. The updated Robeson's upper bound for CO_2/N_2 with the cross-linked PDMSPNB in this study is shown in **Figure 24**.

4.6 Gas Solubility Measurements

CO_2 mass uptakes for cross-linked PDMSPNB membranes with different cross-link densities and conventional cross-linked PDMS were measured. Due to the low absorption value, the change of mass was in the 0.15% to 0.20% (0.075 to 0.1 mg) range. The sorption isotherms were calculated from the mass uptake. From the sorption isotherms, the solubility of each membrane was obtained from Equation 9:

$$S \equiv C/p \tag{9}$$

in which S is gas solubility, C is the sorption isotherm, and p is the pressure.

It can be noted in **Table 4** that the calculated CO_2 solubility showed very small differences as a function of cross-link density. When compared to the conventional cross-linked PDMS membrane, the solubility of the cross-linked PDMSPNB membranes showed a slight decrease.

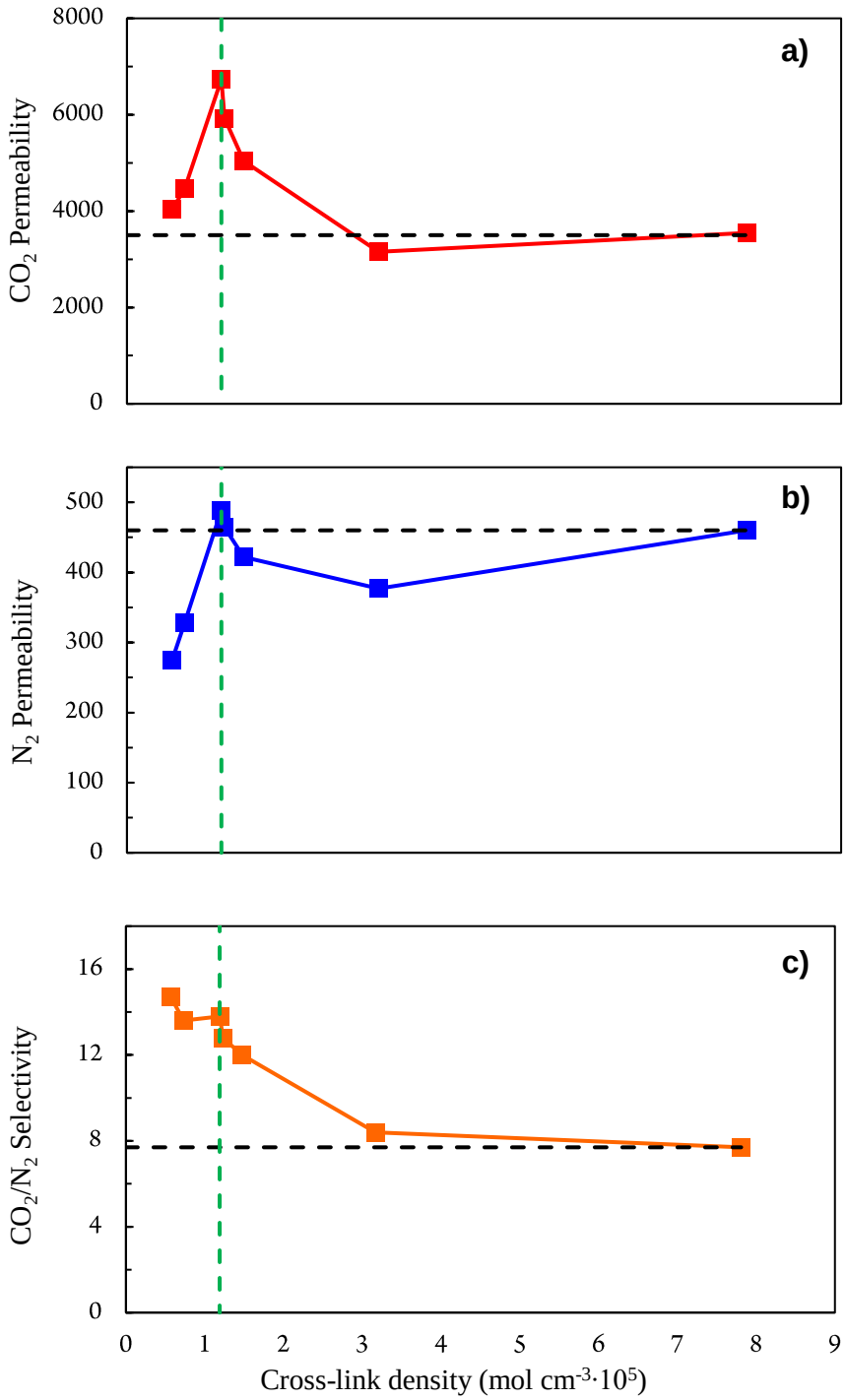

Figure 23. a) CO_2 permeability, **b)** N_2 permeability, and **c)** CO_2/N_2 selectivity as a function of cross-link density for the cross-linked PDMSPNB membranes. Horizontal dashed lines represent the gas permeability and selectivity values for conventional cross-linked PDMS; vertical dashed lines mark the sample with the highest CO_2 permeability.

Table 3. Summary of gas permeability and CO_2/N_2 selectivity as a function of cross-link density.

Sample	Cross-link density (mol $cm^{-3}x10^5$)	Permeability [Barrer]		CO_2/N_2 Selectivity
		CO_2	N_2	
A	0.57	4030	275	14.7
B	0.73	4474	329	13.6
C	1.19	6734	489	13.8
D	1.23	5929	464	12.8
E	1.47	5040	422	12.0
F	3.17	3154	377	8.4
-	7.81 (PDMS)	3545	460	7.7
C-mixed gas	1.19	6343	434	14.6

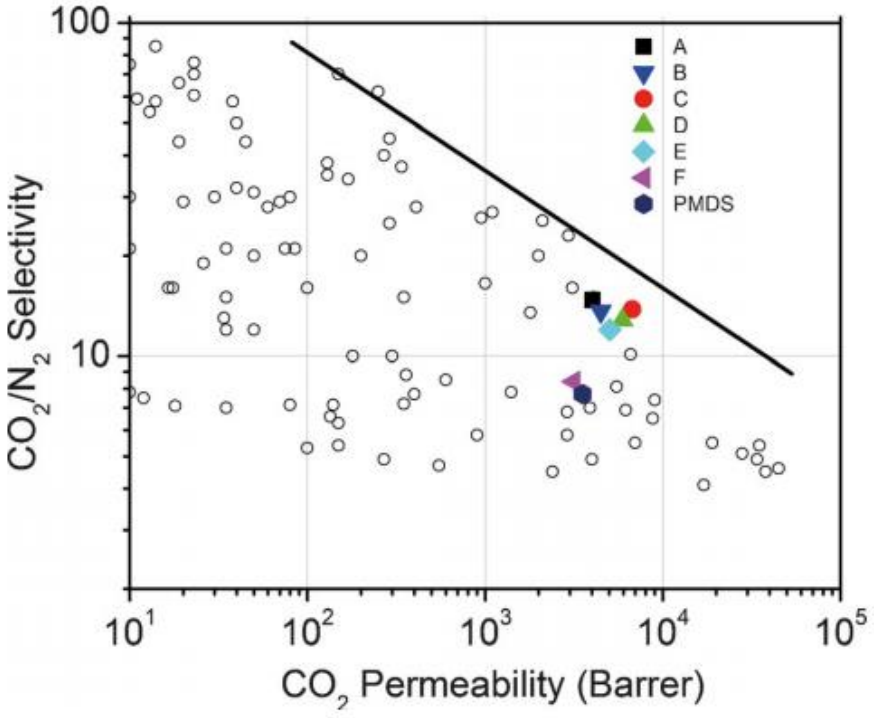

Figure 24. Summary of the cross-linked PDMSPNB and conventional PDMS membranes in the Robeson plot.

Table 4. Summary of gas solubility and PALS results as a function of cross-link density.

Cross-link density (mol/cm^{3}x10^5)	S (cm^3(STP)cm^{-3}bar^{-1})	Average Positron lifetime (ns)	Pore diameter (nm)	Average trapping rate (ns^{-1})	Relative Pore Concentration
0.57	0.86±0.030	2.647	0.676	1.9664	1.00
0.73	1.04±0.053	2.751	0.691	2.6633	1.35
1.19	1.10±0.012	2.537	0.659	2.3937	1.21
1.47	0.97±0.035	2.511	0.655	3.0143	1.53
3.17	1.03±0.011	2.431	0.643	2.6459	1.34
7.81 (PDMS)	1.25±0.044	2.615	0.671	2.6794	1.36

4.7 PALS Measurements

For rubbery polymeric membranes, we expect the diffusivity to be influenced by both the free volume and segmental dynamics. In order to study free volume effect, PALS measurements were carried out. Three separate positron lifetimes are commonly observed in polymers. The first lifetime (τ_1) indicates the positrons being annihilated in the bulk of the materials (< 200 ps). The second lifetime, τ_2, is attributed to the positrons being annihilated in defects (300-500 ps). The third lifetime, τ_3, refers to ortho-positronium (*o*-Ps), a parallel spin complex of a positron and electron, which forms in low electron density regions of the polymer, such as free volumes, holes, interfaces, and pores. The *o*-Ps lifetime and intensity are often associated with the size and concentration of the open volume in a polymer, respectively. Therefore, the experimentally obtained positron lifetime was fitted by three exponential components. From the fitting procedure, one obtains positron lifetimes and intensities. The *o*-Ps lifetime, τ_3, is typically related to the average radius of a free volume element, *r*, which is assumed to be spherical, by Tao-Eldrup model (Equation 10).[116-117]

$$\tau_3 = \frac{1}{2}\left(1 - \frac{r}{r+\Delta r} + \frac{1}{2\pi} sin\left[2\pi \frac{r}{r+\Delta r}\right]\right)^{-1} \quad (10)$$

Trapping model is applied here to extract the average concentration of the free volume (Equation 11).[118]

$$\kappa_2 = \frac{I_2}{I_1}[I_3(\lambda_2 - \lambda_3) + (\lambda_b - \lambda_2)]$$
$$\kappa_3 = \frac{I_3}{I_1}[I_2(\lambda_3 - \lambda_2) + (\lambda_b - \lambda_3)] \quad (11)$$

in which K_2 and K_3 are positron trapping rates in the defects and free volume, respectively; annihilation rate λ_i is equal to the reciprocal lifetime τ_i; λ_b is the bulk annihilation rate, I_i are corresponding intensities and hence through the relation given in Equation 12.

$$\kappa_i = \mu_i C_i \quad (12)$$

in which μ_i is the specific trapping coefficient for one trapping site, the trapping site density could be obtained. By assuming the μ_3 is the same for all of the membranes considered herein, the concentration of free volume is proportional to the trapping rate calculated by Equation 11.

4.8 Dynamics Study by BDS Measurements

Dynamics of synthesized membranes were measured using broadband dielectric spectroscopy. **Figure 25** shows the representative dielectric loss spectra and their fits at -114 °C.

Two Havriliak-Negami (HN) functions are used to describe the main relaxation process in the dielectric spectrum (Equation 13):

$$\varepsilon^*(\omega) = \varepsilon_\infty + \frac{\Delta\varepsilon_1}{[1 + (i\omega\tau_{HN1})^{\alpha_1}]^{\beta_1}} + \frac{\Delta\varepsilon_2}{[1 + (i\omega\tau_{HN2})^{\alpha_2}]^{\beta_2}} \quad (13)$$

in which $\varepsilon^*(\omega)$ is the complex dielectric permittivity, $\varepsilon_\infty = \lim_{\omega\to\infty} \varepsilon'(\omega)$ is the value of $\varepsilon'(\omega)$ at infinite frequency, $\Delta\varepsilon$ is the dielectric relaxation strength, $\omega = 2\pi f$ is the angular frequency, τ_{HN} is the HN relaxation time, and α and β are the shape parameters.

The frequency of the ε'' maximum is used to calculate the relaxation time (τ_{max}). The τ_{max} is related to the Havriliak-Negami relaxation time τ_{HN}, and shape parameters α and

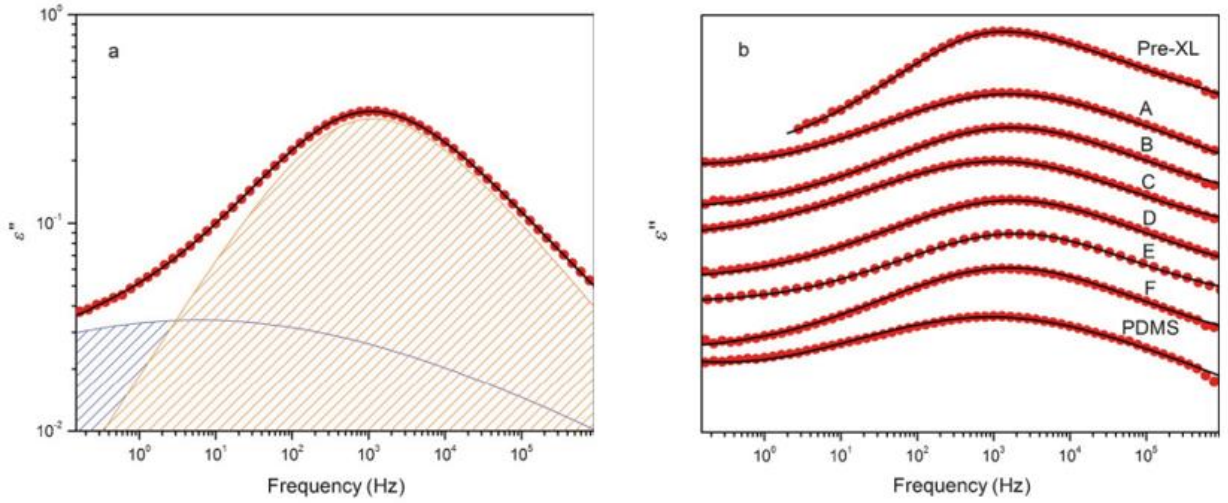

Figure 25. a) Dielectric loss spectra of sample C (c_x = 1.19x10^{-5} mol·cm^{-3}) at -114 °C (red solid symbols). Lines show the fit of the dielectric spectrum; two relaxation processes were used. **b)** Dielectric loss peaks for pre-crosslinked PDMSPNB, PDMSPNB with different cross-linked densities, and conventional PDMS membranes at -114 °C. The peaks have been shifted vertically to illustrate the systematic change of the peak shape and positron. The black curves show the fits to the Havriliak-Negami (HN) function.

β by Equation 14:

$$\tau_{max} = \tau_{HN}\left(sin\frac{\alpha\beta\pi}{2+2\beta}\right)^{1/\alpha}\left(sin\frac{\alpha\pi}{2+2\beta}\right)^{-1/\alpha} \quad (14)$$

The temperature dependence of the segmental relaxation time (higher frequency peak) of different samples determined from the HN fitting function (Equation 13) is presented in **Figure 26**. The behavior is described by the well-known Vogel-Fulcher-Tammann (VFT) equation (Equation 15) in the studied temperature range:

$$\tau = \tau_0 exp\left(\frac{B}{T-T_0}\right) \quad (15)$$

In which τ_0 is the infinite temperature relaxation time, τ_0 is the so-called VFT temperature, and B is a material-specific parameter. The dynamic glass transition temperature (T_g) is usually defined at the temperature at which the segmental relation time τ = 100 s. By extrapolating the VFT curves to τ = 100 s, a glass transition temperature can be estimated. The T_g values of all samples are given in **Table 2**.

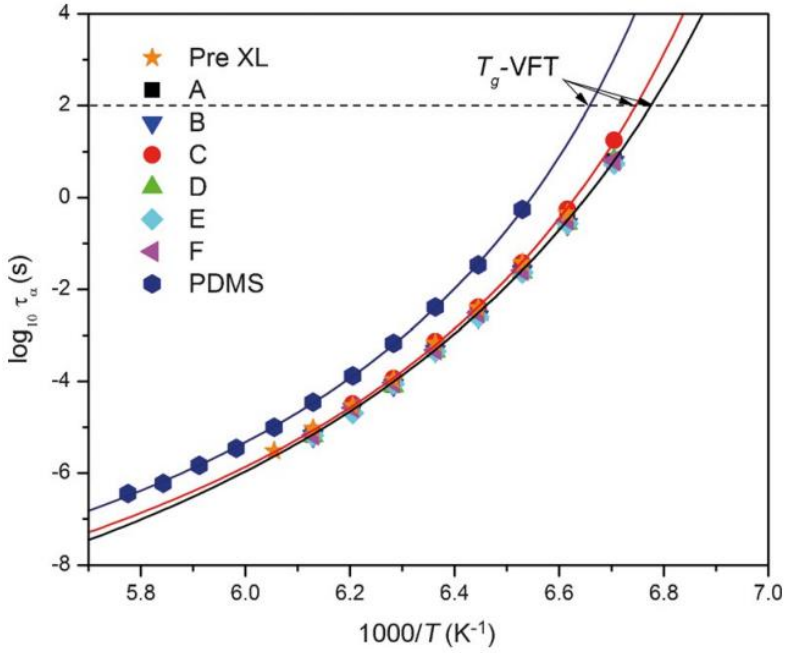

Figure 26. Temperature dependence of the segmental relaxation time measured by BDS for different samples. Solid lines were fit to the VFT equation. The glass transition temperature (T_g) was determined by VFT extrapolation of the segmental relaxation time to τ_α = 100 s ($\log_{10}\tau_\alpha$ = 2).

4.9 Effect of Catalyst Ratio on Cross-link Density

As shown in **Figure 21** and **Table 2**, the G' values generally increase with the higher catalyst ratio, while the calculated M_x values show a decreasing trend. In case of a linear polymer with monofunctionality, the amount of catalyst controls the resulting molecular weight; however, for the difunctional PDMSPNB, the catalyst ratio should control the cross-link density as well as the reaction kinetics. The rheology data show that a higher catalyst ratio resulted in a stronger shear response because the higher catalyst ratios increase the numbers of cross-link junctions in the membrane, thereby generating shorter average chain lengths between cross-links. It is also worth mentioning that the cross-link density in the PDMSPNB membranes is controlled by multiple factors. The catalyst ratio is a dominant factor but the reaction kinetics during in-situ membrane formation could also influence the cross-link density. However, due to the fast reaction rate, it is difficult to kinetically control the formation of cross-link networks within the time range

demonstrated in this study. The deviation of the trend for G' versus catalyst ratio in **Figure 21** is likely due to a combination of variation of reaction kinetics and other possible factors.

4.10 Gas Separation Properties of Cross-linked PDMSPNB Membranes

The slopes of the CO_2 and N_2 permeabilities in **Figure 22** clearly show much higher CO_2 permeability than that of N_2. As seen in **Figure 23a** and **Figure 23b**, for cross-linked PDMSPNB membranes, the permeability of both the CO_2 and N_2 showed an increasing trend with the initial increase of cross-link density, and then permeability reaches a maximum (c_x =1.19×10^{-5} mol·cm^3) and decreases with farther increase in cross-link density. The permeation of CO_2 and N_2 of the cross-link density 1.19×10^{-5} mol·cm^3 showed the highest flux than any other membranes in this study. From the Robeson plot (**Figure 24**), the cross-linked PDMSPNB membrane achieved much better CO_2/N_2 separation property than the majority of polymers.[16] The mixed gas permeation measurements of sample C showed very comparable results to that of single gas measurements, which suggests that the PDMSPNB membranes perform similarly well in a mixed gas permeation, which is more relevant to real industrial circumstances.

Compared to conventional cross-linked PDMS, the cross-linked PDMSPNB membrane show higher permeability and higher selectivity, and the performance is very close to the Robeson upper bound. The conventional cross-linked PDMS utilizes short chains of PDMS as precursor and requires high cross-link density to make it a free-standing film. The use of difunctional macromonomer PDMSPNB in this work allowed us to prepare free-standing films with much lower cross-link density. This membrane fabrication approach to prepare cross-linked membranes has revealed that tuning cross-link densities of PDMSPNB using these macromonomers can improve the performance of CO_2/N_2 separation significantly. Our best performance membrane with cross-link density 1.19×10^{-5} mol·cm^3 is approximately a factor of two improvement in CO_2 permeability and CO_2/N_2 selectivity over the well-studied conventional cross-linked PDMS. The excellent permeability and good selectivity of the cross-linked PDMSPNB membranes provides a promising perspective (**Figure 23** and **Figure 24**) for future

development of membranes for CO_2 separation. However, a deeper understanding of the physical and chemical mechanism behind the outstanding gas separation property is also crucial. To elucidate how cross-links affect the solubility and diffusivity, the study of CO2 solubility and free volume were carried out.

4.11 Influence of Solubility and Free Volume

As described in the chapter introduction, researchers reported different trends of gas permeability change with the change of cross-link density. However, for our rubbery cross-linked membranes, the permeability does not follow a monotonous trend. We expected the change in gas permeability to be a combined effect of many factors. From the CO_2 solubility measurements, all the tested cross-linked PDMS membranes are similar within the range of uncertainty (**Table 4**), which indicates that the solubility did not play a key role in the enhancement of permeability and selectivity for the PDMSPNB membranes. The N_2 solubility of the PDMSPNB membranes was lower than the measurable limit of the device and could not be measured.

The PALS measurements show that the pore size of the PDMS was similar to that of PDMSPNB membranes (**Table 4**), indicating that the difference of the cross-link density did not influence much the pore size, which is within our expectation due to the use of the same polymer matrix. With the increase of cross-link density, the concentration of pores shows fluctuations, which could be interpreted as the small changes in the total free volume. However, due to the relatively large error bar, the fluctuations still lie well within the range of uncertainty for these measurements.

4.12 Effect of Dynamics in Gas Permeability

Dielectric loss peaks in **Figure 25** shows that the α-relaxation of all the cross-linked samples broadened at the low frequency side compared to that of the pre cross-link sample. Similar results were reported for cross-linked PDMS networks[119] and other polymers.[120] The authors ascribed the broadening of the peaks to the slowing down of segments in the proximity to the cross-link junction. For our end cross-linked PDMSPNB

membranes, the mobility of the segments near the end junctions are expected to be restricted, which could explain the broadening of the peak at lower frequencies. It can also be noticed that the peak position of the conventional cross-linked PDMS membrane, which has much higher cross-link density than those of the PDMSPNB membranes, was shifted around one order in frequency. This indicates approximately ten times faster segmental motion in our membranes relative to conventional cross-linked PDMS at the studied (by dielectric spectroscopy) temperatures. However, our PDMSPNB membranes were only slightly cross-linked, i.e. the concentration of junctions was very small. Thus, compared to pre-crosslinked (pre-XL) sample, no apparent shift of the peak position to lower frequencies was observed. The pre-XL and cross-linked PDMSPNB samples did not show any changes in T_g (**Table 2**), indicating that although some segmental motions in cross-linked PDMSPNB samples were restricted, the influence on average segmental relaxation time was not significant. However, the cross-linked PDMSPNB did show faster dynamics than the conventional cross-linked PDMS membranes, which in part, might explain the significant increase in gas permeability between these two types of membranes. To relate quantitatively the observed increase in gas diffusivity to change in segmental dynamics, measuring the dynamics at the same ambient temperature would be ideal, while unfortunately PDMS segmental dynamics at T = 298 K is too fast for our spectrometer. Despite the difference of the measured temperature range, this dynamic study indicates that the most significant enhancement of CO_2 separation of PDMSPNB over conventional cross-linked PDMS should be ascribed to the much faster segmental dynamics despite their similar free volume.

4.13 Conclusions

A facile room temperature cross-linking reaction of PDMSPNB membranes was developed via in-situ ROMP. The resulting free-standing films were ductile and flexible, and could be readily fabricated to different shapes and coatings. Our membrane fabrication approach to preparing cross-linked PDMS has revealed that tuning cross-link densities of PDMS membranes using these macromonomers can improve CO_2/N_2 separation significantly. The novel cross-linked PDMSPNB membranes achieved

excellent CO_2 permeability with good selectivity (a factor of two improvements in CO_2 permeability and CO_2/N_2 selectivity over the well-studied conventional cross-linked PDMS), and their performance is very close to the Robeson upper bound line. The unprecedented performance by a careful design of the macromolecular architecture and cross-link mechanism has revealed the strong potential of the rubbery polymer, PDMS, for gas separation. This finding can open up a new approach to enhance performance for gas separation and could elucidate additional factors for the gas separation mechanisms in rubbery polymers. To the best of our knowledge, this study is the first report to identify that lightly cross-linked PDMS membranes synthesized by difunctional PDMS macromonomers enhance both CO_2 permeability and CO_2/N_2 selectivity. Moreover, from an industrial viewpoint, according to Merkel et al.'s study,[38] the cross-linked PDMSPNB membrane could offer the permeance of ~6,300 gas permeation units (GPU) if 1 μm membranes could be cast and coated on the gas separation media. This should allow reduction of CO_2 capture cost to less than $20 per ton. Although the complete quantitative level of understanding of the obtained results has not yet been achieved, we could ascribe the key factor to the faster segmental dynamics in our membranes and probably improved solubility selectivity. Our next goal is to incorporate CO_2-philic groups into the PDMSPNB matrix, to achieve a better selectivity without significant loss in permeability. These findings will contribute to the fundamental understanding of gas transport through polymer membranes, with potentially broad applications.

Chapter 5. Accessing Siloxane Functionalized Polynorbornenes via Vinyl-Addition Polymerization for CO_2 Separation Membranes

A version of this chapter was originally published by Kevin R. Gmernicki, Eunice Hong, Christopher R. Maroon, Shannon M. Mahurin, Alexei P. Sokolov, Tomonori Saito, and Brian K. Long:

Reprinted with permission from Kevin R. Gmernicki, Eunice Hong, Christopher R. Maroon, Shannon M. Mahurin, Alexei P. Sokolov, Tomonori Saito, Brian K. Long "Accessing Siloxane Functionalized Polynorbornenes via Vinyl-Addition Polymerization for CO_2 Separation Membranes" *ACS Macro Letters* 5 (7) (2016): 879-883. DOI: 10.1021/acsmacrolett.6b00435 Copyright 2016 American Chemical Society and Kevin R. Gmernicki, Eunice Hong, Christopher R. Maroon, Shannon M. Mahurin, Alexei P. Sokolov, Tomonori Saito, Brian K. Long "Correction to Accessing Siloxane Functionalized Polynorbornenes via Vinyl-Addition Polymerization for CO_2 Separation Membranes" *ACS Macro Letters* 6 (1) (2017): 41-41. DOI: 10.1021/acsmacrolett.6b00956 Copyright 2016 American Chemical Society

The author directly contributed to the entirety of this published manuscript and was aided in the synthesis of the catalyst by Eunice Hong, synthesis of the monomers and polymers by Christopher R. Maroon, obtaining wide-angle X-ray scattering data by Shannon M. Mahurin, and aided in the writing and discussions with Alexei P. Sokolov and Tomonori Saito.

Experimental and supplemental information available in Appendix E: Experimental Methods and Supporting information for Chapter 5

5.1 Abstract

The vinyl addition polymerization of norbornyl-based monomers bearing polar functional groups is often problematic, leading to low molecular weight polymers in poor yield. Herein, we provide proof-of-principle evidence that addition-type homopolymers of siloxane-substituted norbornyl-based monomers may be readily synthesized using the catalyst *trans*-$[Ni(C_6F_5)_2(SbPh_3)_2]$. Polymerizations using this catalyst reached moderate to high conversion in just 5 minutes of polymerization and produced siloxane-substituted polymers with molecular weights exceeding 100 kg/mol. These polymers showed excellent thermal stability (T_d ≥ 362 °C) and were cast into membranes that displayed high CO_2 permeability and enhanced CO_2/N_2 selectivity as compared to related materials.

5.2 Background on Vinyl-added Polynorbornenes for Gas Separation Membranes

In 2014, the U.S. released approximately 6.87 billion metric tons of carbon dioxide (CO_2) into Earth's atmosphere.[121] These CO_2 emissions account for approximately 81%

of all greenhouse gas emissions and have been linked to increasing global temperatures, rising sea levels, varying weather patterns, and changes to ecosystems and habitats. A particularly concerning source of these emissions is due to electrical energy generation by coal-fired power plants in which flue gas streams are vented into the atmosphere.

In an effort to reduce greenhouse gas emissions, technologies such as cryogenic distillation and amine absorption have emerged as promising methods to capture CO_2 from flue gas. Unfortunately, implementation of these technologies is quite energy intensive, thereby reducing the overall energy output of any power plant employing these methods. In contrast, membrane-based gas separation technologies present an inherent advantage in that they are passive systems, requiring low energy input and providing promise as an energy efficient method of CO_2 capture and sequestration.[38] As a result, the fundamental advancement of materials within the field of membrane-based CO_2 separations remains at the forefront of current research efforts.

A class of polymeric gas separation membranes that has shown tremendous promise for gas separations are polynorbornenes (PNBs) synthesized by vinyl-addition (VA) polymerization.[43-45] Polynorbornenes synthesized via VA polymerization differ from their more commonly encountered counterparts, which are synthesized by ring-opening metathesis polymerization (ROMP), in that the resultant VA polymers retain the rigid, bicyclic core of the norbornyl ring and that no residual alkenes are present along the polymer backbone. These features are well-known to enhance chemical stability, elevate thermal transition temperatures, and increase the fractional free volume within the solid-state polymer matrix.[43] These characteristics are highly desirable for membrane-based applications in which harsh environments and enormous gas volumes are encountered, such as post-combustion CO_2 separation from coal-fired power plants.[38]

A particular VA polymer that has drawn considerable interest is poly(5-trimethylsilyl-2-norbornene). When compared to other glassy polymers, this silane-substituted polymer has shown exceptional CO_2 permeability (4350 barrer)[46] but has only achieved moderate levels of CO_2/N_2 selectivity (α = 14.7). Because of this, further improvements in silyl substituted PNB's CO_2/N_2 selectivity (α) is highly desirable to promote their use as efficient CO_2 separation membranes. To achieve this goal, we hypothesized that

replacement of the silane moieties within poly(5-trimethylsilyl-2-norbornene) with siloxane-based functionalities could provide the desired increase in CO_2/N_2 selectivity. The incorporation of siloxane-based moieties into polymers such as polysiloxanes and other related siloxane-derived materials has often resulted in membranes possessing exceptional selectivity and permeability for a variety of gases, as well as providing a host of desirable mechanical properties such as flexibility, solubility, and heat resistance.[40,44,122-124]

Toward this pursuit, a survey of literature quickly revealed that only a few such reports exist in which VA PNBs bearing siloxane functionalities have been synthesized. Furthermore, in each of those reports the siloxane-functionalized monomers were not homopolymerized, but rather copolymerized with other norbornyl-based monomers. In each of these copolymers, the siloxane-functionalized monomer was only incorporated in a meager 5-25 mol%.[44,125-127] We surmised that this lack of literature concerning siloxane-functionalized PNB homopolymers is likely due to the poor tolerance of most commonly employed vinyl-addition polymerization catalysts in the presence of polar and/or heteroatom-functionalized monomers (**Figure 27**).[128]

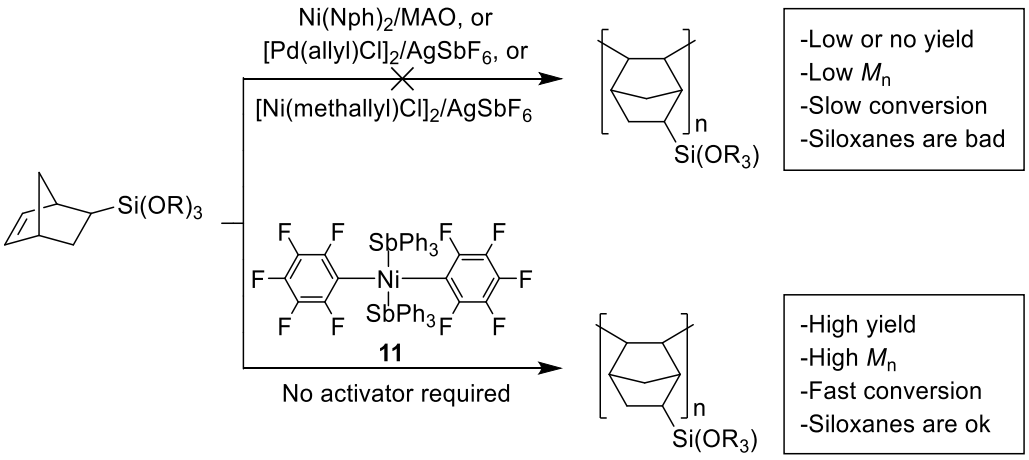

Figure 27. Comparison of commercially available vinyl-addition polymerization catalysts versus *trans*-$[Ni(C_6F_5)_2(SbPh_3)_2]$ (**11**) for the polymerization of siloxane functionalized norbornene monomers.

To circumvent this issue, herein we provide proof-of-principle evidence that addition-type homopolymers of siloxane substituted norbornyl-based monomers may be readily synthesized using the catalyst *trans*-[Ni(C_6F_5)$_2$($SbPh_3$)$_2$] (**Figure 27**). These siloxane-substituted PNBs can be produced in much higher yield than when using other commercially available VA polymerization catalysts, and that remarkably high molecular weights (M_n >100 kg/mol) may be accessed by polymerizations lasting only five minutes. Lastly, the resulting polymers were cast into large, defect-free membranes that show enhanced selectivity for the separation of CO_2 from N_2 when compared to the benchmark material, poly(5-trimethylsilyl-2-norbornene).

5.3 Investigations into Various Vinyl-addition Catalysts

The monomers chosen for this study (**12a-e**) were either commercially available or synthesized according to **Figure 28**. Therein, dicyclopentadiene provided a source of cyclopentadiene (after thermal cycloreversion) that underwent Diels-Alder cycloaddition with the appropriate vinyl silane or vinyl siloxane. These reactions were conducted at elevated temperatures in sealed pressure tubes, yielding the corresponding mono-functionalized norbornene monomers **12b-e** in moderate yields (32.7-59.8%). All monomers were obtained as a mixture of *endo*- and *exo*-isomers, which was determined via ^{1}H NMR spectroscopy, and were thoroughly purified via successive distillations to remove impurities and adventitious water.

Each monomer (**12a-e**) was polymerized using either a Ni- or Pd-based transition metal catalyst under an inert atmosphere to evaluate each catalyst's efficacy toward that

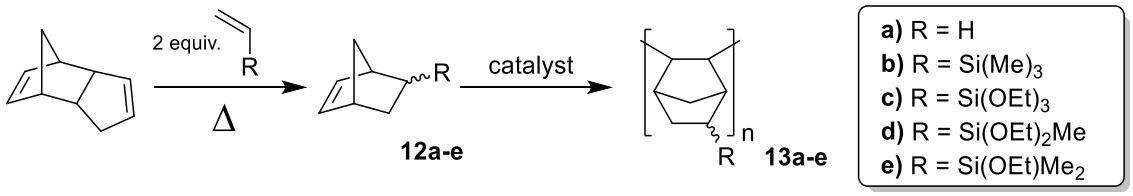

Figure 28. Scheme for the synthesis of monomers **12a-e** and polymers **13a-e**.

monomer. The catalysts examined consisted of nickel naphthenate ($Ni(Nph)_2$),[46] methallylnickel chloride dimer ($[Ni(methallyl)Cl]_2$),[129-130] allylpalladium chloride dimer ($[Pd(allyl)Cl]_2$),[130-131] and *trans*-$[Ni(C_6F_5)_2(SbPh_3)_2]$ (**11**). $Ni(Nph)_2$ is commercially available and has been shown to readily synthesize poly(5-trimethylsilyl-2-norbornene), which is a benchmark norbornyl-based VA polymer.[46] The catalysts $[Ni(methallyl)Cl]_2$ and $[Pd(allyl)Cl]_2$ are also commercially available and are well-known to be active for the VA polymerization of norbornenyl monomers bearing polar functionalities, making them ideal for this investigation.[130] Lastly, *trans*-$[Ni(C_6F_5)_2(SbPh_3)_2]$ (**11**) has also been reported to successfully polymerize norbornyl monomers bearing polar functionalities.[132] Though catalyst **11** is not commercially available, it was readily synthesized on a gram-scale in good yield by a modified synthetic route requiring only a single one-pot reaction (see Supporting Information).[132-133]

The catalysts $Ni(Nph)_2$, $[Ni(methallyl)Cl]_2$, and $[Pd(allyl)Cl]_2$ each require activation using methylaluminoxane (MAO) or $AgSbF_6$ respectively to generate the cationic Ni or Pd active site for polymerization. In contrast, catalyst **11** does not require the use of any activator or cocatalysts due to the lability of the bulky $SbPh_3$ ligands and its ability to propagate via a neutral Ni active site.[132-133] Initially, each catalyst was tested for the homopolymerization of norbornene (**12a**), trimethylsilylnorbornene (**12b**), and triethoxysilylnorbornene (**12c**) to systematically investigate the effects that both monomer sterics and siloxane moiety presence had with regard to polymerization yield and molecular weight (**Table 5**, entries 1-12).

As expected, all four catalysts readily polymerized unsubstituted norbornene (**12a**) to high conversion (67-87%) and yielded polymers with molecular weights (M_n) exceeding 100 kg/mol (**Table 5**, entries 1-4). Polymerizations involving the sterically encumbered trimethylsilyl-functionalized norbornene **12b** resulted in decreased or no polymer yield (0-57%) and produced polymers with molecular weights significantly lower than those obtained when polymerizing unsubstituted norbornene (**12a**) (**Table 5**, entries 5-8). This decreased yield was somewhat expected as severe steric interactions are known to hinder catalyst coordination and insertion.[128] More specifically, it has been reported that

Table 5. Polymerization of monomers **12a-e** with $Ni(Nph)_2$, $Ni(methallyl)_2Cl_2$, $Pd(allyl)_2Cl_2$, and *trans*-$Ni(C_6F_5)_2(SbPh_3)_2$ (**11**).

entry	monomer (*endo:exo*) [b]	catalyst	yield (%)	M_n [c] (kg/mol)	M_w/M_n [c]
1[d]	**12a**	$Ni(Nph)_2$	67	100	4.06
2[e]	**12a**	$[Ni(methallyl)Cl]_2$	83	142	2.58
3[e]	**12a**	$[Pd(allyl)Cl]_2$	82	285	2.32
4	**12a**	$Ni(C_6F_5)_2(SbPh_3)_2$	87	145	2.61
5[d]	**12b** (32:68)	$Ni(Nph)_2$	10	21	1.89
6[e]	**12b** (32:68)	$[Ni(methallyl)Cl]_2$	57	26	2.20
7[e]	**12b** (32:68)	$[Pd(allyl)Cl]_2$	0	-	-
8	**12b** (32:68)	$Ni(C_6F_5)_2(SbPh_3)_2$	42	77	2.52
9[d]	**12c** (65:35)	$Ni(Nph)_2$	0	-	-
10[e]	**12c** (65:35)	$[Ni(methallyl)Cl]_2$	15	25	1.67
11[e]	**12c** (65:35)	$[Pd(allyl)Cl]_2$	25	22	1.71
12	**12c** (65:35)	$Ni(C_6F_5)_2(SbPh_3)_2$	71	150	1.47

[a]Polymerizations conducted using 5 mmol of monomer, 5 µmol of catalyst, and 2 mL of DCM for 24 h unless otherwise noted. [b]*Endo*/*exo* ratios were determined via ^1H NMR spectroscopy in $CDCl_3$ at 25 °C. [c]Molecular weights for entries 1-4 were measured using gel permeation chromatography (GPC) equipped with triple detection at 140 °C in 1,2,4-trichlorobenzene, entries 5-14 were measured using GPC relative to polystyrene standards at 40 °C in THF. [d]Polymerizations using $Ni(Nph)_2$ were conducted using 15 mmol monomer, 15 µmol catalyst, 6 mL of toluene, and activated using 100 equiv of MAO. [e]Activated with 2.1 equiv. of $AgSbF_6$.

this deleterious steric effect is further amplified when sterically demanding moieties are positioned on the *endo*-face of the norbornene ring, thereby hindering coordination of the catalyst specifically to the *endo*-olefin face.[46] Monomers **12b-e** each contained between 46-68% *endo*-substitution.

It should also be noted that though catalyst **11** only reached a modest 42% conversion for the polymerization of **12b**, it did yield polymer with molecular weights that were approximately 3-4 times greater than the commercially available catalysts $[Ni(methallyl)Cl]_2$ and $[Pd(allyl)Cl]_2$ (**Table 5**, entries 5-8). Perhaps even more intriguing was that $[Pd(allyl)Cl]_2$ showed no activity for the polymerization of **12b** (**Table 5**, entry 7) despite the increased functional group tolerance typically associated with the use of Pd-based catalysts.[134] Though we are currently unsure of the origins of this inactivity, literature reports have shown that Pd-based catalysts often require catalyst loadings that are one or more orders of magnitude higher than what was used during these investigations.[135]

Polymerizations of siloxane-substituted monomer **12c** (**Table 5**, entries 9-11) confirmed our hypothesis that the presence of siloxane moieties would dramatically hinder catalyst activity. When $Ni(Nph)_2$ was used (**Table 5**, entry 9), virtually all catalytic activity was eliminated. The catalysts $[Ni(methallyl)Cl]_2$ and $[Pd(allyl)Cl]_2$ did yield polymer, but at severely reduced yields (15-25%) and they only produced polymers having low molecular weights (M_n = 22-25 kg/mol) (**Table 5**, entries 10-11). We postulate that the cationic nature of these activated catalytic species plays a pivotal role in this observation, and the observed results are due to undesired chelation of the Lewis acidic metal center by the oxygen-containing siloxane moiety, thereby hindering subsequent monomer coordination and severely limiting VA polymerization activity.

In contrast to those results, catalyst **11** was shown to be highly active for the polymerization of siloxane monomer **12c** reaching conversions greater than 70% and producing polymers with notably high molecular weight (M_n = 150 kg/mol) (**Table 6**, entry 12). We propose that in similarity to previous reports that have demonstrated the tolerance of catalyst **11** toward monomers bearing some polar functionality, that its tolerance toward siloxane-based derivatives can be attributed to the active catalytic

Table 6. Polymerization of monomers **12c-e** using *trans*-Ni(C_6F_5)$_2$($SbPh_3$)$_2$ (**11**)[a]

entry	monomer (*endo:exo*) [b]	time	yield (%)	M_n [c] (kg/mol)	M_w/M_n [c]	T_d (°C)[d]
1	**12c** (65:35)	24 h	71	150	1.47	380
2	**12d** (56:44)	24 h	74	176	2.95	362
3	**12e** (46:54)	24 h	66	120	2.11	364
4	**12c** (65:35)	5 min	78	154	1.78	-[e]
5	**12d** (56:44)	5 min	54	107	2.12	-[e]
6[f]	**12e** (46:54)	5 min	45	112	2.26	-[e]

[a]Polymerizations conducted using 5 mmol of monomer, 5 µmol of catalyst, and 2 mL of DCM. [b]*Endo*/*exo* ratios were determined via ^{1}H NMR spectroscopy in $CDCl_3$ at 25 °C. [c]Determined using GPC relative to polystyrene standards at 40 °C in THF. [d]Determined by thermogravimetric analysis and reported as temperature at ~5 % mass loss. [e]Not determined. [f]Polymerization ran with 5 mL of DCM.

species propagating via a neutral Ni site rather than the more oxophillic cationic site encountered with the activated forms of Ni(Nph)$_2$, [Ni(methallyl)Cl]$_2$, and [Pd(allyl)Cl]$_2$.[132] Furthermore, catalyst **11** is advantageous in that no co-catalyst is required for activation, which greatly simplifies reaction setup and eliminates another potential source of impurities that could hinder polymerization activity.

In similarity to monomer **12c**, catalyst **11** was readily able to synthesize analogous siloxane-functionalized homopolymers **13d** and **13e** (**Table 6**, entries 1-3) from the monomers **12d-e**. Each monomer was converted to VA polymer in good overall yields (≥ 66 %) and reached high molecular weights ($M_n \geq 120$ kg/mol). Furthermore, it was determined that although initial polymerizations were conducted for 24 h to ensure maximum monomer conversion, catalyst **11** could produce polymers **13c-e** in similarly high conversion (≥ 45 %) and molecular weights ($M_n \geq 107$ kg/mol) within only 5 min of polymerization (**Table 6**, entries 4-6). Lastly, the thermal stability of siloxane-functionalized PNBs **13c-e** were examined via thermogravimetric analysis (TGA) in which each homopolymer showed exceptional thermal stability (see Appendix E: Experimental Methods and Supporting information for Chapter 5) More specifically, polymers **13c-e** retained greater than 95% of their initial mass at temperatures ≥ 362 °C (**Table 6**, entries 1-3).

5.4 Membrane Preparation and CO_2/N_2 Separation Performance

Polymers **13c-e** showed excellent solubility in common organic solvents such as THF, DCM, and diethyl ether, and membranes were readily prepared via solution casting methods onto a clean glass substrate. Optimal casting conditions were observed at 5 wt. % loadings of polymer in THF, and large, virtually defect-free films with thickness ranging from 90-125 μm could be reproducibly formed. To evaluate the performance of these polymer films as potential candidates for post-combustion CO_2 separation, membranes were tested via the constant-volume variable-pressure gas flux method to obtain ideal permeability and selectivity values (**Figure 29**).[14]

Siloxane-functionalized polymers **13c-e** displayed CO_2 permeability values ranging from 410-936 Barrer (**Table 7**) depending on the number of methyl versus ethoxy subsitutents appended the siloxane functionality. These values are lower than has been reported for poly(5-trimethylsilyl-2-norbornene) (4350 Barrer),[46] but are significantly higher than many other previously reported glassy polymers.[16] We hypothesized that the decreased CO_2 permeability of polymers **13c-e** relative to poly(5-trimethylsilyl-2-norbornene) could be attributed to greater chain packing density within these siloxane substituted polymers.

5.5 Conclusions

To support this hypothesis, densities of polymers **13c-e** were measured using Archimedes Principle, which yielded values of 1.027-1.089 g/cm^3 (**Table 7**). These densities are greater than poly(5-trimethylsilyl-2-norbornene) (density = 0.883 g/mL) and support that PNBs bearing siloxane moieties may indeed pack more tightly than polymers bearing simple silanes. Furthermore, the fractional free volume (FFV) of polymers **13a-c** were estimated to range from 0.108 to 0.139, as calculated using the Bondi Method (**Table 7**).[136] These values are notably smaller than the FFV reported for poly(5-trimethylsilyl-2-norbornene) (FFV = 0.275)[46] and further support the hypothesis that the observed decrease in CO_2 permeability for polymers **13c-e** may be due to increased chain packing within their thin-film matrices. Lastly, wide-angle X-ray scattering (WAXS) was

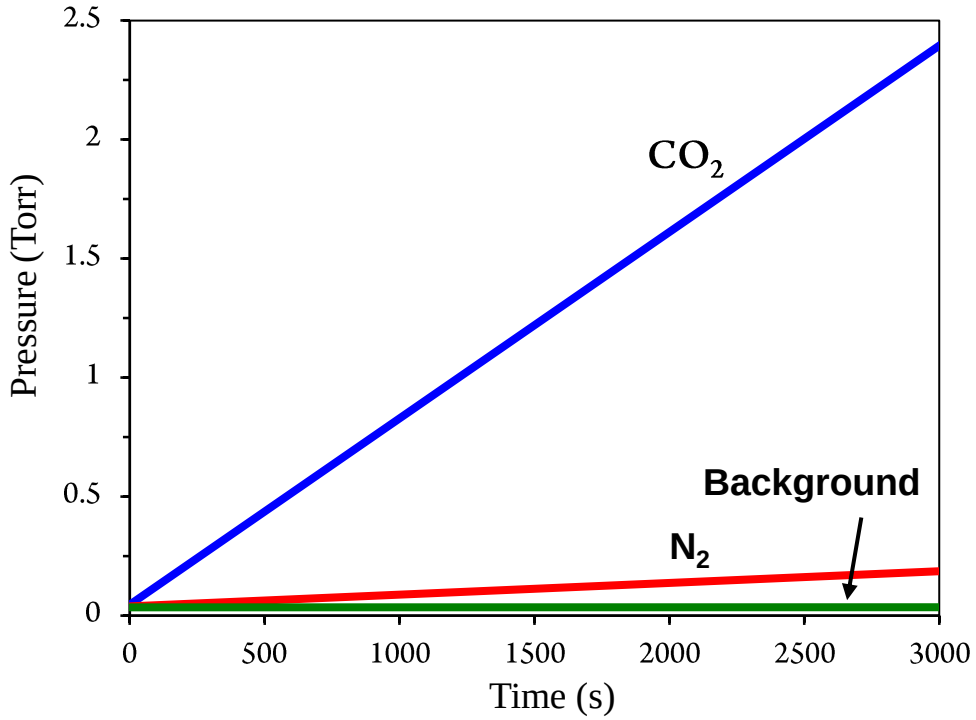

Figure 29. Plot of pressure flux data for polymer **13c** with CO_2 (blue, top), N_2 (red, middle), and instrument background leak rate (green, bottom).

Table 7. Permeability and ideal selectivity of polymers **13c-e**.

					d spacing, Å[c]		*P* (Barrer)[d]		
polymer	density (g/cm^3)[a]	FFV[b]	$(2\theta)_1$, deg[c]	$(2\theta)_2$, deg[c]	$(d_B/d_{ic})_1$	$(d_B/d_{ic})_2$	CO_2	N_2	α (CO_2/N_2)
13c	1.081 (±0.009)	0.131 (±0.007)	6.2	13.7	14.2/ 17.4	6.5/ 7.9	936.6 (±14.9)	57.3 (±2.3)	16.4 (±0.4)
13d	1.089 (±0.012)	0.108 (±0.010)	6.6	14.7	13.4/ 16.3	6.0/ 7.3	474.2 (±12.0)	24.5 (±0.3)	19.3 (±1.1)
13e	1.027 (±0.012)	0.139 (±0.010)	7.1	15.3	12.4/ 15.2	5.8/ 7.0	470.7 (±15.2)	24.9 (±1.1)	18.9 (±1.5)

[a]Determined using Archimedes Principle in MeOH at 22 °C. [b]Estimated using the Bondi method. [c]Determined using wide-angle X-ray diffraction. The first value is the Bragg's distance $d_B = \lambda/(2 \sin \theta)$, the second one is the interchain distance $d_{ic} = 1.22 d_B$.[137] [d]Permeability values of free-standing polymer films were obtained using the constant-volume variable-pressure gas flux method as detailed in the Supporting Information.

utilized to determine if any crystallinity is present within polymers **13c-e**, which is known to hinder gas permeability.[138] From these WAXS spectra (see Appendix E: Experimental Methods and Supporting information for Chapter 5), only broad peaks were observed, clearly indicating that polymers **13c-e** are completely amorphous. Likewise, calculation of their periodicity (d spacing)[137] yielded values quite similar to poly(5-trimethylsilyl-2-norbornene) (**Table 7**). In contrast to permeability, siloxane-functionalized PNB's **13c−e** displayed increased ideal selectivity values ranging from 16.4 to 19.3 (**Table 7**), which are approximately 12-31% higher than those reported for poly(5-trimethylsilyl-2-norbornene) (α = 14.7).[46] This is a meaningful increase in selectivity and is similarly attributed to the increased chain packing within the thin-film matrices of polymers **13c−e**. It should be noted that polymers **13c-e** display remarkably low N_2 permeabilities, which can be easily seen in the raw pressure flux data presented in **Figure 29** (**13c**, 100 μm thick membrane), further highlighting the enhanced ideal CO_2 selectivity of these materials. Lastly, it should be noted that the observed increase in selectivity and simultaneous decrease in permeability follows the so-called "permeability-selectivity trade-off" that has been extensively detailed in the literature.[15-16,87] In conclusion, proof-of-principle evidence was provided that addition-type homopolymers of siloxane substituted norbornenes may be readily synthesized. Synthesis of these polymers was facilitated by the use of neutral nickel catalyst **11**, which produced polymers **13c-e** in moderate to high yield (45-78%) and having consistently high-molecular weights (M_n ≥ 107 kg/mol). Furthermore, catalyst **11** was shown to achieve these results in polymerizations as short as 5 min at room temperature and requiring no additional activator or cocatalyst. Polymers **13c-e** displayed remarkable thermal stability (T_d ≥ 362 °C) and improved solubility as compared to unsubstituted PNB. They showed enhanced CO_2 selectivity relative to their silane-functionalized counterparts and higher CO_2 permeability than many commercially available glassy polymers.[16,43] Though permeability values as high as 937 Barrer (**Table 7**) make these materials attractive candidates for future studies, they display lower CO_2 permeability than the benchmark material poly(5-trimethylsilyl-2-norbornene). This decreased permeability is attributed to increased chain packing density within these siloxane-substituted polymers relative to their silane-based

counterparts, and this hypothesis is supported via density, FFV, and WAXS calculations/measurements.

Chapter 6. Gas Permeation and Mechanical Properties of Addition-type Polynorbornenes Bearing $Si(OEt)_3$ Side Groups

A portion of this chapter has been submitted for publication by Nikolay Belov, Roman Nikiforov, Ludmila Starannikova, Kevin R. Gmernicki, Christopher R. Maroon, Brian K. Long, Viktor Shantarovich, and Yuri Yampolskii:

Nikolay Belov, Roman Nikiforov, Ludmila Starannikova, Kevin R. Gmernicki, Christopher R. Maroon, Brian K. Long, Viktor Shantarovich, and Yuri Yampolskii "Synthesis and Gas Permeation Properties of Addition-type Polynorbornenes bearing $Si(OEt)_3$ Side Groups" Macromolecules *Submitted*

The author directly contributed to this body of work by synthesizing all of the materials necessary to perform the experiments and conducted the characterization of the polymers thermal and mechanical properties.

6.1 Abstract

Poly(5-triethoxysilyl-2-norbornene) was prepared in good yield (71%) by vinyl-addition polymerization using the catalyst *trans*-[$Ni(C_6F_5)_2(SbPh_3)_2$]. This polymer is completely amorphous, highly optically transparent, mechanically tough with a tensile modulus of 0.915 GPa, has a high glass transition temperature (325 °C), and investigation of its gas permeation parameters showed that it has relatively high gas permeabilities for a variety of gases (i.e. $P(O_2)$ is ~200 Barrer). A unique feature of poly(5-triethoxysilyl-2-norbornene) is that it exhibits solubility controlled permeation of hydrocarbons. The permeability coefficient of butane ($P(C_4H_{10})$) is as high as 5 x 10^3 Barrer, whereas its butane/methane selectivity ($P(C_4H_{10})/P(CH_4)$) is 21 ± 3. Analysis of poly(5-triethoxysilyl-2-norbornene)'s permeability coefficients, diffusion coefficients, solubility coefficients, and free volume demonstrate that this polymer combines the attractive properties of both a rubbery polymer and a glassy polymer.

6.2 Introduction

Following the development of the *trans*-[$Ni(C_6F_5)_2(SbPh_3)_2$] catalyst system for siloxane-functionalized vinyl-added polynorbornenes, we established an active collaboration with Professor Yuri Yampolskii at the Petrochemical Institute of Moscow to further investigate the membrane properties of poly(5-triethoxysilyl-2-norbornene) (**13c**).

Although initially developed for CO_2/N_2 separations, the following chapter will show that poly(5-triethoxysilyl-2-norbornene) (**13c**) also exhibits excellent membrane performance for separating larger hydrocarbons in addition to dramatic improvements in mechanical properties compared to vinyl-added polynorbornene (**Figure 30**).

One of the most important, and only partly solved tasks of membrane science and technology is the development of membrane materials capable of separating gaseous hydrocarbons of different molecular masses in natural and petroleum gases. Polymers that operate by diffusivity controlled mechanisms are currently not capable of it is widely accepted that solubility-selective materials are required. Originally, it was understood that this requirement was only fulfilled in the case of rubbery materials or semi-crystalline polyolefins.[42,139-140] Later, however, it became evident that polymers with rigid main chains and very high glass transition temperatures (T_g), may also demonstrate such behavior as has been observed for polyacetylenes and vinyl-addition polynorbornenes bearing silane substituents.[42,46,141]

In the same vein, another class of polynorbornenes with similar properties was recently prepared and extensively studied.[44,142] These polymers consist of norbornyl monomers with Si-O-Si side chains that were synthesized by both ROMP and vinyl-addition polymerization. Regardless of polymerization pathway, these polymers possessed high glass transition temperatures, have modest gas permeability, and exhibit solubility controlled permeation of hydrocarbons that was concluded to be the result of the flexible Si-O bonds in the pendant side chains rather than the polymer main-chain.

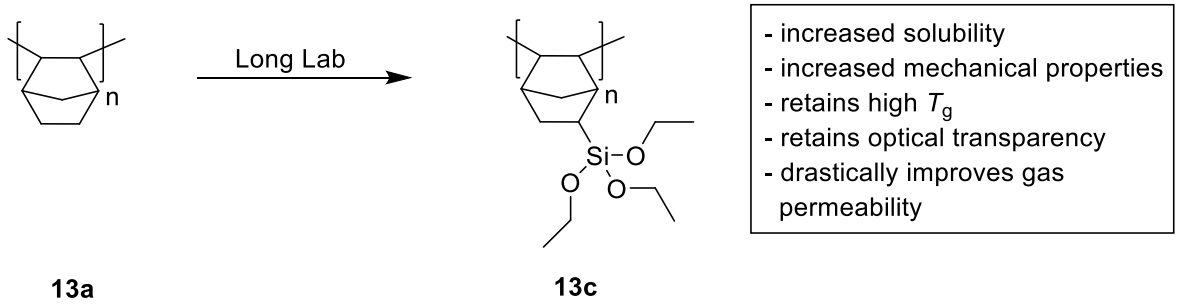

Figure 30. Changes in polymer properties for adding triethoxysilyl substituents to VAPNB.

This conclusion was confirmed by the results of the spin probe method in which a stable free radical, in this case TEMPO, was found to rotate in these polymers much faster than in common metathesis polynorbornenes.[143] In this regard, these glassy materials are remarkably similar to rubbery siloxane-based polymers, which is quite unusual behavior. Additional confirmation of this viewpoint was provided in two recent reports in which solubility controlled transport of C_1-C_4 hydrocarbons were shown for both ROMP and vinyl addition polynorbornenes containing Si-O-Et substituents rather than Si-O-Si moieties.[144-145]

In this chapter, we will demonstrate that poly(5-triethoxysilyl-2-norbornene) also exhibits the unique behavior of both glassy and rubbery materials, and we will provide a thorough and detailed investigation into its gas permeation parameters (permeability, diffusion and solubility coefficients) for a number of gases ranging from He to C_4H_{10}, its free volume by means of positron annihilation lifetime spectroscopy (PALS), its remarkable optical transparency, its temperature service window, and its tensile strength.

6.3 Synthesis and Polymer Characterization

For the results described herein, the monomer, 5-triethoxysilyl-2-norbornene, and its homopolymer, poly(5-triethoxysilyl-2-norbornene) (**13c**), were synthesized as previously described (Appendix E: Experimental Methods and Supporting information for Chapter 5. The polymer, **13c**, is readily soluble in a host of common organic solvents including DCM, THF, acetone, toluene, and diethyl ether. Polymer membranes were solution cast via a slow evaporation process yielding free-standing polymer films that are highly transparent, defect free, and flexible in nature. Immediately upon film casting, the optical transparency that is characteristic of vinyl-added norbornene polymers is observed (**Figure 31d**). For **13c**, optical transparencies were greater than 80% across the entire visible spectrum and reached 82.2% at wavelengths of 550 nm (**Figure 31c**). Analysis of these films using wide-angle X-ray diffraction (WAXD) showed that **13c** is a completely amorphous material with inter-chain distances (d_{ic} spacing) calculated to be 17.4, 7.9, and 5.2 Å (**Figure 31b,** and **Table 7**). The density of **13c** was 1.08 g/cm^3 and the fractional free volume FFV of the polymer was determined to be 0.131 as was estimated using the Bondi method.[146]

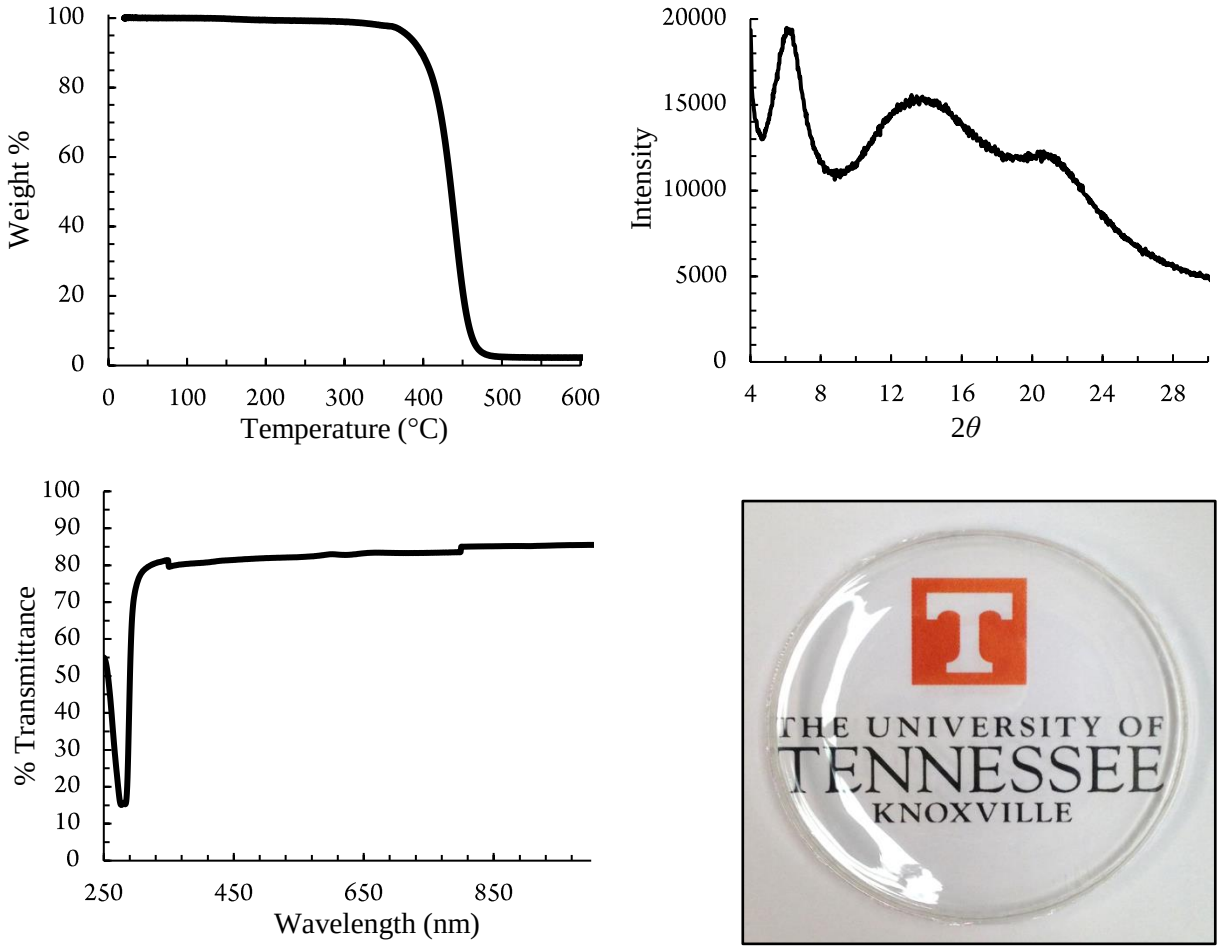

Figure 31. a) Thermal Gravimetric analysis (TGA) of **13c** showing 5 % mass loss appearing at 380 °C. **b)** Wide-angle X-ray diffraction (WAXS) spectra of **13c** showing amorphous character and significant peaks at θ = 3.1, 6.9, and 10.5. **c)** UV-Vis spectroscopy of **13c** showing high optical transparency in the visible region. **d)** Picture of a free-standing film of poly(5-triethoxysilyl)-2-norbornene (**13c**) over a UTK logo.

Thermogravimetric analysis (TGA) showed that **13c** had a remarkably high decomposition temperature (T_d = 380 °C at 5% mass loss) (**Figure 31a**), while differential scanning calorimetry (DSC) did not reveal any distinguishable glass transition temperatures (T_g). Dynamic mechanical analysis (DMA) showed that **13c**'s storage modulus was higher than its loss modulus across the polymer's temperature service window (-150 – 325 °C), which is typical of glassy materials, and also revealed that a glass transition does exist prior to polymer decomposition as was evidenced by a clear tan delta peak at 325 °C (**Figure 32**). In tandem with DMA, **13c**'s tensile strength was evaluated using an Instron according to the ASTM D638 method. The modulus calculated from this method agreed well with the DMA giving a value of 0.92 GPa and an elasticity of 10% which is a drastic improvement over standard vinyl-added polynorbornene. The culmination of these properties indicate that **13c** exhibits a unique combination of flexibility, thermal stability, and optical transparency that is only rivaled by engineering plastics such as colorless polyimides. Although these materials were originally designed as gas separation membranes, siloxane-functionalized polynorbornenes have the potential for use in medicinal packaging applications or thermally robust transparent coatings.

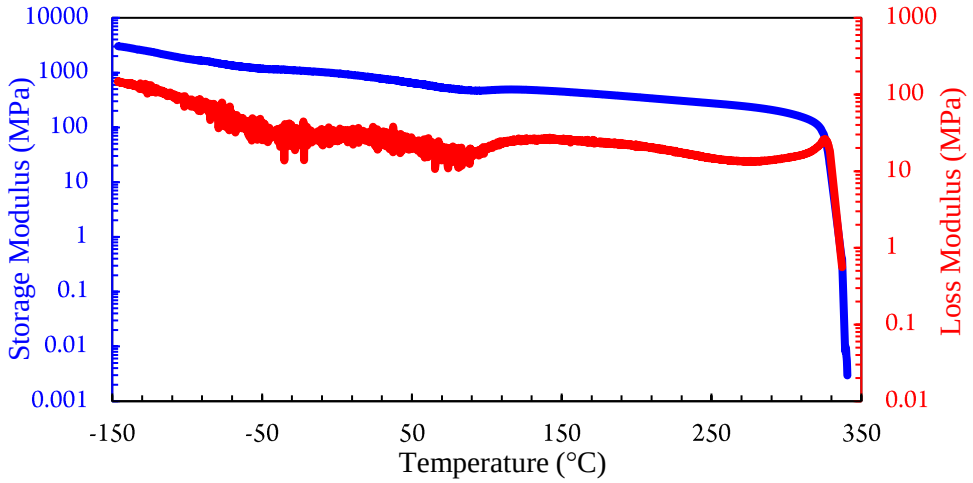

Figure 32. Dynamic mechanical analysis of poly(5-triethoxysilyl)-2-norbornene (**13c**) showing remarkable thermal stability at glass transition temperature at 325 °C.

6.4 Gas Permeation Parameters and Free Volume

The permeability coefficients of **13c** were measured for various gases using both barometric (*Baratron*) and gas chromatographic (*GC*) based methods (Appendix F: Experimental Methods and Supporting information for Chapter 6) and those results are detailed in **Table 8**. A good agreement between the results obtained via gas chromatographic and barometric methods was observed, which are also in reasonable agreement with the hydrocarbon permeability data reported by Sundall et al.,[144] who also studied this polymer. It should be noted that the values reported in **Table 8** differed from the values that we reported in **Table 7** for CO_2 and N_2 by about 30%, which we attribute to the use of a different film casting solvent (THF) than was used for the measurements detailed herein (toluene).

The $P(CO_2)/P(N_2)$ selectivity observed in this work and in the previous chapter are in strong agreement (17.6 and 16.4 respectively). The ideal selectivity of **13c** films for different gas pairs are shown in **Table 9**. The observed O_2 permeability coefficient and O_2/N_2 selectivity are on the same order of magnitude as those reported for polydimethylsiloxane (PDMS), which according to Robb[139] are $P(O_2)$ = 600 Barrer and $\alpha(O_2/N_2)$ = 2.1 and according to Reitlinger et al.[147] are $P(O_2)$ = 500 Barrer and $\alpha(O_2/N_2)$ = 2.0. Even more similar values of $P(O_2)$ and $\alpha(O_2/N_2)$ were observed for polyorganosiloxanes with side groups larger than methyl.[148] The same is true for siloxane containing block-copolymers: $P(O_2)$ = 200-300 Barrer, $\alpha(O_2/N_2)$ = 2.0-2.4.[149] Another even more important common feature of **13c** and related polysiloxanes is their solubility controlled, or reverse selectivity, transport of hydrocarbons.

It can be seen in **Table 8** that **13c**'s permeability coefficients increase as the size of hydrocarbon penetrant increases. Such behavior has been shown for rubbery polymers and for high free volume polymers such as polyacetylenes or poly(tricyclononene)s polymerized via vinyl-addition polymerization.[42] However, **13c** cannot be ascribed to the latter category as its permeability coefficients are smaller by an order of magnitude than those observed in poly(trimethylsilyl propyne)[141] (PTMSP) or addition type $SiMe_3$-

Table 8. Permeability coefficients (*P*) of poly(5-triethoxysilyl-2-norbornene) measured by either the gas chromatographic method (*GC*) or barometric method (*Baratron*)[a]

Gas	*P* (Baratron)[b]	*P* (GC) (as cast)[c]	*P* (GC) (EtOH)[d]	*P* Literature
He	217	263	227	–
H_2	430	467	402	–
O_2	211	204	189	–
N_2	85	78.5	72.8	57.3[e]
CO_2	1.50×10^3	1.35×10^3	1.30×10^3	936.6[e]
CH_4	266	246	236	176.2[f]
C_2H_6	538	468	440	–
C_3H_8	693	714	731	499.1[f]
n-C_4H_{10}	4.5×10^3	5.43×10^3	5.8×10^3	3837.6[f]

[a]All permeability values are reported in units of Barrer. [b]Measurements taken using barometric method (Baratron) at 22 ± 2 oC and 1 atm gas pressure. [c]Measurements of "as cast" films using gas chromatographic (GC) method. [d]Measurements of "EtOH" treated films using gas chromatographic (GC) method. [e]Permeability from ref. 154. fPermeability from ref. 152.

Table 9. Ideal selectivity (P_i/P_j) of poly(5-triethoxysilyl-2-norbornene) for different gas pairs.

Gas pair	Baratron[a]	GC (as cast)[b]	GC (EtOH)[c]	Literature
O_2/N_2	2.5	2.6	2.6	–
CO_2/CH_4	5.6	5.5	5.5	–
CO_2/N_2	17.6	17.2	17.9	16.4[d]
He/N_2	2.6	3.4	3.1	–
H_2/CH_4	1.6	1.9	1.7	–
C_3/C_1	2.6	2.9	3.1	2.8[e]
C_4/C_1	17.0	22.1	24.5	21.8[e]

[a]Measurements taken using barometric method (Baratron) at 22 ± 2 °C and 1 atm gas pressure. [b]Measurements of "as cast" films using gas chromatographic (GC) method. [c]Measurements of "EtOH" treated films using gas chromatographic (GC) method. [d]Permeability from ref. 154. [e]Permeability from ref. 152.

substituted poly(tricyclononene)s.[150] Furthermore, **13c**'s FFV value (0.131) is significantly smaller than those of most other highly permeable glassy polymers (0.27-0.34),[46,141] and large differences can be also noted in comparison of free volume estimated via the PALS method.

Positron annihilation lifetime spectroscopy (PALS) was used to estimate the size of free volume elements (FVE or microcavities) within **13c** based on application of a semi-empirical Tao-Eldrup equation shown below:[116-117]

$$\tau_i = 1/2\left[1 - \left(\frac{R_i}{R_0}\right) + \left(\frac{1}{2\pi}\right)\sin\left(\frac{2\pi R_i}{R_0}\right)\right]^{-1} \qquad (16)$$

where i = 3 or 4, to relate the ortho-positronium lifetimes (τ_i) to the average radius of spherical FVE (R_i). Here, $R_o = R_i$ + DR (the adjustable parameter DR = 1.66 Å). **Table 10** presents components of the lifetime spectra and corresponding radii of FVE in **13c**.

Two types of lifetime distributions were tested and it was found that a four-component lifetime distribution provided the best fit. For "as cast" PTESN films, the lifetimes (τ_3 and τ_4) and FVE radii (R_3 and R_4) were found to be similar to those observed for polymers with only modest permeability, such as poly(vinyltrimethyl silane).[151] As a reference, PDMS has a lifetime of approximately 4 ns.[152] Interestingly, treatment with ethanol resulted in a noticeable increase in the *ortho-positronium* lifetimes and the FVE radii (**Table 10**). Usually, such increases in the size of FVE results in an increase in permeability and/or diffusivity in a parallel manner.[153] However, this is not the case for PTESN, ethanol treatment did not increase permeability of this polymer (**Table 8**). Because of this, we can conclude that the transport properties of **13c** do not depend

Table 10. Components of lifetime spectrum and the radii of FVE in poly(5-triethoxysilyl-2-norbornene).[a]

PTESN state	τ_3, ns	I_3, %	τ_4, ns	I_4, %	R_3/R_4, Å
As cast	2.22 ± 0.28	14.40 ± 3.57	4.33 ± 0.14	37.00 ± 3.90	3.05/4.42
EtOH treated	2.88 ± 0.14	27.09 ± 2.80	5.75 ± 0.26	21.94 ± 2.97	3.56/5.09

[a]Performed under a N_2 atmosphere using a nickel-foil-supported [^{44}Ti] titanium (IV) chloride radioactive positron source. The time resolution was 300 ps. Values are reported as averages of several spectra collected having an integral number of counts of at least 10^6 in each spectrum.

directly on its free volume. This independent relationship between transport behavior and free volume has not been noted for other polymers with rigid chains and high glass transition temperatures.[42,46,141,150]

An important property of highly permeable glassy polymers is that they traditionally display dramatic increases in gas permeability after treatment with non-solvents (lower alcohols) that can cause strong swelling of the polymer matrix.[91] As can be seen from **Table 8**, this is not the case for **13c** in which permeability coefficients were observed even to decrease slightly after the polymer films were treated with EtOH. In this regard, the behavior of **13c** is more similar to that of a rubbery material than that of a glassy material, in spite of its observed high glass transition temperature.

Because permeability coefficients include contributions from both diffusivity and solubility, i.e. $P = D \cdot S$, the diffusivity coefficients D in **13c** were measured and the solubility coefficients were estimated as the ratio $S = P/D$. The obtained values (**Table 11**) are

Table 11. Diffusivity coefficients (D) and solubility coefficients (S) of poly(5-triethoxysilyl-2-norbornene) as compared to other well-known polymers.

	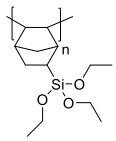	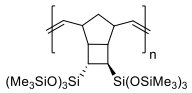 ref.[154]	PDMS ref.[139]	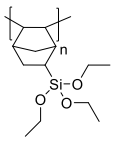	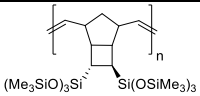 ref.[154]	PDMS refs.[139,148]
Gas	D 10^8 (cm^2s^{-1})[a]			S (cm^3(STP)cm^{-3} atm)[b]		
O_2	236	425	1600	0.68	0.74	0.31
N_2	133	227	1500	0.49	0.60	0.15
CO_2	214	273	1100	5.3	3.3	2.2
CH_4	104	179	1270	1.9	1.5	0.57
C_2H_6	29	46.1	–	14	8.6	–
C_3H_8	11.7	13.1	–	45	27	6.45
n-C_4H_{10}	7.1	5.0	500	177	91	15

[a]Diffusivity coefficients (D) of poly(5-triethxoysilyl)-2-norbornene were measured using the Daynes-Barrer time-lag method. [b]Solubility coefficients (S) of poly(5-triethoxysilyl)-2-norbornene were calculated using $S = P/D$.

compared to traditional cross-linked PDMS[139,148] and a related ROMP polymerized glassy polymer containing multiple Si-O-Si bonds in their side chains, which was previously described to possess gas diffusion properties intermediate between a traditional glassy or rubbery material.[154] It should also be noted that a quantitative comparison to rubbery PDMS (**Table 11**) is problematic as samples studied across various reports often differ by degree of cross-linking and the presence of a filler material. For example, varying *D* values of PDMS have been reported elsewhere (e.g. by Merkel et al.[40]) but the qualitative conclusion is the same: the presence of flexible Si-O-Si bonds in the main chain of PDMS increases diffusivity much more significantly than when flexible bonds are present in side groups.

Table 11 shows that the differences between the permeability of **13c** and PDMS can be partially explained by greater diffusivity coefficients of the latter. In addition, **13c** is compared to the polymer studied by Belov *et al.*,[154] which includes a larger number of Si-containing groups than **13c** (**Table 11**), but only minor differences in the diffusion coefficients when comparing polymers bearing Si-O-Si and C-Si-O side chains (especially for heavier penetrants). What is perhaps most interesting, is that both **13c** and the polymer containing Si-O-Si side groups are distinguished by solubility controlled permeation and each have similar solubility coefficients that are greater than those of PDMS. Glassy polymers with high free volume (i.e. FFV = 0.27-0.34), such as (PTMSP)[91] and polymers of intrinsic microporosity (PIM)[17] are known to have solubility coefficients greater than rubbers; however, because **13c** has a high glass transition temperature paired with far lower free volume (FFV = 0.131),[155] it is evident that **13c** combines properties of both polymer glasses and rubbers.

The pressure dependence of permeability and diffusion coefficients in **13c** were studied for hydrocarbons C_1-C_4 and those results are shown in **Figure 33** and **Figure 34**. Both *P* and *D* values of ethane, propane and butane increase as a function of pressure, while for methane, *P* and *D* values are independent of pressure. This is a common behavior of polymers, and good examples of such dependences can be found in the literature.[40,148] We also observed that the pressure dependence of the diffusion coefficient (*D*(p)) for butane is especially strong. If these trends are extrapolated to zero pressure,

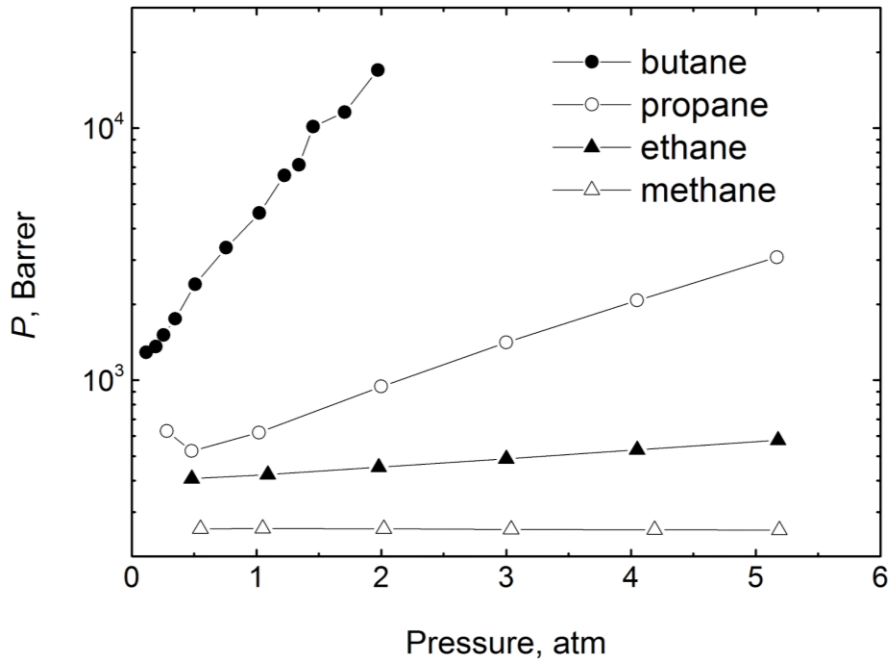

Figure 33. Pressure dependence of the permeability coefficients (*P*) of hydrocarbons in poly(5-triethoxysilyl-2-norbornene).

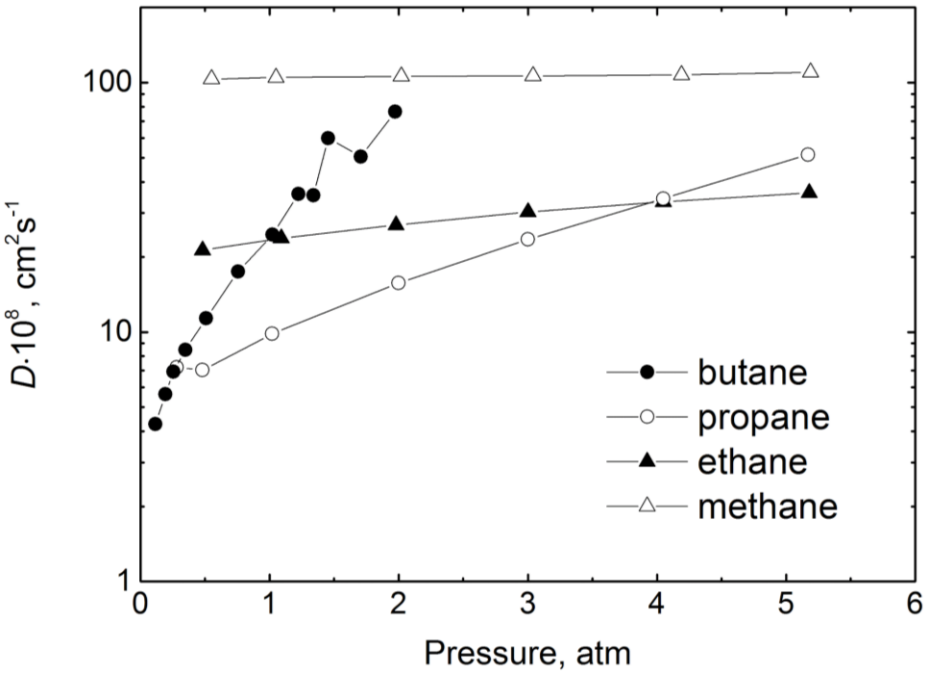

Figure 34. Pressure dependence of the diffusivity coefficients (*D*) of hydrocarbons in poly(5-triethoxysilyl-2-norbornene).

the following ('normal') inequality holds: $D(C_4H_{10}) < D(C_3H_8)$, while at higher pressures (above 0.5 atm) an opposite inequality is observed (see **Figure 34**).

As was mentioned above, the solubility coefficients of **13c** were estimated as $S = P/D$ and the plot of pressure dependence of S can be seen in **Figure 35**. A very weak dependence of S as a function of pressure is observed for all hydrocarbons studied, but some reduction in S values can be discerned. From this result, we can safely assume that the sorption isotherms of hydrocarbons C_2-C_4 must be concave to the pressure axis. This behavior is characteristic for sorption in glassy polymers, while rubbery materials often display increasing solubility coefficients with pressure and isotherms that are concave to the gas concentration axis. In this respect, **13c** clearly behaves as a glassy polymer, though deviations from linear isotherms are rather small. For typical glassy polymers,[150] sorption isotherms have a form strongly concave to the pressure axis in the same range of pressure examined herein.

Plots of $\ln(D)$ versus d^2, where d is the kinetic diameter of the diffusing molecule,[156] are often considered in order to evaluate the average selectivity of diffusion for a particular membrane. **Figure 36** presents an example of such a correlation for **13c**, as well as cross-linked PDMS and polycarbonate (PC) as prototypical examples of the behavior of a rubbery or glassy material, respectively The slope of the correlations can be regarded as the unified selectivity of diffusion for a specific polymer, and at low pressure, the selectivity of diffusion for **13c** is intermediate between those of rubbery (PDMS) and that of glassy (PC) polymers.[157] This once again highlights a manifestation of the dual behavior of **13c**. If this correlation is plotted for diffusion coefficients that were measured at higher pressures, this dual mode behavior becomes less evident, thereby indicating that **13c** becomes somewhat plasticized and has behavior more akin to rubbery polymers (**Figure 36**).

Finally, several examples of polymers bearing flexible side chains attached to relatively rigid main chains can be found in the literature.[158-159] In most of these examples, the incorporation of a flexible pendant group results in a dramatic decrease in T_g. As an example, substituted polystyrenes often display a strong self-plasticization effect in which glass transition temperatures have been shown to decline by ~50-70 °C when flexible

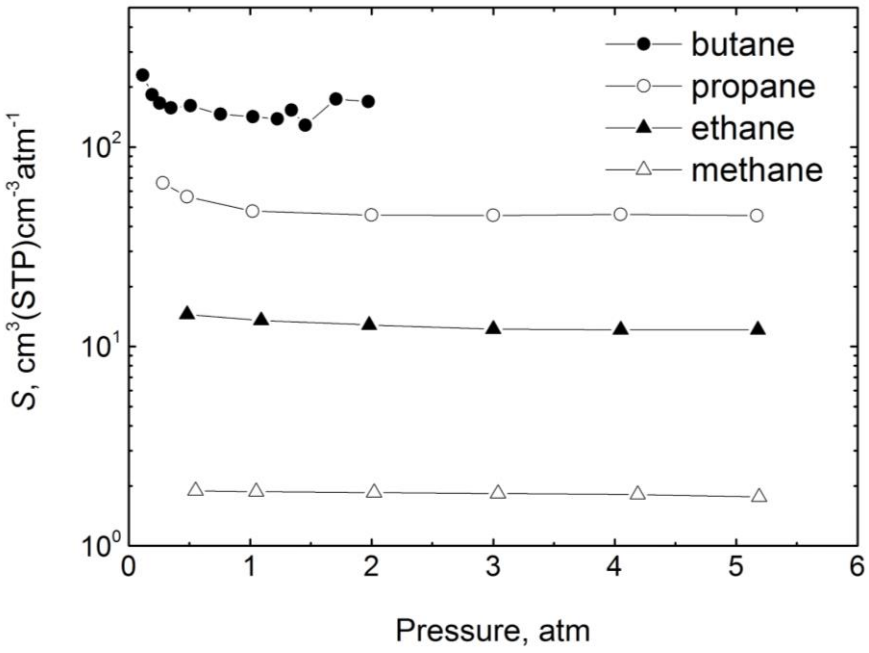

Figure 35. Pressure dependence of the solubility coefficients (*S*) of hydrocarbons in poly(5-triethoxysilyl-2-norbornene).

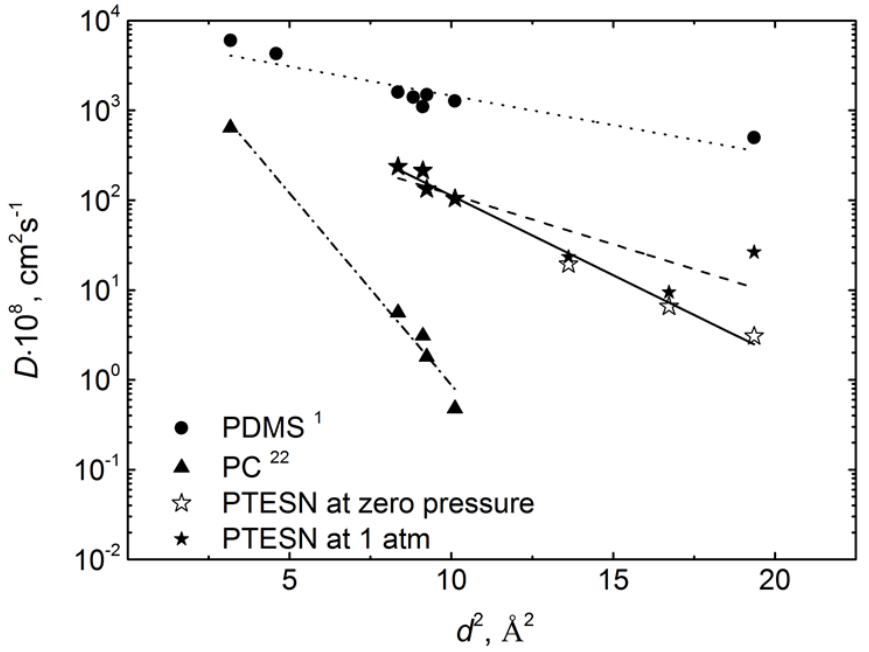

Figure 36. Correlation of gas diffusion coefficients (*D*) versus the square of the penetrant gas kinetic diameter (d^2) in semilogarithmic coordinates for PDMS, polycarbonate (PC), and poly(5-triethoxysilyl-2-norbornene) at zero pressure and at 1 atm.

side groups containing Si-O-Si bonds are appended.[158] In stark contrast to this, **13c** maintains its high T_g despite having flexible silicon containing side groups. Similar behavior has been reported for other polynorbornenes synthesized via both metathesis and vinyl-addition routes, and introduction of Si-O-Si-containing side groups has even resulted in increased T_g values.[44,142,159] This suggests that the flexibility of the $Si(OEt)_3$ groups have little to no influence over PTESN's glass transition temperature, though further investigations, such as computational modeling, are required to better understand this effect.

6.5 Conclusions

In conclusion, we have synthesized and studied in detail the gas transport properties of vinyl-addition poly(5-triethoxysilyl-2-norbornene) (**13c**). In contrast to many previously reported polymers that contain side groups consisting of Si-O-Si bonds,[44,142] **13c** instead contains flexible Si-O-C bonds in its side groups. It was discovered that despite **13c**'s high glass transition temperature, its permeability and permselectivity are more similar to those of rubbery siloxanes and not Si-containing high free volume glassy polymers. Investigations into **13c**'s diffusion and solubility coefficients revealed that it represents a remarkable example of a glassy polymer that exhibits solubility controlled permeation, which is a trait more commonly found in rubbery materials. Treatment of **13c** with EtOH resulted in an increase in the size of free volume elements as determined by PALS, but this increase did not lead to an enhancement of its gas permeability. Lastly, its selectivity via diffusivity is intermediate between that of rubbery PDMS and that of many conventional glassy polymers. All of this evidence supports the hybrid behavior of this material: a glassy polymer with properties of a rubber and make it an attractive material for membrane-based separations of hydrocarbons.

Chapter 7. Enhancing CO_2/N_2 Selectivity of Addition-type Polynorbornene for Post Combustion Carbon Dioxide Sequestration

7.1 Abstract

A structure-activity relationship between siloxane-functionalized vinyl-added polynorbornenes (VAPNBs) and CO_2/N_2 permeation performance was conducted. Through the use of *trans*-[$Ni(C_6F_5)_2(SbPh_3)_2$], poly(5-triethoxysilyl-2-norbornene), poly(5-tris(2-methoxyethoxy)silyl-2-norbornene), and a series of copolymers were successfully synthesized and solution-cast into thin-film polymer mem-branes. It was observed that by increasing the concentration of tris(2-methoxyethoxy)silane, CO_2/N_2 selectivity increased substantially (223.8 %), and CO_2 permeability decreased by only 19.4 %. This trend in gas separation performance does not adhere to the traditional permeability/selectivity "trade-off", and ultimately results in permeability and selectivity values that reach the 2008 Robeson Upper Bound, 754.8 Barrer and 36.7 respectively. The work described herein utilizes the copolymer series to incrementally probe changes in CO_2 and N_2 permeability, CO_2/N_2 selectivity, fractional free volume, crystallinity, interchain spacing, and gas solubility.

7.2 Background

With access to polar functionalities within vinyl-added polynorbornenes, we aimed to expand the intricacy of the norbornene monomers towards functionalities known to show high performance in CO_2/N_2 separations. Hundreds of polymers have been explored for the separation of CO_2 and N_2 gas with notable performers including polymers of intrinsic microporsity (PIMs)[17,160-167] polyacetlyenes,[88,91,124,168-169] modified polydimethylsiloxanes,[122,170] poly(ethylene oxide),[39,171-174] and modified addition-type polynorbornenes.[42-46,155] Midst these polymers, there are several noteworthy features that include rigid polymer backbones and pendant functionality rich in Lewis basicity and/or steric bulk such as nitriles, carbonyls, sulfones, ether linkages, as well as steric bulk such as trimethylsilyl groups.[43,175-177] Ethylene oxide units are a functionality that is well-known to increase CO_2/N_2 selectivity with notable examples including poly(ethylene oxide) (PEO),[39] poly(ethylene oxide) – poly(butylene terephthalate) (PEO-PBT) copolymers,[178] and poly(ethylene oxide) – poly(ether imide) copolymers [179] exhibiting CO_2/N_2 selectivity's

of 48, 52, and 68 respectively. Using those functionalities as inspiration, we proposed the synthesis of the following sequence of VAPNB copolymers as described in **Figure 37.** Analyzing this series as a whole produces a structure-activity relationship capable of investigating the changes in membrane performance as the pendant functionality triethyoxysilane is gradually upgraded into tris-(2-methoxyethoxy)silane. The end result is a change in CO_2 permeability and CO_2/N_2 selectivity that disobeys the traditional "trade-off" with values that practically reach the 2008 Robeson "Upper Bound".[16] In this chapter, we detail the synthesis and characterization of these new polymer materials as well as describe our initial findings for permeability and selectivity values of CO_2 and N_2.

7.3 Polymerization Results and Physical Properties

Siloxane-functionalized norbornene monomers are readily synthesized through Diels-Alder chemistry of dicyclopentadiene and the appropriate silyated vinyl reagent. Silylated vinyl reagents such as vinyltriethoxysilane and vinyltris(2-methoxyethoxy)silane are cheap, commercially available chemicals that lead to the formation of 5-triethoxysilyl-2-norbornene (**12c**) and 5-tris(2-methoxyethoxy)silyl-2-norbornene (**14**) in respectable yields (30-60 %). It is worthy to note that to our knowledge, this is the first reported

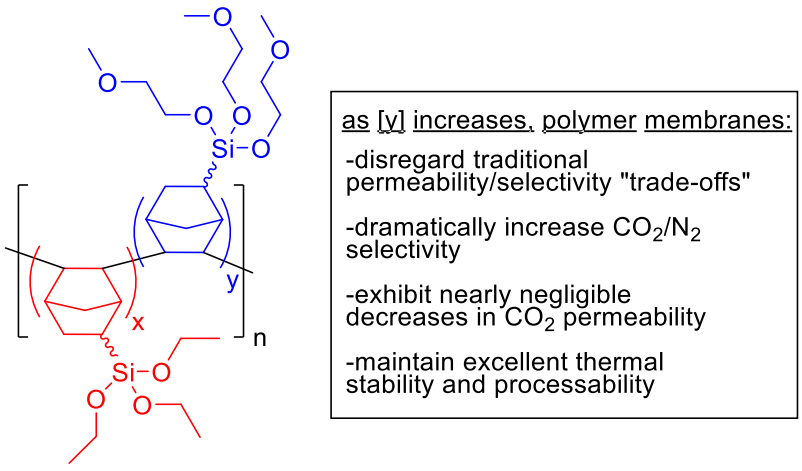

Figure 37. Structure-activity relationship between copolymers of (5-triethoxysilyl-2-norbornene) (red) and (5-(tris(2-methoxyethoxy)-2-norbornene) (blue) and how the membrane's performance changes.

synthesis of 5-tris(2-methoxyethoxy)silyl-2-norbornene. The pure product was isolated via vacuum distillation as a clear liquid and its structure was confirmed by NMR spectroscopy and high-resolution mass spectrometry (Supporting Information). An *endo-exo* ratio was calculated to be 63:37, placing it among similarly functionalized norbornene monomers.

As discussed previously, *trans*-[Ni(C_6F_5)$_2$($SbPh_3$)$_2$] is believed to propagate through a neutral Ni site rather than an oxophilic cationic metal center which allows for increased activity in the vinyl-addition polymerization of electron-rich monomers compared to traditional vinyl-addition catalysts.[155] This hypothesis is reinforced by the successful polymerization of **14**, a monomer which contains twice the number of oxygen atoms per repeat unit than **12c** (**Figure 38**), which to our knowledge represents the first reported synthesis of poly(5-tris(2-methoxyethoxy)silyl-2-norbornene) (**15d**). However, we should emphasize that for the random copolymer series **13c**, **15a-d**, there is evidence of a decrease in polymerization activity as the oxygen content of the repeat unit increases as described in **Table 12**. As the the mole fraction of repeat unit of **14** increases in the copolymer, a decrease in polymerization yield is observed by a factor of 1.6. Similarly, the rates of monomer incorporation are skewed in favor of increased x content that deviate further from the initial feed ratio as y content increases (**Table 12**, entries 2 – 4). In spite of this slight decrease in catalytic performance, **Figure 39** demonstrates the successful synthesis of the copolymer gradient we aimed to achieve. Defining features of polymer **13c** appear at 3.86 and 1.32 ppm that represent the protons in the ethyl chain of the siloxane pendant group (**Figure 39**, red), while polymer **15d** is defined by NMR signals at 4.00, 3.64, and 3.63 ppm signifying the protons involved in the ethylene oxide units as well as the terminal methoxy group (**Figure 39**, purple). Siloxane-functionalized VAPNBs exhibit excellent solubility in common organic solvents allow them to be easily cast from THF into large, homogeneous thin films.

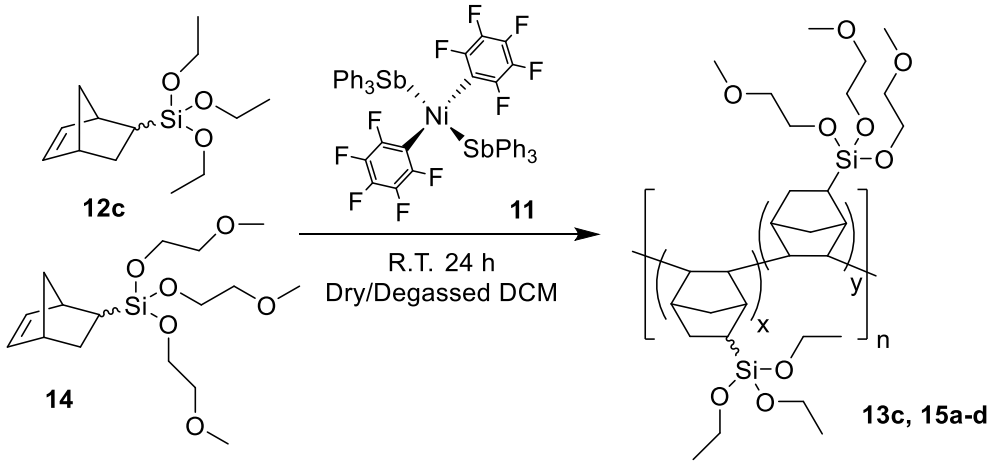

Figure 38. Synthetic scheme for the vinyl-added polymerization of **12c** and **14** in different quantities to generate polymer series **13c**, **15a-d**.

Table 12. Polymerization of Monomers **12c** and **14** with *trans*-Ni(C_6F_5)$_2$($SbPh_3$)$_2$ (**11**) and the Resultant Polymers (**13c**, **15a-d**) Physical Properties[a]

entry	polymer	feed ratio[b] (x:y)	actual ratio[c] (x:y)	yield (%)	*M*n[d] (kg/mol)	*M*w/*M*n[d] (kg/mol)
1	13c	100:0	100:0	71	150	1.47
2	15a	75:25	79:21	66	176	1.77
3	15b	50:50	59:41	54	175	1.64
4	15c	25:75	43:57	46	161	1.56
5	15d	0:100	0:100	44	115	1.93

[a]Polymerizations conducted using 5 mmol of monomer, 5 μmol of catalyst, and 2 mL of DCM for 24 h. [b]Monomers were combined in solution by molar contributions before catalyst addition. [c]Actual incorporation ratio is calculated via ^{1}H NMR spectroscopy of the polymer sin $CDCl_3$ at 25 °C. [d]Molecular weights and dispersity indices were measured using gel permeation chromatography (GPC) equipped relative to polystyrene standards at 40 °C in THF.

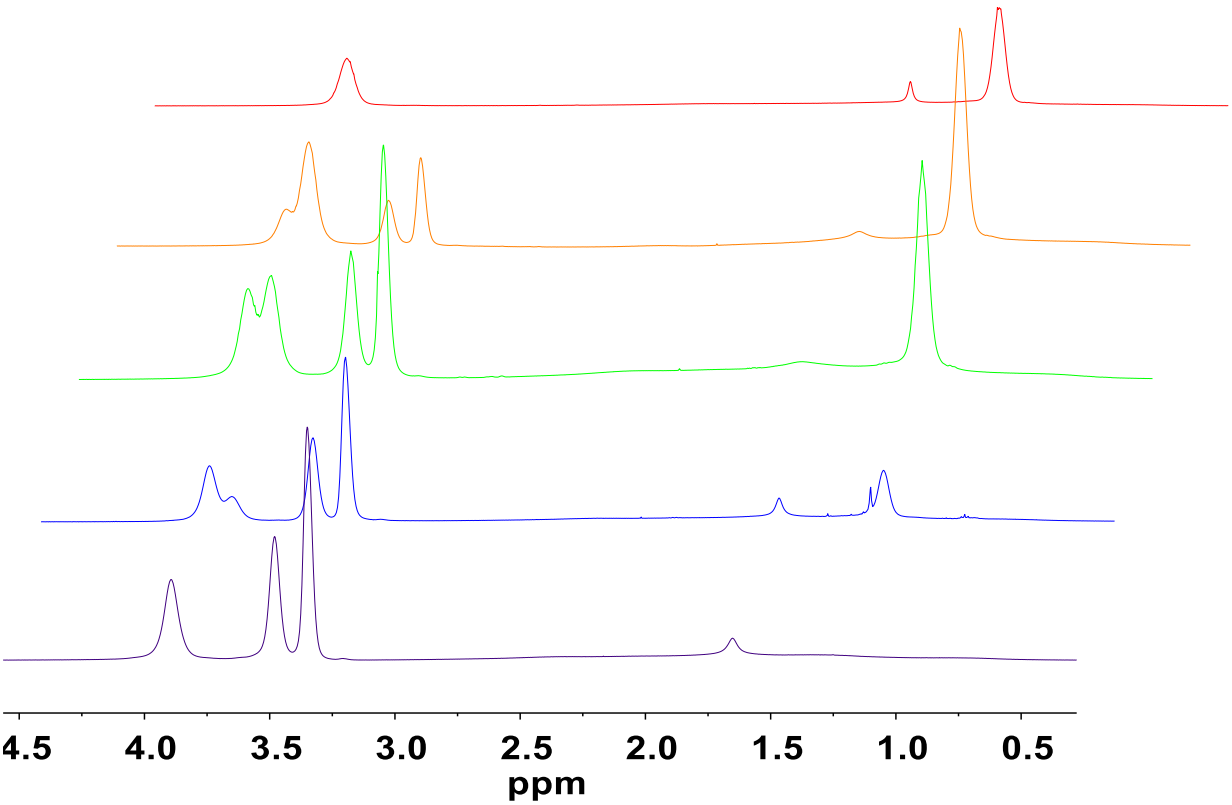

Figure 39. Stacked NMR spectra of polymers **13c**, **15a-d** showing the gradient of monomer inclusion.

7.4 Gas Separation Performance

Thin-film membranes of **13c**, **15a-d** were evaluated as post-combustion CO_2 separation membranes by measuring permeability and ideal selectivity values of CO_2 and N_2 via the constant-volume variable-pressure gas flux method. The gas separation data attained is tabulated in **Table 13** and displayed on a Robeson Plot against the 2008 Upper Bound (**Figure 40**). Immediately, it is apparent that the increase in performance amongst this copolymer series defies the traditional permeability-selectivity trade-off that plagues membrane development. As the content of y increases, CO_2 permeability decreases by 19.4%, N2 permeability decreases by 276.8%, resulting in CO_2/N_2 selectivity to increase by 223.8%. The amalgamation of these changes results in poly(5-tris(2-methoxyethoxy)silyl-2-norbornene) (**15d**) having a CO_2 permeability of 754.8 Barrer and a CO_2/N_2 selectivity of 36.7, placing it among the highest performing polymer membranes for this binary gas pair and close to the 2008 Robeson Upper Bound. These results are very encouraging for both actual membrane performance and the behavior of the series being unusual to the Upper Bound relationship. At the time of this writing, we are working at full capacity to understand the exact mechanisms of gas diffusion that are changing as a result of changing the silyl substituent. Based on the permeation results, **15d** has a N_2 permeability that is significantly lower than **13c**. Given the lack of diffusivity control typically associated with CO_2/N_2 separations, we hypothesize that the nitrogen solubility is decreasing heavily and causing increased CO_2/N_2 selectivity. Another possible explanation is that by making the siloxane functionality larger, we are making changes into what allows these polymers to act as rubbers and glasses simultaneously as discussed in Chapter 6. If the changes in the polymer structure are able to tap into the benefits of both glasses and rubbers while minimizing the negative effects on diffusion, this could lead to unusual gains in gas separation behavior that would defy the typical permeability-selectivity trade-offs.

Table 13. Permeability and Ideal Selectivity of Polymers **13c**, **15a-e**.

		P (Barrer)		
entry	polymer	CO_2	N_2	α (CO_2/N_2)
1	13c	936.6 (±14.9)	57.3 (±2.3)	16.4 (±0.4)
2	15a	868.4 (±125.7)	40.5 (±8.2)	21.6 (±1.3)
3	15b	733.3 (±66.7)	27.5 (±4.2)	26.8 (±1.6)
4	15c	640.7 (±64.1)	19.6 (±2.0)	32.7 (±1.3)
5	15d	754.8 (±40.5)	20.7 (±2.6)	36.7 (±2.8)

[a]Permeability values of free-standing polymers films were obtained using the constant-volume variable-pressure gas flux method, as detailed in section 1.3 The Solution-Diffusion Model and Mechanisms of Gas Diffusion. [b]Ideal selectivity calculated by a ratio of CO_2 and N_2 permeabilites.

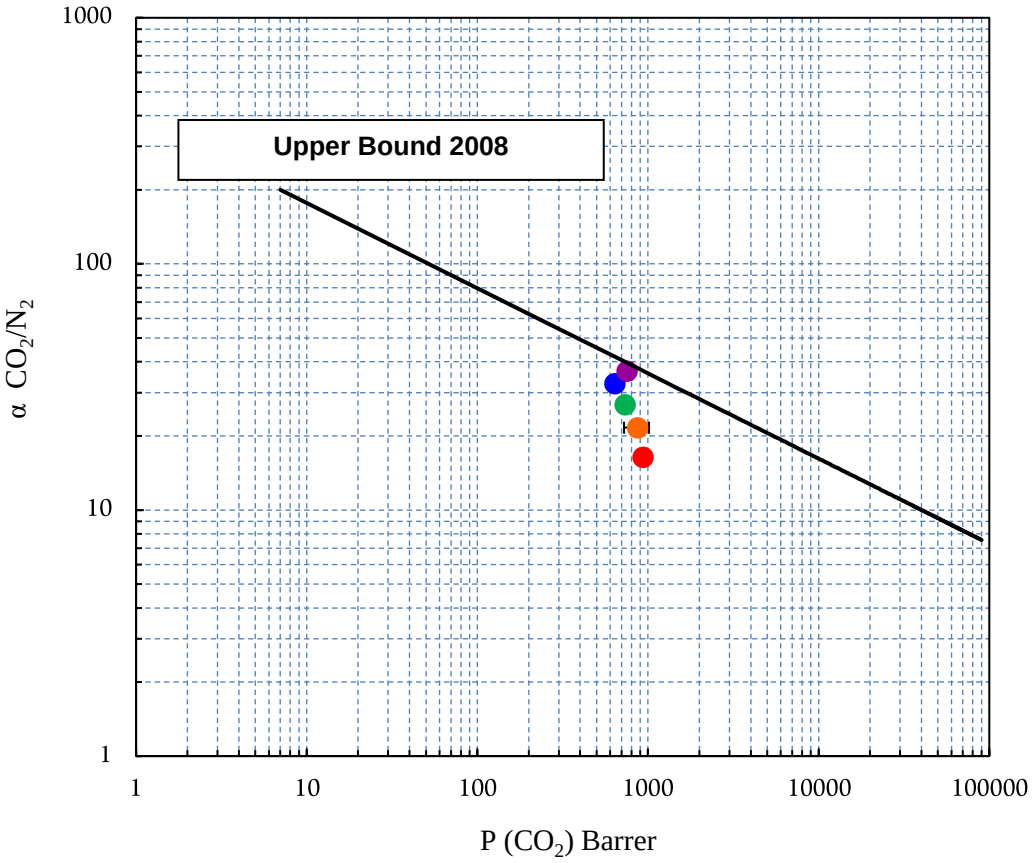

Figure 40. Robeson plot of polymers **13c**, **15a-d** and the 2008 Upper Bound. **13c** red circle, **15a** orange circle, **15b** green circle, **15c** blue circle, **15d** purple circle with error bars.

7.5 Conclusions

The preliminary work described in this chapter is particularly encouraging and is an excellent example of how the catalyst system designed in Chapter 5 has unlocked the potential for new next-generation membranes. Catalyst 11 demonstrated that as long as norbornyl monomers are attainted in purities of greater than 99%, even polar functionality to the degree of 5-tris(2-methoxyethoxy)silyl-2-norbornene can be polymerized to high molecular weight vinyl-added polymer in decent yields. Monomers can also be mixed in different feed ratios to produce copolymers that we can use as critical synthetic tools to probe incremental changes in gas separation performance. The copolymer gradient of 13c, 15a-d was characterized by NMR to show gradual changes of each monomer in the polymer matrix. Increases in permselectivity that disobey the permeability-selectivity trade-off were observed and ultimately produced polymer membranes that exist among the highest performing membranes for CO2/N2 separations (754.8 Barrer and 36.7 selectivity). The source of this behavior is currently unknown and investigations are still ongoing. We are hopeful in that the source of these increases in membrane performance will provide additional information about the permeability-selectivity trade-off and that will directly influence the design of polymer membranes in the future.

Chapter 8. Summary, Conclusions, and Future Work

8.1 Summary and Conclusions

In summary, the work in this dissertation describes the continued impact of norbornene-based polymers, transition metal catalyst design, and advanced analytical techniques in the development of gas separation membranes and engineering plastics. At a fundamental level, structure-property relationships between chemical structure and membrane performance are paramount in solidifying our knowledge of gas transport in polymer systems and ultimately producing high performing membranes. Specifically, Chapter 3 highlighted a particular radical copolymer with a rigid main chain where we attempted to implement thermally-rearranged oxazoles in a different polymer system than polyimides. Although not entirely successful in this endeavor due to molecular weight and thermal stability limitations, the fundamental work in that chapter showed that the electronic differences between maleimide and maleic anhydride caused deviations to what was assumed in the literature to be a perfectly alternating copolymerization. Chapter 4 was the product of our participation in a massive collaboration at Oak Ridge National Laboratory (ORNL) that aimed at increasing the selectivity of existing membranes. By using terminal norbornene units on PDMS, we simultaneously created additional rigidity and tailored cross-link density that led to a 90% increase in permeability and an 80% increase in selectivity when compared to conventional cross-linked PDMS. This work inspired future directions in this project by first focusing our attention on the combination of norbornene and siloxane functionality and second, encouraging us to design materials with complex polymer assemblies and unique packing properties instead of just tailoring interactions between the gas penetrants and the side chains.

This work also highlights the importance of fundamental catalyst development. In order to introduce high concentrations of siloxane functionality into addition-type polynorbornenes, a new catalytic system was needed to effectively initiate polymerization. Initial attempts to polymerize siloxane-functionalized norbornene monomers with commercially available vinyl-addition catalysts were unsuccessful, but the work in Chapter 5 illustrates that *trans*-[$Ni(C_6F_5)_2(SbPh_3)_2$] exhibits high activity in the polymerization of these polar siloxane monomers by producing high molecular weight

polymers (>107 kDa), in moderate yields (45-78%), and with reaction times as short as five minutes. Following extensive characterization of these new materials, we discovered that the incorporation of $Si(OEt)_3$ substituents drastically improved gas separation performance, polymer solubility, flexibility, and tensile strength over vinyl-added polynorbornene while retaining high thermal stability and optical transparency. Chapter 6 is a full analysis of poly(5-triethoxysilyl)-2-norbornene's membrane properties that investigates the sub-parameters of permeability, diffusivity and solubility, for He, CO_2, N_2, O_2, CH_4, C_2H_6, C_3H_8, and C_4H_{10}. The results are quite remarkable and indicate that poly(5-triethoxysilyl)-2-norbornene exhibits properties of both glassy and rubbery polymers, such as high glass transition temperatures and solubility controlled selectivity of hydrocarbons. This makes poly(5-triethoxysilyl)-2-norbornene highly desirable for the separation of larger hydrocarbons such as butane from petroleum or natural gas mixtures. Lastly, Chapter 7 shows the robust nature of *trans*-$[Ni(C_6F_5)_2(SbPh_3)_2]$ polymerizing monomers with increased oxygen content in the monomer side chain and producing one of the highest performing membranes in the CO_2/N_2 literature, poly(5-tris(2-methoxyethoxy)silyl)-2-norbornene).

8.2 Future Aims

Following the completion of this doctoral dissertation, there are several aspects of membrane development that will continue to be pursued by the Long lab. The first of which will be to expand upon the mechanical properties studies of Chapter 6, as described. Given the advantages that arise from the inclusion of the $Si(OEt)_3$ side group, we propose to publish a more complete study that varies the amount of ethoxy substituents in the side chain in a similar fashion than was described in Chapter 5 (**13c**-**13e**). For this copolymer series, we will measure changes in optical transparency, polymer solubility, tensile modulus, elasticity, and hydrophobicity. These values will be compared to vinyl-added polynorbornene (**13a**) and other rival engineering plastics to demonstrate the unique combinations of optical transparency, thermal stability, and mechanical properties present in siloxane-functionalized vinyl-added polynorbornenes. Similarly, we want to expand upon the work described in Chapter 7 with a full investigation

into why that copolymer series appears to disobeys the permeability-selectivity trade-off. This will include experiments similar to those detailed in Chapter 6, as well as computational investigations into the binding energies of CO_2 and N_2 with these polymers.

On top of finishing these endeavors in the short term, we have several long term plans on how to continue to our research in this field. The first of which is to continue iterative expansion of our siloxane side chains in addition-type polynorbornenes of which there are dozens of possibilities. More specifically, we would like to examine how changes in tether link, alkyl steric bulk, or extending ethylene oxide functionality affect polymer chain packing and ultimately CO_2 permeability and CO_2/N_2 selectivity (**Figure 41**). We propose that changing tether link and/or steric bulk of the siloxane side chain will substantially effect the chain packing ability of the polymer by either frustrating packing to create more free volume elements or fill voids generated by the main chain to eliminate free volume elements. Then, we propose that by adding another ethylene oxide layer to the side chain of poly(5-tris(2-methoxyethoxy)silyl)-2-norbornene, we can continue to increase the solubility selectivity of these membranes for CO_2/N_2 separations. Some preliminary computational investigations suggest that the CO_2 binding interactions of **20** are significantly greater than that of **13c** and **15d**.

The second major avenue we will be actively pursuing is the continued development of catalytic systems. As a whole, vinyl-addition polymerization is a chaotic process that is lacking in reports demonstrating controlled polymerization conditions. With the discovery of living systems, we would have the potential to synthesize well-defined vinyl-added block copolymers and as a result, access to complex polymer morphologies. One example that we envision is to make segmented block copolymers with a highly permeable block and a highly selective block (**Figure 42**). We can vary the amounts of each of these blocks and monitor the changes in membrane performance. Toward this goal, we will screen several reaction conditions with *trans*-$[Ni(C_6F_5)_2(SbPh_3)_2]$ that include diluting the reaction mixture, running the polymerization at lower temperatures, and the implementation of the Grubb's slowdown method in the hopes of slowing down the polymerization rate and achieving more control over the polymerization. If initial experiments are unsuccessful, the synthesis of new catalyst systems with varying ligand

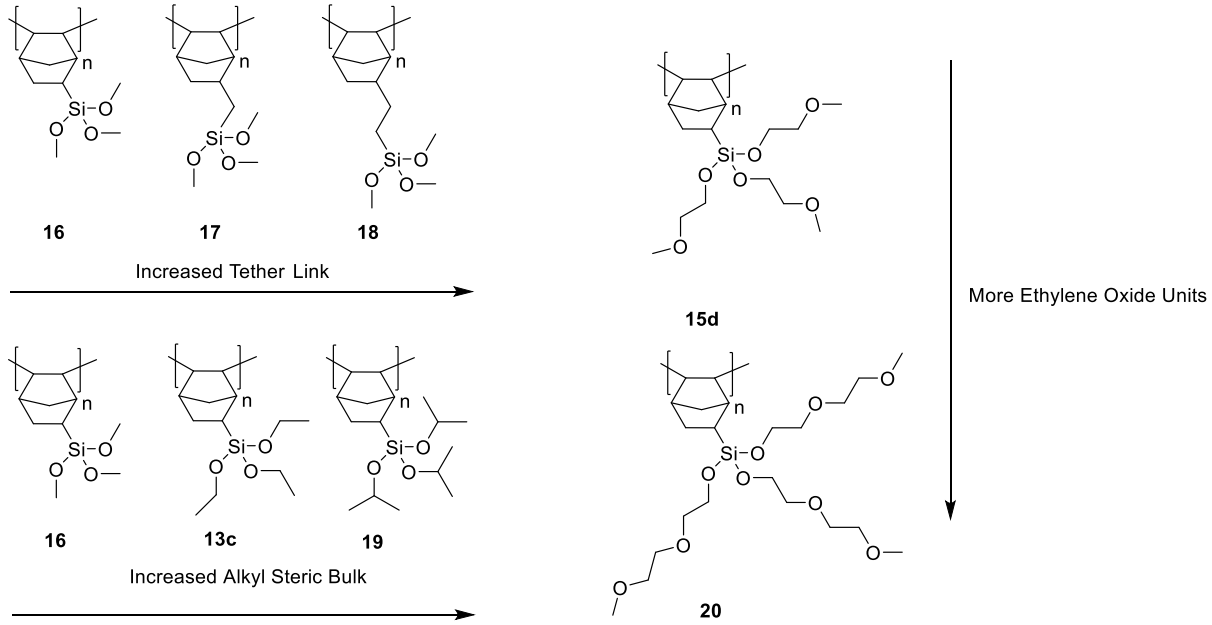

Figure 41. Future siloxanes targeted for implementation into vinyl-added polynorbornenes.

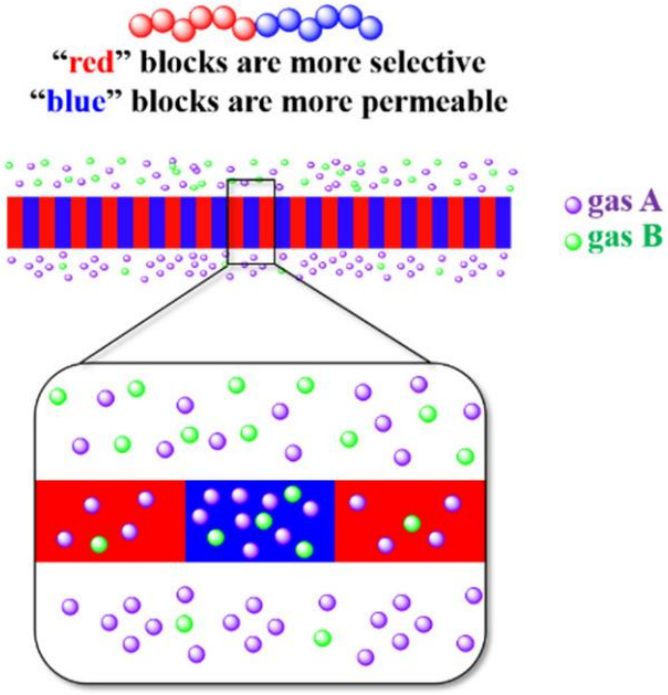

Figure 42. Scheme of proposed segmented block copolymers.

structures and different metal centers will continue in the pursuit of living vinyl-added polynorbornene polymers. In tandem with trying to achieve control of vinyl-addition polymerizations, the same approach can be applied to Ruthenium-based Grubbs catalysts that are well documented to perform living ROMP.[180] Also, given the inclusion of polar monomers will remain a theme for the development of CO_2/N_2 separation membranes, we expect that catalyst development will likely continue in parallel with the synthesis of new polymer membranes.

To end, we want to explore post-polymerization modifications to polymer structure and polymer films that we believe will increase membrane performance. In terms of polymer structure, groups such as tetrazoles, and amidoxime groups are known to have significant binding energies towards CO_2 and are excellent candidates for incorporation into vinyl-added polynorbornenes.[164,181] However, the abundance of nitrogen atoms in these groups make them incompatible with current vinyl-addition catalysts. Alternatively, a scheme for incorporating these types of functionalities in shown in **Figure 43**. Bromine-

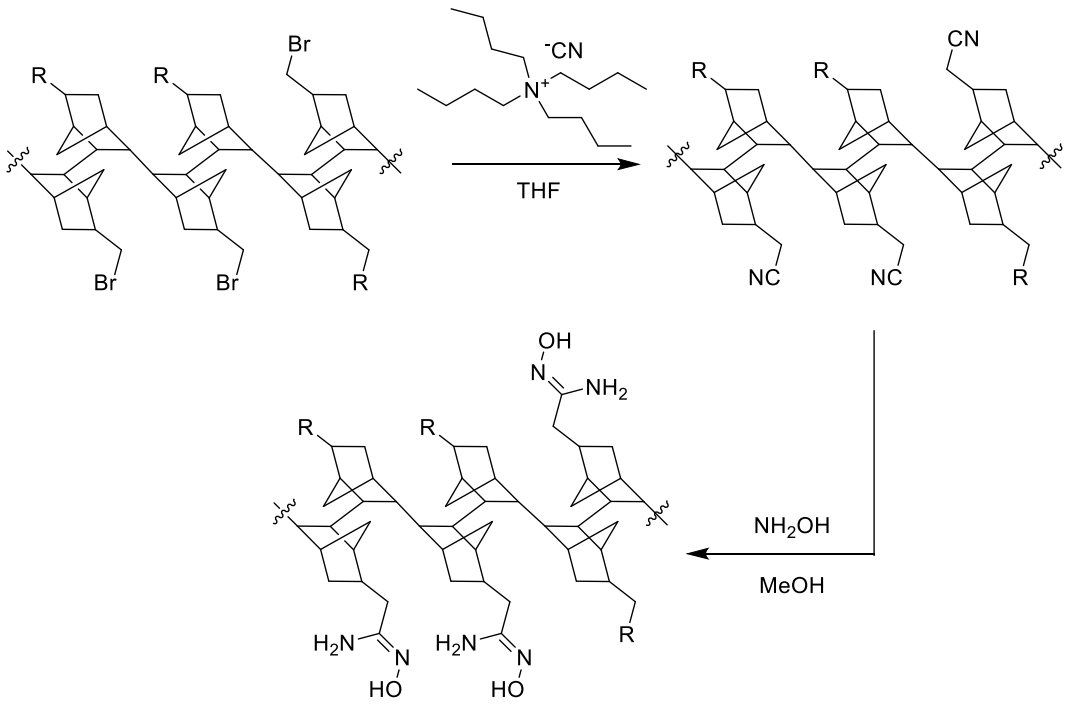

Figure 43. Scheme of proposed post-polymerization modifications to amidoxime functionality.

functionalized norbornene are compatible with *trans*-[Ni(C_6F_5)$_2$($SbPh_3$)$_2$] to produce VAPNBs with good leaving groups that can be combined with an appropriate nucleophile to yield the desired polymer structure. In terms of modifying film properties, we would like to explore polymer blends, using 3D printing to specifically organize the polymer chains, or utilize both organic and inorganic additives such as porous organic crystals and MOFs to introduce additional free volume elements in the polymer film. Overall, research in polymer membranes is a prosperous research avenue that has the potential to produce short-term solutions to reducing greenhouse gas emissions allowing us to consume fossil fuels responsibly.

References

1) Pandey, P.; Chauhan, R. S., "Membranes for gas separation." *Prog. Polym. Sci.* **2001,** *26*, 853-893.
2) Amjad, Z., "Reverse Osmosis: Membrane Technology, Water Chemistry, and Industrial Applications." Van Nostrand Reinhold: New York, 1993.
3) Perry, R. H.; Green, D. W., "Perry's Chemical Engineers' Handbook, 7th ed." McGraw-Hill: New York, 1997.
4) Baker, R. W., "Membrane Technology and Applications." John Wiley & Sons, Ltd.: Chichester, 2004.
5) Ronco, C.; Ghezzi, P. M.; Bowry, S. K., "Membranes for hemodialysis". Springer: Netherlands, 2004; pp 301-323.
6) Diban, N.; Stamatialis, D., "Polymeric hollow fiber membranes for bioartificial organs and tissue engineering applications." *J. Chem. Technol. Biotechnol.* **2014,** *89* (5), 633-643.
7) Scholes, C. A.; Stevens, G. W.; Kentish, S. E., "Membrane gas separation applications in natural gas processing." *Fuel* **2012,** *96*, 15-28.
8) Castle, W. F., "Air separation and liquefaction: recent developments and prospects for the beginning of the new millenium." *Int. J. Refrig.* **2002,** *25*, 158-172.
9) Gibson, J. A. A.; Mangano, E.; Shiko, E.; Greenaway, A. G.; Gromov, A. V.; Lozinska, M. M.; Friedrich, D.; Campbell, E. E. B.; Wright, P. A.; Brandani, S., "Adsorption Materials and Processes for Carbon Capture from Gas-Fired Power Plants: AMPGas." *Ind. Eng. Chem. Res.* **2016,** *55* (13), 3840-3851.
10) Kohl, A.; Nielson, R., "Gas Purification (5th ed.)." Gulf Publishing: Houston, TX, 1997.
11) Wijmans, J. G.; Baker, R. W., "The solution-diffusion model: a review." *J. Membr. Sci.* **1995,** *107*, 1-21.
12) Paul, D. R.; Paciotti, J. D.; Ebra-Lima, O. M., "Hydraulic permeation of liquids through swollen polymer networks." *J. Appl. Polym. Sci.* **1975,** *19*, 1837-1845.
13) Paul, D. R.; Paciotti, J. D., "Driving force for hydraulic and pervaporation transport in homogeneous membranes." *J. Polym. Sci., Polym. Phys. Ed.* **1975,** *13*, 1201-1214.
14) Czichos, H.; Saito, T.; Smith, L., "Springer Handbook of Materials Measurement Methods." Springer International Publishing: Berlin Heidelberg, 2006.
15) Robeson, L. M., "Correlation of separation factor versus permeability for polymeric membranes." *J. Membr. Sci.* **1991,** *92*, 168-185.
16) Robeson, L. M., "The upper bound revisited." *J. Membr. Sci.* **2008,** *320* (1-2), 390-400.
17) Budd, P.; McKeown, N.; Ghanem, B.; Msayib, K.; Fritsch, D.; Starannikova, L.; Belov, N.; Sanfirova, O.; Yampolskii, Y.; Shantarovich, V., "Gas permeation parameters and other physicochemical properties of a polymer of intrinsic microporosity: Polybenzodioxane PIM-1." *J. Membr. Sci.* **2008,** *325* (2), 851-860.
18) Budd, P.; Msayib, K.; Tattershall, C.; Ghanem, B.; Reynolds, K.; McKeown, N.; Fritsch, D., "Gas separation membranes from polymers of intrinsic microporosity." *J. Membr. Sci.* **2005,** *251* (1-2), 263-269.

19) Ma, Q.; Tipping, R. H., "The distribution of density matrices over potential-energy surfaces: Application to the calculation of the far-wing line shapes for CO_2." *J. Chem. Phys.* **1998,** *108*, 3386-3399.
20) Karl, T. R.; Trenberth, K. E., "Modern Global Climate Change." *Science* **2003,** *302* (5651), 1719-1723.
21) see http://www.eia.gov/electricity/monthly/epm_table_grapher.cfm?t=epmt_1_01
22) Study, M. I., "The Future of Coal - Options for a Carbon Constrained World." 2007.
23) see https://www.epa.gov/ghgemissions/overview-greenhouse-gases#overview
24) Feely, R. A., "State of the Climate in 2007." *Bulletin of the American Meteorological Society* **2008,** *89* (7), S58.
25) see https://www.esrl.noaa.gov/gmd/ccgg/trends/
26) see Chapter 8.3.2 of IPCC (2013)
27) see http://earthobservatory.nasa.gov/Features/WorldOfChange/decadaltemp.php
28) Feely, A. R.; Sabine, C. L.; Lee, K.; Berelson, W.; Kleypas, J.; Fabry, V. J.; Millero, F. J., "Impact of Anthropogenic CO_2 on the $CaCO_3$ System in the Oceans." *Science* **2004,** *305* (5682), 362-366.
29) Jacobson, M. Z., "Studying ocean acidification with conservative, stable numerical schemes for nonequilibrium air-ocean exchange and ocean equilibrium chemistry." *J. Geophys. Res.* **2005,** *110*, 1-17.
30) Albright, R.; Mason, B.; Miller, M.; Langdon, C., "Ocean acidification compromises recruitment success of the threatened Caribbean coral *Acropora palmata*." *Proc. Natl. Acad. Sci. USA* **2010,** *107* (47), 20400-20404.
31) Rossi, T.; Connell, S. D.; Nagelkerken, I., "Silent oceans: ocean acidification impoverishes natural soundscapes by altering sound production of the world's noisiest marine invertebrate." *Proceedings of the Royal Society B: Biological Sciences* **2016,** *283* (1826), 20153046/1-20153046/7.
32) Ross, P. M.; Parker, L.; O'Connor, W. A.; Bailey, E. A., "The impact of ocean acidification on reproduction, early development and settlement of marine organisms." *Water (Basel, Switz.)* **2011,** *3*, 1005-1030.
33) Zeebe, R. E., "History of seawater carbonate chemistry, atmospheric CO_2, and ocean acidification." *Annu. Rev. Earth Planet. Sci.* **2012,** *40*, 141-165.
34) Solomon, S.; Plattner, G. K.; Knutti, R.; Friedlingstein, R., "Irreversible climate change due to carbon dioxide emissions." *Proc. Natl. Acad. Sci. USA* **2009,** *106*, 1704-1709.
35) Liu, J.; Hou, X.; Park, H. B.; Lin, H., "High-Performance Polymers for Membrane CO_2/N_2 Separation." *Chemistry* **2016,** *22* (45), 15980-15990.
36) see https://www.epa.gov/cleanpowerplan/clean-power-plan-existing-power-plants
37) Current and Future Technologies for Power Generation with Post-Combustion Carbon Capture (DOE/NETL-2012/1557), National Energy Technology Laboratory 2012
38) Merkel, T. C.; Lin, H.; Wei, X.; Baker, R., "Power plant post-combustion carbon dioxide capture: An opportunity for membranes." *J. Membr. Sci.* **2010,** *359* (1-2), 126-139.

39) Lin, H.; Freeman, B. D., "Gas solubility, diffusivity and permeability in poly(ethylene oxide)." *J. Membr. Sci.* **2004,** *239* (1), 105-117.
40) Merkel, T. C.; Bondar, V.; Nagai, K.; Freeman, B. D.; Pinnau, I., "Gas Sorption, Diffusion, and Permeation in Poly(dimethylsiloxane)." *J. Polym. Sci., Part B: Polym. Phys.* **2000,** *38*, 415-434.
41) Ismail, A. F.; Khulbe, K.; Matsuura, T., "Gas Separation Membranes: Polymeric and Inorganic." Springer International Publishing: Switzerland, 2015.
42) Yampolskii, Y.; Starannikova, L.; Belov, N.; Bermeshev, M.; Gringolts, M.; Finkelshtein, E., "Solubility controlled permeation of hydrocarbons: New membrane materials and results." *J. Membr. Sci.* **2014,** *453*, 532-545.
43) Finkelshtein, E. S.; Bermeshev, M. V.; Gringolts, M. L.; Starannikova, L. E.; Yampolskii, Y. P., "Substituted polynorbornenes as promising materials for gas separation membranes." *Russ. Chem. Rev.* **2011,** *80* (4), 341-361.
44) Bermeshev, M. V.; Syromolotov, A. V.; Gringolts, M. L.; Starannikova, L. E.; Yampolskii, Y. P.; Finkelshtein, E. S., "Synthesis of High Molecular Weight Poly[3-{tris(trimethylsiloxy)silyl}tricyclononenes-7] and Their Gas Permeation Properties." *Macromolecules (Washington, DC, U. S.)* **2011,** *44* (17), 6637-6640.
45) Starannikova, L.; Pilipenko, M.; Belov, N.; Yampolskii, Y.; Gringolts, M.; Finkelshtein, E., "Addition-type polynorbornene with $Si(CH_3)_3$ side groups: Detailed study of gas permeation and thermodynamic properties." *J. Membr. Sci.* **2008,** *323* (1), 134-143.
46) Finkelshtein, E. S.; Makovetskii, K. L.; Gringolts, M. L.; Rogan, Y. V.; Golenko, T. G.; Starannikova, L. E.; Yampolskii, Y. P.; Shantarovich, V. P.; Suzuki, T., "Addition-Type Polynorbornenes with $Si(CH_3)_3$ Side Groups: Synthesis, Gas Permeability, and Free Volume." *Macromolecules (Washington, DC, U. S.)* **2006,** *39*, 7022-7029.
47) Sanders, D. P., "Advances in patterning materials for 193 nm immersion lithography." *Chem. Rev.* **2010,** *110* (1), 321-360.
48) Brown, R. S., "The influence of remote substituents upon ionization potential. Part I. The effect of two allylic oxygens upon the ionization of the pi-bond." *Can. J. Chem.* **1975,** *54*, 805-812.
49) Pasquale, A. J.; Long, T. E.; Truong, H.; Allen, R. D., "Investigations of the Adhesion of Maleic Anhydride/Cyclic Olefin Alternating Copolymers to Silicon Substrates: Improved Materials for 193 nm Lithography." *J. Adhesion* **2002,** *78* (1), 1-13.
50) Janiak, C.; Lassahn, P., "Metal Catalysts for the Vinyl Polymerization of Norbornene." *J. Mol. Catal.* **2001,** *166*, 193-209.
51) Houlihan, F. M.; Wallow, T. I.; Nalamasu, O.; Reichmanis, E., "Synthesis of Cycloolefin-Maleic Anhydride Alternating Copolymers for 193 nm Imaging." *Macromolecules* **1997,** *30*, 6517-6524.
52) Jung, C. H.; Lee, J. E.; Han, S. H.; Park, H. B.; Lee, Y. M., "Highly permeable and selective poly(benzoxazole-co-imide) membranes for gas separation." *J. Membrane Sci.* **2010,** *350* (1-2), 301-309.

53) Vargas, J.; Martínez, A.; Santiago, A. A.; Tlenkopatchev, M. A.; Aguilar-Vega, M., "Synthesis and gas permeability of new polynorbornene dicarboximide with fluorine pendant groups." *Polymer* **2007,** *48* (22), 6546-6553.
54) Raharjo, R. D.; Lee, H. J.; Freeman, B. D.; Sakaguchi, T.; Masuda, T., "Pure gas and vapor permeation properties of poly[1-phenyl-2-[p-(trimethylsilyl)phenyl]acetylene] (PTMSDPA) and its desilylated analog, poly[diphenylacetylene] (PDPA)." *Polymer* **2005,** *46* (17), 6316-6324.
55) Dai, Y.; Guiver, M. D.; Robertson, G. P.; Bilodeau, F.; Kang, Y. S.; Lee, K. J.; Jho, J. Y.; Won, J., "Modified Polysulfones 5: synthesis and characterization of tetramethyl polysulfones containing trimethylsilyl groups and their gas transport properties." *Polymer* **2002,** *43*, 5369-5378.
56) Bondar, V. I.; Kukharskii, Y. M.; Yampol'Skii, Y. P.; Finkelshtein, E. S.; Makovetskii, K. L., "Permeation and Sorption in Polynorbornenes with Organosilicon Substituents." *J. Poly. Sci. Part B: Polym. Phys.* **1993,** *31*, 1273-1283.
57) Ichiraku, Y.; Stern, S. A., "An Investigation of the High Gas Permeability of Poly (1-trimethylsilyl-1-propyne)." *J. Membrane Sci.* **1987,** *34*, 5-18.
58) Yamamoto, D.; Matsumoto, A., "Controlled Radical Polymerization of 3-Methylenecyclopentene with *N*-Substituted Maleimides To Yield Highly Alternating and Regiospecific Copolymers." *Macromolecules* **2013,** *46* (24), 9526-9536.
59) Hisano, M.; Takeda, K.; Takashima, T.; Jin, Z.; Shiibashi, A.; Matsumoto, A., "Sequence-Controlled Radical Copolymerization of N-Substituted Maleimides with Olefins and Polyisobutene Macromonomers To Fabricate Thermally Stable and Transparent Maleimide Copolymers with Tunable Glass Transition Temperatures and Viscoelastic Properties." *Macromolecules* **2013,** *46* (19), 7733-7744.
60) Lutz, J. F.; Schmidt, B. V.; Pfeifer, S., "Tailored polymer microstructures prepared by atom transfer radical copolymerization of styrene and *N*-substituted maleimides." *Macromol. Rapid Commun.* **2011,** *32* (2), 127-135.
61) Zhao, C.; Dong, J.; Li, S.; Fan, Z., "Synthesis and characterization of heat-resistant N-phenylmaleimide-styrene-maleic anhydride copolymers and application in acrylonitrile-butadiene-styrene resin." *J. Appl. Polym. Sci.* **2012,** *126* (1), 169-178.
62) Hill, D. J. T.; Shao, L. Y.; Pomery, P. J.; Whittaker, A. K., "The radical homopolymerization of *N*-phenylmaleimide, *N*-*n*-hexylmaleimide, and *N*-cyclohexylmaleimide in tetrahydrofuran." *Polymer* **2001,** *42*, 4791-4802.
63) Li, A.; Lu, J., "Controlled/living RAFT polymerization of *N*-phenyl maleimide and synthesis of its block copolymers." *J. Appl. Polym. Sci.* **2009,** *114* (4), 2469-2473.
64) Wang, H.; Wei, J.; Jiang, X.; Yin, J., "Novel polymerizable *N*-aromatic maleimides as free radical initiators for photopolymerization." *Polym. Int.* **2006,** *55* (8), 930-937.
65) Chen, G.-Q.; Wu, Z.-Q.; Wu, J.-R.; Li, Z.-C.; Li, F.-M., "Synthesis of Alternating Copolymers of N-Substituted Maleimides with Styrene via Atom Transfer Radical Polymerization." *Macromolecules* **2000,** *33*, 232-234.
66) Roy, R. K.; Lutz, J. F., "Compartmentalization of single polymer chains by stepwise intramolecular cross-linking of sequence-controlled macromolecules." *J. Am. Chem. Soc.* **2014,** *136* (37), 12888-12891.

67) Srichan, S.; Mutlu, H.; Lutz, J.-F., "On the synthesis of sequence-controlled poly(vinyl benzyl amine-co-N-substituted maleimides) copolymers." *Eur. Polym. J.* **2015,** *62*, 338-346.
68) Matsumoto, A.; Kubota, T.; Otsu, T., "Radical Polymerization of *N*-(Alkyl-substituted phenyl)maleimides: Synthesis of Thermally Stable Polymers Soluble in Nonpolar Solvents." *Macromolecules (Washington, DC, U. S.)* **1990,** *23*, 4508-4513.
69) Pasquale, A. J.; Allen, R. D.; Long, T. E., "Fundamental Investigations of the Free Radical Copolymerization and Terpolymerization of Maleic Anhydride, Norbornene, and Norbornene *tert*-Butyl Ester: *In-Situ* Mid-Infrared Spectroscopic Analysis." *Macromolecules (Washington, DC, U. S.)* **2001,** *34*, 8064-8071.
70) Cousinet, S.; Ghadban, A.; Allaoua, I.; Lortie, F.; Portinha, D.; Drockenmuller, E.; Pascault, J.-P., "Biobased vinyl levulinate as styrene replacement for unsaturated polyester resins." *J. Polym. Sci. Part A: Polym. Chem.* **2014,** *52* (23), 3356-3364.
71) Jaacks, V., "A Novel Method of Determination of Reactivity Ratios in Binary and Ternary Copolymerizations." *Die Makromolekulare Chemie* **1972**, 161-172.
72) Pasquale, A. J.; Long, T. E., "Real-time Monitoring of the Stable Free Radical Polymerization of Styrene via in-Situ Mid-Infrared Spectroscopy." *Macromolecules (Washington, DC, U. S.)* **1999,** *32*, 7954-7957.
73) Cincu, C.; Chatzopoulos, F.; Montheard, J.-P., "Alternating copolymers: maleic anhydride with cyclic olefins. Influence of the cyclic olefin on the copolymerization process and properties of the copolymers." *Macromol. Rep.* **1996,** *33* (2), 83-91.
74) Wu, D.-C.; Hong, C.-Y.; Pan, C.-Y.; He, W.-D., "Study on controlled radical alternating copolymerization of styrene with maleic anhydride under UV irradiation." *Polym. Int.* **2003,** *52* (1), 98-103.
75) Pasquale, A. J.; Long, T. E., "Determination of Monomer Reactivity Ratios Using In situ FTIR Spectroscopy for Maleic Anhydride/Norbornene-Free-Radical Copolymerization." *J. Appl. Polym. Sci.* **2004,** *92*, 3240-3246.
76) Mayo, F. R.; Lewis, F. M., "A Basis for Comparing the Behavior of Monomers in Copolymerization; The Copolymerization of Styrene and Methyl Methacrylate." *J. Am. Chem. Soc.* **1944,** *66* (9), 1594-1601.
77) Mazo, L. D.; Ezrielev, A. I.; Roskin, E. S., "Reactivity ratios of acrylonitrile copolymerization with bicyclo[2.2.1.]hept-5-ene-2,3-dicarboxylic acid and its anhydride in different solvents and in bulk." *Vysokomol. Soedin., Ser. B* **1968,** *10* (8), 615-619.
78) Morton Fineman; Ross, S. D., "Linear Method for determining monomer reactivity ratios in copolymerization." *J. Poly. Sci.* **1950,** *5* (2), 259-262.
79) Floyd, S., "A Theoretical Interpretation of Reactivity Ratio Products in Copolymers Formed from Two Fractions Differing in Composition." *J. Appl. Polym. Sci.* **1987,** *34*, 2559-2574.
80) Higashimura, T.; Masuda, T.; O'Driscoll, K. F., "Index of copolymerizability." *J. Polym. Sci. Part C: Pol. Lett.* **1968,** *6*, 841-847.
81) Sanders, D. F.; Smith, Z. P.; Ribeiro, C. P.; Guo, R.; McGrath, J. E.; Paul, D. R.; Freeman, B. D., "Gas permeability, diffusivity, and free volume of thermally rearranged polymers based on 3,3′-dihydroxy-4,4′-diamino-biphenyl (HAB) and 2,2′-bis-(3,4-

dicarboxyphenyl) hexafluoropropane dianhydride (6FDA)." *J. Membr. Sci.* **2012,** *409-410*, 232-241.
82) Buller, F.; Mannocci, L.; Zhang, Y.; Dumelin, C. E.; Scheuermann, J.; Neri, D., "Design and synthesis of a novel DNA-encoded chemical library using Diels-Alder cycloadditions." *Bioorg. Med. Chem. Lett.* **2008,** *18* (22), 5926-5931.
83) Deka, N.; Mariotte, A.-M.; Boumendjel, A., "Microwave mediated solvent-free acetylation of deactivated and hindered phenols." *Green Chem.* **2001,** *3* (5), 263-264.
84) Metz, B.; Davidson, O.; Coninck, D.; Loos, M.; Meyer, L., "*IPCC*, Cambridge Uniersity Press: Cambridge, 2005.
85) Alivisatos, P.; M., B., "Basic Research Needs for Carbon Capture: Beyond 2020". 2010; pp 4-5.
86) see http://www1.eere.energy.gov/manufacturing/industries_technologies/imf/pdfs/separationsreport.pdf
87) Freeman, B. D., "Basis of Permeability/Selectivity Tradeoff Relations in Polymeric Gas Separation Membranes." *Macromolecules (Washington, DC, U. S.)* **1999,** *32* (2), 375-380.
88) Mizumoto, T.; Masuda, T.; Higashimura, T., "Polymerization of [o-(Trimethylgermyl)phenyl]acetylene and Polymer Characterization." *J. Polym. Sci., Part A: Polym. Chem.* **1993,** *31*, 2555-2561.
89) Thomas, S.; Pinnau, I.; Du, N. Y.; Guiver, M. D., "Pure- and mixed-gas permeation properties of a microporous spirobisindane-based ladder polymer (PIM-1)." *J. Membr. Sci.* **2009,** *333*, 125-131.
90) Staiger, C. L.; Pas, S. J.; Hill, A. J.; Cornelius, C. J., "Gas Separation, Free Volume Distribution, and Physical Aging of a Highly Microporous Spirobisindane Polymer." *Chem. Mater.* **2008,** *20* (8), 2606-2608.
91) Nagai, K.; Masuda, T.; Nakagawa, T.; Freeman, B. D.; Pinnau, I., "Poly[1-(trimethylsilyl)-1-propyne] and related polymers: synthesis, properties, and functions." *Prog. Polym. Sci.* **2001,** *26*, 721-798.
92) Stern, S. A.; Shah, V. M.; Hardy, B. J., "Structure-permeability relationships in silicone polymers." *J. Polym. Sci., Part B: Polym. Phys.* **1987,** *25* (6), 1263-1298.
93) Shah, V. M.; Hardy, B. J.; Stern, S. A., "Solubility of carbon dioxide, methane, and propane in silicone polymers." *J. Polym. Sci., Part B: Polym. Phys.* **1993,** *31* (3), 313-317.
94) Bélanger, M.-C.; Marois, Y., "Hemocompatibility, biocompatibility, inflammatory and *in vivo* studies of primary reference materials low-density polyethylene and polydimethylsiloxane: A review." *J. Biomed. Mater. Res., Part A* **2001,** *58* (5), 467-477.
95) Nakagawa, T.; Nishimura, T.; Higuchi, A., "Morphology and gas permeability in copolyimides containing polydimethylsiloxane block." *J. Membr. Sci.* **2002,** *206*, 149-163.
96) Jullok, N.; Martínez, R.; Wouters, C.; Luis, P.; Teresa Sanz, M.; Van der Bruggen, B., "A Biologically Inspired Hydrophobic Membrane for Application in Pervaporation." *Langmuir* **2013,** *29* (5), 1510-1516.

97) Jia, M.-D.; Pleinemann, K.-V.; Behling, R.-D., "Preparation and characterization of thin-film zeolite-PDMS composite membranes." *J. Membr. Sci.* **1992,** *73*, 119-128.
98) Tsujita, Y.; Yoshimura, K.; Yoshimizu, H.; Takizawa, A.; Kinoshita, T., "Structure and gas permeability of siloxane-imide block copolymer membranes: 1. Effect of siloxane content." *Polymer* **1993,** *34* (12), 2597-2601.
99) Smaihi, M.; Schrotter, J.-C.; Lesimple, C.; Prevost, I.; Guizard, C., "Gas separation properties of hybrid imide-siloxane copolymers with various silica contents." *J. Membr. Sci.* **1999,** *161*, 157-170.
100) Sadrzadeh, M.; Shahidi, K.; Mohammadi, T., "Effect of operating parameters on pure and mixed gas permeation properties of a synthesized composite PDMS/PA membrane." *J. Membr. Sci.* **2009,** *342*, 327-340.
101) Berean, K.; Zhen Ou, J.; Nour, M.; Latham, K.; McSweeney, C.; Paull, D.; Halim, A.; Kentish, S.; Doherty, C. M.; Hill, A. J.; Kalantar-zadeh, K., "The effect of crosslinking temperature on the permeability of PDMS membranes: Evidence of extraordinary CO_2 and CH_4 gas permeation." *Sep. Purif. Technol.* **2014,** *122*, 96-104.
102) Ghosal, K.; Freeman, B. D., "Gas separation using polymer membranes: an overview." *Polym. Adv. Technol.* **1994,** *5* (11), 673-697.
103) Freeman, B. D.; Pinnau, I., "Separation of gases using solubility-selective polymers." *Trends Polym. Sci. (Cambridge, U. K.)* **1997,** *5* (5), 167-173.
104) Amouroux, N.; Léger, L., "Effect of Dangling Chains on Adhesion Hysteresis of Silicone Elastomers, Probed by JKR Test." *Langmuir* **2003,** *19* (4), 1396-1401.
105) Perutz, S.; Kramer, E.; Baney, J.; Hui, C.-Y., "Adhesion Between Hydrolyzed Surfaces of Poly(dimethylsiloxane) Networks." *Macromolecules* **1997,** *30* (25), 7964-7969.
106) Stafie, N.; Stamatialis, D. F.; Wessling, M., "Effect of PDMS cross-linking degree on the permeation performance of PAN/PDMS composite nanofiltration membranes." *Sep. Purif. Technol.* **2005,** *45* (3), 220-231.
107) Esteves, A. C. C.; Brokken-Zijp, J.; Laven, J.; Huinink, H. P.; Reuvers, N. J. W.; Van, M. P.; de With, G., "Influence of cross-linker concentration on the cross-linking of PDMS and the network structures formed." *Polymer* **2009,** *50* (16), 3955-3966.
108) Nguyen, Q. T.; Bendjama, Z.; Clément, R.; Ping, Z., "Poly(dimethylsiloxane) crosslinked in different conditions. Part II. Pervaporation of water-ethyl acetate mixtures." *Phys. Chem. Chem. Phys.* **2000,** *2*, 395-400.
109) Choi, S.-H.; Kim, J.-H.; Lee, S.-B., "Sorption and permeation behaviors of a series of olefins and nitrogen through PDMS membranes." *J. Membr. Sci.* **2007,** *299* (1-2), 54-62.
110) Rao, H.-X.; Liu, F.-N.; Zhang, Z.-Y., "Preparation and oxygen/nitrogen permeability of PDMS crosslinked membrane and PDMS/tetraethoxysilicone hybrid membrane." *J. Membr. Sci.* **2007,** *303* (1-2), 132-139.
111) Lue, S. J.; Tsai, C. L.; Lee, D.-T.; Mahesh, K. P. O.; Hua, M. Y.; Hu, C.-C.; Jean, Y. C.; Lee, K.-R.; Lai, J.-Y., "Sorption, diffusion, and perm-selectivity of toluene vapor/nitrogen mixtures through polydimethylsiloxane membranes with two cross-linker densities." *J. Membr. Sci.* **2010,** *349* (1-2), 321-332.

112) Tin, P. S.; Chung, T. S.; Liu, Y.; Wang, R.; Liu, S. L.; Pramoda, K. P., "Effects of cross-linking modification on gas separation performance of Matrimid membranes." *J. Membr. Sci.* **2003,** *225* (1-2), 77-90.
113) Lin, H.; Kai, T.; Freeman, B. D.; Kalakkunnath, S.; Kalika, D. S., "The Effect of Cross-Linking on Gas Permeability in Cross-Linked Poly(Ethylene Glycol Diacrylate)." *Macromolecules (Washington, DC, U. S.)* **2005,** *38*, 8381-8393.
114) Wind, J. D.; Staudt-Bickel, C.; Paul, D. R.; Koros, W. J., "The Effects of Crosslinking Chemistry on CO_2 Plasticization of Polyimide Gas Separation Membranes." *Ind. Eng. Chem. Res.* **2002,** *41* (24), 6139-6148.
115) Li, S.-Y.; Srivastava, R.; Parnas, R. S., "Separation of 1-butanol by pervaporation using a novel tri-layer PDMS composite membrane." *J. Membr. Sci.* **2010,** *363* (1-2), 287-294.
116) Tao, S. J., "Positronium Annihilation in Molecular Substances." *J. Chem. Phys.* **1972,** *56* (11), 5499-5510.
117) Eldrup, M., "The temperature dependence of positron lifetimes in solid pivalic acid." *Chem. Phys.* **1981,** *63*, 51-58.
118) Seeger, A., "The study of defects in crystals by positron annihilation." *Appl. Phys. A: Mater. Sci. Process.* **1974,** *4* (3), 183-199.
119) Schroeder, M. J.; Roland, C. M., "Segmental Relaxation in End-Linked Poly(dimethylsiloxane) Networks." *Macromolecules (Washington, DC, U. S.)* **2002,** *35*, 2676-2681.
120) Roland, C. M., "Constraints on Local Segmental Motion in Poly(vinylethylene) Networks." *Macromolecules (Washington, DC, U. S.)* **1994,** *27* (15), 4242-4247.
121) see http://www3.epa.gov/climatechange/ghgemissions/inventoryexplorer/#allsectors/allgas/gas/current
122) Hong, T.; Zhenbin, N.; Xunxiang, H.; Gmernicki, K.; Cheng, S.; Fan, F.; Johnson, C.; Hong, E.; Mahurin, S. M.; Jiang, D.-e.; Long, B.; Mays, J.; Sokolov, A.; Saito, T., "Effect of Cross-Link Density on Carbon Dioxide Separation in Polydimethylsiloxane-Norbornene Membranes." *ChemSusChem* **2015,** *8* (21), 3524.
123) Mark, J. E., "Some Interesting Things About Polysiloxanes." *Acc. Chem. Res.* **2004,** *37* (12), 946-953.
124) Merkel, T. C.; Gupta, R. P.; Turk, B. S.; Freeman, B. D., "Mixed-gas permeation of syngas components in poly(dimethylsiloxane) and poly(1-trimethylsilyl-1-propyne) at elevated temperatures." *J. Membr. Sci.* **2001,** *191*, 85-94.
125) Grove, N. R.; Kohl, P. A.; Allen, S. A. B.; Jayaraman, S.; Shick, R., "Functionalized Polynorbornene Dielectric Polymers: Adhesion and Mechanical Properties." *J. Polym. Sci., Part B: Polym. Phys.* **1999,** *37*, 3003-3010.
126) Tetsuka, H.; Hagiwara, M.; Kaita, S., "Addition-type poly(norbornene)s with siloxane substituents: synthesis, properties and nanoporous membrane." *Polym. J. (Singapore)* **2010,** *43* (1), 97-100.
127) Tetsuka, H.; Isobe, K.; Hagiwara, M., "Synthesis and Properties of Addition-Type Poly(norbornene)s with Siloxane Substituents." *Polymer Journal* **2009,** *41* (8), 643-649.

128) Blank, F.; Janiak, C., "Metal catalysts for the vinyl/addition polymerization of norbornene." *Coord. Chem. Rev.* **2009,** *253* (7-8), 827-861.
129) Walter, M. D.; Moorhouse, R. A.; White, P. S.; Brookhart, M., "Vinyl addition polymerization of norbornene with cationic (allyl) Ni catalysts: Mechanistic insights and characterization of first insertion products." *J. Polym. Sci., Part A: Polym. Chem.* **2009,** *47* (10), 2560-2573.
130) Reinmuth, A.; Mathew, J. P.; Melia, J.; Risse, W., "(n^3-Allyl)palladium(II) catalysts for the addition polymerization of norbornene derivatives with functional groups." *Macromol. Rapid Commun.* **1996,** *17*, 173-180.
131) Huffman, J. C., "Addition Polymerization of Norbornene-Type Monomers. High Activity Cationic Allyl Palladium Catalysts." *Macromolecules (Washington, DC, U. S.)* **2002,** *35*, 8969-8977.
132) Martínez-Arranz, S.; Albéniz, A. C.; Espinet, P., "Versatile Route to Functionalized Vinylic Addition Polynorbornenes." *Macromolecules* **2010,** *43* (18), 7482-7487.
133) Casares, J. A.; Espinet, P.; Martín-Alvarez, J. M.; Martínez-Ilarduya, J. M.; Salas, G., "Stable Nickel Catalysts for Fast Norbornene Polymerization: Tuning Reactivity." *Eur. J. Inorg. Chem.* **2005,** *2005* (19), 3825-3831.
134) Tao, W. J.; Nakano, R.; Ito, S.; Nozaki, K., "Copolymerization of Ethylene and Polar Monomers by Using Ni/IzQO Catalysts." *Angew. Chem., Int. Ed. Engl.* **2016,** *55* (8), 2835-9.
135) Commarieu, B.; Claverie, J. P., "Bypassing the lack of reactivity of endo-substituted norbornenes with the catalytic rectification–insertion mechanism." *Chem. Sci.* **2015,** *6* (4), 2172-2181.
136) Bondi, A., "van der Waals Volume and Radii." *J. Phys. Chem.* **1964,** *68* (3), 441-451.
137) Klug, H. D.; Alexander, L. E., "X-ray diffraction procedures for polycrystalline and amorphous materials." Wiley: New York, 1964.
138) Tena, A.; Marcos-Fernández, Á.; de la Viuda, M.; Palacio, L.; Prádanos, P.; Lozano, Á. E.; de Abajo, J.; Hernández, A., "Advances in the design of co-poly(ether-imide) membranes for CO_2 separations. Influence of aromatic rigidity on crystallinity, phase segregation and gas transport." *Eur. Polym. J.* **2015,** *62*, 130-138.
139) Robb, W. L., "Thin Silicone Membranes-Their Membranes Permeation Properties and Some Applications." *Ann. N. Y. Acad. Sci.* **1968,** *146*, 119-137.
140) Henley, E. J., "Permeation of vapors through polymers at low temperature and elevated pressures." *AIChE J.* **1967,** *13* (6), 1117-1119.
141) Pinnau, I.; Toy, L. G., "Transport of organic vapors through poly(1-trimethylsilyl-1-propyne)." *J. Membr. Sci.* **1996,** *116* (2), 199-209.
142) Bermeshev, M. V.; Syromolotov, A. V.; Starannikova, L. E.; Gringolts, M. L.; Lakhtin, V. G.; Yampolskii, Y. P.; Finkelshtein, E. S., "Glassy Polynorbornenes with Si–O–Si Containing Side Groups. Novel Materials for Hydrocarbon Membrane Separation." *Macromolecules (Washington, DC, U. S.)* **2013,** *46* (22), 8973-8979.

143) Barashkova, I. I.; Bermeshev, M. V.; Wasserman, A. M.; Yampolskii, Y. P., "Mobility of the spin probe TEMPO in glassy metathesis polymers with substituents containing flexible Si-O-Si groups." *Polym. Sci., Ser. A* **2015,** *57* (3), 279-284.
144) Vaughn, J. T.; Harrigan, D. J.; Sundell, B.; Lawrence, J. A.; Yang, J., "Reverse selective glassy polymers for C_{3+} hydrocarbon recovery from natural gas." *J. Membr. Sci.* **2017,** *522*, 68-76.
145) Sundell, B.; Lawrence, J. A.; Harrigan, D. J.; Vaughn, J. T.; Pilyugina, T. S.; Smith, D. R., "Alkoxy Functionalized Polynorbornenes with Enhanced Selectivity for Heavy Hydrocarbon Separations." *RSC Adv.* **2016,** *6* (57), 51619-51628.
146) Gmernicki, K. R.; Hong, E.; Maroon, C. R.; Mahurin, S. M.; Sokolov, A.; Saito, T.; Long, B. K., "Correction to Accessing Siloxane Functionalized Polynorbornenes via Vinyl-Addition Polymerization for CO_2 Separation Membranes." *ACS Macro Lett.* **2017,** *6* (1), 41.
147) Reitlinger, S. A.; Maslennikova, A. A.; Yarkho, I. S., "Gas permeability of organosiloxane rubbers." *Zh. Tech. Fiz.* **1956,** *26*, 2553-2557.
148) Stern, S. A.; Shah, V. M.; Hardy, B. J., "Structure - permeability relationship in silicone polymers." *J. Polym. Sci., Part B: Polym. Phys.* **1987,** *25*, 1263-1298.
149) Aoki, T., "Macromolecular design of permselective membranes." *Prog. Polym. Sci.* **1999,** *24*, 951-993.
150) Chapala, P. P.; Bermeshev, M. V.; Starannikova, L. E.; Belov, N. A.; Ryzhikh, V. E.; Shantarovich, V. P.; Lakhtin, V. G.; Gavrilova, N. N.; Yampolskii, Y. P.; Finkelshtein, E. S., "A Novel, Highly Gas-Permeable Polymer Representing a New Class of Silicon-Containing Polynorbornens As Efficient Membrane Materials." *Macromolecules (Washington, DC, U. S.)* **2015,** *48* (22), 8055-8061.
151) Yampolskii, Y.; Shantarovich, V., "Chapter 6. Positron Annihilation Lifetime Spectroscopy and Other Methods for Free Volume Evaluation in Polymers". *Materials Science of Membranes for Gas and Vapor Separation*, Yampolskii, Y.; Pinnau, I.; Freeman, B. D., Eds. John Wiley & Sons: Chichester, UK, 2006.
152) Hughes, D. J.; Roussenova, M. V.; Beavis, P.; Swain, A. C.; Alam, M. A., "Positron lifetime study of poly(dimethylsiloxane) based polymer-nanoparticle composites." *J. Phys.: Conf. Series* **2013,** *443* (1), 012045.
153) Nagel, C.; Guenther-Schade, K.; Fritsch, D.; Strunskus, T.; Faupel, F., "Free volume and transport properties in highly selective polymer membranes." *Macromolecules (Washington, DC, U. S.)* **2002,** *35*, 2071-2077.
154) Belov, N.; Nizhegorodova, Y.; Bermeshev, M.; Yampolskii, Y., "Detailed study of the gas permeation parameters of a glassy poly(tricyclononene) with Si–O–Si side groups." *J. Membr. Sci.* **2015,** *483*, 136-143.
155) Gmernicki, K. R.; Hong, E.; Maroon, C. R.; Mahurin, S. M.; Sokolov, A. P.; Saito, T.; Long, B. K., "Accessing Siloxane Functionalized Polynorbornenes via Vinyl-Addition Polymerization for CO_2 Separation Membranes." *ACS Macro Lett.* **2016,** *5* (7), 879-883.
156) Teplyakov, V.; Meares, P., "Correlation aspects of the selective gas permeabilities of polymeric materials and membranes." *Gas Sep. Purif.* **1990,** *4* (2), 66-74.

157) Pixton, M. R.; Paul, D. R., "Relationship between structure and transport properties for polymers with aromatic backbones". *Polymeric Gas Separation Membranes*, Paul, D. R.; Yampolskii, Y., Eds. CRC Press: Boca Raton, 1994; pp 83-154.
158) Kawakami, Y.; Imae, I., "Functionality and stereochemical design of silicon-containing polymers." *Macromol. Chem. Phys.* **1999,** *200* (6), 1245-1256.
159) Katsumata, T.; Shiotsuki, M.; Sanda, F.; Masuda, T., "Synthesis and properties of polynorbornenes bearing oligomeric siloxane pendant groups." *Polymer* **2009,** *50* (6), 1389-1394.
160) Mei Wu, X.; Gen Zhang, Q.; Ju Lin, P.; Qu, Y.; Mei Zhu, A.; Lin Liu, Q., "Towards enhanced CO_2 selectivity of the PIM-1 membrane by blending with polyethylene glycol." *J. Membr. Sci.* **2015,** *493*, 147-155.
161) Tocci, E.; De Lorenzo, L.; Bernardo, P.; Clarizia, G.; Bazzarelli, F.; McKeown, N. B.; Carta, M.; Malpass-Evans, R.; Friess, K.; Pilnáček, K.; Lanč, M.; Yampolskii, Y. P.; Straranníkova, L.; Shantarovich, V.; Mauri, M.; Jansen, J. C., "Molecular Modeling and Gas Permeation Properties of a Polymer of Intrinsic Microporosity Composed of Ethanoanthracene and Tröger's Base Units." *Macromolecules* **2014,** *47* (22), 7900-7916.
162) Carta, M.; Malpass-Evans, R.; Croad, M.; Rogan, Y.; Jansen, J. C.; Bernardo, P.; Bazzarelli, F.; McKeown, N. B., "An Efficient Polymer Molecular Sieve for Membrane Gas Separations." *Science* **2013,** *339*, 303-307.
163) Du, N.; Park, H. B.; Robertson, G. P.; Dal-Cin, M. M.; Visser, T.; Scoles, L.; Guiver, M. D., "Polymer nanosieve membranes for CO_2-capture applications." *Nat Mater* **2011,** *10* (5), 372-5.
164) Du, N.; Robertson, G. P.; Dal-Cin, M. M.; Scoles, L.; Guiver, M. D., "Polymers of intrinsic microporosity (PIMs) substituted with methyl tetrazole." *Polymer* **2012,** *53* (20), 4367-4372.
165) Fritsch, D.; Bengtson, G.; Carta, M.; McKeown, N. B., "Synthesis and Gas Permeation Properties of Spirobischromane-Based Polymers of Intrinsic Microporosity." *Macromol. Chem. Phys.* **2011,** *212* (11), 1137-1146.
166) Du, N.; Robertson, G. P.; Song, J.; Pinnau, I.; Thomas, S.; Guiver, M. D., "Polymers of Intrinsic Microporosity Containing Trifluoromethyl and Phenylsulfone Groups as Materials for Membrane Gas Separation." *Macromolecules* **2008,** *41*, 9656-9662.
167) Ghanem, B. S.; McKeown, N. B.; Budd, P. M.; Al-Harbi, N. M.; Fritsch, D.; Heinrich, K.; Starannikova, L.; Tokarev, A.; Yampolskii, Y., "Synthesis, Characterization, and Gas Permeation Properties of a Novel Group of Polymers with Intrinsic Microporosity: PIM-Polyimides." *Macromolecules* **2009,** *42* (20), 7881-7888.
168) Morisato, A.; Shen, H. C.; Sankar, S. S.; Freeman, B. D.; Pinnau, I.; Casillas, C. G., "Polymer Characterization and Gas Permeability of Poly(1-trimethylsilyl-1-propyne) [PTMSP], Poly(1-phenyl-1-propyne) [PPP], and PTMSP/PPP Blends." *J. Polym. Sci., Part B: Polym. Phys.* **1996,** *34*, 2209-2222.

169) Gomes, D.; Nunes, S. P.; Peinemann, K.-V., "Membranes for gas separation based on poly(1-trimethylsilyl-1-propyne)–silica nanocomposites." *J. Membr. Sci.* **2005,** *246* (1), 13-25.
170) Senthilkumar, U.; Reddy, B., "Polysiloxanes with pendent bulky groups having amino-hydroxy functionality: Structure–permeability correlation." *J. Membr. Sci.* **2007,** *292* (1-2), 72-79.
171) Wang, Y.; Li, H.; Dong, G.; Scholes, C.; Chen, V., "Effect of Fabrication and Operation Conditions on CO_2 Separation Performance of PEO–PA Block Copolymer Membranes." *Ind. Eng. Chem. Res.* **2015,** *54* (29), 7273-7283.
172) Wang, Y.; Hu, T.; Li, H.; Dong, G.; Wong, W.; Chen, V., "Enhancing Membrane Permeability for CO_2 Capture Through Blending Commodity Polymers with Selected PEO and PEO-PDMS Copolymers and Composite Hollow Fibres." *Energy Procedia* **2014,** *63*, 202-209.
173) Tena, A.; Marcos-Fernández, A.; Lozano, A. E.; de Abajo, J.; Palacio, L.; Prádanos, P.; Hernández, A., "Influence of the PEO length in gas separation properties of segregating aromatic–aliphatic copoly(ether-imide)s." *Chem. Eng. Sci.* **2013,** *104*, 574-585.
174) Liu, S. L.; Shao, L.; Chua, M. L.; Lau, C. H.; Wang, H.; Quan, S., "Recent progress in the design of advanced PEO-containing membranes for CO_2 removal." *Prog. Polym. Sci.* **2013,** *38* (7), 1089-1120.
175) Koros, W. J., "Simplified Analysis of Gas/Polymer Selective Solubility Behavior." *J. Polym. Sci., Part B: Polym. Phys.* **1985,** *23*, 1611-1628.
176) Lin, H.; Freeman, B. D., "Materials selection guidelines for membranes that remove CO_2 from gas mixtures." *J. Mol. Struct.* **2005,** *739* (1-3), 57-74.
177) Kazarian, S. G.; Vincent, M. F.; Bright, F. V.; Liotta, C. L.; Eckert, C. A., "Specific Intermolecular Interaction of Carbon Dioide with Polymers." *J. Am. Chem. Soc.* **1996,** *118*, 1729-1736.
178) Yave, W.; Car, A.; Funari, S. S.; Nunes, S. P.; Peinemann, K.-V., "CO_2-Philic Polymer Membrane with Extremely High Separation Performance." *Macromolecules (Washington, DC, U. S.)* **2010,** *43* (1), 326-333.
179) Okamoto, K.-i.; Fujii, M.; Okamyo, S.; Suzuki, H.; Tanaka, K.; Kita, H., "Gas Permeation of Properties of Poly(ether imide) Segmented Copolymers." *Macromolecules (Washington, DC, U. S.)* **1995,** *28*, 6950-6956.
180) Bielawski, C. W.; Grubbs, R. H., "Living ring-opening metathesis polymerization." *Prog. Polym. Sci.* **2007,** *32* (1), 1-29.
181) Swaidan, R.; Ghanem, B. S.; Litwiller, E.; Pinnau, I., "Pure- and mixed-gas CO_2/CH_4 separation properties of PIM-1 and an amidoxime-functionalized PIM-1." *J. Membr. Sci.* **2014,** *457*, 95-102.
182) Scholes, C. A.; Tao, W. X.; Stevens, G. W.; Kentish, S. E., "Sorption of methane, nitrogen, carbon dioxide, and water in Matrimid 5218." *J. Appl. Polym. Sci.* **2010,** *117* (4), 2284-2289.
183) Carraher, J., E., "Seymour/Carraher's Polymer Chemistry. 7th ed." Marcel Dekker: New York, 2000.

184) Xu, B.; Wu, J.; McKenna, G. B., "Mechanical and Swelling Behaviors of End-Linked PDMS Rubber and Randomly Cross-Linked Polyisoprene." *Macromolecules* **2013,** *46* (5), 2015-2022.
185) Hiemenz, P. C.; Lodge, T. P., "Polymer Chemistry, 2nd Ed." Taylor & Francis: New York, 2007.
186) Mahurin, S. M.; Lee, J. S.; Baker, G. A.; Luo, H.; Dai, S., "Performance of nitrile-containing anions in task-specific ionic liquids for improved CO_2/N_2 separation." *J. Membr. Sci.* **2010,** *353* (1-2), 177-183.
187) Hill, A. J.; Freeman, B. D.; Jaffe, M.; Merkel, T. C.; Pinnau, I., "Tailoring nanospace." *J. Mol. Struct.* **2005,** *739* (1-3), 173-178.
188) Pethrick, R. A., "Positron Annihilation - A Probe for Nanoscale Voids and Free Volume?" *Prog. Polym. Sci.* **1997,** *22*, 1-47.
189) Jean, Y. C.; Mallon, P. E.; Schrader, D. M., *Principles and Applications of Positron and Positronium Chemistry*. World Scientific: Singapore, 2003.
190) Saito, H.; Nagashima, Y.; Kurihara, T.; Hyodo, T., "A newpositron lifetime spectrometer using a fast digital oscilloscope and BaF_2 scintillators." *Nucl. Instrum. Methods Phys. Res., Sect. A* **2002,** *487*, 612-617.
191) Hu, X.; Xu, D.; Wirth, B. D., "Quantifying He-point defect interactions in Fe through coordinated experimental and modeling studies of He-ion implanted single-crystal Fe." *J. Nucl. Mater.* **2013,** *442* (1-3), S649-S654.

Appendices

Appendix A: Construction of Constant-Volume Variable Pressure Permeation Instrument

As our interest in this area continued to grow, we chose to build our own permeation instrument to evaluate polymer membrane performance in our laboratory. This humbling process was integral in obtaining the membrane data within this work and driving the future success of this project. Before going into detail, I would like to specifically thank Kevin Stevens and Dr. Benny Freeman of the University of Texas-Austin with all their help in this endeavor for without them this process would have been much more difficult. The following appendix will detail the instrument assembly, the calibration process, and the construction of computer interfaces that streamline the process of measuring polymer samples. The instrument as a whole can be visualized as being built around the EMD Millipore sample chamber (**Figure 44**, label 14). These commercially available sample chambers can withstand pressures up to 700 bar, maintain significant vacuum, and provide a porous stainless steel support that can support our membrane samples throughout the experiment. From this centerpiece, equipment that connects to the top of the sample chamber will be referred to as the upstream or feed side, and equipment that connects to the bottom of the sample chamber will be referred to as the downstream or permeate side.

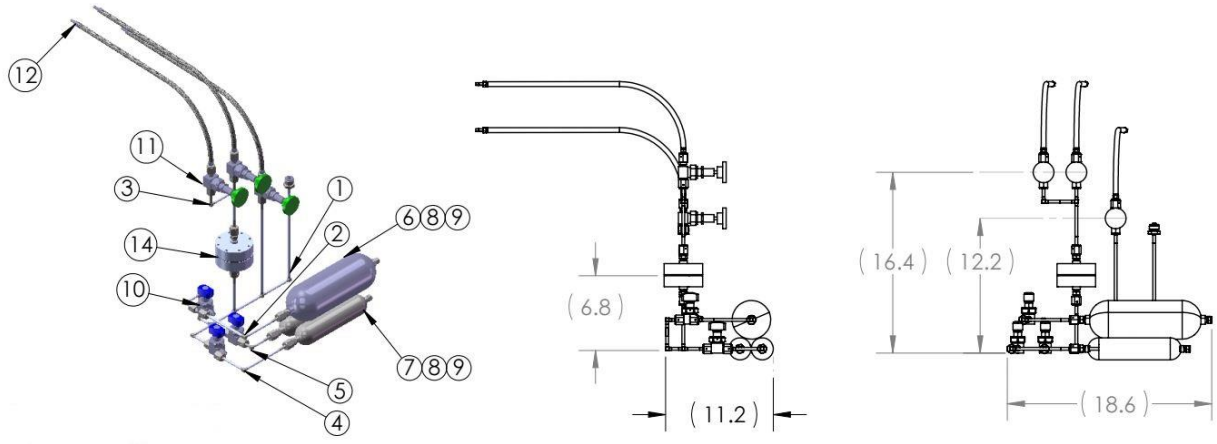

Figure 44. Initial design diagrams of the constant-volume variable-pressure permeation instrument.

The upstream assembly's critical functions include the ability to evacuate the system, deliver a feed gas to the sample chamber at a consistent pressure, and to monitor that pressure in real time. When choosing a piping solution, it is ideal that we minimize the leak rates across all aspects of the instrument. However, cost-effective solutions can be implemented where gas leaks are less critical. For example, the upstream system will be pressurized significantly during instrument operation and will not be as sensitive to minor vacuum leaks as the downstream assembly will be. With this in mind, we opted for 1/4" stainless steel piping and standard Swagelok connections to build the upstream. Some noteworthy additions to the system include the input of the vacuum pump through 1/4" stainless steel tubing, a hookup for gas cylinders through 1/8" stainless steel tubing, an NPT connection for the Honeywell Super TJE Ultra Precision Pressure Transducer (STJE), a self-venting K-series regulator to precisely adjust feed pressures from 30-250 PSI, a central valve that separates the vacuum line from the feed piping, and a purge valve for each line. The majority of these parts were pre-assembled from Ridge Valve and Fitting (Swagelok) and mounted to the wooden board as shown in **Figure 45**.

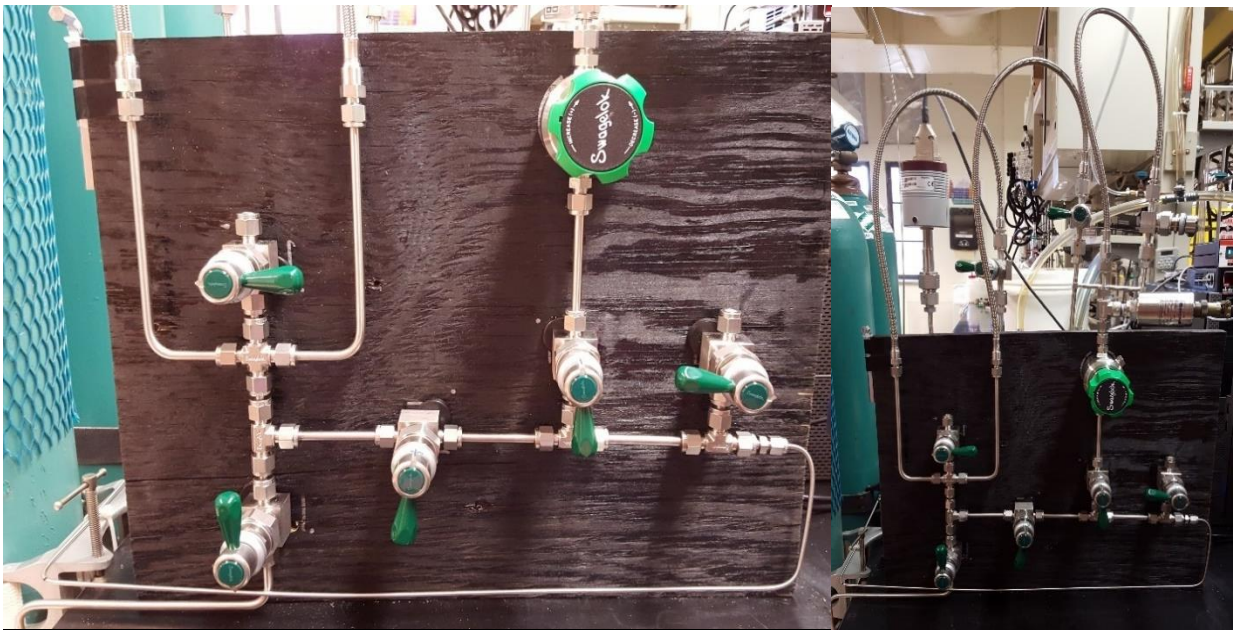

Figure 45. Photographs of the completed upstream assembly of the instrument.

After the initial pipe assembly was completed, appropriate tubing was cut, bent, and routed to the vacuum and ultra-high purity gas cylinders. A Cert nXDS10i 100-127/200-240V 1ph 50/60H scroll pump was chosen due to an oil-free design that eliminates the possibility of machine oil vapors having negative interactions with the high free volume materials considered for membrane applications. At the gas inlet port, 1/8” tubing outputs to a quick connect male adapter in order to easily switch between different thanks of ultra-high purity gas. Lastly, the STJE is mounted into the NPT port with and is connected to the SC500 power supply/readout through the provided cable. In order to output the signal of the Honeywell SC500 power supply/readout to a PC, a serial cable (RS 232) that is compatible with the SC500 needed to be manually constructed. Honeywell provides a 12-pin green adapter that plugs into the unit as well as a serial communications guide that provides the pinouts for a variety of interfaces. Through the aid of the department’s electronic shop, a cable was constructed by manually soldering wired connections to the appropriate pinout shown in **Figure 46**.

The process of assembling the downstream setup followed a similar procedure,

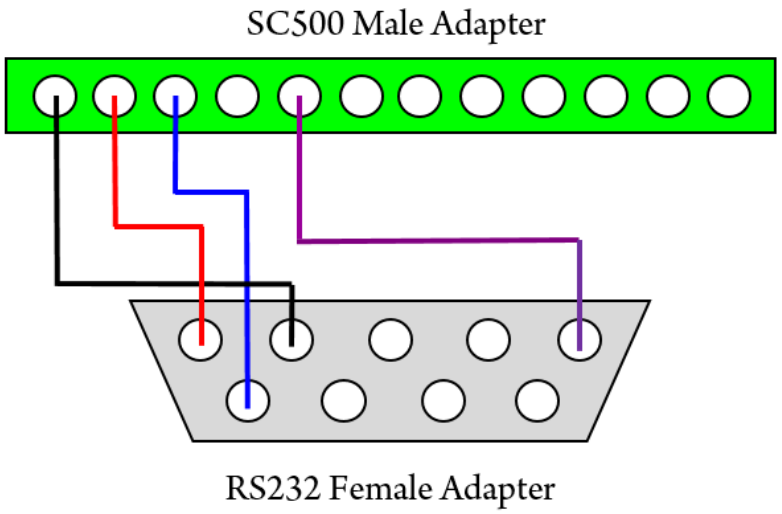

Figure 46. Diagram depicting the cable routing involved in outputting the signal from the Honeywell SC500 readout to a RS232 serial port. Black wire is data being transmitted from the SC500 to the serial port. Red wire is data being transmitted from the serial port to the SC500. Blue wire is data set ready. Purple wire is signal ground.

however, the design criteria for the permeate side differs greatly from the feed side of the sample chamber. The permeate side of the system will operate exclusively under high vacuum conditions where the leak rate will directly affect the sensitivity of the measurement. Although most of the materials that we target will be high performing membranes, having the capability to measure low permeability samples could prove useful in future studies. As a result, the majority of connections in the downstream system are welded and the rest use Swagelok VCR joints which are the highest quality vacuum seal. The simplest downstream assembly would consist of 1/4” stainless steel tubing that goes straight from the sample chamber to the 626C Baratron capacitance manometer with an input for the vacuum line. However, due to the sensitivity of the Baratron, the maximum pressure this system can measure is 10 torr. If the downstream volume is small, high flux samples can reach this maximum pressure before they achieve steady-state permeation which doesn’t allow for the collection of reliable data. To remedy this, the downstream system is designed with optional stainless steel tanks that can add additional volume to slow the pressure rise (**Figure 47**). In our case, we added two 250 mL tanks

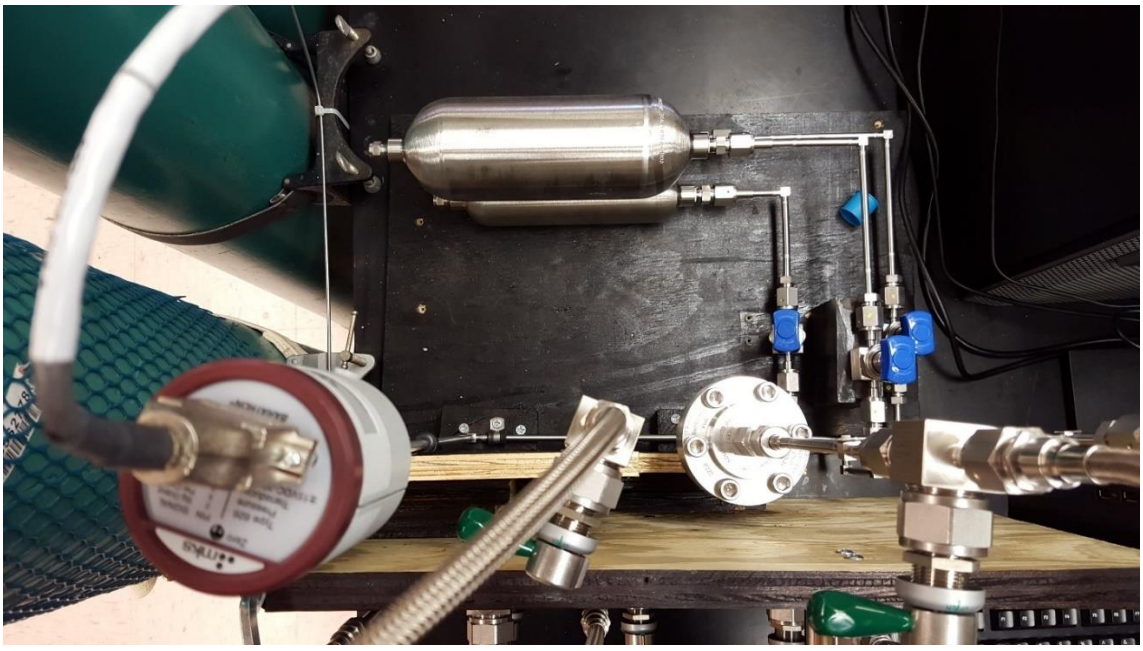

Figure 47. Photograph of the downstream assembly of the instrument.

and a 1000mL tank each with its own valve to allow tuning between samples with different gas throughput. Following the delivery of the welded assembly from Ridge Valve and Fitting, the sample chamber, Baratron, and vacuum line were all affixed to the system. MKS provides cables for both Baratron to PDR2000 connections as well as PDR2000 to RS232 serial port connections. The upstream and downstream systems are mated through stainless steel braided hoses and some slight wood working to produce a completed instrument.

Given the permeability equation in section 1.3 The Solution-Diffusion Model and Mechanisms of Gas Diffusion, accurate permeability calculations require an accurate measurement of the downstream volume (V_d). This is accomplished by first determining a subset of the total volume by filling it with a liquid of known density and measuring the mass change. The volume that was chosen was one of the small tanks and the piping leading up to the valve and was labeled V_1. It was disconnected from the system, cleaned several times with water and methanol and dried in an oven at 150 °C in between each wash until it reached a constant mass. After 24 hours of drying, the system was placed on the balance and measured dry, values recorded as Tank + Pipe, dry, and then the tank and piping was filled with methanol. Extra care was taken to make sure there is no residual air bubbles left in the system and that the mass was measured when the liquid fills the system to its entirety. The mass of the filled system was recorded as Tank + Pipe, full. Given the density of methanol at 20.6 °C is 0.7918 g/cm^3, mass of methanol in the system can be converted to a volume of the interior space. This process was repeated several times and averaged. All values for the measurement of V_1 are displayed in **Table 14** including a small correction factor for the amount of volume in the valve that V_1 connects to. V_1 is reattached and used as a reference volume to calculate the volume of the rest of the system through Burnett gas expansions. In this process, helium, a non-condensable ideal gas, allows us to use modified ideal gas laws to calculate the unknown volumes. The instrument is prepared by equipping the sample chamber with an impermeable film of metal that isolates the upstream and downstream setups. Then, the entire system was evacuated for 48 hours. The first expansion that must be performed is to use the known volume (V_1) to calculate the piping that connects all of the volume tanks,

Table 14. Volume fillings of stainless steel tank V_1 with MeOH.

entry	Tank + Pipe, dry (g)	Tank + Pipe, full (g)	Mass MeOH (g)	Tank + Pipe Volume (mL)	Valve Volume (mL)
1	850.12	1083.82	234.68	295.15	0.52
2	850.15	1084.82	234.67	296.38	0.52
3	850.15	1083.76	233.61	295.04	0.54
4	850.15	1084.55	234.40	296.03	0.54
5	850.15	1084.50	234.35	295.97	0.51
6	850.13	1084.62	234.49	296.15	0.53
7	850.16	1085.29	235.13	296.96	0.55
8	850.16	1083.44	233.29	294.63	0.54
9	850.15	1084.78	234.63	296.33	0.52
			Average	295.85	0.53
				Final volume = 296.38 mL	

the sample chamber, the Baratron, and the vacuum line (V_0). To accomplish this, the other two sample chambers were closed so V_0 and V_1 are the only volumes open and the pressure was recorded as P_0. Since the sample chamber had to be plugged with an impermeable barrier, we were not able to use the upstream system to introduce helium gas as we would in a typical experiment. Instead, gas is carefully via the vacuum line. There is a large discrepancy with the pressures able to be achieved by the regulator on the gas tank (50-500 PSI) and the pressures able to be monitored by the Baratron (0-10 torr). In order to safely introduce gas without damaging the Baratron, the regulator on the gas tank was set to its minimum value of 50 PSI and introduced into the upstream system. The regulator on the helium tank was then closed so the upstream system was under static pressure that was quickly vented to atmosphere through one of the purge valves. At this point, the pressure of helium gas in the upstream system was around 1 atm and carefully introduced into the downstream system by quickly opening and closing the valve on the vacuum line. The resulting pressure in the downstream was recorded as P1 and the valve corresponding to V_1 was closed, trapping that pressure of helium into a container of known volume. After evacuating the rest of the system and closing the

vacuum valve, the gas that was trapped in V_1 was allowed to expand into V_0 resulting in a decreased pressure, P_f. From these values, we used a modification of Henry's Law of partial pressures to ultimately calculate the possible downstream volumes (Equations 17 and 18). The results of all of these experiments are displayed in **Table 15**, **Table 15**, **Table 16**, **Table 17**, and **Table 18**.

$$P = \frac{(P_1 - P_f)}{(P_f - P_0)} \tag{17}$$

$$V_0 = V_1 \cdot P \tag{18}$$

Following the completion of measuring the downstream volumes, LabVIEW was used to create a front-end interface for users to interact with the instrument. With their permission, modules of code were used from Prof. Benny Freeman's laboratory at the University of Texas-Austin. In terms of function, the program needed to be able to monitor both upstream and downstream pressure in real time, export the data to excel, and have a visual indication of the membranes progress towards steady-state permeation. A university license of LabVIEW 2014 and all service packs were obtained through the UTK technology page. NIMAX and Sensotec are manufacturer specific programs that were also required in order to configure serial settings and setup the devices properly before building the LabVIEW program. Serial settings for both Honeywell and MKS systems are found in the device manual and are as follows; 9600 kb/s baud rate, 8 data bits, delay before read 500 ms, parity: none, stop bits 1.0, flow control: none. In LabVIEW, small virtual instruments (VIs) were built to establish effective communications between LabVIEW and each of the pressure transducer readouts (PDR2000 for Baratron and SC500 for STJE). The initial designs for both of these Vis were built upon a sample VI template imbedded in LabVIEW called "Simple Serial". Within that sample VI, strings of language are added that the device will respond to in order to perform the desired function. In the case of the SC500, adding a string for "#00F0" combined with a carrier return prompts the SC500 to transmit the current pressure value by inputting it into the match pattern structure. Following the introduction of that command, the Simple Serial VI is receiving the pressure values from the SC500 every time it parses it for information.

Table 15. Burnett expansions to measure V_0.

entry	P_1 (mtorr)	P_0 (mtorr)	P_f (mtorr)	P (mtorr)	P_{err} (mtorr)	V_0 (mL)	V_{err} (mL)
1	690.6	1.3	604.6	0.1426	3.925×10^{-7}	42.25	0.1072
2	604.6	1.2	529.3	0.1426	4.485×10^{-7}	42.26	0.1072
3	529.3	1.2	463.3	0.1428	5.134×10^{-7}	42.33	0.1074
4	463.3	1.2	405.6	0.1427	5.861×10^{-7}	42.29	0.1073
5	405.6	1.2	355.1	0.1427	6.698×10^{-7}	42.29	0.1073
6	355.1	1.2	310.9	0.1428	7.655×10^{-7}	42.30	0.1073
7	310.9	1.2	272.2	0.1428	8.753×10^{-7}	42.32	0.1074
8	272.2	1.2	238.3	0.1430	1.002×10^{-6}	42.38	0.1075
9	238.3	1.2	208.7	0.1427	1.142×10^{-6}	42.28	0.1073
					V_0 (mL) =	42.30	± 0.04

Table 16. Burnett expansions to measure V_2.

entry	P_1 (mtorr)	P_{2+0} (mtorr)	P_f (mtorr)	P (mtorr)	P_{err} (mtorr)	V_{2+0} (mL)	V_{err} (mL)
1	903.0	3.7	204.5	0.2875	1.834×10^{-6}	1030.97	2.616
2	204.5	3.7	48.5	0.2872	8.210×10^{-6}	1032.03	2.619
3	905.5	3.7	205.0	0.2874	1.828×10^{-6}	1031.36	2.617
4	205.0	3.6	48.6	0.2877	8.189×10^{-6}	1030.08	2.614
5	919.0	3.7	208.1	0.2875	1.802×10^{-6}	1030.80	2.615
6	208.1	3.6	49.2	0.2870	8.060×10^{-6}	1032.77	2.621
7	995.0	3.6	225.0	0.2875	1.663×10^{-6}	1030.76	2.615
8	924.0	3.7	209.0	0.2871	1.791×10^{-6}	1032.20	2.619
9	209.0	3.6	49.4	0.2870	8.024×10^{-6}	1032.79	2.621
				Average	V_{2+0} (mL) =	1031.53	± 0.93
					V_2 (mL) =	989.23	± 0.93

Table 17. Burnett expansions to measure V_3.

entry	P_1 (mtorr)	P_{3+0} (mtorr)	P_f (mtorr)	P (mtorr)	P_{err} (mtorr)	V_{3+0} (mL)	V_{err} (mL)
1	888.3	3.7	417.7	1.1367	3.789×10^{-6}	336.90	0.855
2	417.7	3.7	197.1	1.1406	8.137×10^{-6}	338.06	0.858
3	197.1	3.7	94.1	1.1394	1.739×10^{-5}	337.69	0.857
4	952.7	3.7	448.1	1.1355	3.527×10^{-6}	336.53	0.854
5	448.1	3.7	211.3	1.1407	7.581×10^{-6}	338.06	0.858
6	211.3	3.6	100.7	1.1390	1.619×10^{-5}	337.58	0.857
7	860.3	3.7	404.4	1.1378	3.918×10^{-6}	337.21	0.856
8	404.4	3.5	190.8	1.1404	8.401×10^{-6}	337.99	0.858
9	190.8	3.5	91.0	1.1406	1.798×10^{-5}	338.04	0.858
				Average	V_{3+0} (ml) =	337.56	± 0.29
					V_3 (ml) =	295.26	± 0.29

Table 18. Usable volumes for permeation instrument.

entry	Volume (mL)
V_0	42.299 cm^3
V_{10}	338.676 cm^3
V_{20}	1031.526 cm^3
V_{30}	337.559 cm^3
V_{120}	1327.903 cm^3
V_{130}	633.936 cm^3
V_{230}	1326.786 cm^3
V_{all}	1623.163 cm^3

The program was additionally modified to format the response into an indicator with the correct units and a chart that graphs the values versus time. To accomplish this, the string being exported from the instrument was outputted into another case structure that accepts additional string language to make modifications to the raw signal from the device. As can be seen by comparing **Figure 48** and **Figure 49**, a scan from string structure with the string “01 TK %.5F” attached was added to format the signal with the correct decimal places and units. Once properly formatted, the data string was connected to an indicator window and a waveform chart to display data over time. Following the successful communication between LabVIEW and the SC500, we continued a similar procedure on a separate VI for the PDR 2000 (**Figure 50**). The specific string this system recognizes to output the pressure signal is “p” and data strings come from the device in a format that doesn’t require any additional formatting. With both of these programs functioning independently, they were combined into a single program and configured to operate within the same time structure. As a visual indication of sample’s progress towards steady-state permeation, the Freeman laboratory built a sub-VI that automatically monitors the slope of the pressure flux in the downstream (**Figure 51**). As long as the upstream pressure is held constant, a constant slope in the downstream system indicates a sample at steady-state. By intercepting the data streams going to both the upstream and downstream indicators and feeding them into this sub-VI as well, this tool will output the slope of both upstream and downstream systems every ten minutes while the instrument is running. Lastly, LabVIEW has a built-in sub-VI for writing data to excel that intercepted data in the same way as the slope-monitoring module (**Figure 52**). This sub-VI was configured to be idle by default to save disk space and was given a button to toggle the recording on and off. To make the data analysis process more intuitive, an array of strings was used to create text inputs for things such as the gas being tested, the sample name, and the date to assist in creating the name of the data file and specifying the data path. Furthermore, a separate array ensured that the columns of the exported excel file are appropriately labeled with the correct information. After verifying the successful operation of all key features, the front panel is organized in a manner to hide serial settings and only display functions the user should be interacting with leaving us

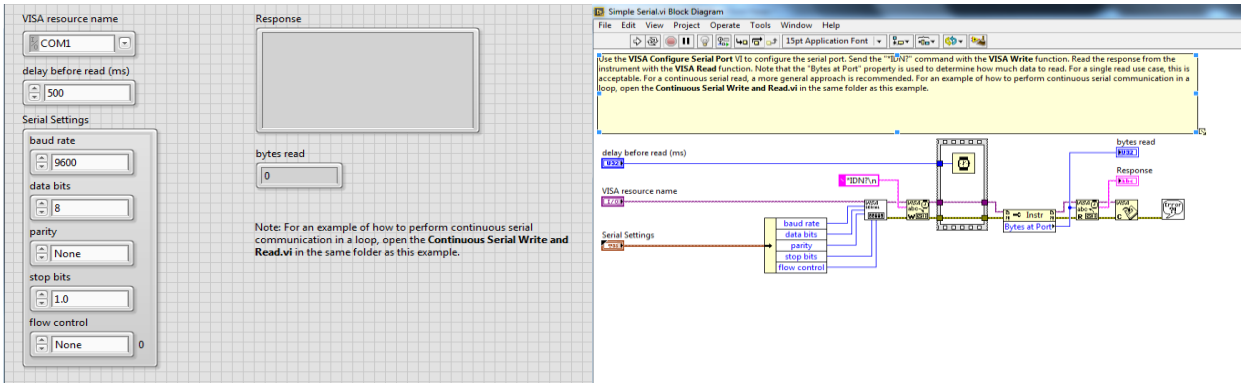

Figure 48. Simple Serial sample VI.

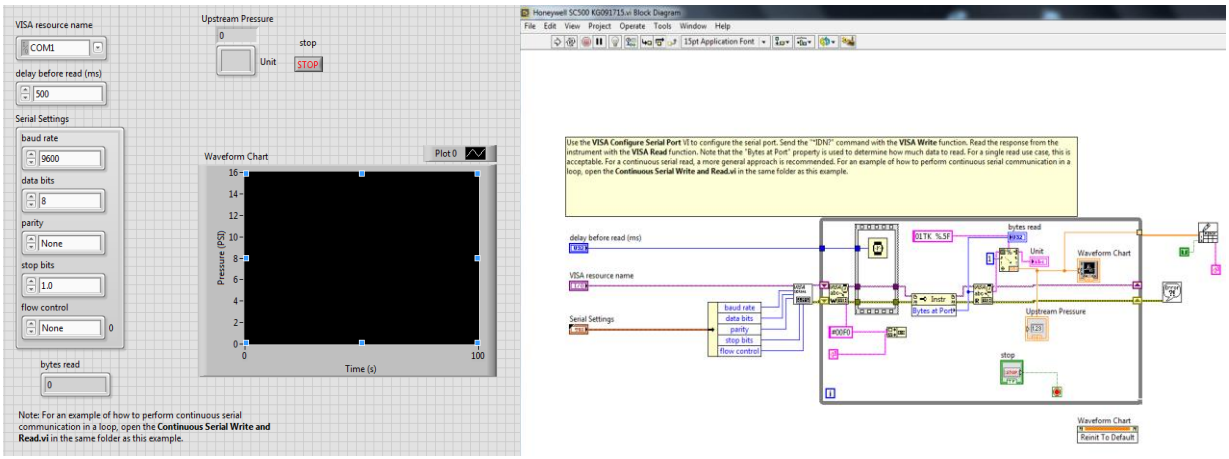

Figure 49. Simple Serial modified VI to communicate with the Honeywell SC500 readout.

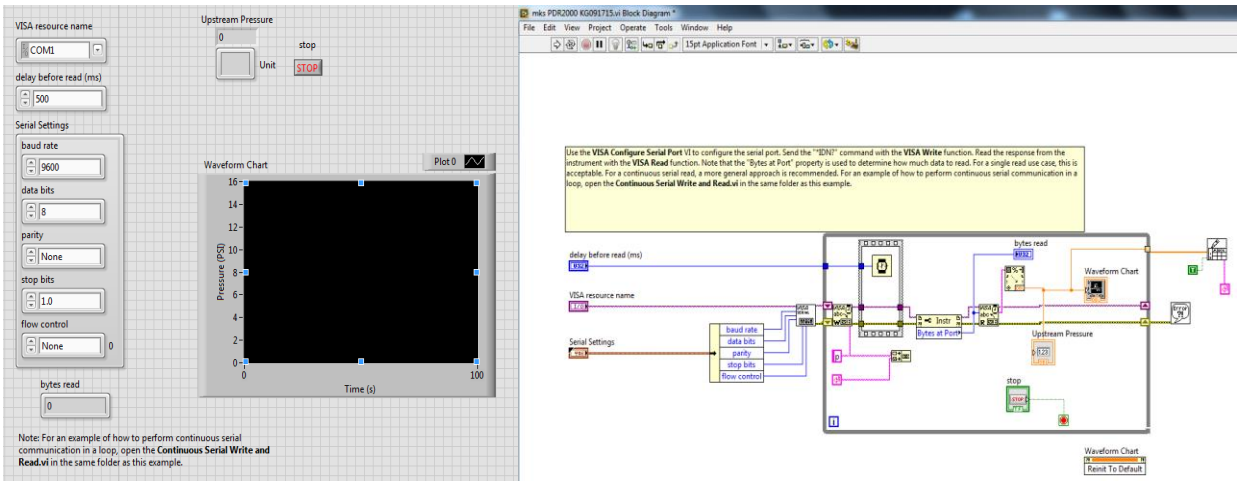

Figure 50. Simple Serial modified VI to communicate with the MKS PDR2000 readout.

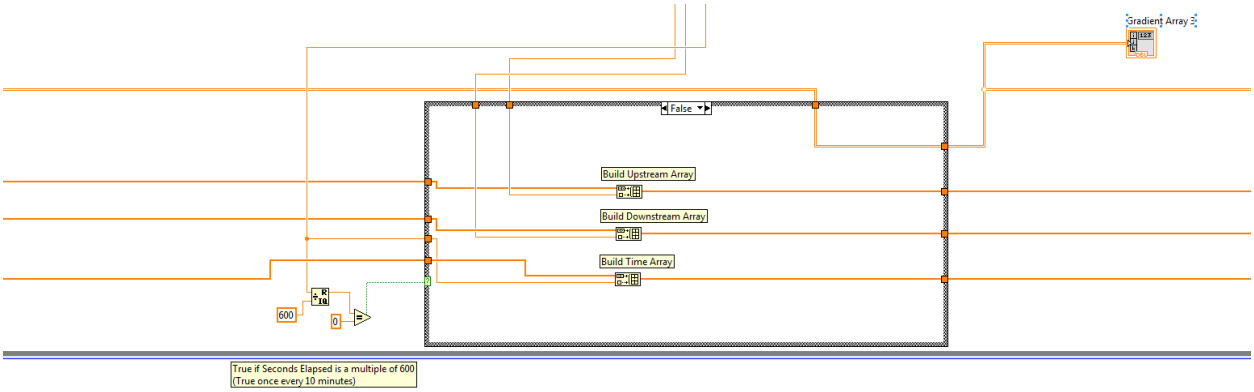

Figure 51. Slope monitoring sub-VI.

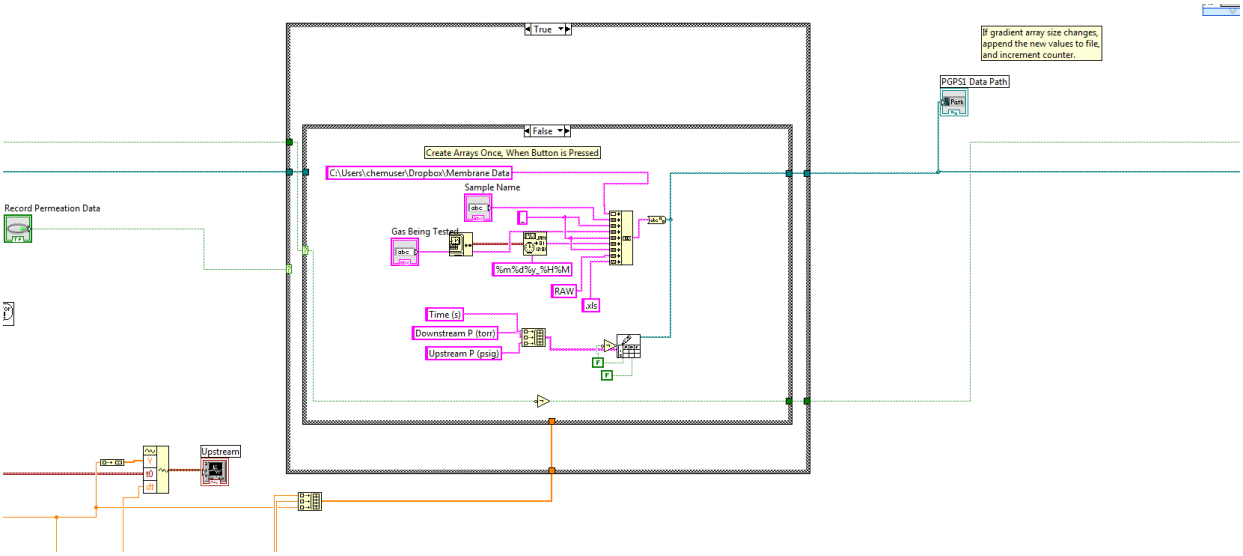

Figure 52. Sub-VI for exporting data to excel.

with the final product (**Figure 53**). The final product was exported as an executable (.exe) that is much less resource intensive than the LabVIEW suite and allows multiple programs off of one machine. Outside of LabVIEW, an excel template for rapidly calculating permeability and selectivity was developed (**Figure 54**). This spreadsheet allows users to input various experimental parameters and automatically converts the data to the correct units and generates permeability and selectivity values for CO_2 and N_2. With all of the tools completed, the instrument was calibrated by measuring a polycarbonate sample that was also measured on the instruments in the Freeman lab. On our system, N_2 permeability of this sample was observed to be 0.273 Barrer and the Freeman lab measured the sample to be 0.269 Barrer.

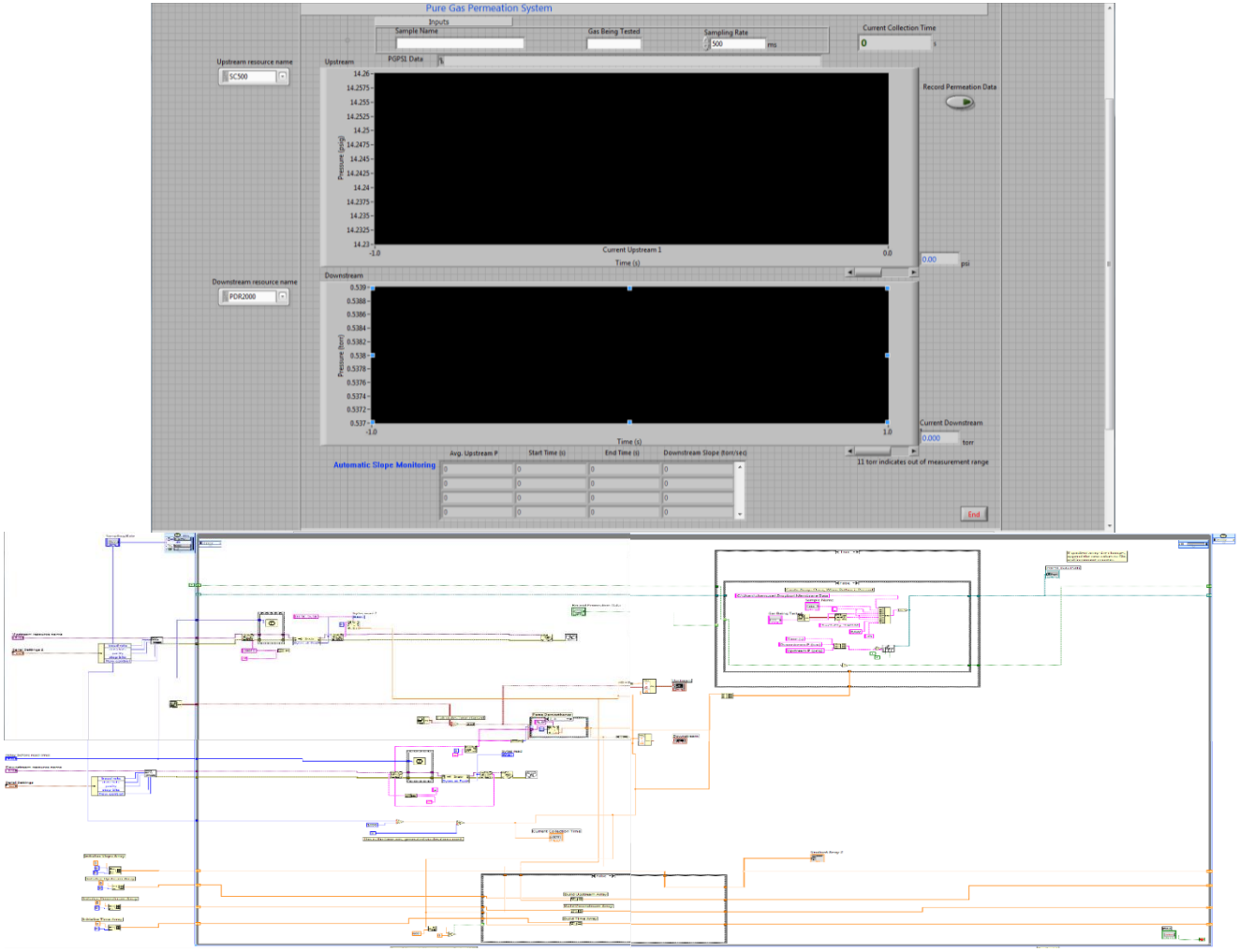

Figure 53. Complete LabVIEW VI for the permeation instrument.

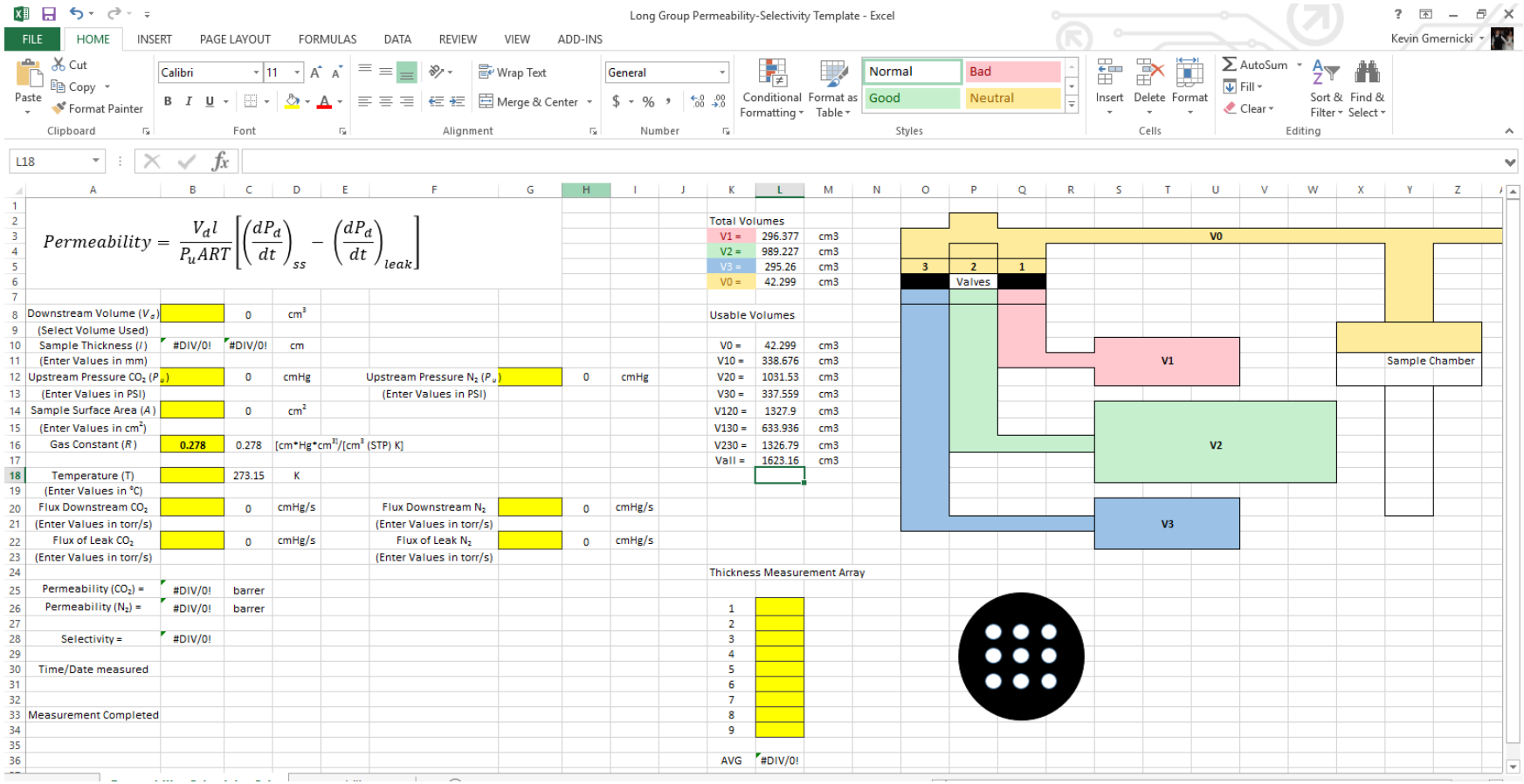

Figure 54. Long group permeability and selectivity calculation spreadsheet.

Appendix B: Construction of Dual-Volume Pressure-Decay Gas Sorption Instrument

A dual volume pressure decay gas sorption Instrument allows for the accurate determination of gas solubility coefficients. The following appendix will highlight our processes for instrument construction, measuring the internal volume, building the interface, and instrument calibration. A scheme of the dual-volume pressure-decay sorption instrument design is shown in **Figure 55** which consists of two chambers with similar volumes each equipped with a Honeywell STJE pressure transducer and bellows valve. The instrument was constructed exclusively with Swagelok VCR fittings and 1/4" stainless steel piping exclusively in order to minimize potential gas leaks. A single quick-connect adapter at one the end of the instrument allows for either the introduction of ultra-high purity gas or vacuum while a VCR cap at the other end can be removed and replaced to introduce sample. The volume closest to the gas/vacuum line is referred to as the charge cell (V_c) and the other volume is the sample cell (V_s). The bellows valves that separate these volume cells need to be modified beforehand due to the PTFE tips that create a seal having a quantifiable gas solubility. To eliminate this effect, Swagelok offers replacement tips that are made of copper metal that were installed prior to instrument calibration.

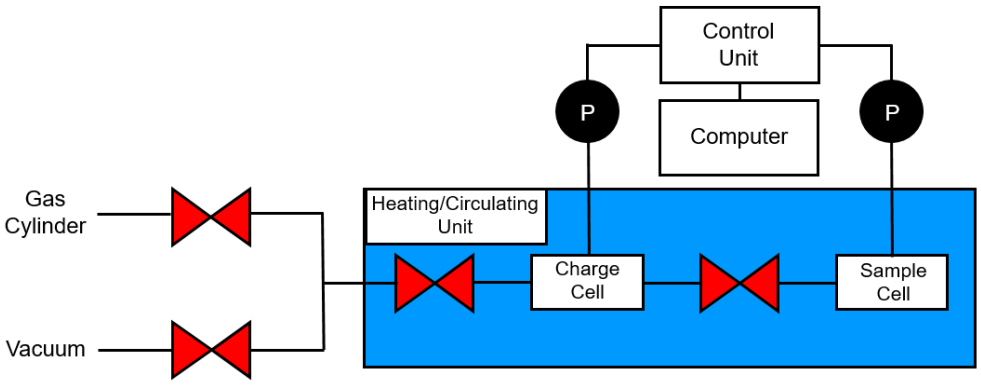

Figure 55. Diagram of temperature-controlled dual-volume pressure-decay gas sorption instrument.

Once assembled, the instrument is placed into a large water bath equipped with a water heater/circulator combo that can keep the instrument at a consistent temperature over the course of the entire measurement. In the literature, polymer solubility is measured at a variety of temperatures but is commonly reported at 35 °C. Using this as a standard, all calibrations were performed at 35 °C unless otherwise noted. Gas solubility is typically measured at high pressures (>20 atm), STJE pressure transducers that are rated for 500 PSI were chosen and installed in the NPT connections using Teflon tape. In this system we ordered an SC2000 2-channel readout to power and manage both transducers simultaneously. Similar to the procedure described in Appendix A: Construction of Constant-Volume Variable Pressure Permeation Instrument, transducers are connected to the readout via the provided cables and a RS232 serial cable to output data from the SC2000 to the PC was constructed by the department's electronic shop. Then, an upstream assembly capable of delivering vacuum and feed pressure was designed with Ridge Valve and Fitting and delivered to the lab. Key features include hookups for an oil free Cert nXDS10i 100-127/200-240V 1ph 50/60H scroll pump, 1/8" tubing to a quick connect male adapter to easily switch between gas tanks, and a needle valve to incrementally introduce gas into the system. The final product of the actual instrument can be seen in **Figure 56** and **Figure 57**.

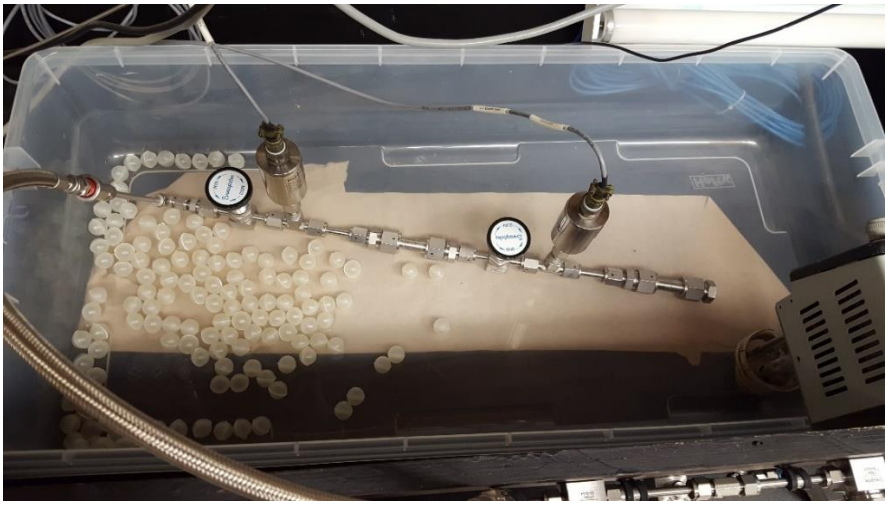

Figure 56. Photograph of dual-volume pressure-decay sorption instrument.

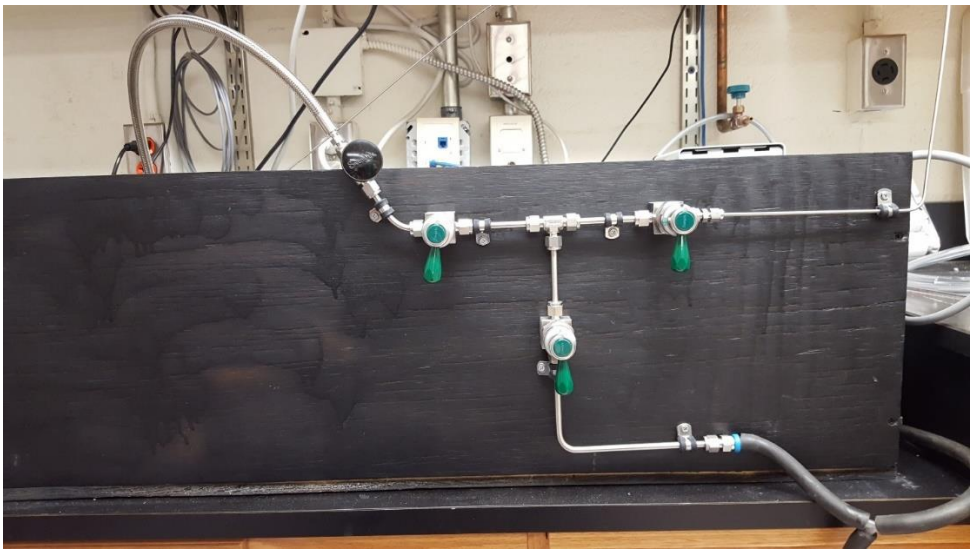

Figure 57. Photograph of upstream assembly for the dual-volume pressure-decay sorption instrument.

Similar to the permeation instrument, knowing the internal volumes of the individual cells of the instrument is essential to the accurate calculation of solubility coefficients. In this case, a two-step Burnett expansion process from the Springer Handbook was employed that started with evacuating the entire system for 48 hours. Vacuum was trapped in the sample cell by closing the bellows valve in between V_c and V_s while the charge cell was filled to a known pressure (P_0). The gas from the charge cell was allowed to expand into V_s and the decrease in pressure was recorded (P_f). This process was repeated several times at various pressure values to develop a plot of P_0/P_f versus P_0, **Figure 58**, where the y-intercept is $(V_c+V_s)/V_c$ according to equation 19.

$$\frac{P_f}{P_0} = \frac{B * V_s}{V_c} P_0 + \frac{V_c + V_s}{V_c} \tag{19}$$

The process was then repeated with a slight variation. The volume of a non sorbing solid, in our case metal ball bearings, was determined using a Mettler Toledo density kit based upon Archimedes principle. By placing the non-sorbing solid of known volume (V_m) in the

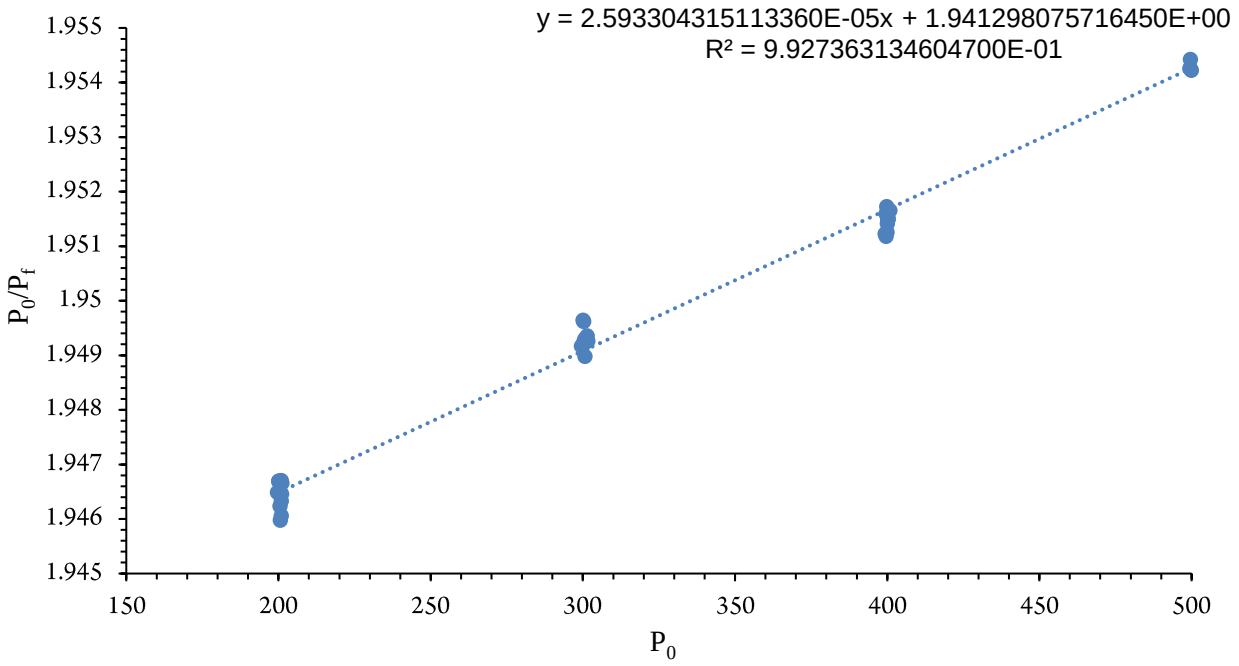

Figure 58. Burnett expansions of empty sorption instrument at various pressures.

sample chamber, we can replace the variable V_s in equation 18 with $V_s - V_m$ to generate equation 20 which creates additional relationships between the unknown volumes of our cells with the known volume of our solid and the pressure ratio we directly measure allowing for the algebraic determination of both V_c = 18.5521 cm^3 and V_s = 17.4631 cm^3. The data for the second set of Burnett expansions are displayed in **Figure 59**.

$$\frac{P_f}{P_0} = \frac{B * (V_s - V_m)}{V_c} P_0 + \frac{V_c + V_s - V_m}{V_c} \tag{20}$$

With the accurate determination of instrument volumes, we moved towards building the front-end interface for users to interact with the instrument via a computer. This will follow a modified process that is described in Appendix A: Construction of Constant-Volume Variable Pressure Permeation Instrument and requires the installation of the same software packages to ensure effective communication between the SC2000 and the PC. The program for the permeation instrument was stripped of the slope monitoring and Baratron modules to use as the foundation for the sorption interface. Since the SC2000 and SC500 are both Honeywell instruments, strings for parsing the device for

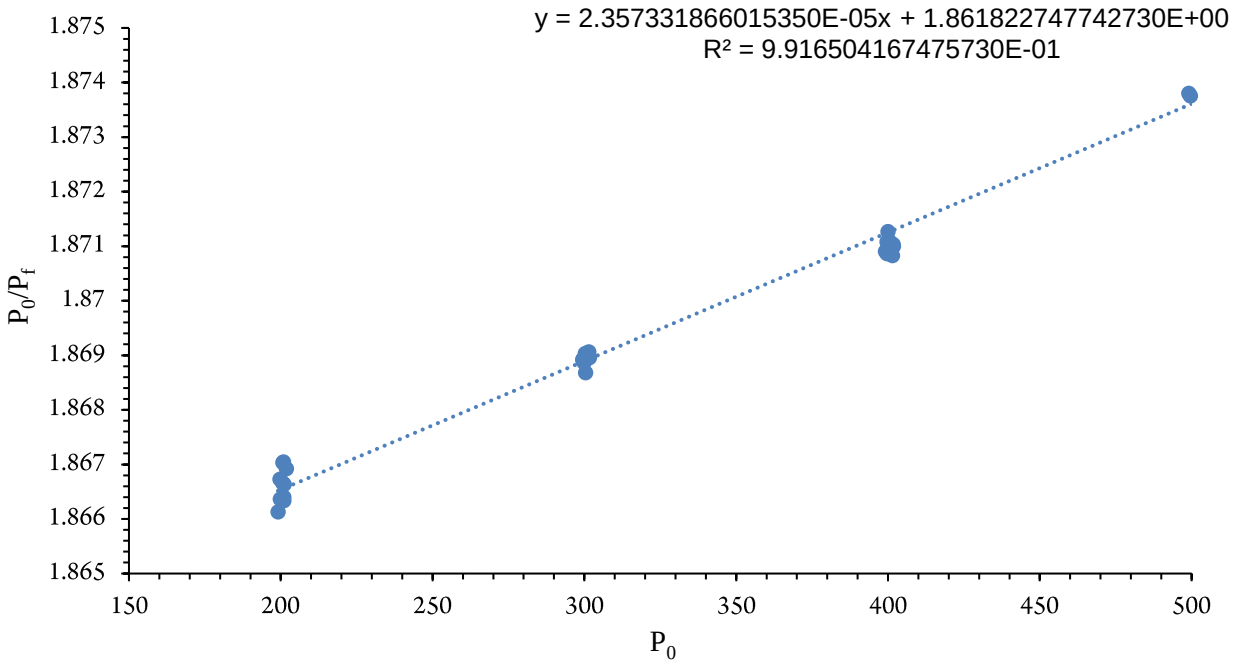

Figure 59. Burnett expansions of sorption instrument loading with non-sorbing solids, V_m.

information and formatting the data are similar in nature. Here, the string “00FL” parses the device to send pressure information for both data channels simultaneously. The incoming data will come in with the format “Channel 1, Channel 2 Pressure” (i.e. 014.25 PSIA, 013.87 PSIA). In order to separate this one data string into two data strings, a match pattern structure was used to detect the comma in the data string and separate the left side and right side of the comma into its own data string. These data strings are combined with a singular time axis and the module for exporting to excel to generate a functional pressure vs. time plot for each channel. After applying a few finishing touches such formatting the exported excel sheets, exporting the LabVIEW project as an .exe, hiding unused functions, and building an excel spreadsheet for processing the data, the sorption interface was calibrated using Matrimid polymer films (**Figure 60**).[182]

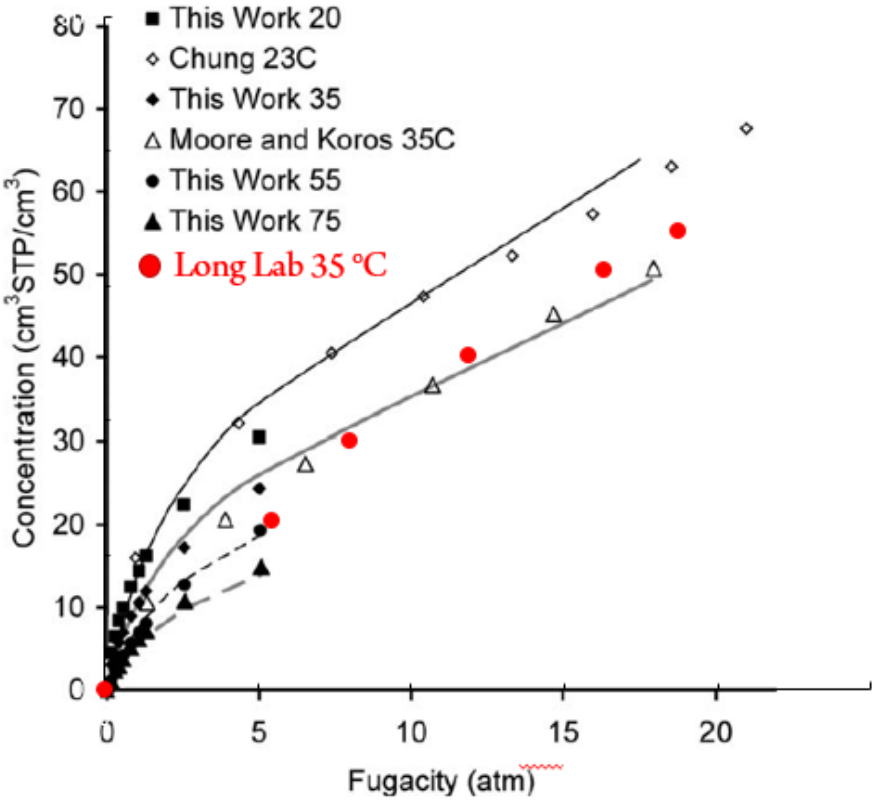

Figure 60. Long group data for the sorption isotherm of CO_2 in Matrimid at 35 °C added onto a figure reprinted with permission from reference 182 Copyright 2009 Elsevier B.V..

Appendix C: Experimental Methods and Supporting information for Chapter 3

General Considerations. Norbornene was purchased from Sigma Aldrich and sublimed *in-vacuo* at room temperature onto a cold finger at 0 °C prior to use. *N*-phenylmaleimide was purchased from TCI chemicals and recrystallized in cyclohexane prior to use. Azobisisobutyronitrile (AIBN) radical initiator was purchased from Sigma Aldrich and recrystallized prior to use by recrystallizing from a supersaturated solution in hot methanol to produce white needles that were stored at -35°C. 1,3,5-Trimethoxybenzene was purchased from Acros Organics and recrystallized three times in diethyl ether prior to use. Anhydrous THF-d_8 was purchased from Cambridge Isotopes Laboratories in ampoules and used as received. Polymerization kinetics were monitored by *in-situ* high-temperature NMR on a Bruker 400 MHz NMR Spectrometer using a broad-band inverse probe set at 75 °C. Molecular weights were determined using an Agilent EcoSEC GPC and molecular weights are reported relative to polystyrene standards. Differential scanning calorimetry measurements were performed on a TA Instruments Q2000 using a standard heat/cool/heat cycle with a heating rate of 10 °C/min and a cooling rate of 5 °C/min.

General Procedure for Copolymerizations. In a typical polymerization, norbornene (2.720 g, 28.87 mmol), *N*-phenylmaleimide (5.000 g, 28.87 mmol), and AIBN (0.047 g, 0.287 mmol) were added to a Schlenk tube. The reaction vessel was purged with dry N_2 gas and 5.82 mL of dry/degassed THF was added via syringe. The Schlenk tube was then sealed and the polymerization was heated to 66 °C for 24 h. After 24 h, the mixture was cooled to room temperature, an additional 15 mL of THF was added and the polymer completely dissolved. The polymer is then precipitated into 200 mL of stirred methanol, filtered and dried under vacuum at 75 °C.

General Procedure for the NMR scale Copolymerizations. In a J. Young NMR tube, norbornene (0.151 g, 1.593 mmol), *N*-phenylmaleimide (0.276 g, 1.593 mmol), and AIBN (0.052 g, 0.319 mmol) were added to 0.75 mL of anhydrous THF-d_8. Additionally, 1,3,5-

trimethoxybenzene (0.054 g, 0.319 mmol) was added as an internal standard for determining NMR integration values. The reaction mixture was degassed (within the J. Young NMR tube) via the freeze, pump, thaw method (× 3) and back-filled with dry N_2 gas. The polymerizations were run for 24 h at 75 °C and terminated by precipitation of the polymer into 20 mL of methanol. The polymer was filtered and dried under vacuum at 75 °C for 24 h.

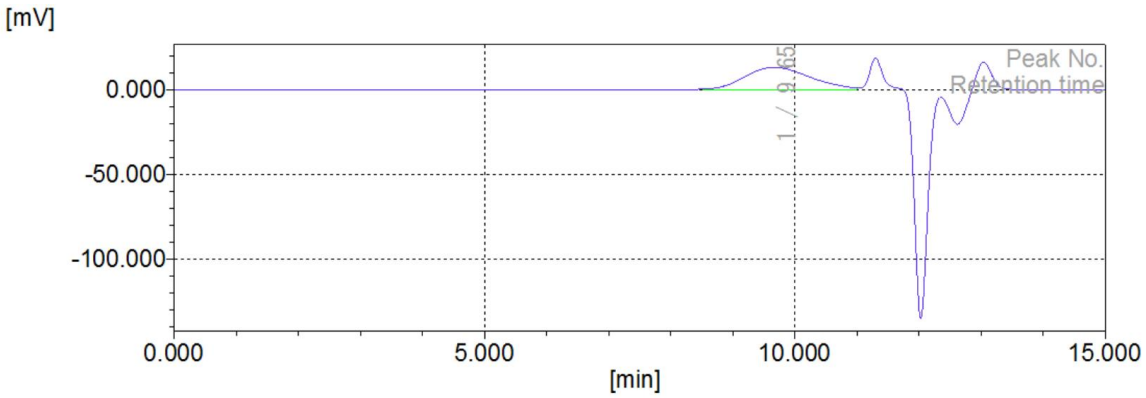

Result of molecular weight calculation (RI)

Peak 1 Valley Peak

	[min]	[mV]	[mol]		
Peak start	8.517	0.112	15,647	Mn	2,280
Peak top	9.652	13.086	3,402	Mw	3,531
Peak end	11.005	0.792	452	Mz	4,983
				Mz+1	6,454
				Mv	3,531
Height [mV]			13.137	Mp	3,403
Area [mV*sec]			960.565	Mz/Mw	1.411
Area% [%]			100.000	Mw/Mn	1.548
[eta]			3530.61408	Mz+1/Mw	1.828

Figure 61. GPC trace and data for 40/60 *N*-phenylmaleimide/norbornene copolymer (**Table 1**, **entry 1**).

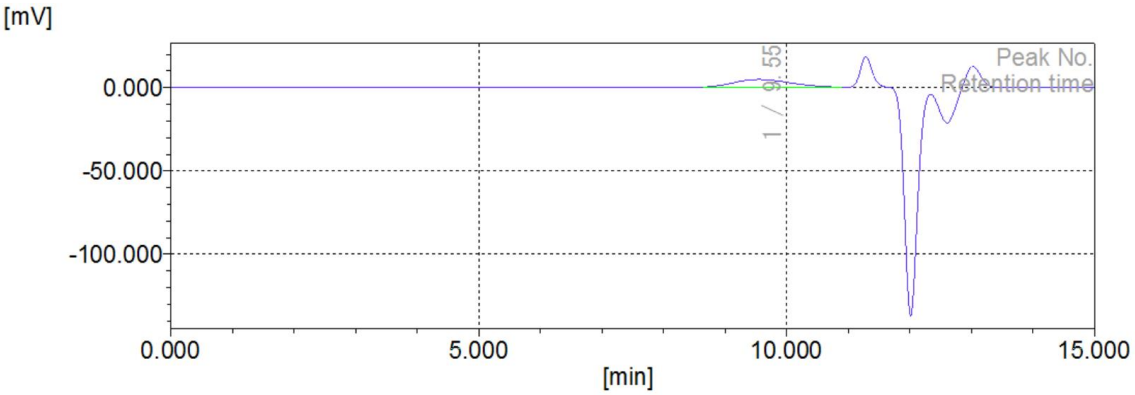

Result of molecular weight calculation (RI)

Peak 1 Valley Peak

	[min]	[mV]	[mol]		
Peak start	8.660	0.258	12,931	Mn	2,732
Peak top	9.558	4.881	3,869	Mw	3,989
Peak end	10.885	0.219	549	Mz	5,325
				Mz+1	6,568
				Mv	3,989
Height [mV]			4.921	Mp	3,870
Area [mV*sec]			334.870	Mz/Mw	1.335
Area% [%]			100.000	Mw/Mn	1.460
[eta]			3989.05074	Mz+1/Mw	1.647

Figure 62. GPC trace and data for 50/50 *N*-phenylmaleimide/norbornene copolymer (**Table 1**, **entry 2**).

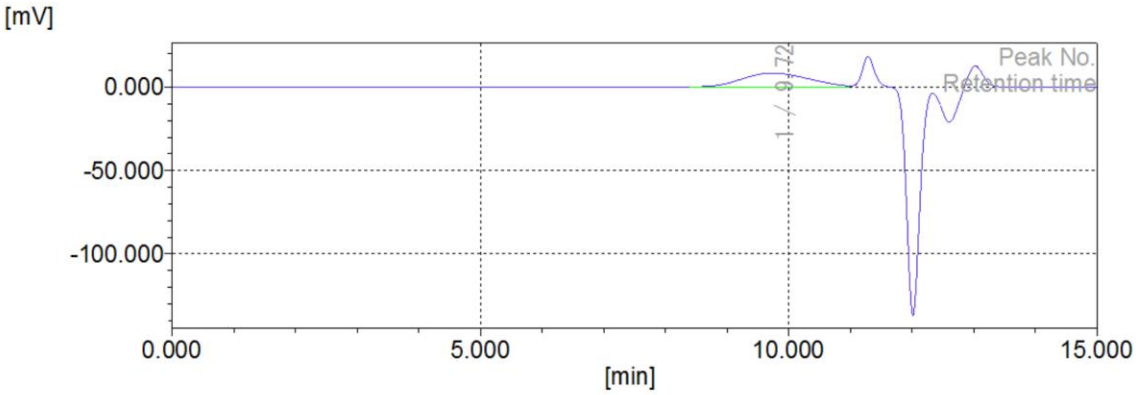

Result of molecular weight calculation (RI)

Peak 1 Valley Peak

	[min]	[mV]	[mol]		
Peak start	8.397	0.053	18,359	Mn	2,136
Peak top	9.727	8.345	3,066	Mw	3,320
Peak end	10.982	0.653	469	Mz	4,811
				Mz+1	6,426
				Mv	3,320
Height [mV]			8.335	Mp	3,067
Area [mV*sec]			628.419	Mz/Mw	1.449
Area% [%]			100.000	Mw/Mn	1.554
[eta]			3320.33393	Mz+1/Mw	1.935

Figure 63. GPC trace and data for 60/40 *N*-phenylmaleimide/norbornene copolymer (**Table 1**, **entry 3**).

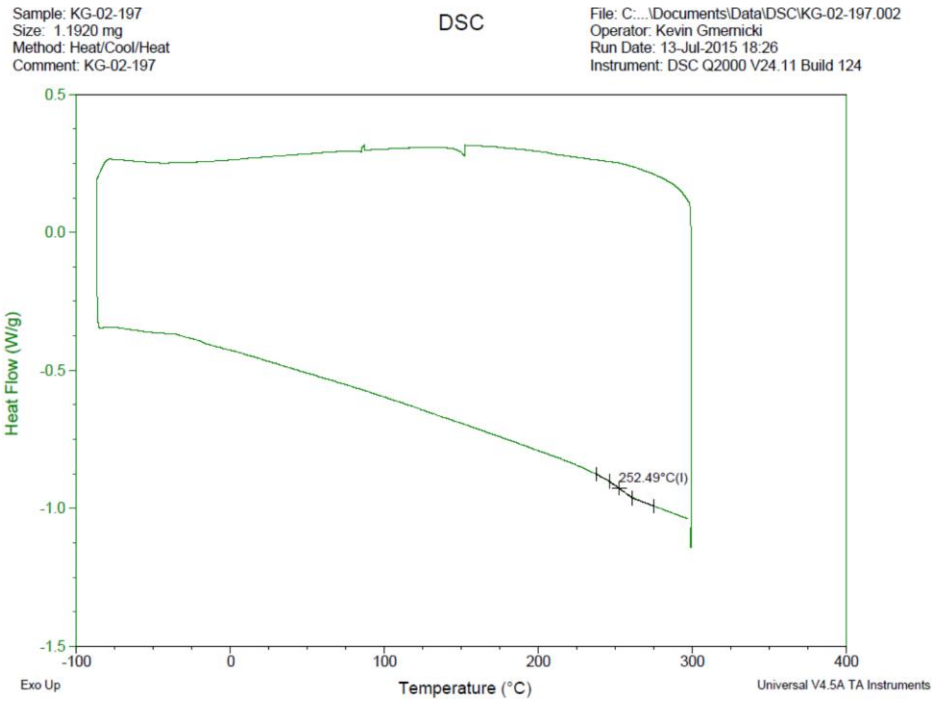

Figure 64. DSC trace obtained for 40/60 *N*-phenylmaleimide/norbornene copolymer (**Table 1**, **entry 1**).

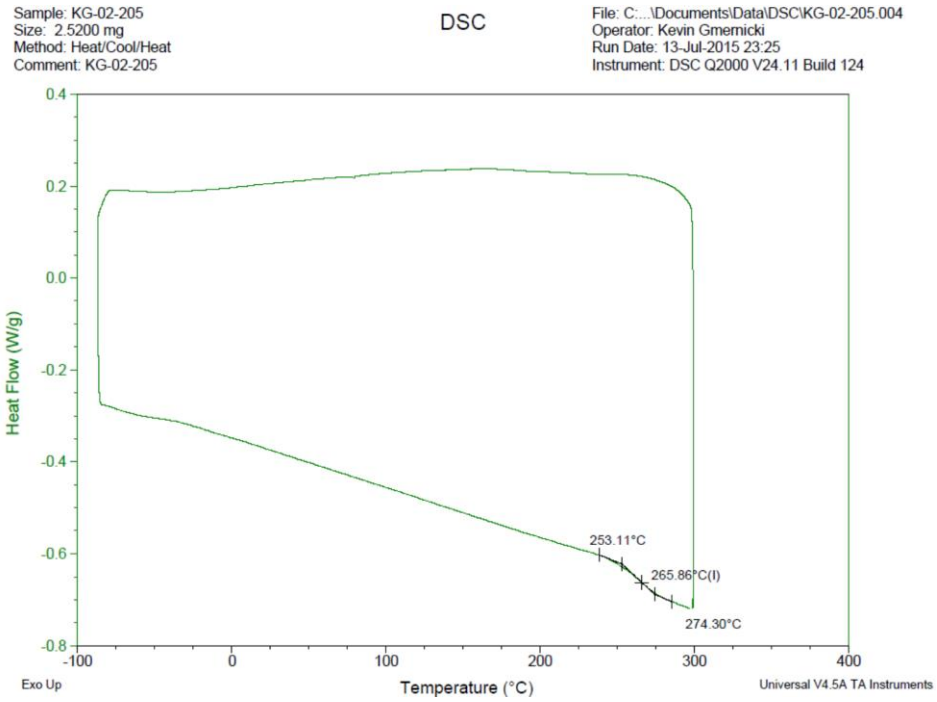

Figure 65. DSC trace obtained for 50/50 *N*-phenylmaleimide/norbornene copolymer (**Table 1**, **entry 2**).

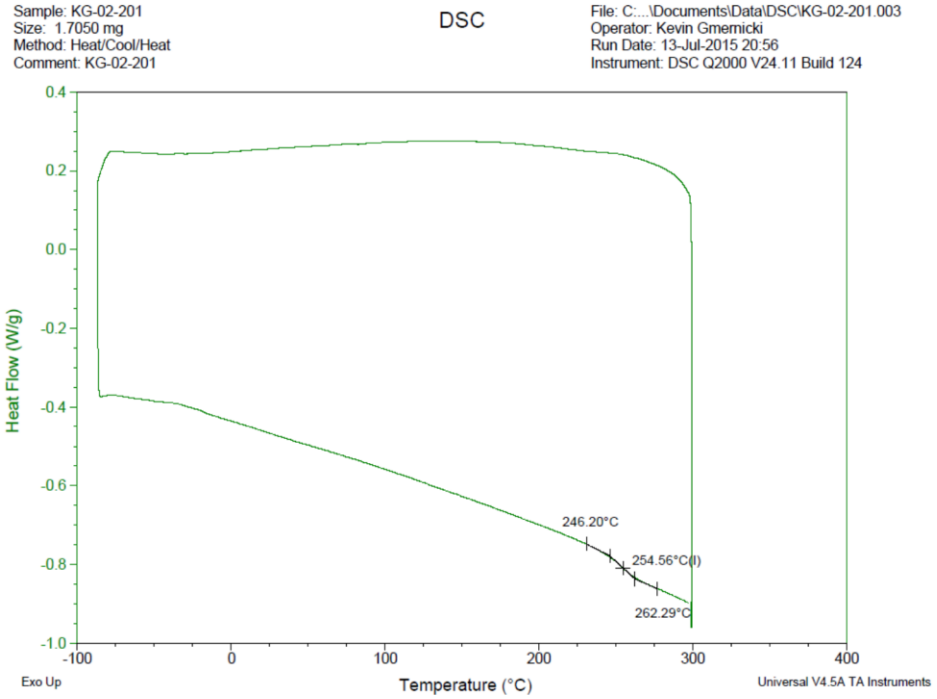

Figure 66. DSC trace obtained for 60/40 *N*-phenylmaleimide/norbornene copolymer (**Table 1**, **entry 3**).

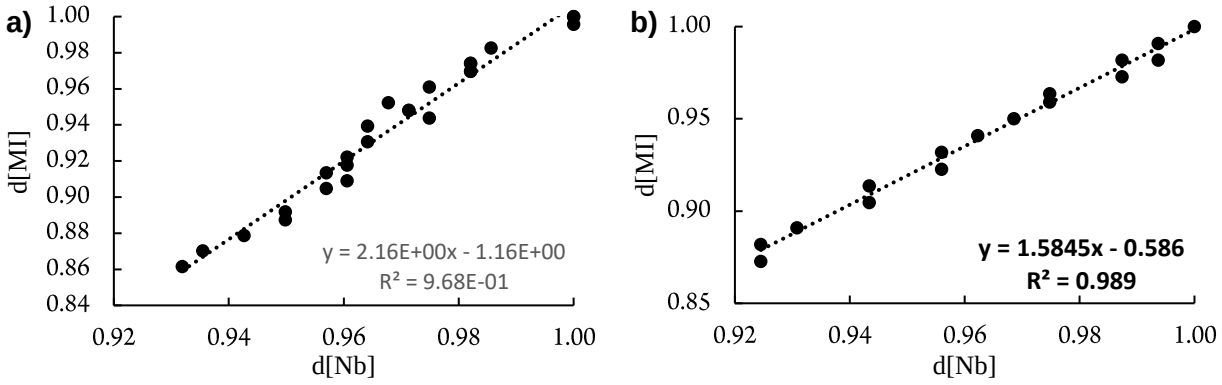

Figure 67. Plots of *N*-phenylmaleimide conversion vs. norbornene conversion for polymerizations of **a)** 40/60 *N*-phenylmaleimide/norbornene and **b)** 60/40 *N*-phenylmaleimide/norbornene, monitored via *in-situ* NMR

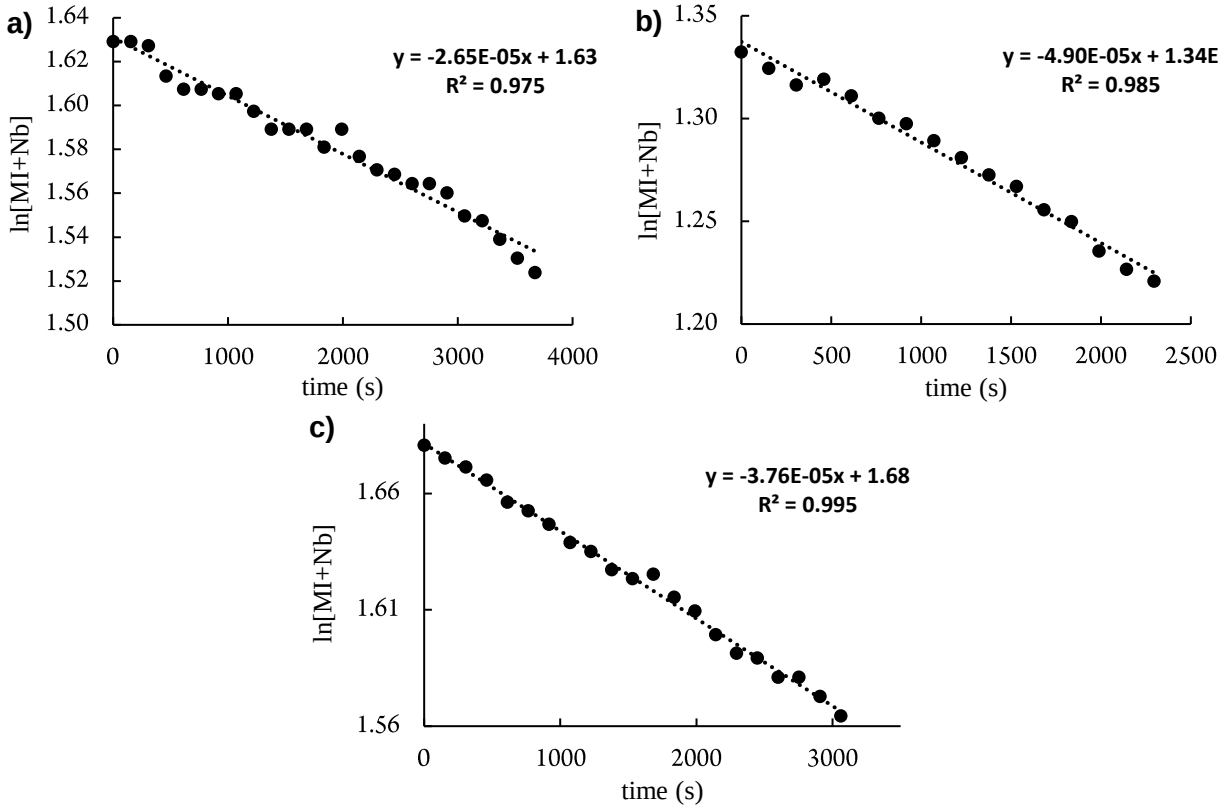

Figure 68. Plots of ln[total monomer peak area] vs. time for polymerizations of **a)** 40/60 *N*-phenylmaleimide/norbornene, **b)** 60/40 *N*-phenylmaleimide/norbornene, monitored via in-situ NMR and **c)** 50/50 *N*-phenylmaleimide/norbornene, monitored via in-situ NMR.

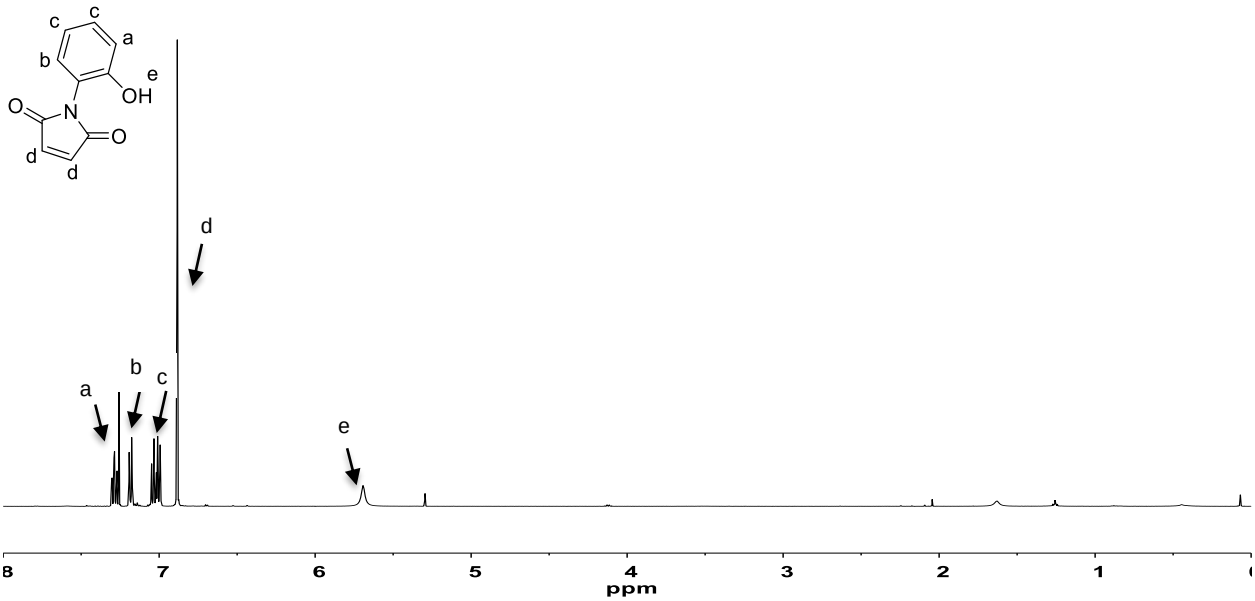

Figure 69. ^{1}H NMR spectra of (*o*-hydroxy)-*N*-phenylmaleimide (**6**).

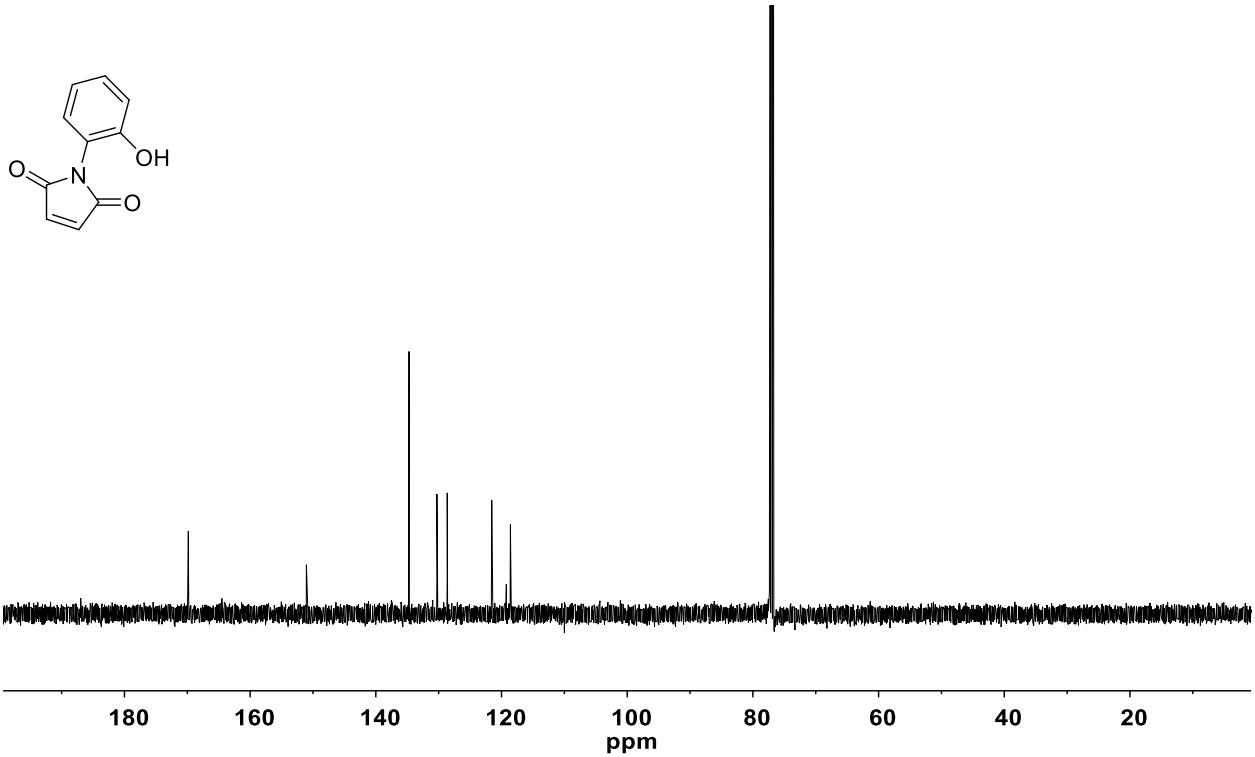

Figure 70. ^{13}C NMR spectra of (*o*-hydroxy)-*N*-phenylmaleimide (**6**).

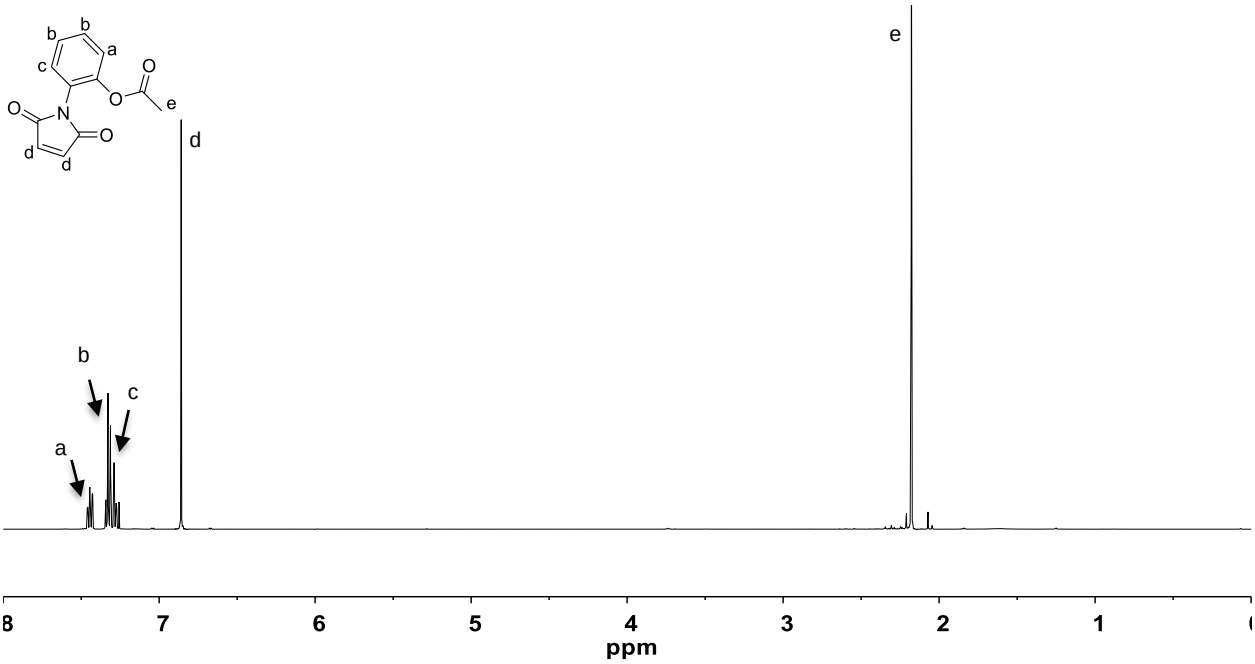

Figure 71. ^{1}H NMR spectra of (*o*-acetate)-*N*-phenylmaleimide (**7**).

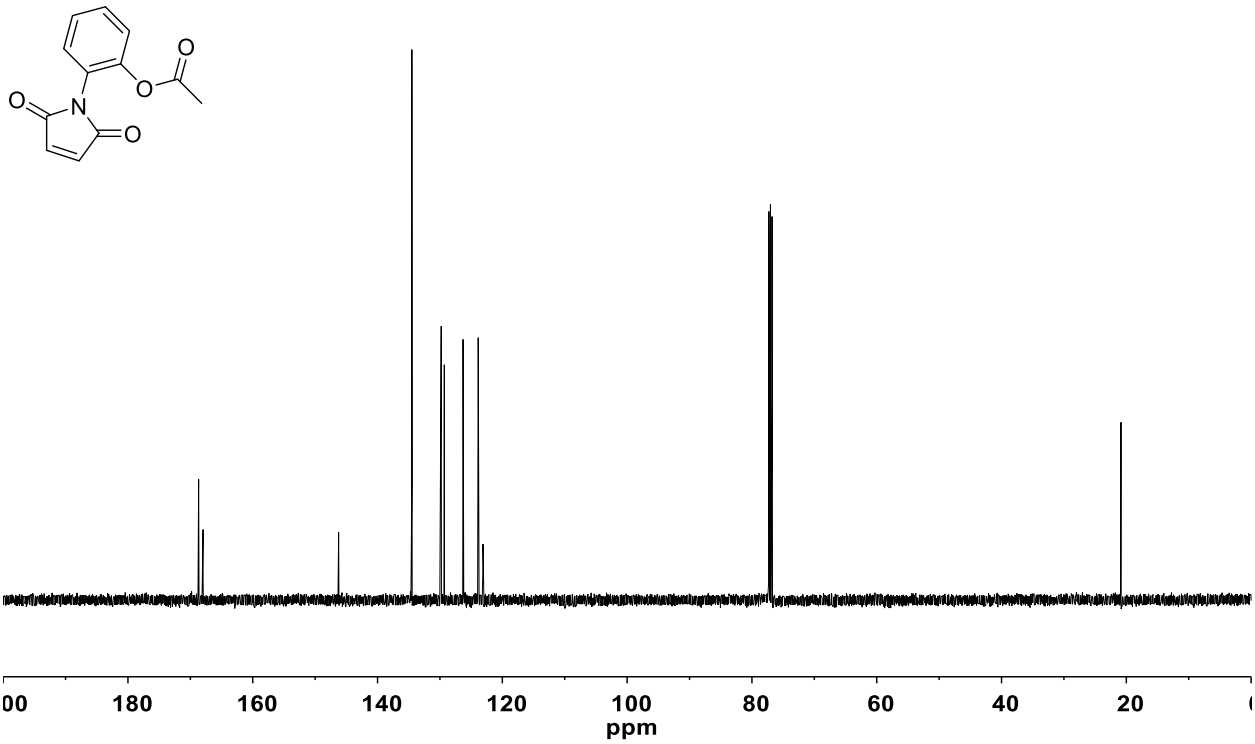

Figure 72. ^{13}C NMR spectra of (*o*-acetate)-*N*-phenylmaleimide (**7**).

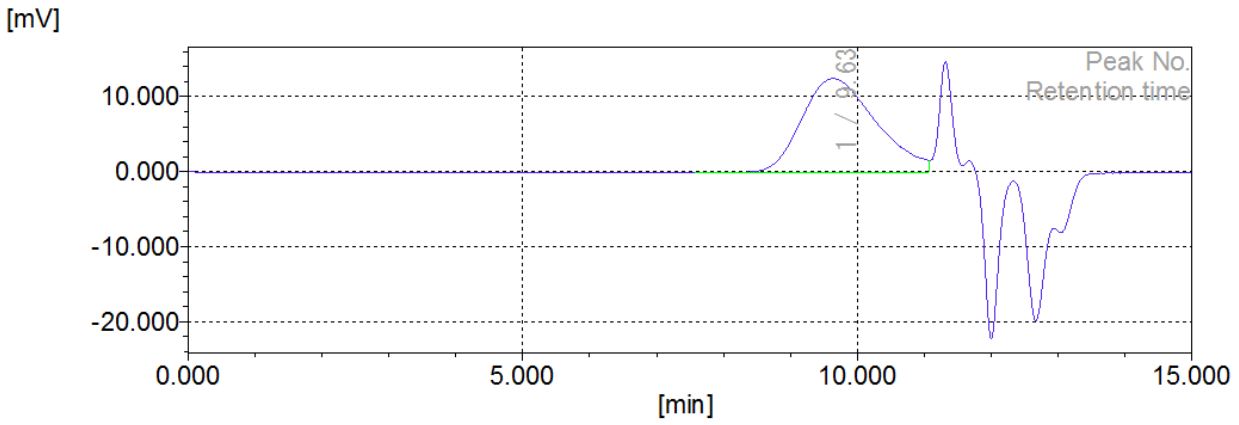

Result of molecular weight calculation (RI)

Peak 1 Valley Peak

	[min]	[mV]	[mol]		
Peak start	7.583	-0.073	72,523	Mn	2,425
Peak top	9.630	12.432	4,713	Mw	4,748
Peak end	11.077	1.449	323	Mz	7,707
				Mz+1	13,460
				Mv	4,748
Height [mV]			12.555	Mp	4,949
Area [mV*sec]			968.099	Mz/Mw	1.623
Area% [%]			100.000	Mw/Mn	1.958
[eta]			4747.57393	Mz+1/Mw	2.835

Figure 73. GPC trace and data for (*o*-acetate)-*N*-phenylmaleimide/norbornene copolymer (**8**).

Appendix D: Experimental Methods and Supporting information for Chapter 4

Density characterization. The density of the membrane samples was measured by using a density-gradient column (American Density Materials, Inc.). The pre-calibrated 0.95 and 1.03 g/cm^3 density floats with an accuracy of ±0.0002 g/cm^3 were added and remained suspended in the column at the level where their densities were the same as that of the liquid. After stabilization of the density floats, cross-linked PDMSPNB membranes were added and allowed to descend to different levels in the columns. A calibration chart was drawn to calculate the densities of the membranes.

Rheology measurements. Small-amplitude oscillatory shear (SAOS) measurements of membrane samples were carried out on an AR2000ex rheometer (TA Instruments) by using 4 mm plates with a parallel-plate geometry. The temperature was controlled by an environmental test chamber with nitrogen as a gas source. Prior to measurements, the sample was purged at 298 K for 3 h under a nitrogen atmosphere to ensure thermal equilibrium was achieved. All samples were measured at 298 K with a frequency sweep from 100 to 0.01 Hz, for which only cross-linked networks contributed to the storage modulus. The cross-link densities of the membranes were calculated by using the measured shear modulus (Equation 21):[183-185]

$$c_x = \frac{\rho}{2M_x} = \frac{G'}{2RT} \tag{21}$$

in which c_x is the number of moles of cross-links per unit volume, 1 is the density of cross-linked polymer, M_x is the number-average molecular weight of the polymer segments between cross-links, G' is the plateau value of the real part of the shear modulus, R is the gas constant, and T is the temperature in Kelvin.

Gas permeability measurements. Single-gas permeation measurements were performed on the cross-linked membranes by using a custom-made test chamber.[186] This system, which consisted of a feed and permeate chamber separated by the test membrane, measured transient permeation through the membranes. Before loading, the

membrane sample was mounted on a 47 mm nonporous aluminum tape sample disc with a hole (typically 10 mm in diameter) cut in the center and the membrane edges were sealed to aluminum by using epoxy (Devcon). The membrane sample was then carefully placed on a highly porous stainless-steel support that provided mechanical stability and negligible resistance to gases, and the entire assembly was installed in the test chamber. After loading the membrane, the chamber was evacuated with a mechanical pump to a base pressure of 20 mtorr (1 torr = 133.322 Pa). The membrane was allowed to remain in the test chamber overnight to fully degas residual solvents and to reach a steady base pressure. The mixed-gas permeation measurements (50/50 mol % CO_2/N_2) of the sample with a PDMSPNB to Grubbs II ratio of 130:1 were carried out. Feed and permeate compositions were determined by using a Buck Scientific gas chromatograph equipped with silica-gel packed and molecular sieve 13 x columns and a thermal conductivity detector (TCD). The gas mixture was controlled by using mass flow controllers (MKS Instruments).

Gas Solubility measurements. Low-pressure CO_2 solubility measurements were acquired by using an Intelligent Gravimetric Analyzer (Hiden Analytical Limited, UK).[186] In a typical experiment, approximately 50 mg of a particular membrane sample was loaded into a quartz container and evacuated to 0.003 bar (1 bar =$1x10^5$ Pa) for 6 h at 150 °C to degas and dry the sample. All measurements were acquired at room temperature. The mass uptake (corrected for buoyancy) was then measured as a function of pressure up to a final pressure of 1 atm (= 101325 Pa) to obtain the absorption isotherm. Desorption isotherms were subsequently acquired by measuring the mass as a function of decreasing pressure to ensure that the solubility behavior was reversible and to test for hysteresis effects. The solubility was then calculated from the slope of the adsorption isotherm in the low carbon dioxide concentration regime.

Positron annihilation lifetime spectroscopy. Positron annihilation lifetime spectroscopy (PALS) is widely used to analyze the free volume in the membrane structure.[187-189] Membranes with different cross-link densities were measured at room

temperature by using a conventional sample–source–sample sandwich geometry. The positron source was made from a solution of ^{22}NaCl evaporated onto the surface of the samples. The two stacked identical membranes were wrapped in thin aluminum foil to generate a sample assembly. The 1.274 MeV gamma ray, which indicated a positron emission event, and the 0.511 MeV annihilation gamma rays were detected by using a fast scintillator (BaF_2), coupled with photomultiplier tubes (PMTs). Different from the traditional experimental setup, a double-stop setup[190-191] was employed in this work. Data were obtained by using a digital oscilloscope with a system timing resolution of 158 ps.

Broadband dielectric spectroscopy. Broadband dielectric spectroscopy (BDS) measurements were performed by using a Novocontrol Concept 80 system in the frequency range of 10^{-2}-10^{7} Hz. The system includes an Alpha-A impedance analyzer, a ZGS active sample cell interface, and a Quatro Cryosystem temperature-control unit. All membrane samples were made as circles with a diameter of 8 mm and placed between two gold-plated electrodes. The Pre-XL PDMSPNB sample was placed between electrodes separated by a Teflon spacer. The system was quenched to -140 °C before the samples were placed in the cryostat to avoid crystallization issues during the measurements. The experiments proceeded from low to high temperatures. The samples were equilibrated at each temperature for 10–20 min before the dielectric measurements were made.

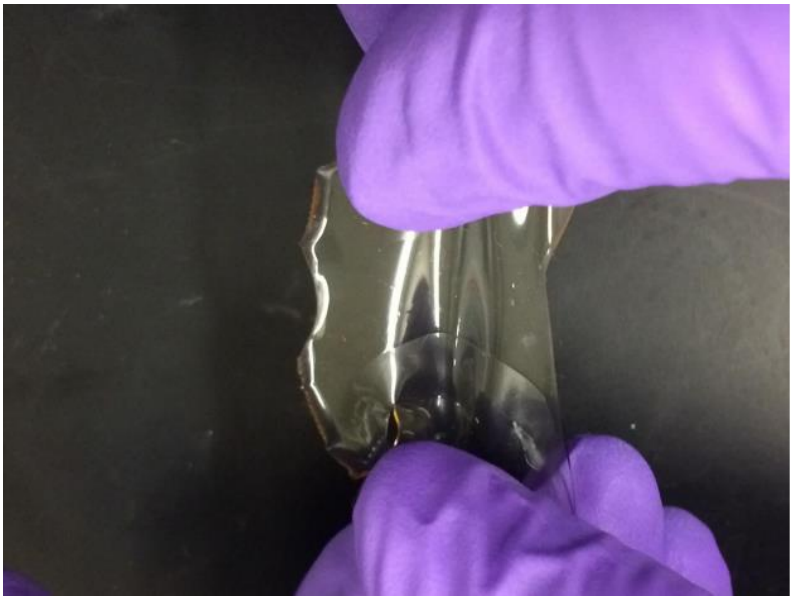

Figure 74. Picture of cross-linked PDMSPNB membrane showing free-standing transparent and mechanically strong properties.

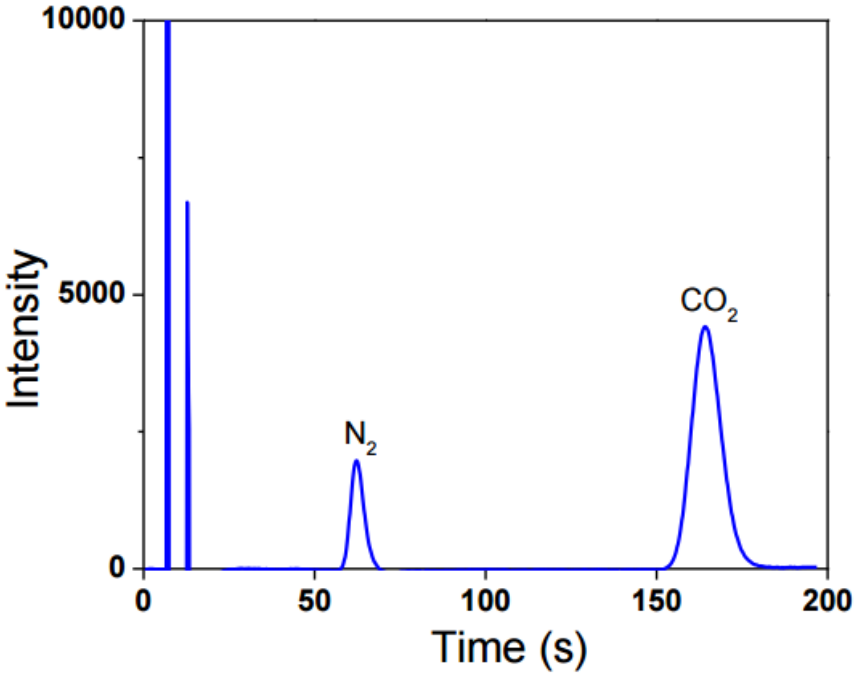

Figure 75. Mixed gas permeability data measured by gas chromatography (GC) in the permeate chamber as CO_2 and N_2 diffuse through the PDMSPNB membrane with c_x = 1.19 x 10^{-5} mol/cm^3. The sharp peaks before t = 25 s relate to the injection of the gas into the GC and can be ignored. The N_2 and CO_2 peaks are noted in the figure.

The CO_2 mole fraction was calculated from the following equations:

$$XCO_2 = \left(\frac{A_{CO_2}}{A_{CO_2} + A_{N_2}}\right)_{feed} \quad (22)$$

$$YCO_2 = \left(\frac{A_{CO_2}}{A_{CO_2} + A_{N_2}}\right)_{permeate} \quad (23)$$

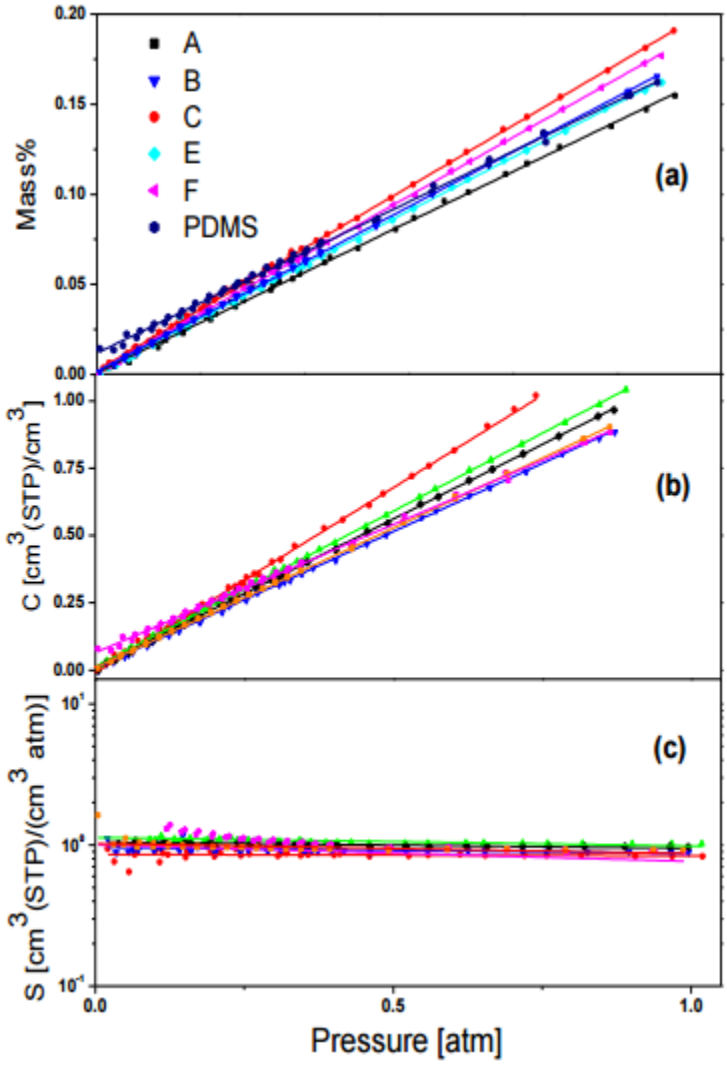

Figure 76. (**a**) Mass uptake of CO_2 in cross-linked PDMSPNB membranes (**b**) Sorption isotherms in cross-linked PDMSPNB membranes (**c**) CO_2 solubility in cross-linked PDMSPNB membranes.

Appendix E: Experimental Methods and Supporting information for Chapter 5.

General Methods and Materials: All air-free reactions were conducted under an inert atmosphere using an MBRAUN glovebox and a dry nitrogen atmosphere. All monomers were distilled from CaH_2 (x2) into a sealed bomb, and degassed via freeze-pump-thaw method (x3). Monomers were stored over 3Å molecular sieves in the glovebox prior to polymerization. Norbornene was purchased from Sigma-Aldrich and sublimed *in vacuo* at room temperature prior to use. Dicyclopentadiene, hydroquinone, calcium hydride, and 1.6M n-butyllithium in hexanes were purchased from Acros Organics and used as received. Cyclopentadiene was obtained by cracking dicyclopentadiene at 180 °C. Dichloromethane, toluene, and tetrahydrofuran were purchased from Fisher Scientific and were purified using an Innovative Technologies PureSolv Solvent Purification System and degassed via freeze-pump-thaw (x3) prior to their use in polymerizations. Methanol for polymer precipitation and tetrahydrofuran for film casting were used as received from Fischer Scientific. Silylated vinyl reagents were purchased from Gelest Inc. and used as received. $Ni_2(allyl)_2Cl_2$, $Pd_2(allyl)_2Cl_2$, $AgSbF_6$, bromopentafluorobenzene, triphenylantimony, $NiBr_2(dme)$, and 30 wt. % $Ni(NPh)_2$ in Toluene were purchased from Strem Chemical and were stored in the glovebox at -25 °C prior to use. Methylaluminoxane (MAO) was gifted from Albemarle Inc. and used as received.

Characterization: ^1H NMR spectroscopy of monomers and polymers were obtained by either a Bruker 400 MHz NMR or a Varian 500 MHz NMR in $CDCl_3$ and referenced to the residual solvent peak at δ = 7.26 ppm. Hi-res Mass Spectrometry was performed by using a JEOL AccuTOF equipped with a DART source. Polymers were characterized using either an Agilent EcoSEC GPC using THF at 40 °C and molecular weights calculated relative to polystyrene standards, or using a Malvern Viscotek HT-GPC with triple detection at 140 °C in 1,2,4-trichlorobenzene. Thermal gravimetric analysis was performed using a TA Instruments Q50 with a ramp rate of 20 °C/minute under a N_2 purge. Polymer densities were determined using a Mettler Toledo balance equipped with a

density kit based upon Archimedes principle. Measurements were taken Wide angle XRD experiments were performed using an Empyrean X-Ray Diffractometer from PANalytical that was equipped with a Cu K_α source run at 45kV and 40mA filtered with a nickel filter.

Membrane Preparation: Polymer membranes were solution cast from 5 wt. % solutions in THF onto a clean glass substrate. As an example, 0.468 g of the desired polymer was added to 10 mL of THF with a stir bar and stirred until fully dissolved. The resultant solution was taken up in a syringe and filtered through a 0.45 micron PTFE syringe filter onto a clean glass dish approximately 6 cm in diameter. After deposition, the solution was covered to slow evaporation and the polymer films were removed from the substrate after 48 hours.

Permeation Analysis: Permeability measurements were obtained using a custom-built permeation instrument operating upon the concept of constant-volume variable-pressure gas flux to obtain as described in the Springer Handbook[14] and by equation (5) For all gas measurements, the downstream volume (V_d) used was calculated by Burnett expansions to be 1327.903 cm^3. Thickness (l) of polymer films were between 90-120 microns. Upstream pressure (P_u) was calculated as an average for the duration of the steady-state permeation measurement. Surface area of the polymer materials were measured using ImageJ software. R = 0.278 [cm·Hg·cm^3]/[cm^3 (STP) K]. Temperature was recorded outside the sample cell over the course of steady-state permeation and averaged to give T. Leak rates of the polymer samples were in the range of 3-6 x 10^{-6} cm·Hg/s, which was always lower than 10 % of the overall system flux. Selectivity is calculated as a ratio of $P(CO_2)/P(N_2)$.

Synthesis of *trans*-[Ni(C_6F_5)$_2$($SbPh_3$)$_2$] catalyst (11). The catalyst *trans*-[Ni(C_6F_5)$_2$($SbPh_3$)$_2$] was synthesized following a modified literature procedure of a structurally similar *trans*-[Ni($C_6Cl_2F_3$)$_2$($SbPh_3$)$_2$] complex.[133] Therein, n-Butyllithium (4.10 mL, 1.6 M solution in hexane, 6.48 mmol) was added dropwise to a solution of bromopentafluorobenzene (1.60 g, 6.48 mmol) in dry Et_2O (50 mL) at -78 °C. The reaction

mixture was stirred at this temperature for 1 h before $SbPh_3$ (2.75 g, 7.78 mmol) and [$NiBr_2$(dme)] (1.00 g, 3.24 mmol) were added sequentially. The resulting suspension was stirred overnight and warmed to room temperature. Wet Et_2O (20 mL) was added and the suspension was evaporated to dryness. The residue was extracted using $CHCl_3$ (60 mL) and the filtrate was evaporated to 5 mL, treated with ethanol (20 mL) where the resulting suspension was filtered, washed with ethanol, and dried *in vacuo* to yield 1.98 g (55.4 % yield) of yellow solid. ^{1}H NMR ($CDCl_3$, 293 K): δ (ppm) = 7.01-7.56 (30H, m, PhH). ^{19}F NMR ($CDCl_3$, 293 K): δ (ppm) = -137.44, -149.75, -160.30.

Synthesis of 5-trimethylsilyl-2-norbornene (12b). To a 50 mL glass pressure tube equipped with a stir bar was added vinyltrimethylsilane (5.00 g, 49.88 mmol), and cyclopentadiene (1.65 g, 25.02 mmol). The pressure tube was sealed and heated to 180 °C for 12 hours. After cooling, the mixture was purified by distillation at reduced pressure (23 torr, 95-100 °C) to yield 2.52 g of the desired monomer **12b** (32.7 % yield) as a mixture of *endo*:*exo* isomers (*endo*:*exo* = 68:32). ^{1}H NMR ($CDCl_3$, 293 K, *endo* isomer): δ (ppm) = 5.96 (1H, m), 5.93 (1H, m), 2.95 (1H, s), 2.88 (1H, s), 1.87 (1H, ddd), 1.20-1.01 (3H, m), 0.94 (1H, m), -0.08 (9H, s) ^{13}C NMR ($CDCl_3$, 293 K, *endo/exo mixture*): δ (ppm) = 138.5, 135.4, 133.9, 133.1, 51.5, 46.8, 44.8, 42.9, 42.5, 42.4, 27.1, 27.0, 25.3, 25.2, -1.4, -2.0 $HRMS^{calc}$ $C_{10}H_{18}Si$ (H^+ adduct) = 167.2560 m/z $HRMS^{expt}$ $C_{10}H_{18}Si$ (H^+ adduct) = 167.1251 m/z.

Synthesis of 5-triethoxysilyl-2-norbornene (12c). To a 50 mL glass pressure tube equipped with a stir bar was added vinyltriethoxysilane (10.00 g, 52.55 mmol), dicyclopentadiene (3.31 g, 25.0 mmol), and hydroquinone (0.010 g, catalytic). The pressure tube was sealed and heated to 180 °C for 12 hours. After cooling, the mixture was purified by distillation at reduced pressure (7 torr, 125-130 °C) to yield 3.84 g of the desired monomer **12c** (59.8 % yield) as a mixture of *endo:exo* isomers (*endo:exo* = 65:35). ^{1}H NMR ($CDCl_3$, 293 K, *endo* isomer): δ (ppm) = 6.09 (1H, m), 5.88 (1H, m), 3.81 (6H, q), 2.88 (2H, s), 1.74 (1H, ddd), 1.19 (9H, t), 1.15-1.02 (3H, m), 0.43 (1H, ddd) ^{13}C NMR ($CDCl_3$, 293 K, *endo/exo mixture*): δ (ppm) = 137.7, 135.2, 134.6, 133.6, 58.4, 58.2,

50.8, 46.9, 44.2, 42.8, 42.4, 42.1, 26.9, 26.2, 20.8, 20.2, 18.3, 18.2 $HRMS^{calc}$ $C_{13}H_{24}O_3Si$ (H^+ adduct) = 257.1573 m/z $HRMS^{expt}$ $C_{13}H_{24}O_3Si$ (H^+ adduct) = 257.1579 m/z.

Synthesis of 5-diethoxymethylsilyl-2-norbornene (12d). To a 50 mL glass pressure tube equipped with a stir bar was added vinyldiethoxymethylsilane (10.00 g, 62.39 mmol), dicyclopentadiene (2.78 g, 29.7 mmol), and hydroquinone (0.010 g, catalytic). The pressure tube was sealed and heated to 180 °C for 12 hours. After cooling, the mixture was purified by distillation at reduced pressure (5 torr, 97-100 °C) to yield 3.66 g of the desired monomer **12d** (50.8 % yield) as a mixture of *endo:exo* isomers (*endo:exo* = 56:44). ^1H NMR ($CDCl_3$, 293 K, *endo* isomer): δ (ppm) = 6.11 (1H, m), 5.88 (1H, m) 3.75 (4H, m), 2.89 (1H, s), 2.84 (1H, s), 1.85 (1H, ddd), 1.27-0.98 (6H, t), 1.10-0.98 (3H, m), 0.42 (1H, ddd), 0.10 (3H, s) ^{13}C NMR ($CDCl_3$, 293 K, *endo/exo mixture*): δ (ppm) = 137.9, 135.5, 134.3, 133.5, 58.2, 58.1, 58.0, 57.9, 51.0, 47.0, 44.1, 42.6, 42.4, 42.2, 26.7, 26.2, 23.2, 18.4, -4.8, -5.4 $HRMS^{calc}$ $C_{12}H_{22}O_2Si$ (H^+ adduct) = 227.1467 m/z $HRMS^{expt}$ $C_{12}H_{22}O_2Si$ (H^+ adduct) = 227.1472 m/z.

Synthesis of 5-ethoxydimethylsilyl-2-norbornene (12e). To a 50 mL glass pressure tube equipped with a stir bar was added vinylethoxydimethylsilane (10.00 g, 76.77 mmol), dicyclopentadiene (4.83 g, 36.6 mmol), and hydroquinone (0.010 g, catalytic). The pressure tube was sealed and heated to 180 °C for 12 hours. After cooling, the mixture was purified by distillation at reduced pressure (5 torr, 100-108 °C) to yield 3.98 g of the desired monomer **12e** (47.7 % yield) as a mixture of *endo:exo* isomers (*endo:exo* = 46:54). ^1H NMR ($CDCl_3$, 293 K, *endo* isomer): δ (ppm) = 5.95 (1H, m), 5.92 (1H, m), 3.66 (2H, q), 2.90 (1H, s), 2.79 (1H, s), 1.60 (1H, ddd), 1.16 (3H, t),1.13-1.04 (3H, m), 0.39 (1H, ddd), 0.10 (6H, d) ^{13}C NMR ($CDCl_3$, 293 K, *endo/exo mixture*): δ (ppm) = 138.1, 135.5, 134.1, 133.3, 58.3, 58.1, 51.3, 46.9, 44.4, 42.6, 42.4, 42.3, 26.9, 26.5, 25.3, 25.2, 18.6, -1.8, -2.1, -2.4, -2.6 $HRMS^{calc}$ $C_{11}H_{20}OSi$ (H^+ adduct) = 197.1362 m/z $HRMS^{expt}$ $C_{11}H_{20}OSi$ (H^+ adduct) = 197.1368 m/z.

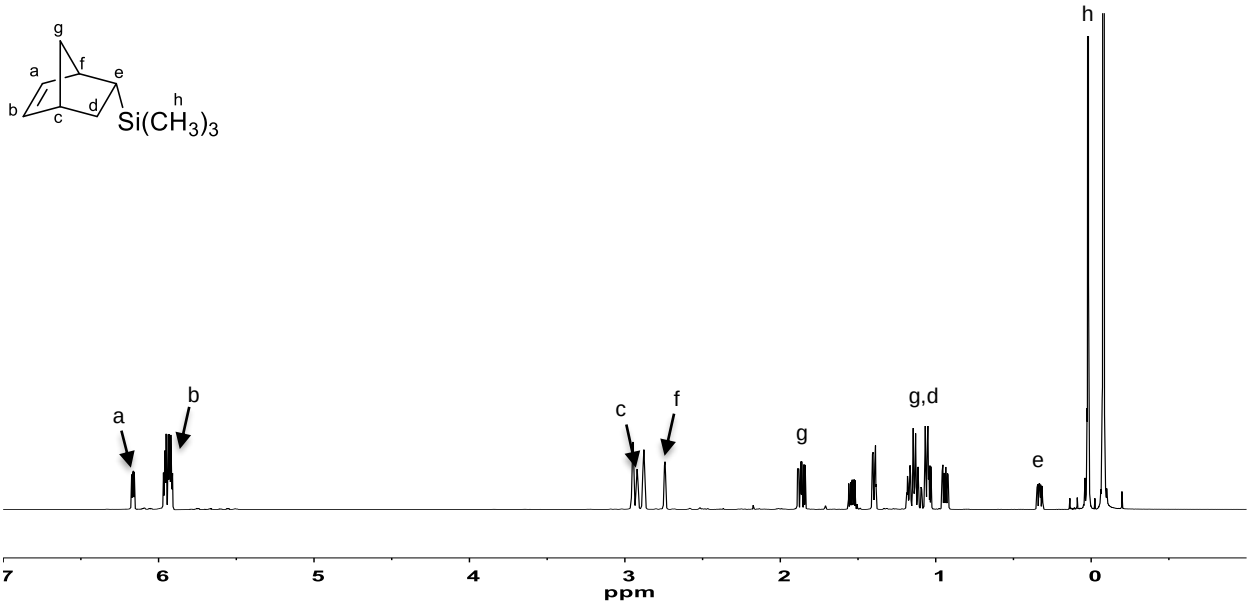

Figure 77. ^{1}H NMR spectra of 5-trimethylsilyl-2-norbornene (**12b**) as *endo:exo* mixture (*endo* isomer labeled).

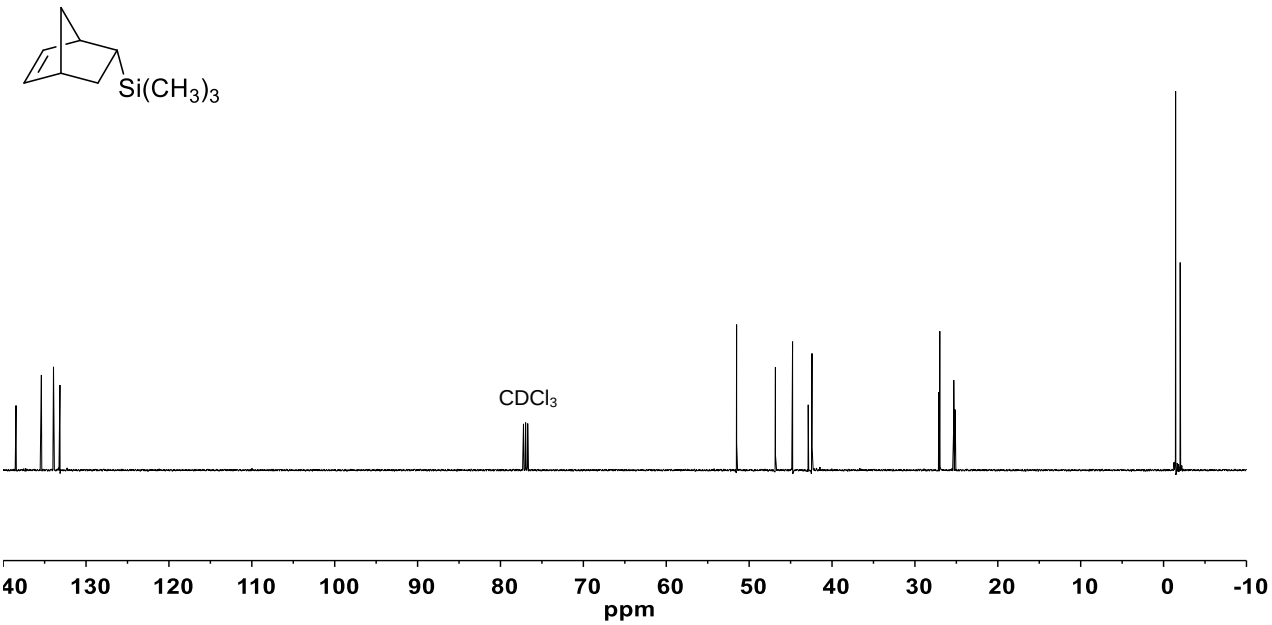

Figure 78. ^{13}C NMR spectra of 5-trimethylsilyl-2-norbornene (**12b**) as *endo:exo* mixture.

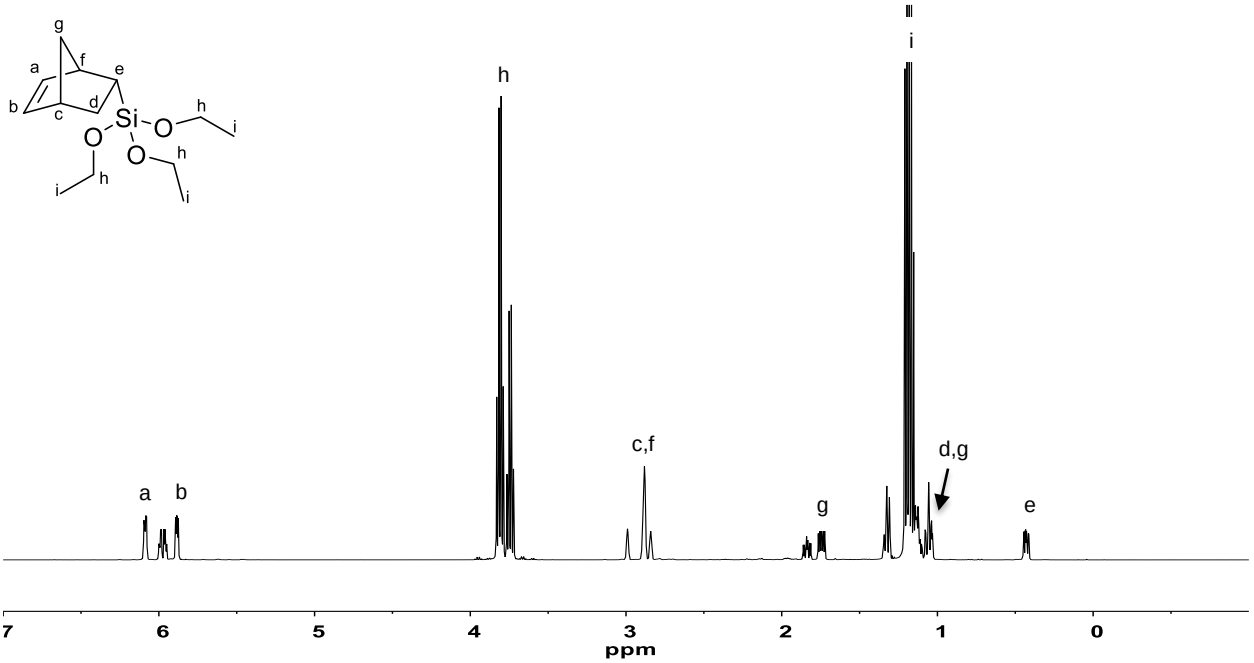

Figure 79. ^{1}H NMR spectra of 5-triethoxysilyl-2-norbornene (**12c**) as *endo:exo* mixture (*endo* isomer labeled).

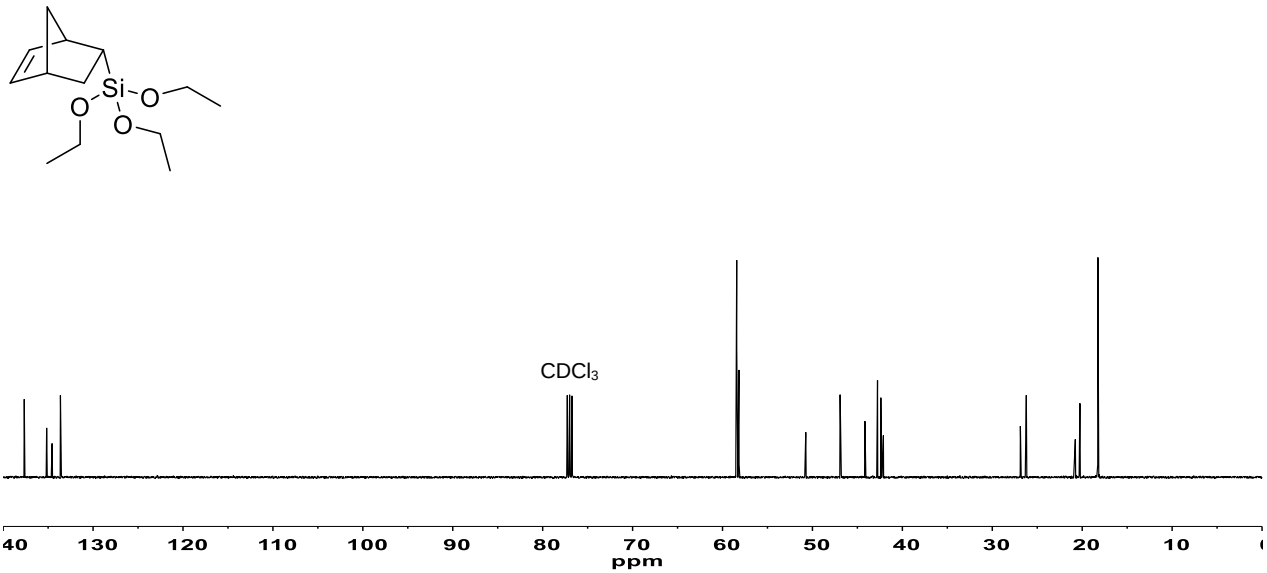

Figure 80. ^{13}C NMR spectra of 5-triethoxysilyl-2-norbornene (**12c**) as *endo:exo* mixture.

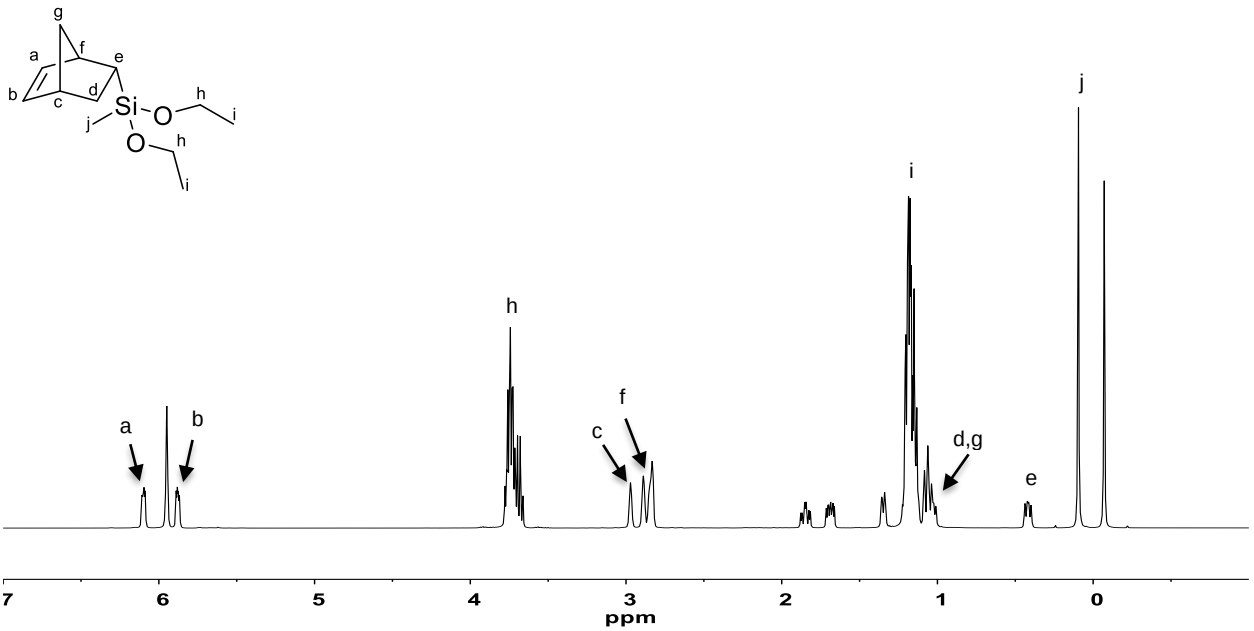

Figure 81. ^{1}H NMR spectra of 5-diethoxymethylsilyl-2-norbornene (**12d**) as *endo:exo* mixture (*endo* isomer labeled).

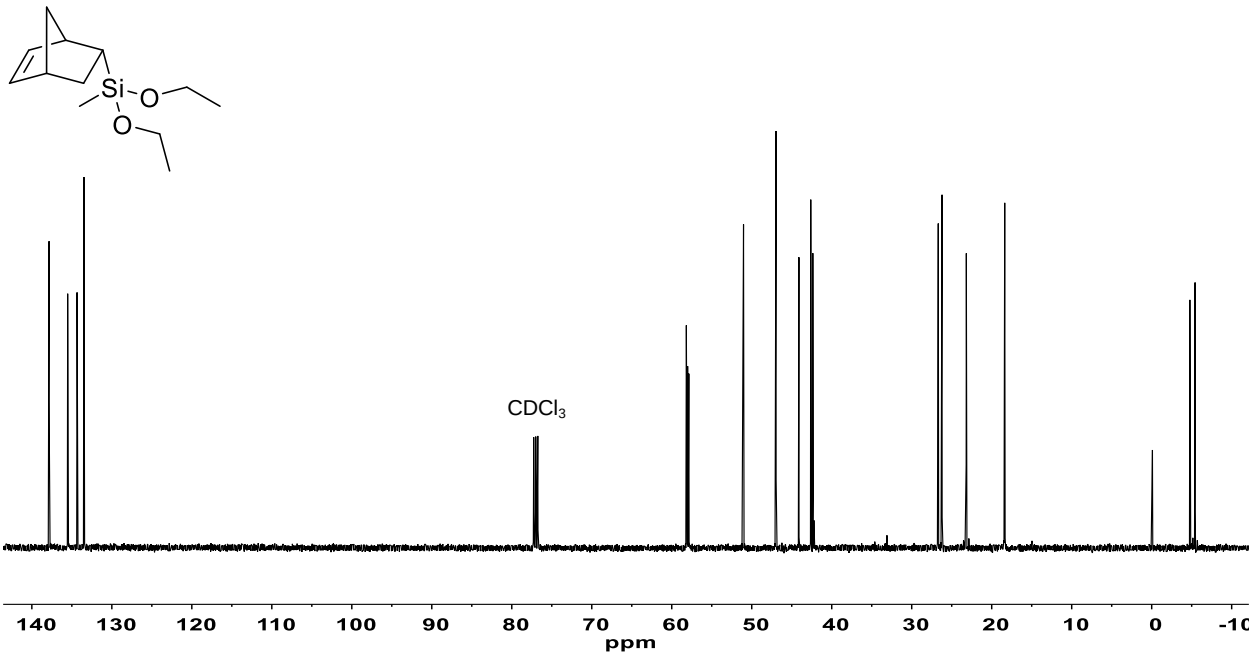

Figure 82. ^{13}C NMR spectra of 5-diethoxymethylsilyl-2-norbornene (**12d**) as *endo:exo* mixture.

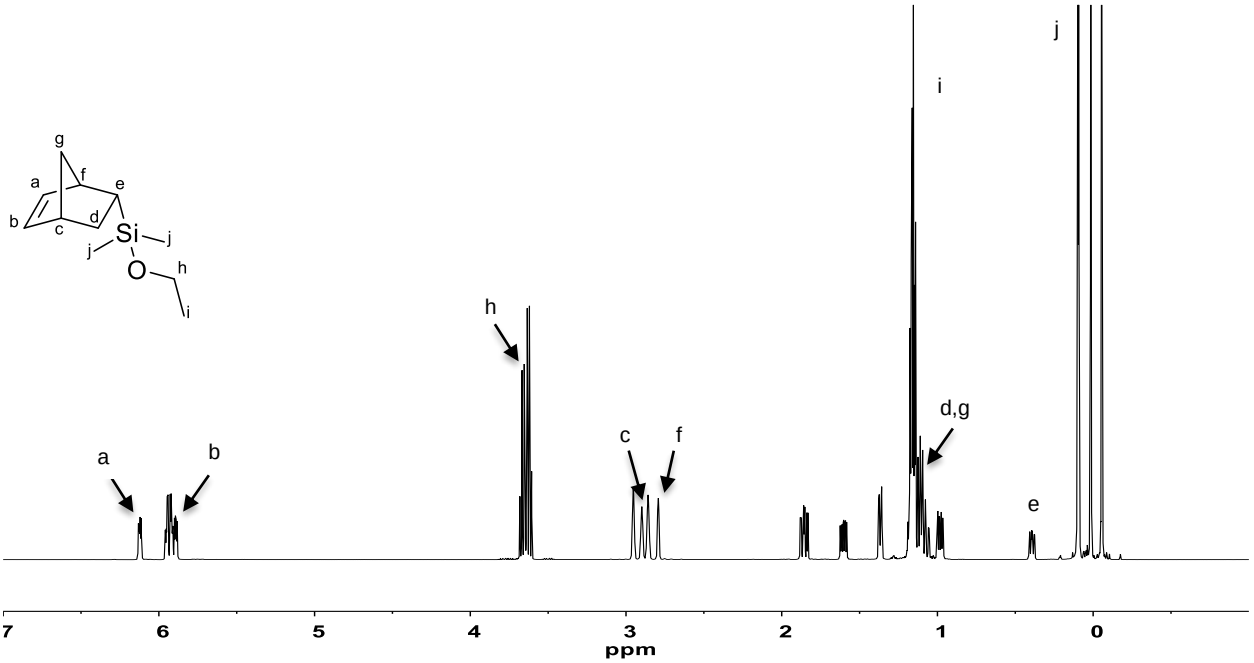

Figure 83. ^{1}H NMR spectra of 5-ethoxydimethylsilyl-2-norbornene (**12e**) as *endo:exo* mixture (*endo* isomer labeled).

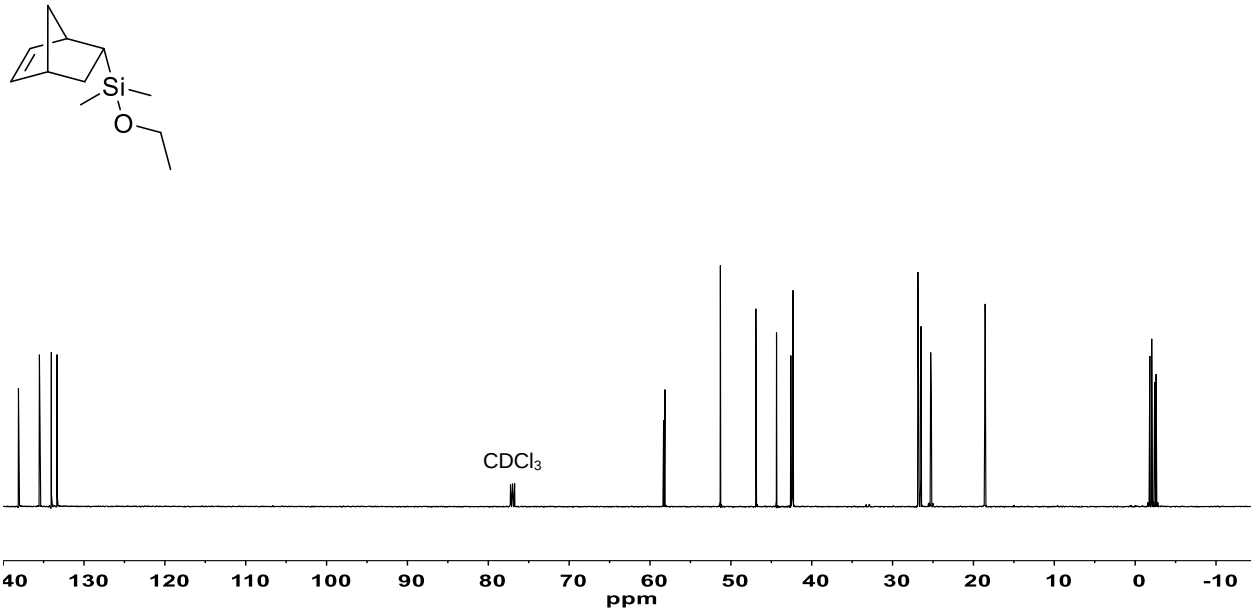

Figure 84. ^{13}C NMR spectra of 5-ethoxydimethylsilyl-2-norbornene (**12e**) as *endo:exo* mixture.

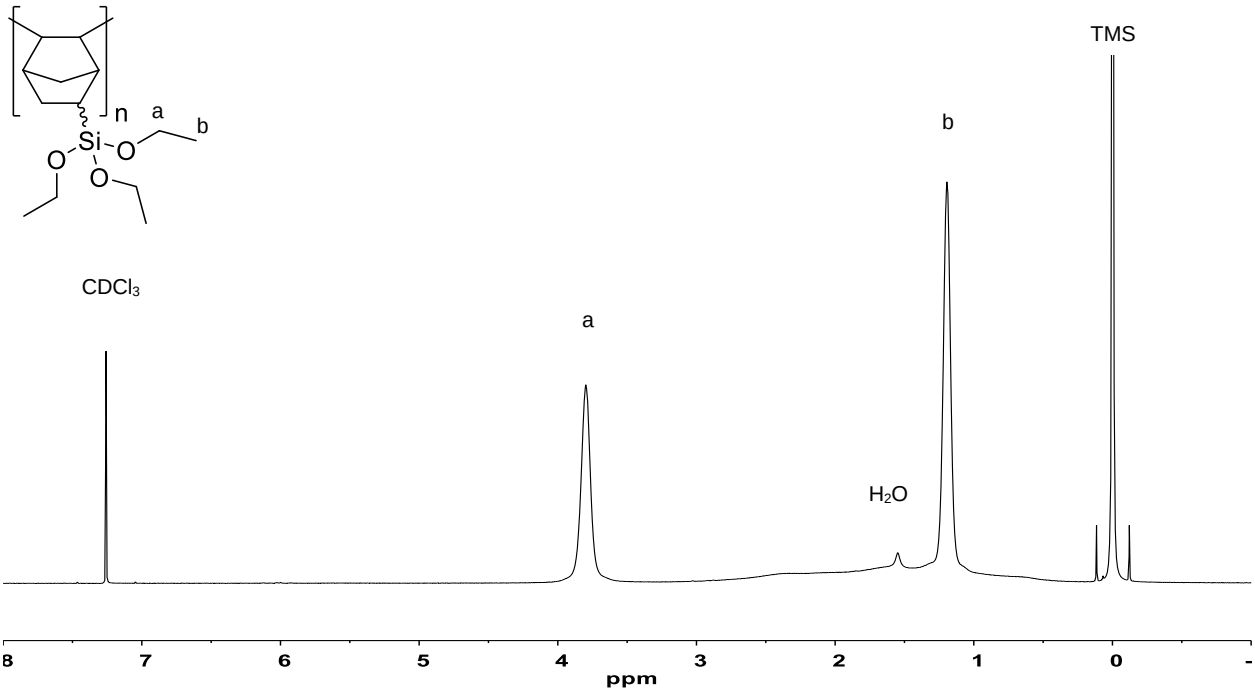

Figure 85. [1]H NMR spectra of poly(5-triethoxysilyl-2-norbornene) (**13c**).

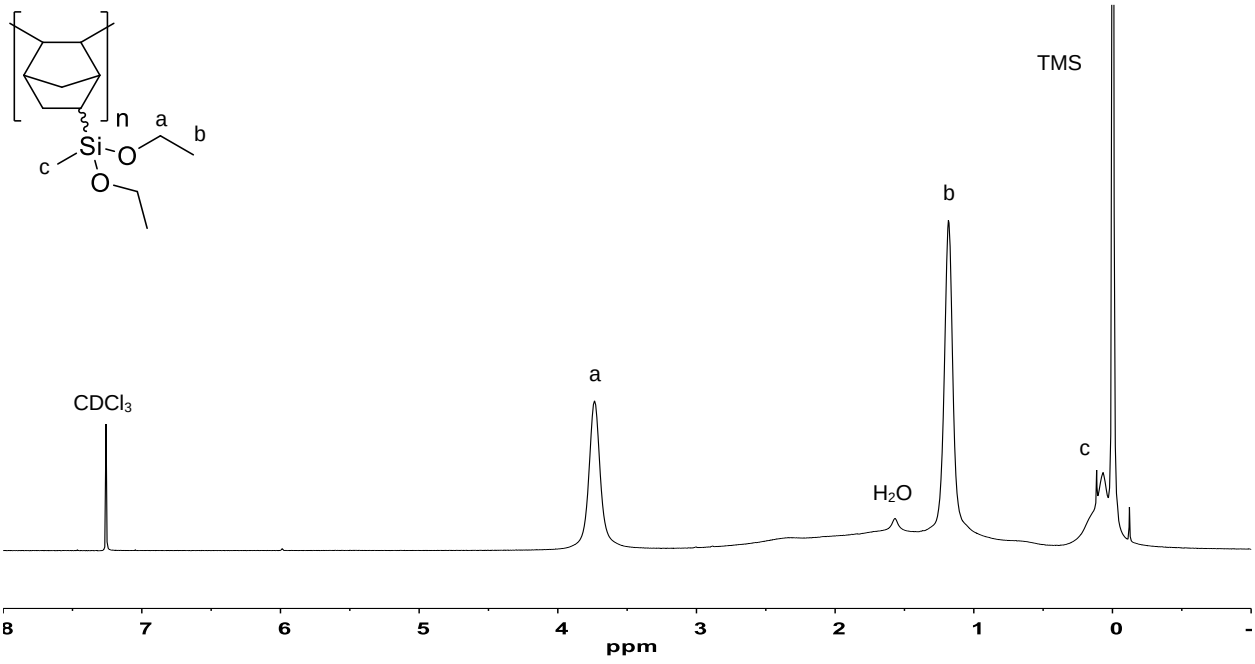

Figure 86. [1]H NMR spectra of poly(5-diethoxymethylsilyl-2-norbornene) (**13d**).

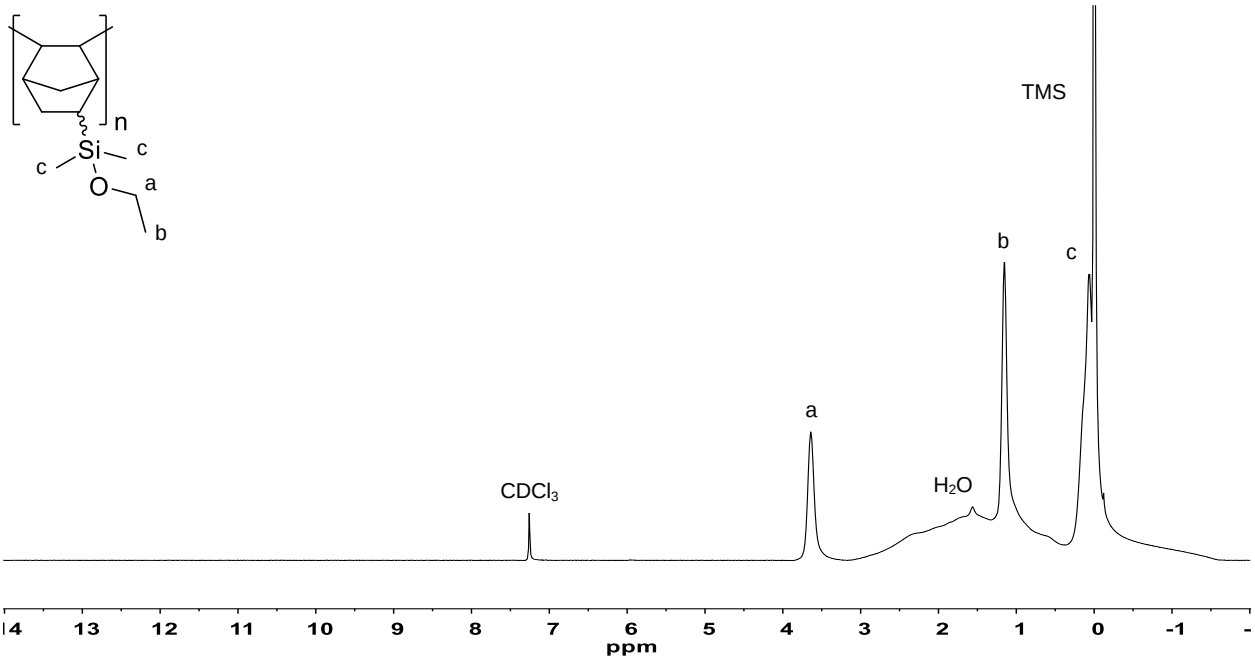

Figure 87. ^{1}H NMR spectra of poly(5-ethoxydimethylsilyl-2-norbornene) (**13e**).

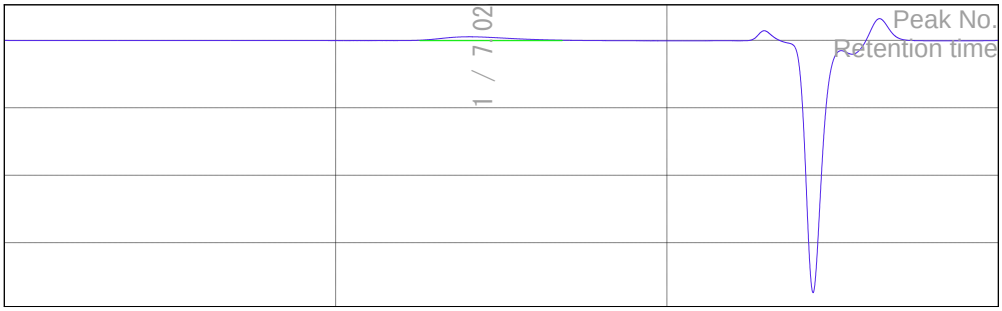

Result of molecular weight calculation (RI)

Peak 1 Valley Peak

	[min]	[mV]	[mol]
Peak start	6.268	0.267	746,022
Peak top	7.020	5.429	232,080
Peak end	8.422	0.294	36,221
Height [mV]			5.773
Area [mV*sec]			418.212
Area% [%]			100.000
[eta]			219637.68758

Mn	149,848
Mw	219,638
Mz	296,541
Mz+1	370,323
Mv	219,638
Mp	220,047
Mz/Mw	1.350
Mw/Mn	1.466
Mz+1/Mw	1.686

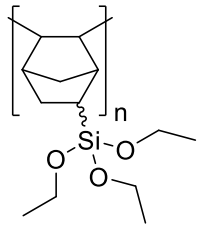

Figure 88. GPC analysis of poly(5-triethoxysilyl-2-norbornene) (**13c**) after 24-hour reaction period (**Table 5**, **entry 12** and **Table 6 entry 1**).

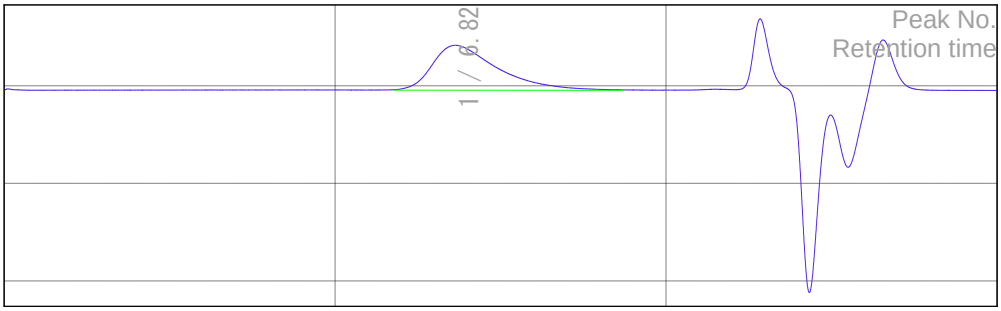

Result of molecular weight calculation (RI)

Peak 1 Valley Peak

	[min]	[mV]	[mol]
Peak start	5.892	-0.763	1,873,675
Peak top	6.820	8.335	302,374
Peak end	9.350	-0.819	8,692
Height [mV]			9.233
Area [mV*sec]			632.292
Area% [%]			100.000
[eta]			275215.39865

Mn	154,434
Mw	275,215
Mz	402,759
Mz+1	563,819
Mv	275,215
Mp	276,904
Mz/Mw	1.463
Mw/Mn	1.782
Mz+1/Mw	2.049

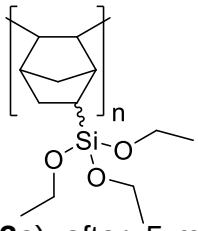

Figure 89. GPC analysis of poly(5-triethoxysilyl-2-norbornene) (**13c**) after 5-minute reaction period (**Table 6**, **entry 4**).

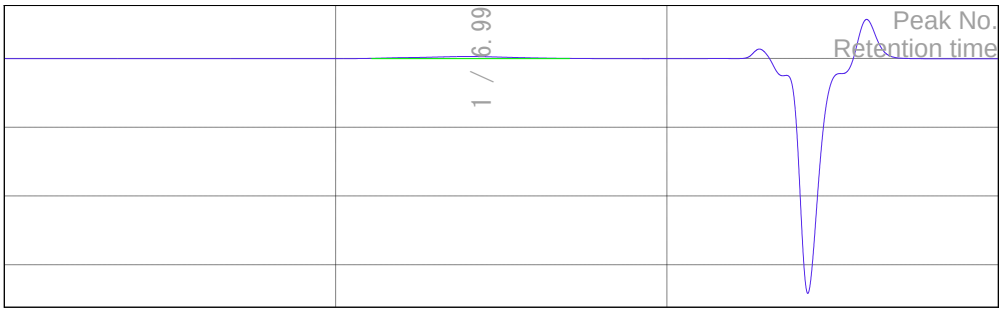

Result of molecular weight calculation (RI)

Peak 1 Valley Peak

	[min]	[mV]	[mol]
Peak start	5.538	0.245	6,691,353
Peak top	6.998	3.015	238,643
Peak end	8.533	0.188	30,678
Height [mV]			3.236
Area [mV*sec]			329.680
Area% [%]			100.000
[eta]			517634.72715

Mn	175,664
Mw	517,635
Mz	1,773,937
Mz+1	3,425,646
Mv	517,635
Mp	220,514
Mz/Mw	3.427
Mw/Mn	2.947
Mz+1/Mw	6.618

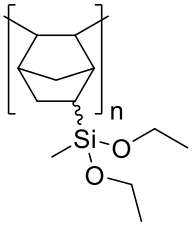

Figure 90. GPC analysis of poly(5-diethoxymethylsilyl-2-norbornene) (**13d**) after 24-hour reaction period (**Table 6**, **entry 2**).

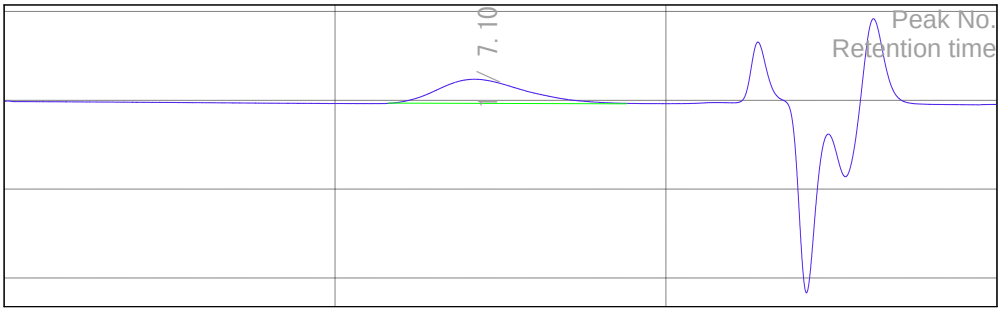

Result of molecular weight calculation (RI)

Peak 1 Valley Peak

	[min]	[mV]	[mol]
Peak start	5.800	-0.653	2,490,510
Peak top	7.105	4.776	208,287
Peak end	9.408	-0.679	7,935
Height [mV]			5.456
Area [mV*sec]			498.027
Area% [%]			100.000
[eta]			226065.70649

Mn	106,878
Mw	226,066
Mz	400,935
Mz+1	651,277
Mv	226,066
Mp	198,471
Mz/Mw	1.774
Mw/Mn	2.115
Mz+1/Mw	2.881

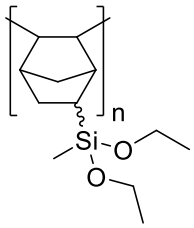

Figure 91. GPC analysis of poly(5-diethoxymethylsilyl-2-norbornene) (**13d**) after 5-minute reaction period (**Table 6**, **entry 5**).

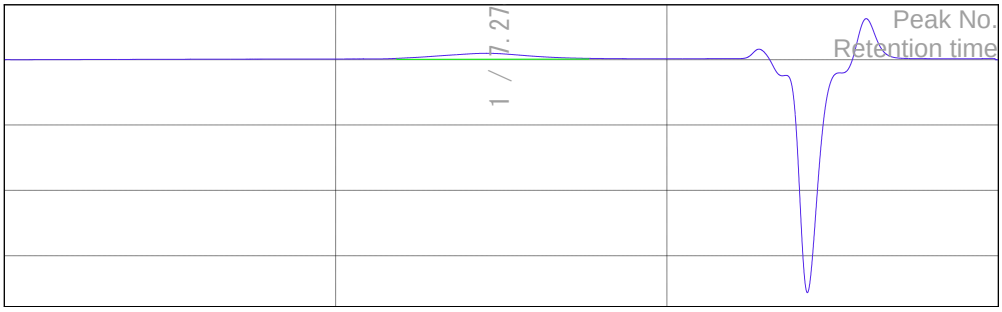

Result of molecular weight calculation (RI)

Peak 1 Valley Peak

	[min]	[mV]	[mol]
Peak start	5.920	2.013	1,725,427
Peak top	7.273	9.827	168,720
Peak end	8.820	2.003	19,833
Height [mV]			9.045
Area [mV*sec]			861.988
Area% [%]			100.000
[eta]			252005.32806

Mn	119,577
Mw	252,005
Mz	509,420
Mz+1	835,721
Mv	252,005
Mp	168,721
Mz/Mw	2.021
Mw/Mn	2.107
Mz+1/Mw	3.316

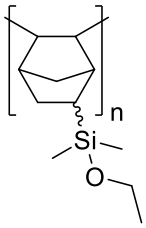

Figure 92. GPC analysis of poly(5-ethoxydimethylsilyl-2-norbornene) (**13e**) after 24-hour reaction period (**Table 6**, **entry 3**).

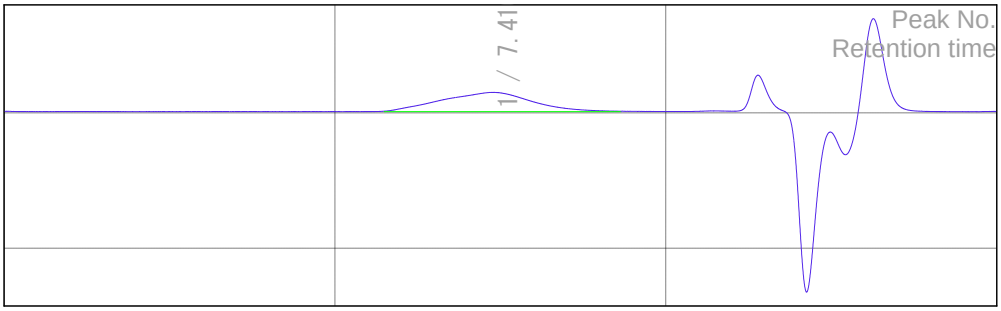

Result of molecular weight calculation (RI)

Peak 1 Valley Peak

	[min]	[mV]	[mol]
Peak start	5.742	0.628	3,031,074
Peak top	7.410	7.609	142,305
Peak end	9.317	0.659	9,156
Height [mV]			7.118
Area [mV*sec]			678.560
Area% [%]			100.000
[eta]			252629.72281

Mn	111,662
Mw	252,630
Mz	571,505
Mz+1	1,083,107
Mv	252,630
Mp	149,277
Mz/Mw	2.262
Mw/Mn	2.262
Mz+1/Mw	4.287

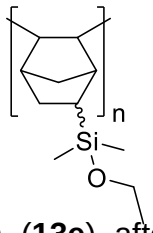

Figure 93. GPC analysis of poly(5-ethoxydimethylsilyl-2-norbornene) (**13e**) after 5-minute reaction period (**Table 6**, **entry 6**).

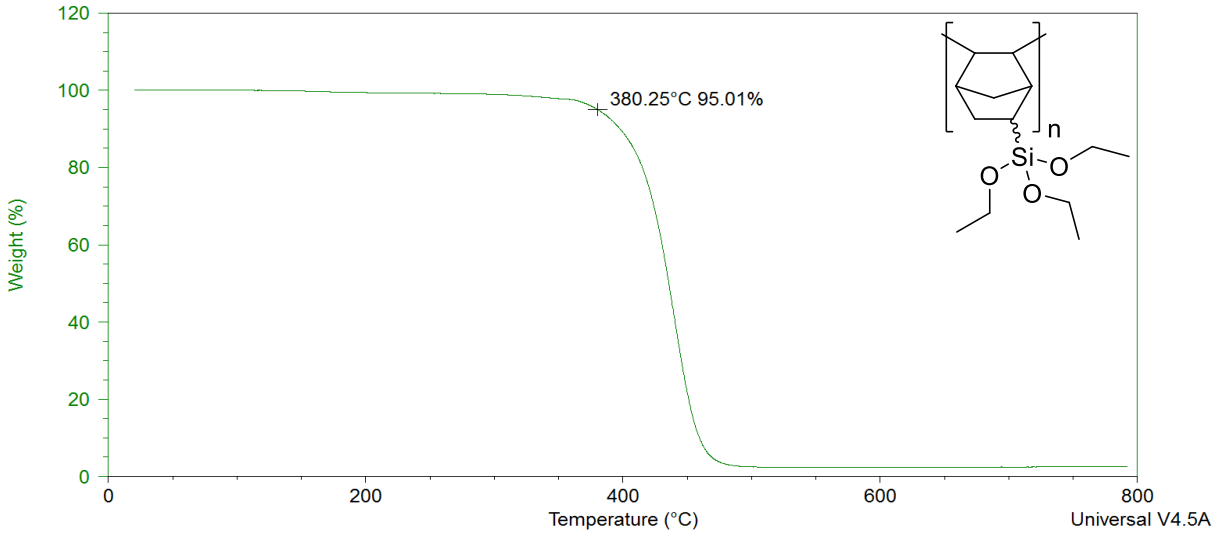

Figure 94. TGA analysis of poly(5-triethoxysilyl-2-norbornene) (**13c**) (**Table 6**, **entry 1**).

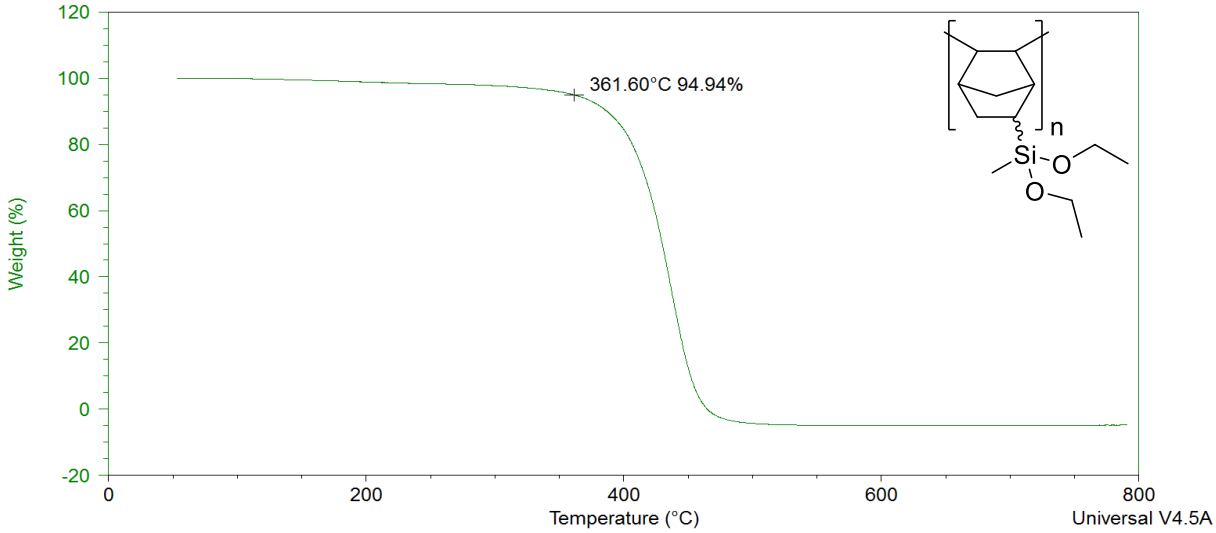

Figure 95. TGA analysis of poly(5-diethoxymethylsilyl-2-norbornene) (**13d**) (**Table 6**, **entry 2**).

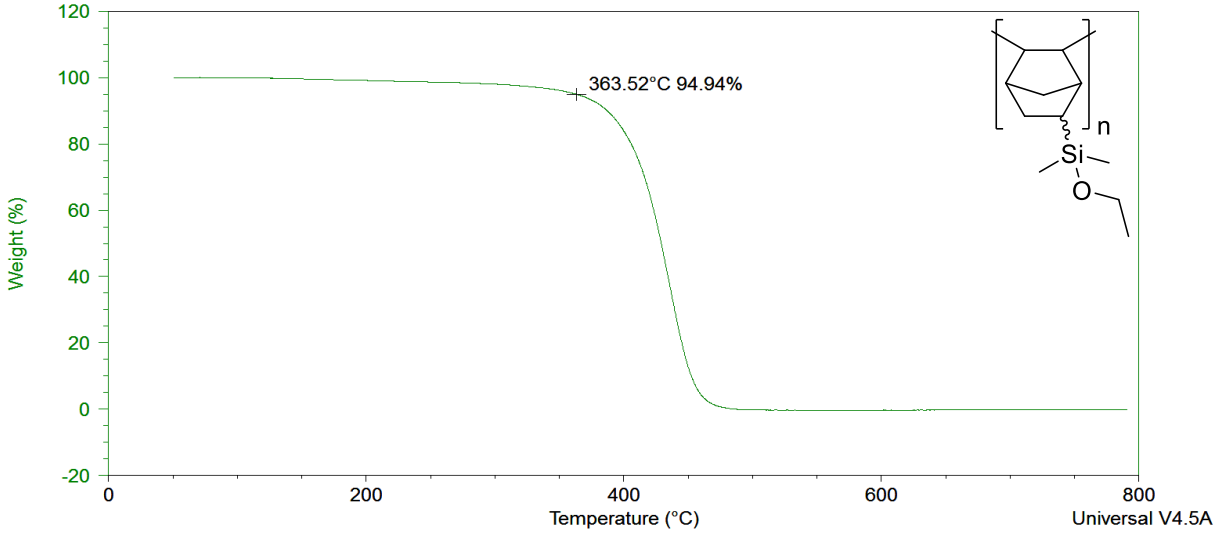

Figure 96. TGA analysis of poly(5-ethoxydimethylsilyl-2-norbornene) (**13e**) (**Table 6**, **entry 3**).

Appendix F: Experimental Methods and Supporting information for Chapter 6

General Methods and Materials. All air-free reactions were conducted under an inert atmosphere using an MBRAUN glovebox and a dry nitrogen atmosphere. Monomers were distilled from CaH_2 (x2) into a sealed bomb, degassed via freeze-pump-thaw method (x3), and stored over 3 Å molecular sieves in the glovebox prior to polymerization. Dicyclopentadiene was purchased from Acros Organics and used as received. Dichloromethane, toluene, and tetrahydrofuran were purchased from Fisher Scientific and were purified using an Innovative Technologies PureSolv Solvent Purification System and degassed via freeze-pump-thaw (x3) prior to their use in polymerizations. Methanol for polymer precipitation and tetrahydrofuran for film casting were used as received from Fisher Scientific. Triethoxyvinylsilane was purchased from Gelest Inc. and used as received. The catalyst *trans*-$[Ni(C_6F_5)_2(SbPh_3)_2]$ was synthesized as previously described11 and stored in the glovebox prior to use.

Monomer and Polymer Characterization. ^1H NMR spectroscopy of monomers and polymers were obtained by either a Bruker 400 MHz NMR or a Varian 500 MHz NMR in $CDCl_3$ and referenced to the residual solvent peak at δ = 7.26 ppm. Hi-res Mass Spectrometry was performed by using a JEOL AccuTOF equipped with a DART source. Polymers were characterized using an Agilent EcoSEC GPC using THF at 40 °C and molecular weights calculated relative to polystyrene standards. Thermal gravimetric analysis was performed using a TA Instruments Q50 with a ramp rate of 20 °C/minute under a N_2 purge. Polymer densities were determined using a Mettler Toledo balance equipped with a density kit based upon Archimedes Principle. Wide angle XRD measurements were performed using an Empyrean X-Ray Diffractometer from PANalytical that was equipped with a Cu K_α source run at 45 kV and 40 mA filtered with a nickel filter.

Film Casting. The films were either cast from 2-3% (w/w) solution of the polymer in toluene onto horizontal surface of cellophane support. Dry films were detached from the support and subjected to vacuum pumping for several days at ambient temperature until they achieved constant weight. In this way so-called 'as cast' samples were obtained. After measurements of permeability the same films were immersed into ethanol, kept there for a night and then subjected again to vacuum pumping until constant weight is achieved. The films prepared in this manner were designated as 'EtOH treated'. The thickness of the films was 95 μm.

Gas Permeation Measurements: Two methods were used for determination of the gas permeation parameters: *Gas chromatographic technique* – In determination of the permeability coefficients using this method, a steady stream of penetrant gases under atmospheric pressure were introduced to the up-stream part of the cell, while a gas-carrier, helium or nitrogen (the latter in measurement of permeation rate of H_2 and He), was introduced into the down-stream portion. The partial pressure of the penetrant gases in the down-stream portion of the cell was close to zero. The permeability coefficients were determined by measuring the penetrant concentration in the gas-carrier and the total flow of this mixture. Temperature in the cell was 20-22 °C. *Barometric technique* – A Baratron (MKS) setup was also used in measuring gas permeability (*P*) and diffusivity (*D*) coefficients. The Daynes-Barrer (time-lag) method was used for the determination of the diffusivity coefficients. The following set of gases were investigated: He, H_2, O_2, N_2, CO_2, CH_4, C_2H_6, C_3H_8, n-C_4H_{10}. For light gases, the pressure range studied was mainly 0.1-2 bar, for hydrocarbons C_1-C_3 it was 0.1-5 bar, for n-butane it was 0.1-2 bar. Diffusivity coefficients were measured for all gases except He and H_2. In these cases, time-lags were too short to be adequately measured so the errors of the estimation of D were too large. Temperature of this experiments was also 20-22 °C.

Positron Annihilation Lifetime Spectroscopy: Positron annihilation lifetime spectroscopy (PALS) experiments were performed in a nitrogen atmosphere. A conventional fast-fast coincidence system EGG@ORTEC "fast-fast" lifetime

spectrometer was used. A nickel-foil-supported [^{44}Ti] titanium (IV) chloride radioactive positron source was used. Two stacks of film samples, each with a total thickness of about 1 mm, were placed on either side of the source. The time resolution was 300 ps (full width at the half maximum (fwhm) of the prompt coincidence curve). The contribution from annihilation in the source material, a background, and instrumental resolution were taken into account in the PATFIT program for treating the experimental lifetime data in four lifetime components. The resulting data were determined as an average value from the several spectra collected for the same sample, having an integral number of counts of at least 10^6 in each spectrum.

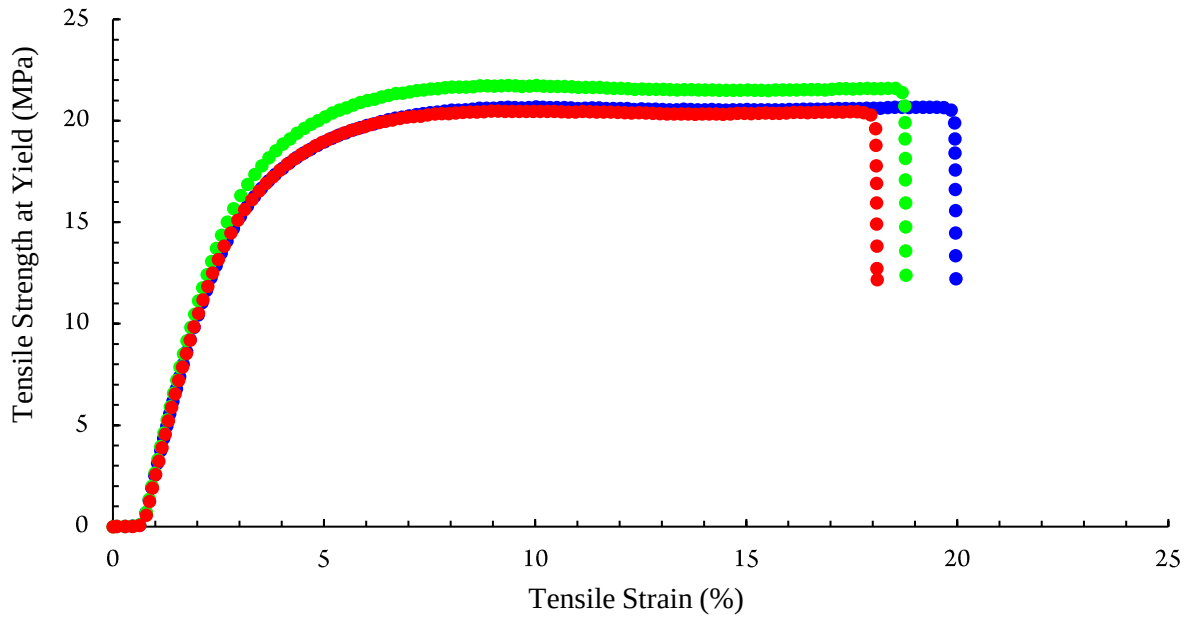

Figure 97. TGA analysis of poly(5-ethoxydimethylsilyl-2-norbornene) (**13e**) (**Table 6**, **entry 3**).

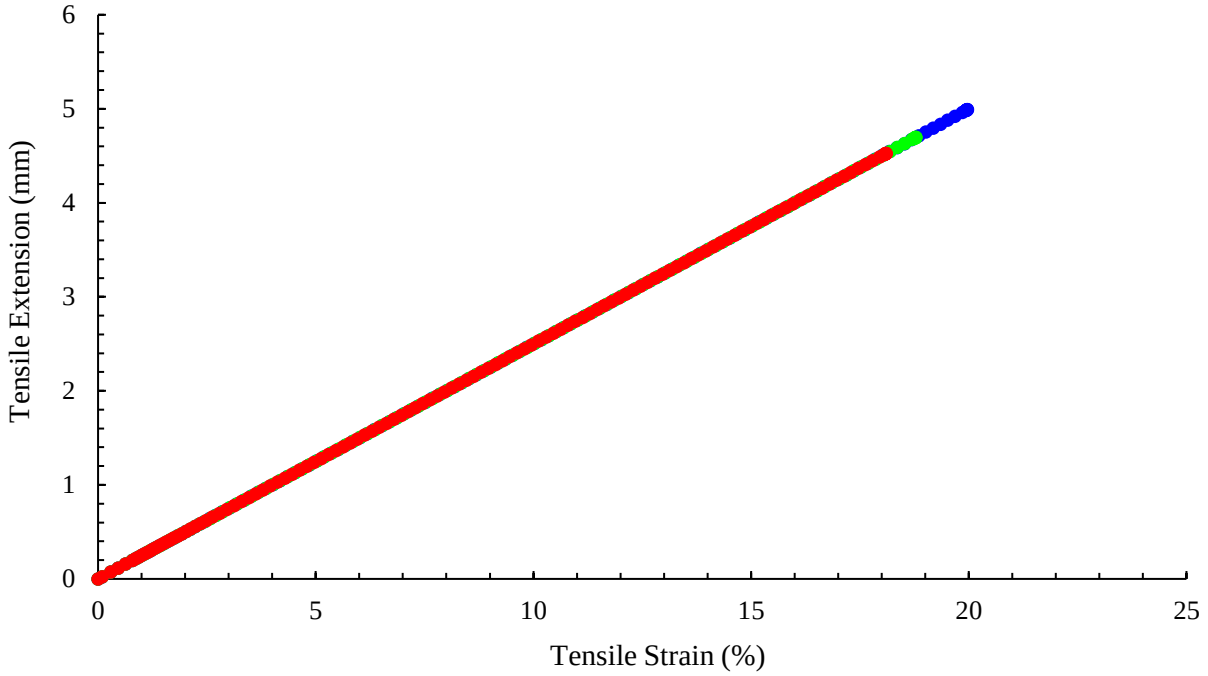

Figure 98. TGA analysis of poly(5-ethoxydimethylsilyl-2-norbornene) (**13e**) (**Table 6**, **entry 3**).

Appendix G: Experimental Methods and Supporting information for Chapter 7

Synthesis of 5-tris(2-methoxyethoxy)silyl-2-norbornene. To a 50 mL glass pressure tube equipped with a stir bar was added vinyltris(2-methoxyethoxy)silane (20.00 g, 71.33 mmol), dicyclopentadiene (4.49 g, 33.97 mmol), and hydroquinone (0.010 g, catalytic). The pressure tube was sealed and heated to 180 °C for 12 hours. After cooling, the mixture was purified by distillation at reduced pressure (0.3 torr, 132-138 °C) to yield 3.63 g of the desired monomer (30.9 % yield) as a mixture of *endo:exo* isomers (*endo:exo* = 62:38). ^{1}H NMR ($CDCl_3$, 293 K, *endo* isomer): δ (ppm) = 6.06 (1H, m), 5.87 (1H, m), 3.88 (6H, t), 3.46 (6H, t), 3.33 (12H, s), 2.89 (1H, s), 2.87 (1H, s), 1.75 (1H, m), 1.33-1.02 (3H, m), 0.48 (1H, ddd) ^{13}C NMR ($CDCl_3$, 293 K, *endo*/*exo* mixture): δ (ppm) = 137.65, 135.36, 134.65, 133.73, 73.70, 73.68, 62.13, 61.89, 58.87, 58.85, 50.70, 46.96, 44.12, 42.71, 42.43, 42.12, 26.87, 26.17, 20.59, 20.05 $HRMS^{calc}$ $C_{16}H_{30}O_6Si$ (H^+ adduct) = 347.1890 m/z $HRMS^{expt}$ $C_{16}H_{30}O_6Si$ (H^+ adduct) = 347.1889 m/z.

Synthesis of Vinyl-added Polynorbornenes. All polymerizations were run under air free conditions in an MBRAUN glovebox using *trans*-$[Ni(C_6F_5)_2(SbPh_3)_2]$ as the vinyl-addition catalyst and dry/degassed DCM as the solvent. In a typical polymerization, 5 µm of catalyst is added to 5 mmol of total monomer in 2 mL of DCM. The polymerization was allowed to react for 24 hours before diluting to 10 mL of DCM and precipitation into 250 mL of anti-solvent. Anti-solvents include methanol, acetonitrile, or hexanes depending on the feed ratio of the monomers. Polymers were isolated by vacuum filtration and dried *in-vacuo*.

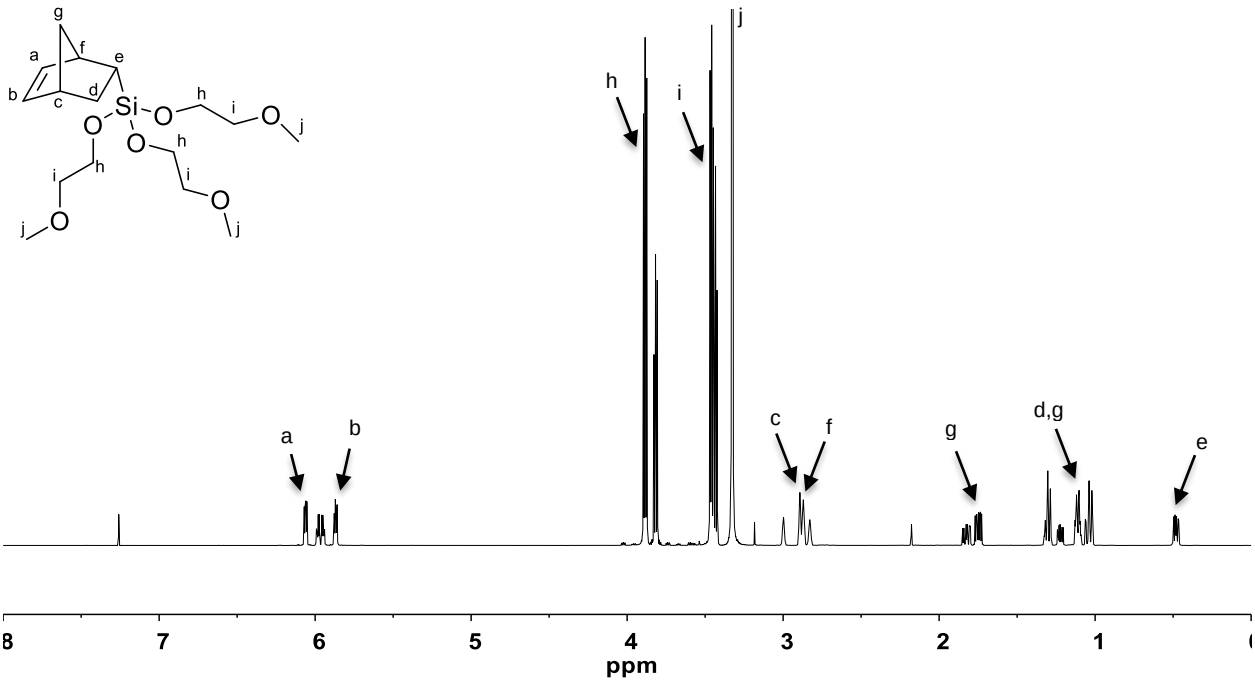

Figure 99. ^{1}H NMR spectra of 5-tris(2-methoxyethoxy)silyl-2-norbornene (**15d**) as *endo:exo* mixture (*endo* isomer labeled).

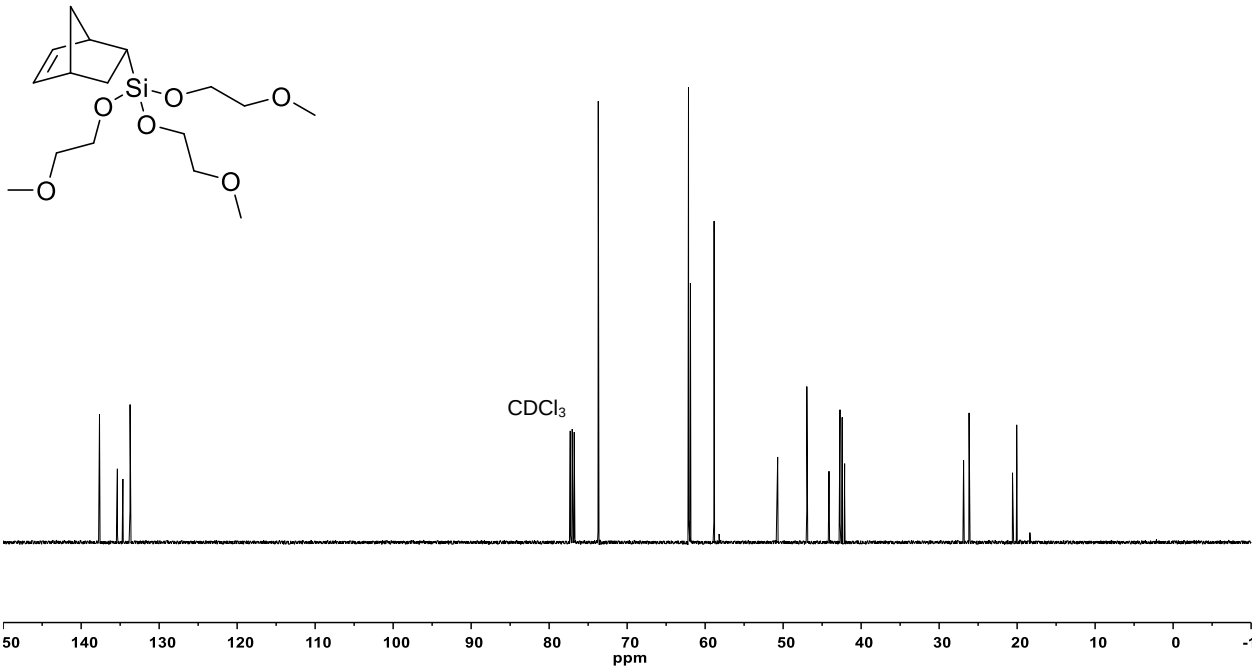

Figure 100. ^{13}C NMR spectra of 5-tris(2-methoxyethoxy)silyl-2-norbornene (**15d**) as *endo:exo* mixture.

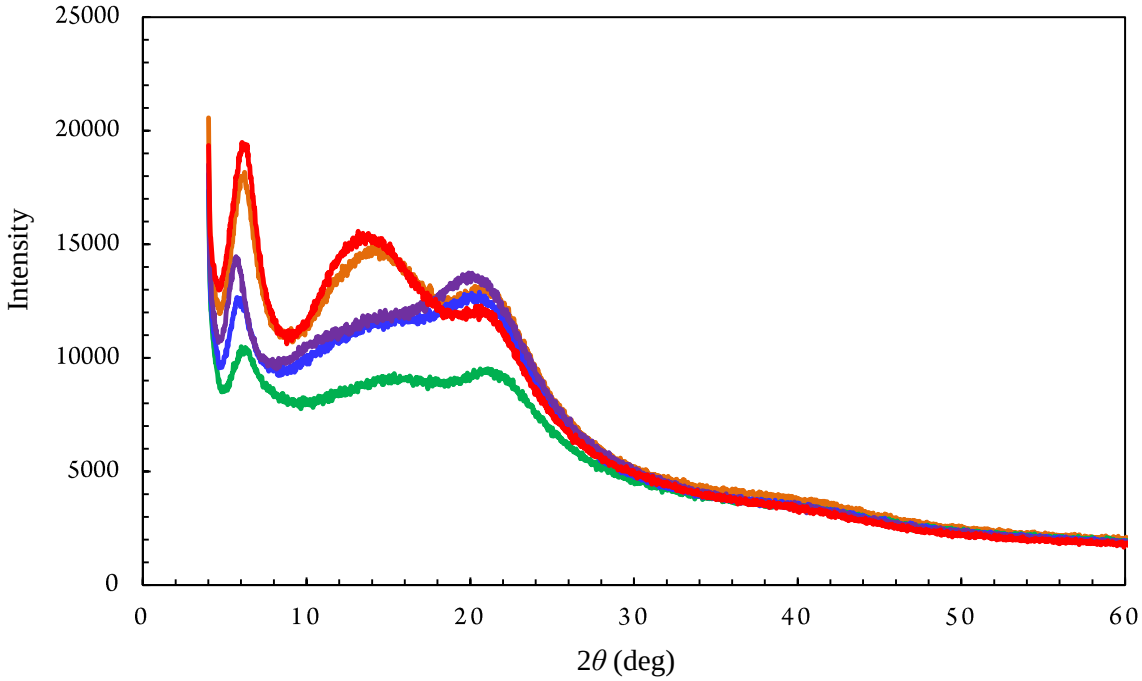

Figure 101. Wide angle XRD of copolymer series **13c**, **15a-d**.

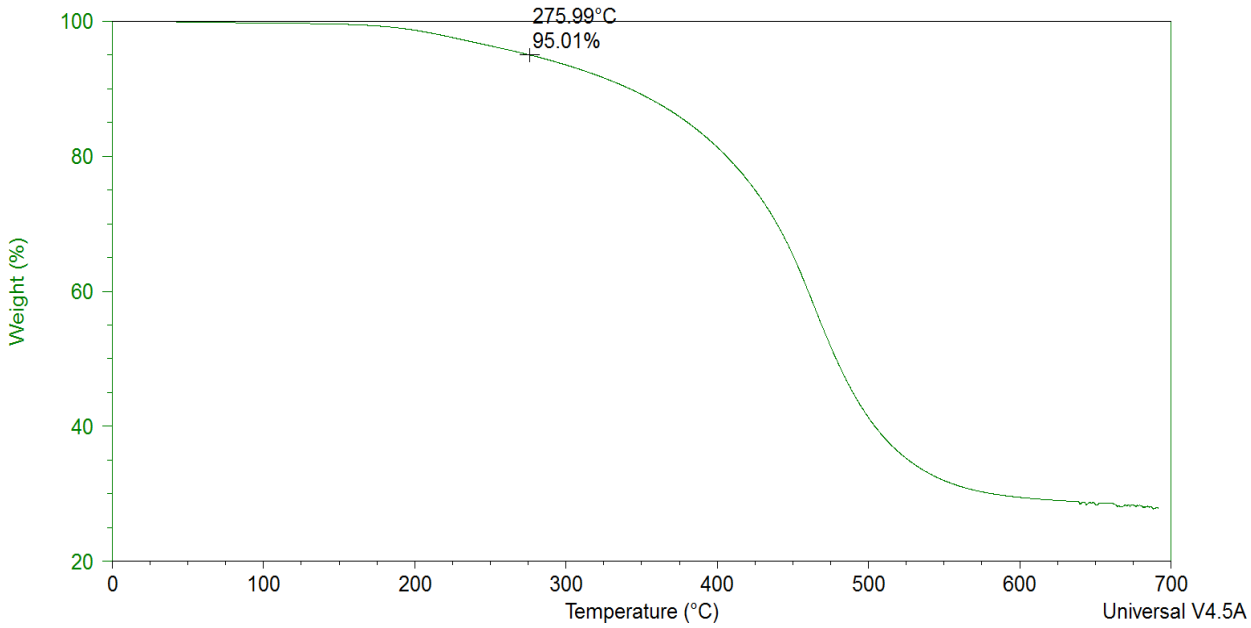

Figure 102. TGA analysis of poly(5-tris(2-methoxyethoxy)silyl-2-norbornene) (**15d**).

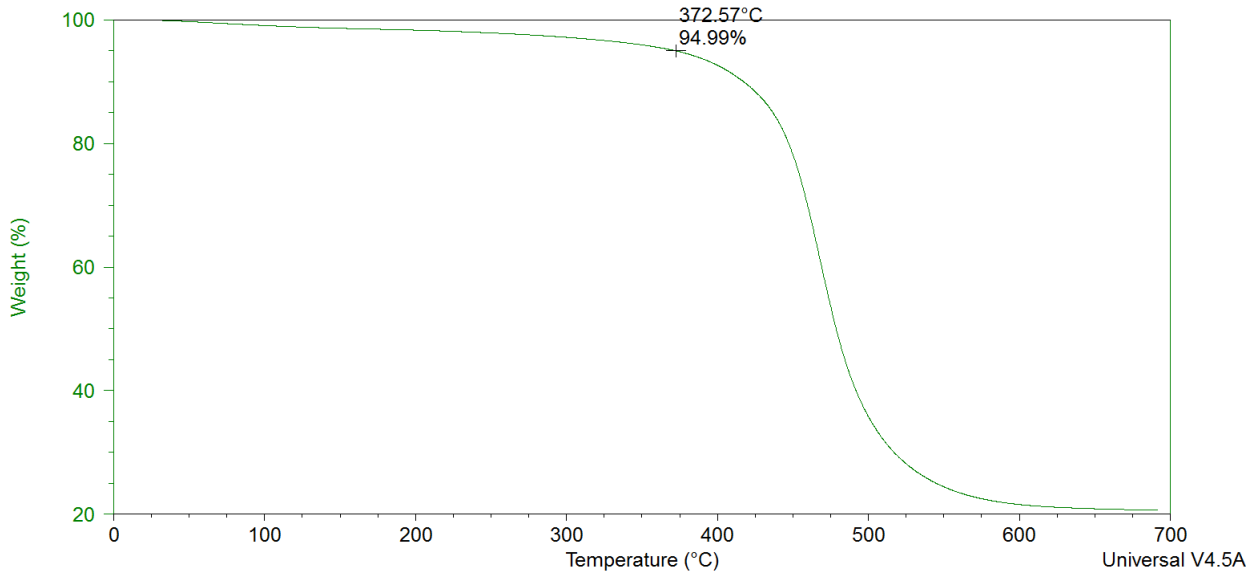

Figure 103. TGA analysis of **15c**.

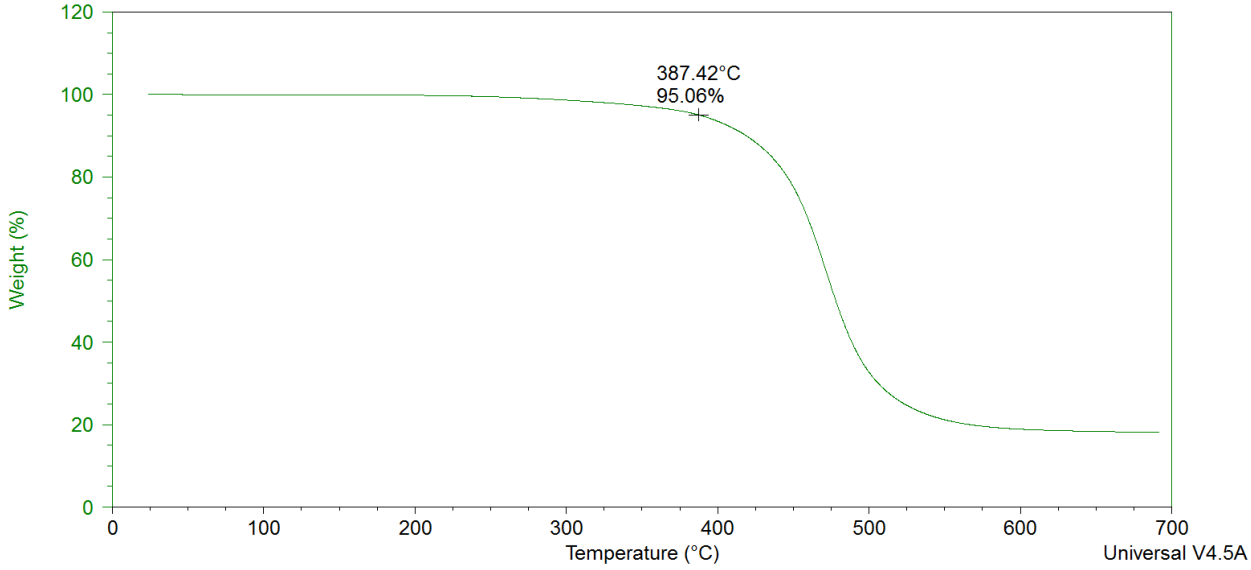

Figure 104. TGA analysis of **15b**.

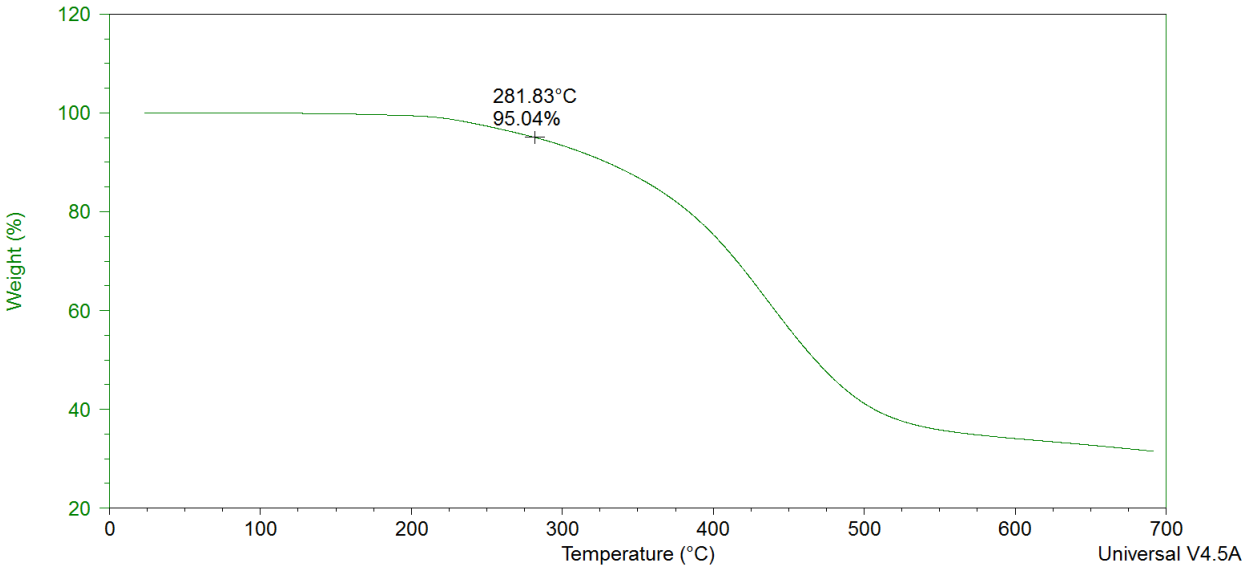

Figure 105. TGA analysis of **15a**.

Vita

Kevin R. Gmernicki was born in Brewster, NY and lived there until the age of 12, where he and his family moved to the metro-Atlanta area until he attended North Georgia College & State University, now known as the University of North Georgia (UNG). Here, he earned his Bachelor of Science in Chemistry with a minor in Mathematics graduating with Magna Cum Laude in 2012. In his undergraduate career, he worked on several research projects from holographic data storage to biocompatible electronics. Most notably, he spent a summer at Princeton University under the direction of Michael McAlpine. Following graduation, with his wife and dog, he moved to Knoxville, TN to start his pursue a Ph.D. in Organic Chemistry. He joined the lab of Dr. Brian K. Long and will be among his first Ph.D. graduates.

After the completion of his doctoral studies, he will have published five publications in peer-reviewed journals, given several presentations, constructed two custom instruments to measure gas permeability and solubility of polymers, and left behind a solid foundation for a new research avenue in the Long Laboratory. During this program, he developed several additional interests including catalyst design, polymers synthesis, material science, and polymer characterization.